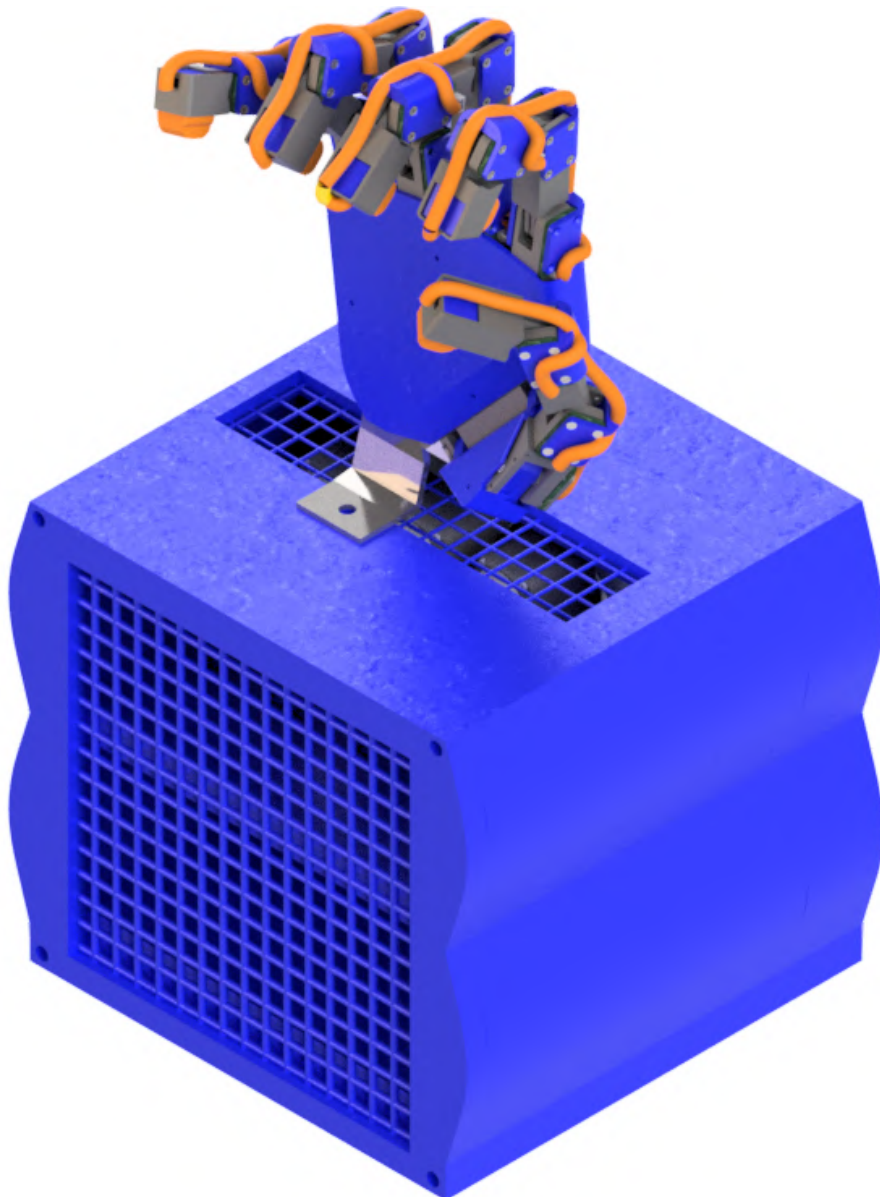


# Design and Manufacture of a 3D-Printed Robot Hand with Soft Tactile Skin

Ahmed Sami Deiri, Mohammed Al Bashar Khan, Kai Page, Jamie Sengun, Talha Tailor  
Supervised by Dr Lorenzo Jamone and Dr Ketao Zhang

MAT7400 - Final Report



School of Engineering and Materials Science  
Queen Mary University of London  
United Kingdom  
May 2020

# Specific Learning Differences Cover Note

Student ID: 160473124

## Guidelines for markers assessing coursework and examinations of students diagnosed with Specific Learning Differences (SpLDs).

As far as the learning outcomes for the module allow, examiners are asked to mark exam/essay scripts sympathetically, ignoring the types of errors that students with SpLDs make and to focus on content and the student's understanding of the subject.

### SpLDs may affect student performance in written work in the following ways:

- Spelling, grammar and punctuation may be less accurate than expected
- Organisation of ideas may be confused, affecting the overall structure of written work, despite including appropriate and interesting content
- Proof reading may be weak with some errors undetected, particularly homophones and homonyms which can avoid spell checkers

Under examination conditions, these difficulties are likely to be exacerbated, particularly towards the end of scripts.

When marking, please ensure the following guidance is adhered to:

- Scan the text for content to gain an overview of the work, to avoid making a judgement based on the structure alone or any minor spelling and grammar errors
- Do not comment solely on spelling and grammar issues, SpLD students are usually aware of this already. If you feel this is a major problem which has affected the sense of the writing, then please encourage the student to use their study skills support from DDS to help with this.
- Include positive and constructive comments amongst the feedback so that students can acknowledge their strengths but work with specialist study skills tutors on developing new strategies for areas of difficulty.
- Use clear English providing specific examples of what is right or wrong, to ensure that the student knows what to improve upon for future work

Colleagues in Schools and Institutes are asked to encourage students with specific learning differences to access the support provided by the Disability and Dyslexia Service (<http://www.dds.qmul.ac.uk/dyslexia/>) if they have any concerns about a student's work.

For more information regarding marking guidelines see the Institutional Marking Practices for Dyslexic Students ([http://adshe.org.uk/wp-content/uploads/marketing\\_guidelines\\_for\\_good\\_practice.docx](http://adshe.org.uk/wp-content/uploads/marketing_guidelines_for_good_practice.docx)) on the DDS webpage.

### Disability and Dyslexia Service

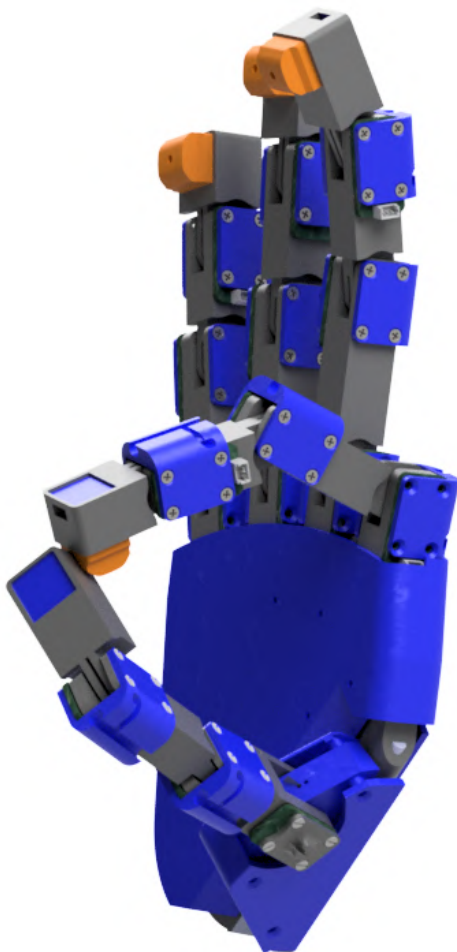
<http://www.dds.qmul.ac.uk/> (<http://www.dds.qmul.ac.uk/>)

Disability and Dyslexia Service  
Room 3.06, Francis Bancroft Building  
Queen Mary University of London  
Mile End Road  
London  
E1 4NS

T: +44 (0) 20 7882 2756 (tel:+442078822756)  
F: +44 (0) 20 7882 5223  
E: [dds@qmul.ac.uk](mailto:dds@qmul.ac.uk) (<mailto:dds@qmul.ac.uk>)  
W: [www.dds.qmul.ac.uk/](http://www.dds.qmul.ac.uk/) (<http://www.dds.qmul.ac.uk/>)

## Declaration

This project report entitled: **Design and Manufacture of a 3D-Printed Robot Hand with Soft Tactile Skin** was composed by us and is based on our own work. Where the work of the others has been used, it is fully acknowledged in the text and in captions to table illustrations. This project report has not been submitted for any other qualification.



Names: Ahmed Sami Deiri, Mohammed Al Bashar Khan, Kai Page, Jamie Sengun, Talha Tailor

Signatures:

Date:

## Acknowledgements

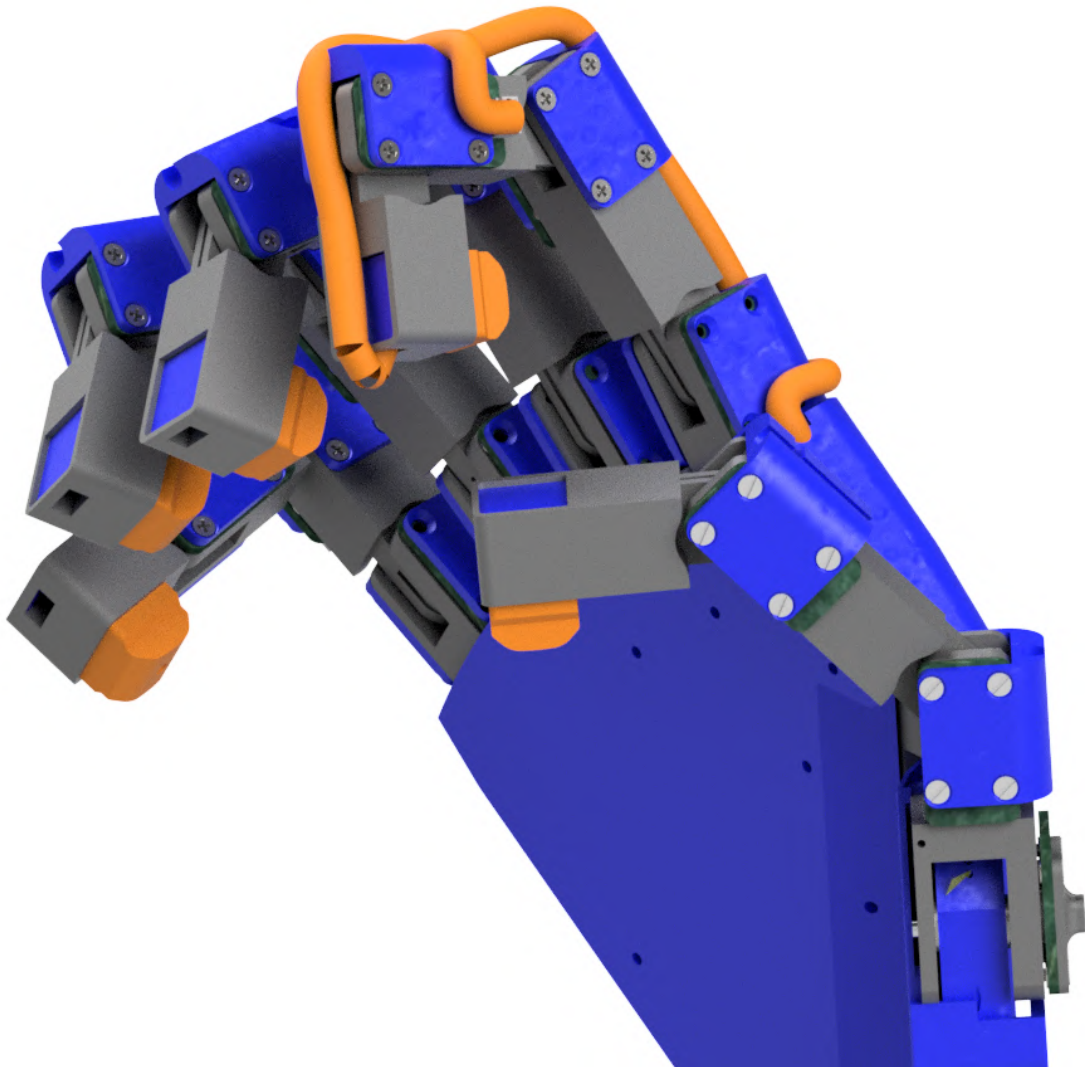
We would like to acknowledge and thank:

Dr Lorenzo Jamone and Dr Ketao Zhang for supervising the project and providing us with invaluable feedback and guidance.

Joshua Brown in the ARQ laboratory for assistance with the use of the Stereolithography (SLA) printing.

Clement Cordery, Nick Duggan, Dennis Ife and James Searles from the Makerspace and Mechanical workshop for their advice and assistance with the metal working for the D-shafts and Fused deposition modelling (FDM) 3D printing.

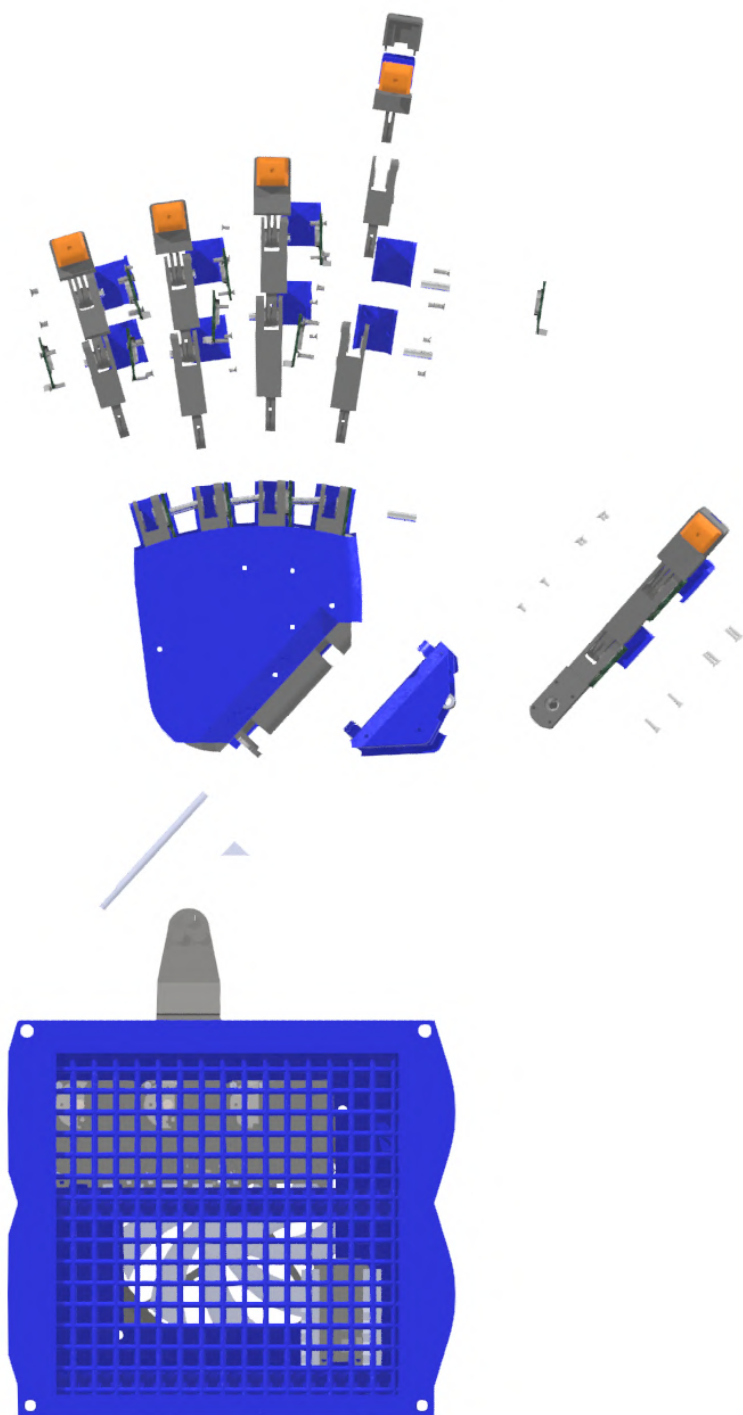
We'd also like to thank all the members of the NHS for working through this crisis and keeping us healthy and able to complete this project.



## COVID 19 Effect on Project

Due to the Covid-10 abruptly disturbing our lives and causing everyone to work remotely, many of the original tasks and plans were adjusted to fit for remote working. This meant the project shifted from physical building of the robot hand to more simulations to prove how each part of the project is tested.

The changes to the tasks and objectives from this effect is outlined in I.



## Abstract

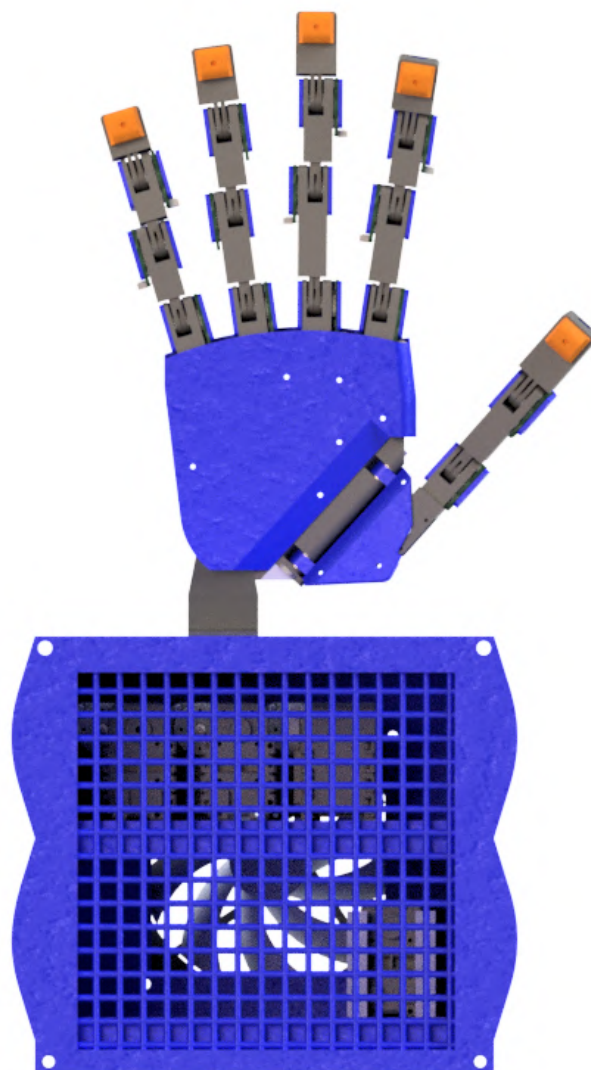
This paper consists of the design and partial fabrication of a 9 DoF, tactile sensing robotic hand. A large portion of the hand utilises 3D printed processes and designed for modularity and to be cost-effective- without sacrificing dexterity and maintaining in-hand manipulation capabilities. The hand is designed to be a self-contained system, all actuation and sensing is built into the hand/ forearm, and mountable on a UR5 robot arm.

The hand has many possible uses including research in grasping, manipulation, and industry quality control. The current hand is a low-cost design and with further development it could have potential uses in other industrial fields such as the supervised manipulation sector.

Rotational potentiometers are fitted at every joint region to measure joint angle- raw voltage readings can be obtained using an Arduino and processed into angles using Python scripting on a Raspberry Pi. Tactile sensing is carried using 3D and 1D hall-effect sensors (1D Honeywell SS495A and 3D Melexis MLX90393). A silicone soft skin is used, embedding the hall effect magnet measuring the flux density with the deformation. Testing was carried out of the moulded silicone fingertips with the 3D MLX90393 hall effect sensors presenting a gradual increase in magnetic field when mass was added, correlating to the magnet in the soft skin moving closer to the MLX90393 sensor. Finite element analysis of the sensor measurement/ displacement range (with respect to normal shear forces) presented the proximity of the magnetic used to sensor, and thus the compliancy of the silicon soft skin.

Various aspects of design and testing could not be fully completed due to the Covid-19 situation. Thus, Mujoco (physics simulation) was carried out to determine sensor placement and possible grasping capabilities. This presented positive results for power grasping of various objects, with the hand capable of also performing various precision grasps including the tripod grasps. Data suggested the addition of tactile sensing on the side of the palm area would provide sensory results when performing certain grasps including the tripod grasp, as well as supporting placement on the fingertip regions. In-hand manipulation testing of the real hand could not be carried out.

The discussed project's CAD files, drawings and software can be accessed at [https://github.com/sam-eee/jamkit\\_robot\\_hand](https://github.com/sam-eee/jamkit_robot_hand)



## Commonly used abbreviations

- CSV - Comma Separated Value, a type of file format for data.
- DIP - Distal Interphalangeal Joints
- DMLS - Direct Metal Laser Sintering
- DOF - Degree of Freedom
- FDM - Fused Deposition modelling (3D printing technology)
- I2C - Inter-Integrated Circuit, a serial data protocol developed by Philips
- ID - Identification Number
- IDE - Integrated Development Environment
- MCP - Metacarpophalangeal Joints
- PCB - Printed Circuit Board
- PIP - Proximal Interphalangeal Joints
- PWM - Pulse Width Modulation
- ROS - Robot Operating System
- SAT - Refers to a 3D model file format
- SDA - Serial Data, the data communication line for the I2C protocol
- SCL - Serial Clock, the clock signal line for the I2C protocol
- SOTA - refers to the State of the Art Report which has already been completed for this project.
- SLA - Stereolithography, refers to the 3D printing process
- STL - Stereolithography, refers to file format for 3D models
- TFX - A small form factor standard for computer power supplies
- TMC - Trapeziometacarpal joint
- WRT. - With respect to



## CONTENTS

<b>I</b>	<b>Part A - Summary of Project</b>	1
I-A	Rationale . . . . .	1
I-B	Aims . . . . .	1
I-C	Objectives . . . . .	1
I-D	Overview of tasks . . . . .	3
I-E	Final Gantt Chart . . . . .	5
<b>II</b>	<b>Design Concepts</b>	8
II-A	Fingertip Design - Kai Page . . . . .	8
II-A1	Design Constraints . . . . .	8
II-A2	Prototype I . . . . .	8
II-A3	Prototype II - Current Design . . . . .	9
II-B	Soft Skin Design - Kai Page . . . . .	10
II-B1	SLA 3D Printed Elastic Resin - Material, Design & Manufacturing - Kai . . . . .	10
II-B2	Moulded Silicone - Material, Design & Manufacturing - Kai . . . . .	11
II-C	Actuation Concept and Evaluation - Ahmed Sami Deiri . . . . .	11
II-D	Link Design Prototyping - Ahmed Sami Deiri . . . . .	12
II-D1	Rolling Joints . . . . .	12
II-D2	Axle based joints . . . . .	12
II-E	Final Link Design - Ahmed Sami Deiri . . . . .	13
II-E1	Modularity in Design . . . . .	14
II-F	Distal Link - Ahmed Sami Deiri . . . . .	15
II-G	2nd Flexion/Extension DOF at the Index and Middle finger - Ahmed Sami Deiri . . . . .	15
II-H	Proprioceptive Sensing - Ahmed Sami Deiri . . . . .	16
II-I	Kinematic Modelling of the Fingers - Ahmed Sami Deiri . . . . .	17
II-J	Link Manufacturing optimisation - Ahmed Sami Deiri . . . . .	17
II-K	Link Lengths - Kai Page . . . . .	18
II-L	Finger Performance and Behaviour - Ahmed Sami Deiri . . . . .	19
II-M	Weight Reduction in the Finger link - Ahmed Sami Deiri . . . . .	20
II-N	Palm Design and covers - Talha Tailor . . . . .	20
II-N1	Tendon and wire routing - Talha, Bashar . . . . .	21
II-O	Thumb design - Talha Tailor . . . . .	22
II-O1	Design constraints . . . . .	22
II-O2	Prototype I, II . . . . .	22
II-O3	Prototype III & Final Design . . . . .	22
II-P	Wrist Design - Mohammed Al Bashar Khan . . . . .	23
II-Q	Motor Placement - Mohammed Al Bashar Khan . . . . .	25
II-Q1	Tendon routing material - Mohammed Al Bashar Khan . . . . .	25
II-R	Wrist Electronics - Mohammed Al Bashar Khan . . . . .	26
II-S	Pulleys - Mohammed Al Bashar Khan . . . . .	26
II-T	Motor Rails - Mohammed Al Bashar Khan . . . . .	26
II-U	Mounting Bracket - Mohammed Al Bashar Khan . . . . .	27
II-V	Electric Power Enclosure - Jamie Sengun . . . . .	27
<b>III</b>	<b>Mujoco Simulation - Talha Tailor</b>	28
III-A	Model Creation - Talha Tailor . . . . .	28
III-B	Simulation Data . . . . .	28
III-B1	Minimum grasping force . . . . .	28
III-B2	Tripod grasping . . . . .	29
III-C	Sensor Placement Analysis - Talha Tailor . . . . .	30
III-D	Validity and Accuracy - Talha Tailor . . . . .	30
<b>IV</b>	<b>Working principle</b>	30
IV-A	Degree of Freedom (DoF) - Kai, Talha . . . . .	30
IV-B	Differential pulley - Talha Tailor . . . . .	30

<b>V</b>	<b>Soft Skin Tactile Sensing - Kai Page</b>	31
V-A	Finite Element Magnetic Model (FEMM) - Kai . . . . .	31
V-B	Experimental Testing - Kai . . . . .	32
	V-B1     Hypotheses . . . . .	32
	V-B2     Methodology . . . . .	32
	V-B3     Results & Discussion . . . . .	33
V-C	Limitations - Kai . . . . .	37
<b>VI</b>	<b>FEM analysis of fingertip - Mohammed Al Bashar Khan</b>	37
VI-A	Finite Element method (FEM) - Mohammed Al Bashar Khan . . . . .	37
VI-B	Geometry - Mohammed Al Bashar Khan . . . . .	38
VI-C	Materials - Mohammed Al Bashar Khan . . . . .	38
VI-D	Load - Mohammed Al Bashar Khan . . . . .	39
VI-E	Boundary Condition - Mohammed Al Bashar Khan . . . . .	39
VI-F	Mesh - Mohammed Al Bashar Khan . . . . .	39
VI-G	Analysis of fingertip response to normal force - Mohammed Al Bashar Khan . . . . .	40
	VI-G1     Stress . . . . .	40
	VI-G2     Displacement . . . . .	41
VI-H	Analysis of fingertip response to shear force - Mohammed Al Bashar Khan . . . . .	42
	VI-H1     Load from the top . . . . .	42
	VI-H2     Load from the Side . . . . .	43
VI-I	Analysis of fingertip reaction with different material - Bashar . . . . .	45
	VI-I1     Normal Force . . . . .	45
	VI-I2     Shear Force . . . . .	46
VI-J	Analysis of results and design improvements - Mohammed Al Bashar Khan . . . . .	47
	VI-J1     Hollow Fingertip . . . . .	47
	VI-J2     Mesh Convergence . . . . .	48
VI-K	Fingertip Material - Mohammed Al Bashar Khan . . . . .	49
VI-L	Result Analysis - Mohammed Al Bashar Khan . . . . .	49
<b>VII</b>	<b>Component Justifications &amp; Bill of Materials</b>	50
VII-A	Bill of Materials - Jamie Sengun . . . . .	50
VII-B	Component Justification . . . . .	50
VII-B1	Dynamixel AX-12A motors - Jamie Sengun . . . . .	50
VII-B2	ROBOTIS U2D2 Controller - Jamie Sengun . . . . .	52
VII-B3	Adafruit TCA9548A I2C Multiplexer - Jamie Sengun . . . . .	52
VII-B4	Melexis MLX90393 - Jamie Sengun . . . . .	52
VII-B5	Honeywell SS495A - Jamie Sengun . . . . .	53
VII-B6	MagnetExpert N42 2 mm diameter, 1 mm thick cylindrical magnets - Jamie Sengun . . . . .	54
VII-B7	Molex Picoblade Connectors & Wire - Jamie Sengun . . . . .	54
VII-B8	Murata SV01A103AEA01B00 - Jamie Sengun . . . . .	54
VII-B9	Arduino Uno, Velleman KA-12 & Wiring - Jamie Sengun . . . . .	55
VII-B10	Raspberry Pi 3B+ - Jamie Sengun . . . . .	55
VII-B11	TFX Power supply unit & Power breakout board - Jamie Sengun . . . . .	55
VII-B12	PowerPro Braided Line 40kg (0.41 mm) - Jamie Sengun . . . . .	56
VII-B13	Artic F12 120 mm Fan, Dust filter - Jamie Sengun . . . . .	56
VII-B14	Ecoflex Silicone Rubber - Kai . . . . .	56
VII-B15	Araldite 2011 - Adhesive paste - Kai Page . . . . .	56
VII-B16	3D Printing Material for Links, Palm and Wrist - Mohammed Al Bashar Khan . . . . .	56
<b>VIII</b>	<b>Electronics Schematic - Jamie Sengun</b>	57
<b>IX</b>	<b>Robot Motor &amp; Sensor Software/Libraries - Jamie Sengun</b>	57
<b>X</b>	<b>ROS Package - Ahmed Sami Deiri</b>	60
X-A	Generating the Simulation Model - Ahmed Sami Deiri . . . . .	61
X-B	Simulation of Model - Ahmed Sami Deiri . . . . .	61
X-C	Simulation of the Proprioceptive Values - Ahmed Sami Deiri . . . . .	61
X-D	Controlling the Motors - Ahmed Sami Deiri . . . . .	62
X-E	Setting a zero position for the hand - Ahmed Sami Deiri . . . . .	63

<b>XI Evaluation &amp; Future Work</b>	63
XI-A Manufacturing . . . . .	63
XI-A1 Weight . . . . .	64
XI-A2 Size . . . . .	65
XI-A3 Maintenance, Customisability and Repair . . . . .	65
XI-B Performance . . . . .	66
XI-B1 Link Lengths . . . . .	66
XI-B2 Fingers and Palm . . . . .	66
XI-B3 Wrist . . . . .	66
XI-C Grasping and manipulation . . . . .	66
XI-D Exteroception Sensing . . . . .	67
XI-E Proprioception Sensing . . . . .	67
XI-F Safety . . . . .	68
XI-G Comparison to State of the Art Technology . . . . .	68
<b>References</b>	69
<b>XII Appendix</b>	71
XII-A Weight Breakdown of the Hand - Ahmed Sami Deiri . . . . .	71
XII-B Part List of all Designed Components - Kai Page . . . . .	73
XII-C Dynamixel Python Motor Control - ax12_open.py - Jamie Sengun . . . . .	74
XII-D Dynamixel Python Motor Control - ax12_close.py - Jamie Sengun . . . . .	74
XII-E Dynamixel Python Motor Control - ax12_move.py - Jamie Sengun . . . . .	74
XII-F Dynamixel Python Motor Control - ax12_getpos.py - Jamie Sengun . . . . .	74
XII-G Dynamixel Python Motor Control - ax12_disable_torque.py - Jamie Sengun . . . . .	75
XII-H Dynamixel Python Motor Control - ax12_enable_torque.py - Jamie Sengun . . . . .	75
XII-I Dynamixel Python Motor Control - Manual sliders. motorsliders.py - Jamie Sengun . . . . .	76
XII-J Arduino Sensors - MLX90393 & Analog sensors. Arduino_sensors.ino - Jamie Sengun . . . . .	78
XII-K Python sensor data gathering for processing Sensor_process.py - Jamie Sengun . . . . .	80
XII-L Split raw sensor data array Sensor_split.py - Jamie Sengun . . . . .	81
XII-M Process raw rotational potentiometer data into angles rot_process.py - Jamie Sengun . . . . .	82
XII-N Process raw hall effect data into magnetic density flux in $\mu\text{T}$ units hf_process.py - Jamie Sengun . . . . .	83
XII-O MLX90393 Sensitivty Parameters - from Datasheet - Jamie Sengun . . . . .	84
XII-P MLX90393 Sensor Range - from Datasheet - Jamie Sengun . . . . .	84
XII-Q MLX90393 maximum output data rate ( <i>ODR</i> ) -from datasheet - Jamie Sengun . . . . .	84

## I. PART A - SUMMARY OF PROJECT

### A. Rationale

When looking at the field of robotic hands we see many implementations of robot hands with a variety of tactile sensors employed. During our research, we have also seen implementations of 1D & 3D soft skin embedded magnet-based force tactile sensors [1] [2] [3] with various implementations, some combining an array of sensors along a fingertip [3] to provide localised forces distributions at the contact points. These systems have been implemented as added sensor arrays onto pre-existing robot hands. For this project we aim to create a commercially viable and reproducible design for a dexterous robot hand that has a magnetic-based tactile sensing array embedded to achieve in-hand manipulation. Unlike the pre-existing designs we aim to explore the ground-up design implications of using such a sensor for in-hand manipulation as our primary focus, with commercial viability and optimisation also being key considerations.

### B. Aims

1. To design and build a dexterous, low cost, and 3D printable robot hand with an embedded tactile sensor suited for grasping and manipulation.
2. To conduct grasp, manipulation and dexterity tests to evaluate the performance of the design

### C. Objectives

#### 1. Performance

- 1.1. To explore how a robotic hand is able to mimic and compares to the kinematics of a human hand for grasping.

**Outcome:** Though initial plan was to do physical testing of the hand, due to the COVID-19 situation, we had to adapt and prove with simulations that it is able to perform kinematics of a human hand for both power and precision grasps such as the tripod grasp.

- 1.2. The hand design must be capable of performing in-hand manipulation of objects with various sizes and shapes.

**Outcome:** We have proved by computer simulations that the hand is able to in-hand manipulation using a pen.

- 1.3. The hand must be able to draw a series of strokes using only the in hand manipulation.

**Outcome:** We highlighted that the hand can perform straight strokes up of at least 20 mm while holding the pen however real world behavior may vary.

- 1.4. The hand must be capable of performing precision grasps on a pen such as the tripod precision grasp.

**Outcome:** The simulated hand model was able to meet this objective by the way the pen was grasped with the index, middle and the thumb; using a tripod grasp.

- 1.5. To explore the hand loading capability for different grasping techniques achieved by the hand.

**Outcome:** Though physical testing of different weights cannot be performed, since all fingers can hold the same load, they will be able hold the same load. However, we were not able to calculate the max loading capability in terms of mass that the hand can hold using its motors. It can afford to carry up to a 2.31 kg payload when mounted onto a UR5 Robot arm (assuming the hand could carry that payload).

### 2. Manufacturing and Structure

- 2.1. The hand must utilise 3D printing.

**Outcome:** FDM 3D printing is utilised throughout for the structure of the main hand (Fingers, thumb, palm) in addition to the wrist supporting structure. SLA 3D Printed was tested initially for creating complex soft skin geometries for use with the tactile sensors; however, due to slow printing turnaround, availability and the COVID-19 situation this method was not utilised past initial print testing.

- 2.2. The hand must have a compliant contact surface to prevent damage to grasped objects.

**Outcome:** Silicone was used to ensure a compliant and soft surface for the fingertips when grasped. However, the idea to cover the whole hand with the same compliant material is added in future works as COVID-19 prevented us from producing the soft skin for the whole hand.

- 2.3. The design should be modular.

**Outcome:** The final proposed design consists of many components that are consistent within the project such as the finger links. All of these parts are designed with the ability for an end user to remove and replace them with minimal effort. This was achieved by relying primarily on temporary joints such as bolts and threaded inserts rather than permanent fixings. The consistent design means the parts could be completely changed as long as the interfacing parts (male and female on the Link body) are maintained.

- 2.4. The hand must be easy to maintain and repair.

**Outcome:** The fingertips have been made to be easily replaceable without causing damage to the rest of the hand by adhering them to an easily replaceable thin sheet of plastic which slots into the fingertip. This focus on easy repairability can be seen throughout the design as the hand is designed with the ability to remove and replace sections along the hand without needing to replace the children. For example, any finger link can be removed using a system of bolts and replaced without needing to modify the other links within the chain. The hand relies on a system of temporary joints using bolts and threaded inserts/nuts rather than permanent joints. The only permanent joint present within the hand is used to adhere the fingertip to a cheap and easily replaceable 3D printed plastic piece.

- 2.5. The design must require minimal skilled labour to manufacture (maximise use of CNC and automa-

tion in production).

**Outcome:** Our design mainly utilises 3D printing which will not require much skills if the CAD models are made, with improvements in 3D printing technologies providing a much more user friendly manufacturing process with industry focus shifting towards reliability and user experience. Most parts produced are able to be printed with minimal or no post-processing required. The assembly process is straightforward and could be done with a set of hex keys and a soldering iron. The printed PCB poses a manufacturing challenge as they require a separate manufacturing process to 3D printing, however, services are able to provide this part for a relatively low cost. PCB parts still meet the minimal skilled labour as surface mounting and assembly could be automated. If demand for production increases, the majority of the parts could be adapted for higher quantity manufacturing processes such as CNC machining, laser cutting, or even injection moulding. These methods may require a more skilled labour force to operate and therefore manufacture.

- 2.6. The hand must be mountable onto a robot arm such as the UR5 robot arm (max weight of 5 kg).

**Outcome:** The total weight of the hand assembly to be mounted on the Robot arm was 2.69 kg, with the center of gravity falling within the UR5 specified distance as discussed in section XI-A1. The hand also has a mounting plate which allows for easy mounting onto the robot arm without requiring access to the internals of the wrist assembly, making it a relatively simple mounting process. The mounting plate has 4 holes in the bottom which match the UR5 mounting interface.

### 3. Sensing

- 3.1. The hand design should use sensors where necessary to maintain proprioceptive awareness of its kinematic configuration.

**Outcome:** The hand utilises rotational potentiometers for each rotational joint on the robot hand; totalling to 16 potentiometers, where the raw voltage readings can be obtained using an Arduino and processed into angles using Python scripting on a Raspberry Pi within the provided ROS package, which can be used in the discussed forward kinematic model

- 3.2. The hand should employ tactile sensors to detect normal and shear forces along the fingertips.

**Outcome:** Hall effect sensors, 1D Honeywell SS495A and 3D Melexis MLX90393 are utilised in the fingertips. These sensors measure the magnetic flux density of magnets embedded within a soft deformable skin centred at a distance away from the sensor. Deformation of the soft skin due to a force displaces the magnet which in turn changes the magnetic flux density reading on its respective sensor.

- 3.3. The sensors must allow for force vectoring along the fingertip.

**Outcome:** The current fingertip design utilises a 3D hall effect sensor within the index finger, middle finger and thumb. We have proven that the fingertip utilising these sensors is able to detect 3D displacement of the magnet, which could be combined with knowledge of the soft fingertip to determine the force magnitude and direction. This is not possible with the 1D force sensing implementation seen in the ring and little finger. Due to the use of only one sensor per fingertip we are unable to localise force position on any of our fingers.

- 3.4. Sensor measurement range must be optimised relative to the embedded supporting material and grasp forces by using computer and physical simulations.

**Outcome:** A simulation package; FEMM, was used to determine the displacement range in which the embedded magnet will reach a level of magnetic saturation for the sensor. This determined how close the magnet can get to the sensor, hence exploring how stiff the soft skin should be.

- 3.5. Creation of a software solution for obtaining independent sensor readings and signal processing.

**Outcome:** Arduino code is used to obtain all sensor readings and forward them to Python code running on a Raspberry Pi upon request. Python code is used to format and process the sensor data to a standardised output format for use within ROS, with a modular approach to signal processing relying on publish and subscribe for communication. This could therefore allow any 3rd party to access the sensor information at every level of abstraction if required.

### 4. Control

- 4.1. The hand must allow for accurate kinematic modelling and predictable movement.

**Outcome:** The hand design uses rigid links and revolute joints, which means the motion is well constrained. However, due to the low number of degrees of freedom per finger with some free links, predictable models of the hand would be difficult to achieve. Some level of predictability is afforded by the use of elastic materials which allows for approximate models regarding the ratio of bending to be calculated, but would not provide predictable motion under any resisting load, and may be prone to manufacturing errors. The proprioceptive sensors within the hand would allow for an accurate evaluation of the hand's current configuration, which could be used to move the hand until a desired grasp is achieved. Therefore we can say that the hand configuration is not very predictable unless we account for the elastic material's behaviour due to the unactuated joints along the fingers

- 4.2. Sensors employed in the hand must allow for advanced control techniques and variation in forces applied to objects.

**Outcome:** The rotational potentiometers located on all joints are used to determine joint angles for proprioception. The hall effect sensors on the

- fingertips provide a means of force feedback with respect to the displacement of a magnet embedded in a soft skin to the sensor. Calibration of the tactile feedback setup is required in the future to reliably relate the magnetic flux density measurements of the hall effect sensors to forces in the normal and shear directions with respect to the soft skin and geometry. Normal and shear forces would be determined (MLX90393) for the thumb, index and middle finger. Normal forces would be determined (SS495A) for the ring and little finger. The use of the AX-12 Dynamixel motors provides a very capable actuation system, however more advanced control of the hand configuration and force is made difficult through the use of unactuated joints along the fingers.*
- 4.3. All relevant sensor data and actuator control should be aggregated in a single interface capable master controller/computer (eg. using a Raspberry Pi).
- Outcome:** A raspberry Pi using Python is used to request data from a slave Arduino, where the Arduino consistently records and forwards sensor readings for processing. Additionally, Python scripts on the Raspberry Pi is used to control all AX-12A servo motors. These scripts are all embedded within a ROS package which would be running on the Raspberry Pi, therefore allowing external users to interface directly with the hand using the Raspberry Pi thanks to the distributed architecture afforded through ROS. This system has not been fully implemented in terms of software for this particular configuration and currently sets up packages for local use, however it could be easily implemented when needed due to the modular structure and reliance on ROS for communication between nodes.
- 4.4. The hand control interface should allow for easy future expansion by utilising a modular software solution.
- Outcome:** The Python and Arduino code was designed in a modular sense to allow for the user to be able to plug and play certain parts of code and utilise them in ROS for hand control with additionally ability to use virtual inputs and outputs for testing/operation. This was implemented in the ROS package in a modular way with a reliance on subscriber/publisher and services for the operations. This therefore could allow easy access and modification to the program structure.
- 4.5. To explore and possibly implement a ROS package for the hand that combines the various programs developed.

**Outcome:** A ROS package was created to aggregate the scripts needed to collect and receive the sensor data, and process it. The key concepts behind robotics programming such as variable abstraction levels, modularity and a highly cohesive system with low coupling. Currently the package takes the form of an interface between the hardware of the robot and the developer, providing the

necessary I/O processing and control functionality to provide more abstract information such as joint angle which could be used to implement more advanced control algorithms. The package acts like a "driver" for the hand. This package was not tested with the real physical components due to the COVID crisis, but responded correctly to inputs within the real ranges.

## 5. Actuation

- 5.1. The actuation should be controllable electronically.
- Outcome:** The AX-12A motors are controlled with Python scripts running on a Raspberry Pi via a proprietary serial interface using a proprietary motor controller (ROBOTIS U2D2). All AX-12A motors are programmable through free manufacturer software solutions.
- 5.2. The actuators must allow for proportional positioning of the fingers.
- Outcome:** The proposed actuation system should be able to provide proportional control to the fingers in a limited manner. Firstly the number of actuated links was limited to 10 degrees of freedom, leaving many unactuated joints along the hand. The direction of motion of these links and movement behaviour under 0 load could be easily predicted, however the ability to predict configuration was deemed to be more difficult when a load is experienced along the hand. The ring and little finger are able to extend and flex along the entire finger with little control over individual joint movement during run-time. The index and middle finger had 2DOF with one unactuated joint around J2. This meant that the finger should be able to reliable flex and extend around J1, however rotation around J2 and J3 would be difficult to reliably control during run-time beyond the direction (flexion or extension). The thumb has 3 DOF, with a fully proportionally actuated J1 and J2, and a single actuator for the flexion and extension along J2/J3.
- 5.3. All actuation must be self contained within the robotic system (ie within the hand or a possible wrist).
- Outcome:** The wrist has been designed to include the mounting of all AX-12A motors in addition to the majority of the PCBs: Arduino Uno (incl Velleman KA-12 shield), Raspberry Pi, TCA9584A I2C multiplexer, PCA9685 driver and 6-port AX/MX power hub.

## D. Overview of tasks

The following provides an overview of the tasks located in the Gantt chart located in section I-E; not including the coursework tasks. All tasks assignments were chosen by individuals after a group discussion. The responsibilities for these tasks groupings are highlighted in the Gantt charts.

1. Stage 1 - Joint & finger creation & sensor testing:
  - Hall effect sensor testing:

- Involves the testing of the 3D digital and 1D analog hall effect sensors with an Arduino

- **Joint and Finger design:**

- Creation of the joint and link structure for a finger using CAD & 3D printing; including testing and optimisation design parameters.
- Evaluation of design

2. **Stage 2 - Support & palm+thumb with sensors & soft skin design:**

- **Palm & thumb design:**

- Creation of the palm and thumb mechanism using CAD & 3D printing.
- Evaluation of design

- **Plan hardware required & electrical schematic:**

- Electrical part choosing and justification
- Electrical schematic for whole project
- Complete bill of materials for ordering

- **Completion of motor & sensor Python + Arduino code**

- **Soft skin shape and sensor placement:**

- Soft skin/sensor placement optimisation for grasping and manipulation of objects.
- Optimisation of the magnet size, strength and displacement within the soft skin relative to the hall effect sensors relative to the expected skin deformation and grasping force.
- Magnetic field simulations can be conducted to advise design decisions regarding these parameters.

- **Supporting structure/wrist - PCB + motor housing:**

- Planning for tendon pathing to reduce friction throughout the system.
- Design and manufacturing of the wrist motor housing that supports the hand and includes various electronic PCBs.

3. **Stage 3 - Project refocus due to Covid-19:**

- **RoS package for sensors, motors and MoveIt:**

- Creation of RoS package for the robotic hand model utilising the modular Python scripts for the motors and sensor data gathering and processing

- **Mujoco - Dynamic simulation of hand + sensor + tendons + object manipulation:**

- Dynamic simulation of the hand to explore sensor placement and tendon performance for manipulating and grasping a sphere and a pen shaped object.

- **FEA analysis of soft skin designs (Normal and Shear):**

- Analysis of the soft skin geometries utilising a variety of silicone rubber properties to explore displacement with respect to various normal and shear forces

- **Design of PSU + power breakout enclosure**

## E. Final Gantt Chart

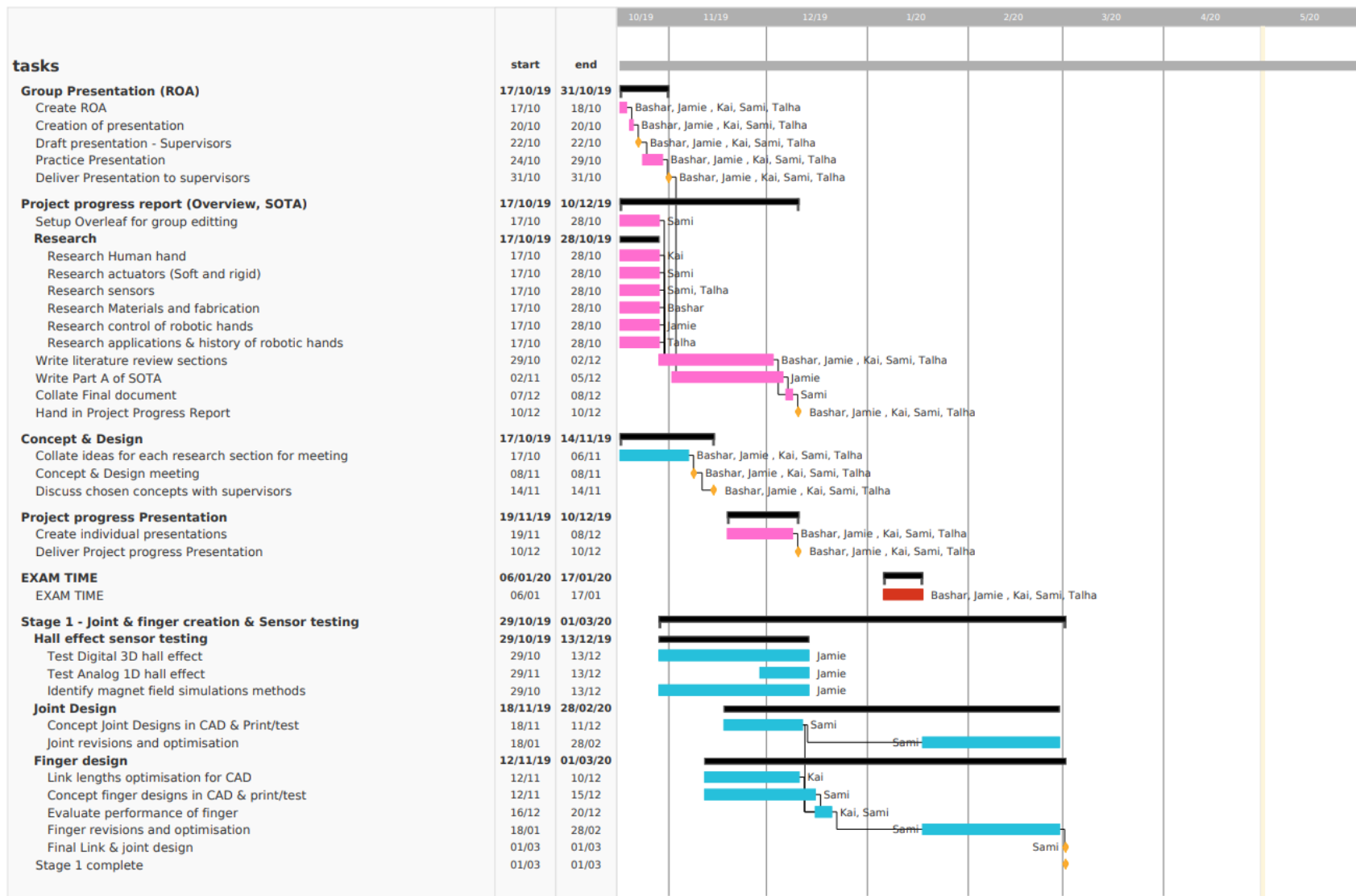


Fig. 1. Gantt chart section 1 - Pink colour indicates coursework, blue colour indicates project task, red colour indicates exam

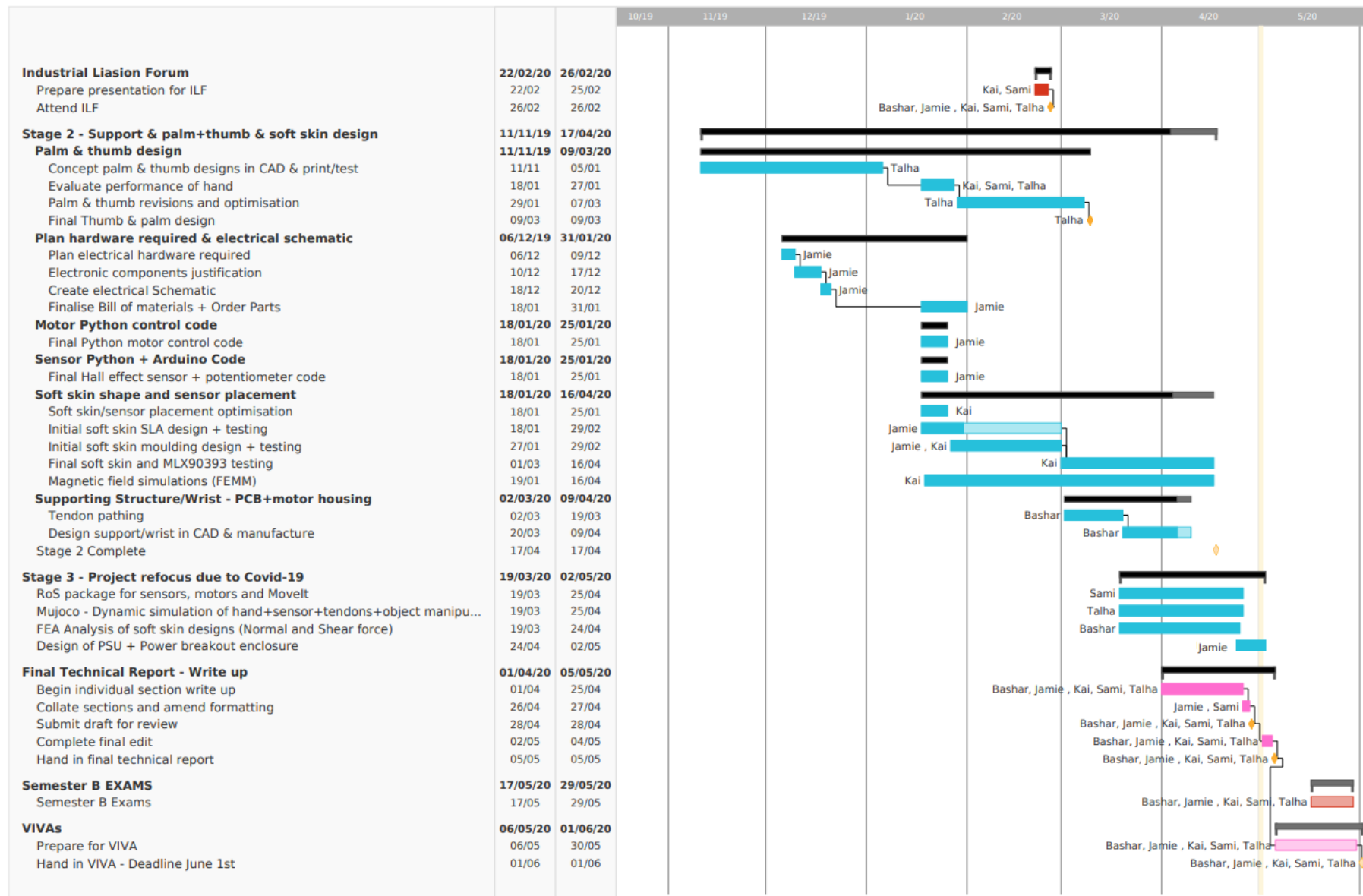


Fig. 2. Gantt chart section 2 - Pink colour indicates coursework, blue indicates project task, red colour indicates exam. **NOTE:** Stage 3 has been changed due to COVID-19, it was initially the physical testing phase of the completed robot hand

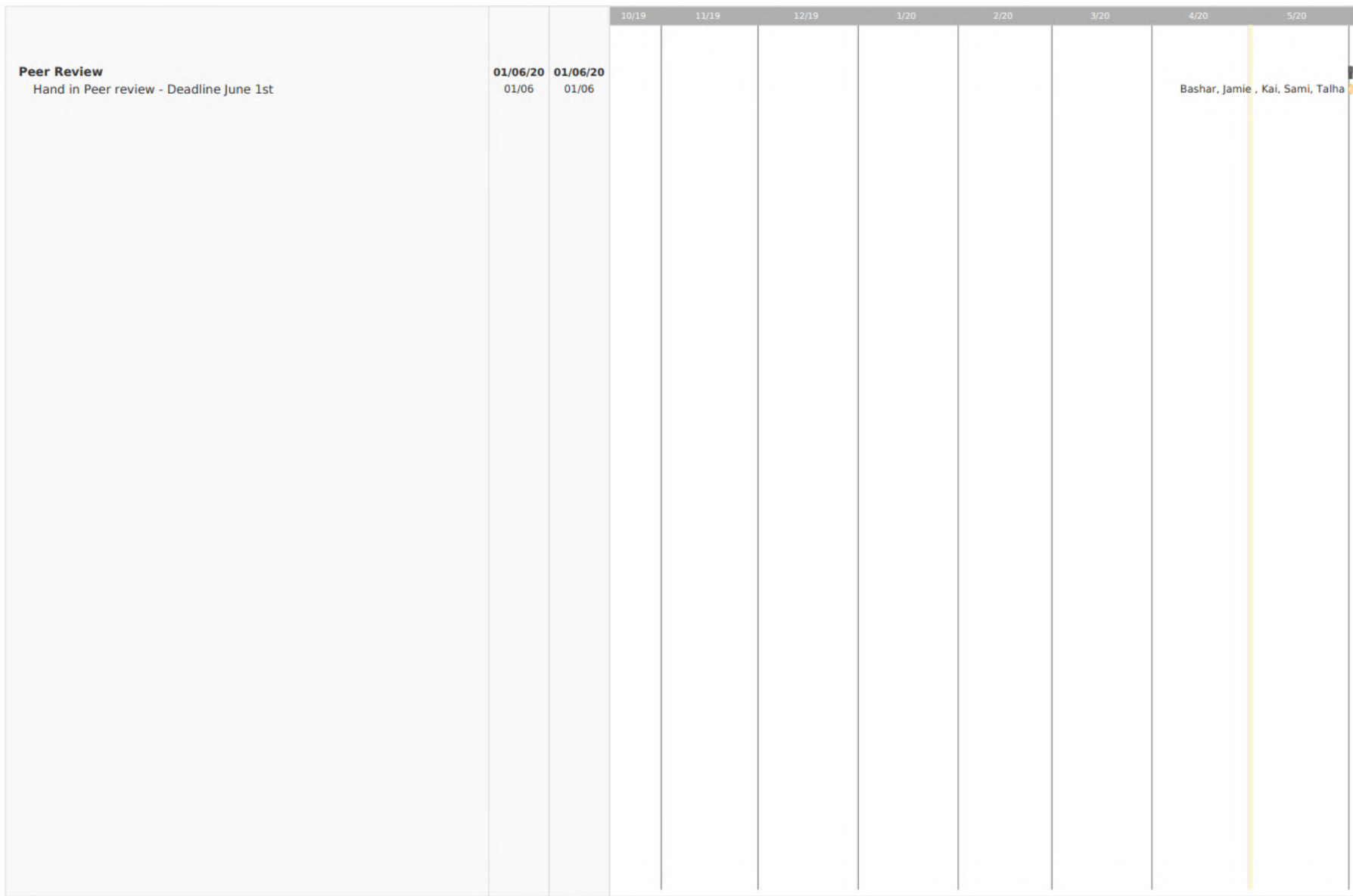


Fig. 3. Gantt chart section 3 - Pink colour indicates coursework, blue indicates project task, red colour indicates exam

## II. DESIGN CONCEPTS

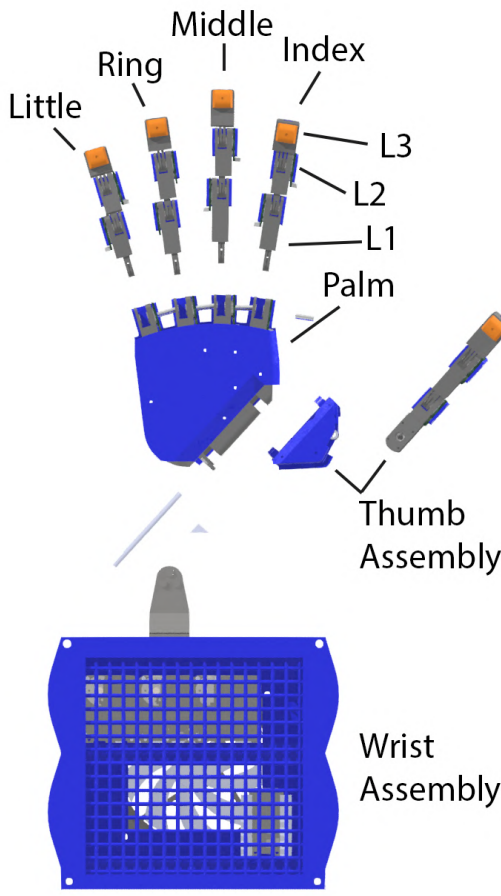


Fig. 4. Render of the robot hand with each part making up the assembly indicated. The finger assemblies and thumb are separate from the palm, which is separated from the wrist. This is for illustration purposes .

### A. Fingertip Design - Kai Page

When considering the design of the whole hand, the question as to where the tactile sensors would fit into arose and the position at which would make sensors most useful. The aim for this hand was to be able to perform both precision and power grasps. According to [4] "Grasp is conducted by forces on contact point of object... In the case of precision grasp, which is carried out by the end of the finger". Hence from previous research, the goal was to design an ergonomic fingertip that would house both the 3D and 1D tactile sensors, as well as other components required to enable the sensors.

*1) Design Constraints:* The biggest constraint about the fingertip design was how to fit both the sensors and its Molex Picoblade connector into the fingertip as compactly as possible. The use of the MLX90393 chip with the custom PCB described in the Bill of Materials VIII explains the need for a PCB with the smallest dimension to minimise the size of the fingertip. As a result of this, the soldering of wires and the connections to the rest of the hand proved to be fragile and increased the risk of breaking the PCB. Therefore, it was necessary for a connector housing that would provide a disconnect and

cancel any tension on the wires between the connector and the PCB. The chosen connector's dimensions were to be as small as possible to provide for a relatively small fingertip that can resemble that of a biological hand. This would also provide a proportional fingertip length to the rest of the designed finger. Reducing the size of the part allows for shorter manufacturing time, ultimately leading to smaller cost.

The fingertip also took into consideration the design to be efficiently manufacturable and as replaceable as possible if there was to be a fault during the robotic hand lifetime. This meant that careful thought went into how the internal components required accessibility for replacing without having to replace the whole hand.

Additionally, a flat surface is required on the palmar side of the exterior of the fingertip to provide a surface that will allow for adhesion with the soft skin that will stick on top of the fingertip.

Finally, the hand was also constructed with the thought of utilising FDM 3D printing as it produces quality parts that requires less cost and time, hence being one of our main objectives. Due to this, design considerations such as wall thickness, tolerances, hole sizes and such characteristics were critical and key.

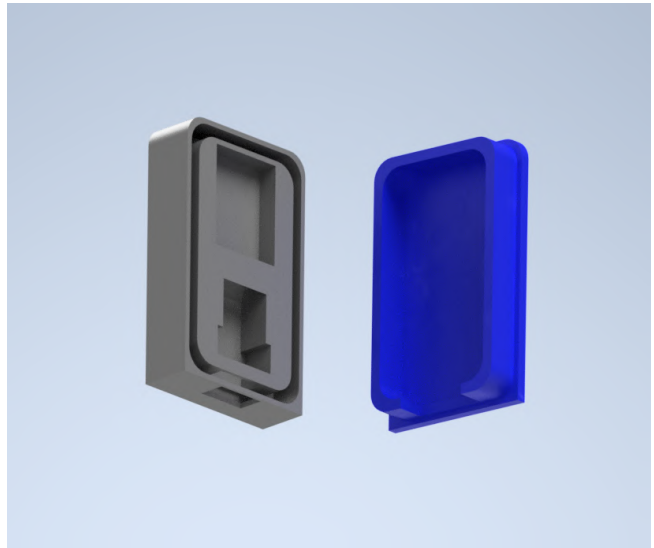


Fig. 5. Fingertip Prototype 1 (left): the isometric view of the fingertip, (right): the isometric view of the fingertip lid.

*2) Prototype I:* The first design was constructed as seen in Fig. 5. This design was made to fit the custom made PCB and the Molex Picoblade male connector housing. The advantages of this design allowed the housing of both crucial components as well as allowing the connection of the wires from the PCB to the connector without any strain on the wires. The creation of the lid that fits directly into the fingertip helps create a flat surface for the attachment of soft skin as well as keeping the internal components in place. The dorsal side of the fingertip is also left flat to keep the shape symmetrical in the z-plane. Denoting from Fig. 5, from top to bottom, the first compartment is designed for the customised PCB with the 3D MLX90393 sensor for a tight fit so that there is no movement in the PCB. Movements could possibly interfere with the

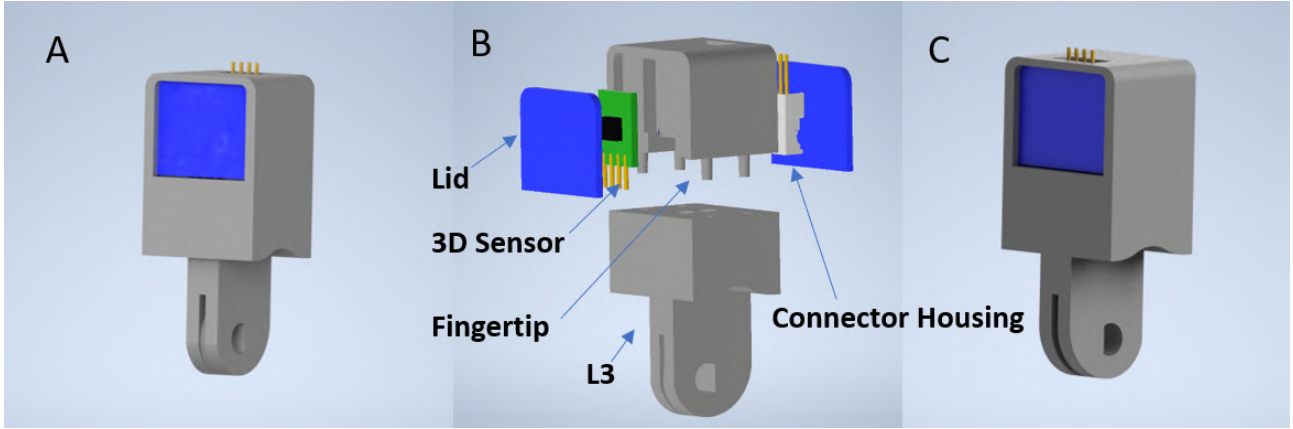


Fig. 6. Assembled fingertip containing 3D sensor and the Molex Picoblade connector (A): palmar view of the fingertip, (B): Exploded view of the fingertip (C): dorsal view of the fingertip.

sensitivity of the sensor and generate inaccurate results. This is followed by a loft extrusion which introduce an opening that allows for the connection of the wires from the PCB to the connector. Then the loft opens into the Molex Picoblade connector housing compartment. From there, an extrusion is made to the tip of the fingertip which leads to an opening that allows wires from the connector to flow out to the rest of the finger.

Some of the design flaws for this part includes the fact that there was no consideration in how the fingertip would attach to the rest of the finger as there would be wires coming out from the bottom part of the component. Another design consideration that disadvantaged the component was that the length of the part contributed a lot to making the complete finger too long. Hence, if the lengths of the robot finger was to be sized to a similar ratio as a biological hand, the whole robotic hand would have to be sized up incredibly to fit this model. Therefore, prototype II was designed with these constraints in mind.

*3) Prototype II - Current Design:* The second prototype design which translated into the current version as shown in Fig. 8. This design took into consideration the flaws of the previous and developed into a component that allows for easier replacement and smaller dimensions. The whole assembly in Fig. 6 consists of three parts: the fingertip, the fingertip lid and Link 3 of each finger. The exploded diagram in Fig. 6B, illustrates how the sensor, and the connector housing on the dorsal side of the fingertip fits internally. Each part of the design is explained in further detail in this section.

The first change includes, increasing the depth of the component from the previous so that the depth of the design could be used to create compartments for the PCB and the connector. This in return resulted in a decreased length of the design. The design compartmentalised the palmar side of the fingertip for the PCB with the sensor and the dorsal side for the Molex Picoblade connector housing. The dimensions for these component extrusions are kept the same as the previous design as the tight interference fit showed great results.

For the Ring and Little fingers, since these do not require the internal slot for a PCB with the 3D sensor, the internal structure is changed slightly to accommodate

for the 1D Honeywell Ratiometric Hall Effect sensor. The working principles of the design is still identical the one explained above. The Picoblade connector house is still used on the dorsal side of the fingertip so prevent tension on the soldered wires on the sensor to the rest of the hand.



Fig. 7. 1D Fingertip Prototype 2 (left): Palmar view of the internal component placement inside the fingertip, (right):Dorsal view of the internal component placement inside the fingertip.

Another problem solved with the new design is by adding on 4 pins at the bottom surface of the fingertip so that it can easily fit into the pin holes of Link 3 (L3) of the finger link, creating an interference fit. The fingertip and L3 together depicts the distal phalanx of a human hand. These circular pins are mirrored in both the x and y axis to create 4 identical pins with a 1.5 mm diameter and 4 mm length.

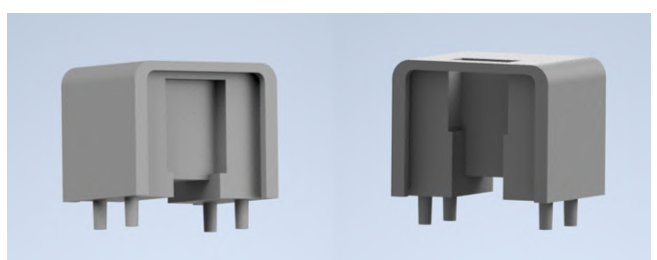


Fig. 8. 3D Fingertip Prototype 2 (left): palmar view of the inside of the fingertip (right): dorsal view of the inside of the fingertip.

To allow the same flat external surface of the fingertip, as well as providing containment of the components inside the fingertip, a lid shown in Fig. 9 was also designed to smoothly slide into the fingertip. Therefore, grooves were extruded along the shape of the fingertip with the thickness

equalling to the thickness of the lids. The design of the lids are simple 1mm thick rectangles, filleted at the distal edges of the fingertip so that the lid can perfectly fit into the filleted edges of the fingertip. The distal filleted edges are there to mimic the biological aesthetics of a finger

To allow the connection of the wires from the sensor to the connector, a passage is provided at the bottom of the fingertip. This meant that the gap just before the bottom surface gives way for the wires to fold in at around 90 degrees to the other face of the fingertip, and towards the connector housing. This same gap also allows some space for the tendon wiring knot, as the end of the tendon route will be at the top of Link 3. Thus, as the 4 shafts fits directly into the 4 holes in L3, the wiring and the tendon will be conveniently covered, without being exposed (Fig. 6). The pins from the fingertip fits perfectly into the holes extruded on the surface of L3 of their respective finger. This allows for the fingertip to be connected to the rest of the finger with the tendon wiring so that the L3 link joins the L2 link at J3.

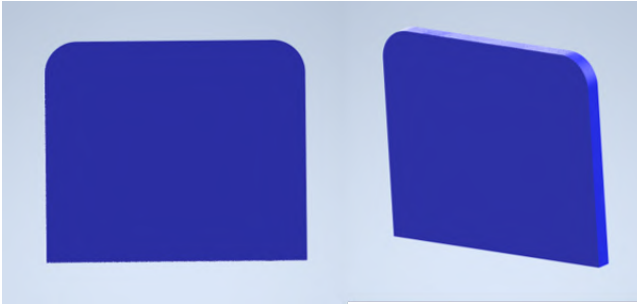


Fig. 9. Fingertip Prototype 2 Lid (left): front view, (right): isometric view.

To conclude, the main importance of the fingertip design was to house the 3D tactile sensors accurately, without causing any damage or movement. Additional to this, the main consideration would be the size (most importantly the length) of the design so that when attached with L3, it didn't create a design that would be out of proportion to the rest of the hand.

#### B. Soft Skin Design - Kai Page

One of our research areas were regarding the use of soft material in the manufacture of the robotic hand. The use of soft skin was chosen so that the use of a 3D tactile hall effect sensors. This can be done by embedding a small magnet inside the soft skin to measure the magnetic flux density with the deformation of the magnet. During the process of this research, the material and manufacture choice for the soft skin was tested. The advantage of using flexible material is to increase contact friction compared to the smooth plastics that are being used for the structure of the hand. However, there is a trade off as the sensitivity, frequency and the range of the sensor response may degrade and vary [5]. These fingertips are designed to fit onto the palmar side of the 3D printed fingertip. This to be done by using adhesives as described in section VIII to place the soft skin onto the fingertip. This is illustrated in Fig. 10 to show the attachment of the soft skin on one finger. Ultimately, this is to be done on all 5 fingers

for tactile sensing embedded in the soft skin. 1D sensors will be embedded into the fingertip in the little and the ring fingers as it is shown from research that the ring and the little can be coupled and used as support for handling and grasping larger objects [6]; in comparison to the middle, index and the thumb being used for more dexterous motions, hence the embedding of 3D sensors.



Fig. 10. Assembled soft skin on the fingertip to demonstrate the attachment of the soft skin.

*1) SLA 3D Printed Elastic Resin - Material, Design & Manufacturing - Kai:* Our first experiment was to print the soft skin in elastic resin on the SLA printer. This is because SLA printers generally prints high quality parts with better resolution; but most importantly is able to print flexible material, creating highly elastic, yet strong enough not to tear during use. The use of 3D printing produces reproducible products and generates complex designs more accurately compared to other traditional moulding and casting techniques. The shape of the printed parts were designed in different layers so that the x and y directions can be decoupled in its and minimise the crosstalk effect [3]. Printing with the SLA required us to carry out some trial and error regarding the wall thickness, the internal lattices, designed shape and the drainage location. This is so that the required stiffness of the part can be achieved when tested with the sensor altogether. Therefore, many lattice structures were trialled ranging from 0.4mm to 1.2mm, with star and column internal structures with 0.8-1.2mm wall thicknesses. The internal lattices were automatically created using Autodesk netfabb.

However, since we had no prior experience in printing elastic resin on the SLA, we were disadvantaged and experienced a few mistakes. Firstly, when designing the soft skin, the drainage hole was only increased to 1.2mm when it should've been made to a minimum of 3.5mm to produce the required shape. Unfortunately, this critical

mistake meant that all the SLA printed parts were not useable. Not being able to drain the excess liquid meant that the shape printed was much stiffer than it should've been as there were no air gaps internally as designed. Moreover, the turn around time for printing these parts were over 2 weeks which meant it was very time consuming when prototyping. The available time for the whole project was very limited and with a 2 week turn around time, it was very inefficient to wait around for these parts.

**2) Moulded Silicone - Material, Design & Manufacturing - Kai:** After failing with the SLA printed parts, we investigated on using silicone as the soft skin for embedding and creating a soft tactile sensor system. Ecoflex 00-50 was used, due to its shore hardness of 00-50, pot life (18 mins), cure time (3 hours) and its cure temperature (room temperature) [7]. Silicon was chosen as the second choice as it was a known material that had been used previously in similar bio-inspired soft tactile sensor systems [8] [3] [5].

The design of the silicone skins were produced identical to the designs from the SLA printed soft skin in an attempt to reduce crosstalk [3]. However, slight changes to the dimension were made for moulding so that it would conform to the size of the designed fingertip in section II-A. The thickness of the soft skin is also determined by running Finite Element Magnetic Model (FEMM) simulations to model the magnetic field of the embedded magnet.

To be able to produce these parts, 3D FDM printing was used to print out the moulds with varying wall thickness, a bulk solid and different shapes on the top surface. Moulding different wall thickness and surface shapes prepared us for testing how the sensor would behave when tested with different objects and its effect due to normal and shear displacement. The design of the mould must open in half longitudinally so that when liquid silicone is poured, it provides a space that will cure and minimise trapped air as we didn't vacuum or degas through it.



Fig. 11. 3D Printed silicone design mould where silicone rubber liquid was poured into and cured to create the silicone soft skins, (left): isometric view of an unassembled mould showing the bottom and the lid of the mould that comes together with bolts (middle) to close the two parts together (right)

As seen in Fig. 11 the two halves of the mould can be held in a tight matter while curing the silicone by screwing bolts into the four corners of the mould. This provides a tight closure to the two halves of the mould so that there are no slippages or spillage. Fig. 12 illustrates the types of shapes and sizes used in the experiment to test the sensor.

The steps to moulding the silicone were taken as follows:

- Screw the two halves of the printed with bolts
- Mix the liquid silicone rubber (LSR) in a 1A:1B ratio at room temperature thoroughly for 3 minutes.

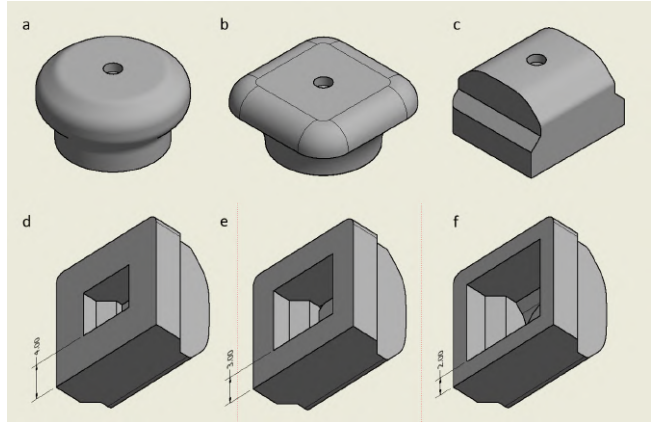


Fig. 12. Silicone moulded fingertips (A): circular surface and base, (B): circular base and square surface with curved edges, (C): rectangular base and surface with two curved edges, (D): same shape as (C) with a 4mm wall thickness, (E): same shape as (C) with a 3mm wall thickness, (F): same shape as (C) with a 2mm thickness.

- Once the mixture is even, pour the mixture into the holes provided in the mould that will help guide the silicone liquid into its place.
- Once all the mould compartments are filled, shake the mould side to side gently (without lifting the mould from the table) so that the liquid can settle quickly.
- Leave the mould to cure for 3 hours at room temperature.
- Once the curing time is up (3 hours [7]), unscrew the bolts and slowly break the two halves of the mould to reveal the final product.

The silicone must be carefully pulled out from the mould as it usually hard to remove small designs that can get stuck. Once removed, the excess can be carefully cut off to perfect the edges of the final products.

### C. Actuation Concept and Evaluation - Ahmed Sami Deiri

The actuation method behind the fingers was a key factor in the design, with a variety of possible designs discussed within the SOTA report. Very early on in the process we determined that the use of a direct drive system with a motor placed within each link was impractical given our size and performance goals, as well as the budget limitations.

We determined that a method of providing remote actuation through fluidic transmission/cable tendons would be ideal as they would allow the actuation mechanism to be placed remotely, and thus make the hand and fingers dexterous enough to meet our goals of in hand manipulation.

A cable driven system was determined to be ideal due to our manufacturing requirements with regards to modularity and ease of maintenance and repair. The fluidic system would have introduced the possibility of leaks and would require tolerances that our designed manufacturing process (FDM 3d printing), would have difficulty achieving. Fluidic actuators often require larger and more complicated actuation which could increase the price and was determined to be difficult to fit on the hand within our 5 kg requirement.

While alternative 3D printing manufacturing may have been able to achieve these requirements, SLA printing is a more expensive process and posed difficulties in manufacturing the final part due to difficulties accessing the SLA printers in comparison to the widely available FDM 3D printers. The actuation for the cable could be provided by a fluidic or electromechanical actuator within the wrist, with the main concern being the transmission of actuation through the finger.

The concept behind cable driven actuation as discussed in the SOTA, relies tension on a cable along the side of a link to create torque around a joint. Pulling a cable fixed to a point results in it applying a force towards the pulling direction. By applying the force at a vector displaced from the axis of rotation, the tension acts as a normal force around the axis of rotation, and therefore provides torque around the joint.

Some preliminary design illustrations and sketches can be seen in the appendix under Link Design.

#### D. Link Design Prototyping - Ahmed Sami Deiri

*1) Rolling Joints:* Initially we explored the possibility of designing a fully bio-mimetic hand as was developed by Zhe Xu et al. [9]. This hand utilised rolling joints based on scans of human bones with artificial tendons designed to mimic the human hand. While this hand presented an appealing product for exploring the human hands performance, the hand posed a challenge in terms of control and modelling. This is due to the hand relying on material properties and elasticity when constraining two links rather than traditional rigid links which could be modelled a single point axis of rotation between two links.

One of the promising prototypes can be seen in Fig. 13 which is based on the joint design discussed by Kim et al [10].

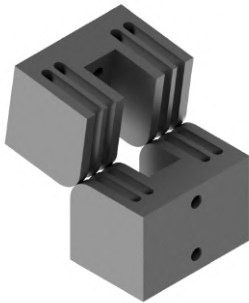


Fig. 13. Rolling joint design based on the design by Kim et al. [10]. This design utilises two rolling parts connected by a string that's knotted through the slots shown.

This design utilised two parts that are constrained together using a cable that is threaded through the channels and holes in the part. This provided a simpler model of the rolling joint in comparison to the Zhe Xu hand [9], as the rolling joint was designed to rotate around a static center of rotation as can be seen in Fig. 14.

This design was ultimately omitted due to it being not ideal for proprioceptive sensing and therefore difficult to model/predict motion for. The constraining cable joint also

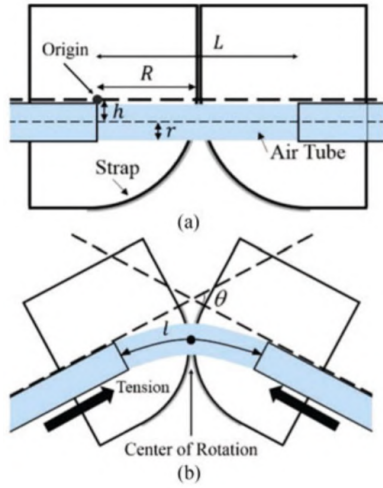


Fig. 14. Rolling joint cross sectional diagram by Kim et al. [10] showing the operational concept behind their rolling joint design. In the displayed design a pneumatic tube was embedded along the center of the joint which provided pneumatic pressure to the fingertip for their fingertip sensor design. Our own interpretation of this design can be seen implemented and tested in Fig. 13. Fig A shows the joint at its neutral state, while Fig (b) shows the joint under tension and therefore actuated. Their design relied on the central tube to provide the restoring force while our interpretation of the design uses 2 antagonistic cables which can be tensioned for flexion/extension

required high tolerances which made this design difficult to manufacture/repair (objective 2.4).

*2) Axle based joints:* After omitting the rolling joint design concept, we proceeded to explore the more traditional axle based design with an axle used as a center of rotation between two links.

The initial design took inspiration from various sources such as the Shadow Arm [11] and Inmoov Hand [12]. These designs utilised a discrete joint mechanism with centers of rotation explicitly defined mechanically in the form of a pin or axle.

The initial design can be seen in Fig. 15, where you can see each joint has a male and female component as indicated on the diagram. The link design allows for any number of links to be attached in series while maintaining the cable routing and pulley system all the way to the fingertip. By doing this, our design is modular and consistent which would allow for easy upgrades and modifications as the link design is consistent.

Early prototypes of the hand tested the possibility of omitting the use of ball bearings along the joints as some 3D printed designs do [12]. We quickly noticed that we experienced a lot of variable friction due to the layer lines produced by the 3D printing process, resulting in a decrease in accuracy and increase torque requirement. Jumping behaviour was also observed as the torque applied increased to overcome the static friction.

We also experienced issues with friction in terms of accuracy due to the variation in surface finish from 3D printing, as well as issues with movement horizontally along the finger due to the clearance fit needed to allow for rotation of the joint. This ultimately led to the addition of bearings within the joint assembly that interfaced with the axle, and therefore provided a high tolerance low friction connection between the joint and the axle. Plain washers

were also used between the two joints as you can see in Fig. 15b. These washers acted as a plain thrust bearing and therefore decreased friction horizontally between the two joint faces.

Due to the choice of using SV01 rotational potentiometers to achieve proprioceptive sensing (as discussed in section II-H), we needed a method of transferring the rotation to the potentiometer which required a 4mm D shaft. We determined the best way to incorporate this sensor was by having the sensor mounted directly connecting to the axle, and use the D shaft as the axle.

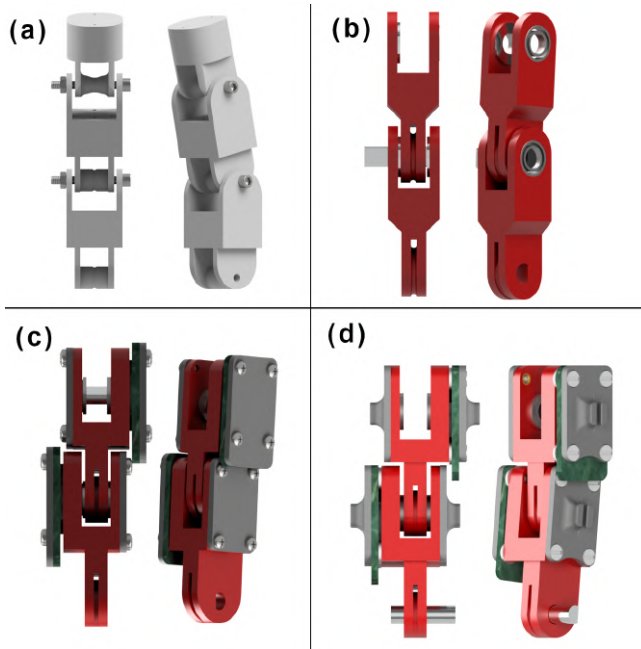


Fig. 15. Diagram illustrating the finger link assemblies at 4 stages of design, with (a) showing the oldest design which used a bolt as an axle and a small pulley system.(b) shows the evolution of that design which involved decreasing the link thickness, using a shaft instead of a bearing, adding bearings and plain thrust bearings (ie washers) to the axles. (c) illustrates the addition of the potentiometer PCB and the use of a D shaft, with a much more compact link design. Two side panels are also added to prevent the shaft from moving horizontally. (d) shows a more optimised version of (c), with a decrease in the height of the male side of the link body along the front to allow the finger to bend further to achieve a max bending angle of 180 degrees.

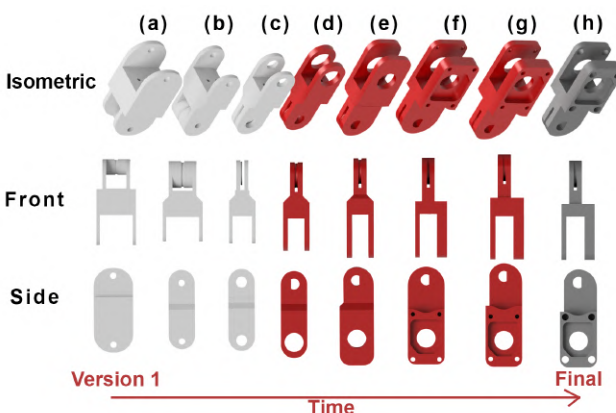


Fig. 16. Diagram showing the chronological evolution of the link body design with an isometric, front and side view of each. The figures are ordered from oldest (a) to the most recent design (h). Some of these links can be seen implemented as full link assemblies in Fig. 15(a).

#### E. Final Link Design - Ahmed Sami Deiri

The final link design can be seen in Fig. 17 with an exploded diagram seen in Fig. 18 which highlights all the key components that make up the link. This design is an evolution of our initial design and incorporates the same modular concept of a consistent link design that can be adapted for different segments of the fingers.

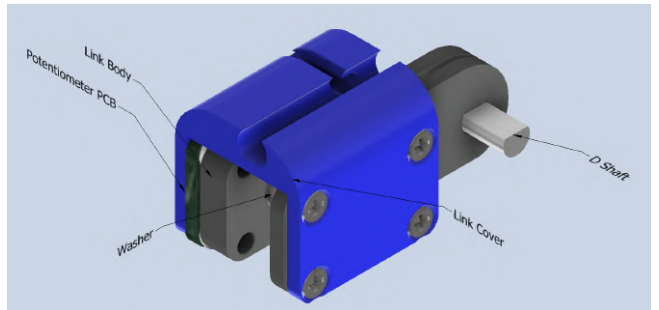


Fig. 17. Assembly of the link illustrating the different components on each link. Each link consists of two 3D printed parts: the Link Body and the Link Cover.

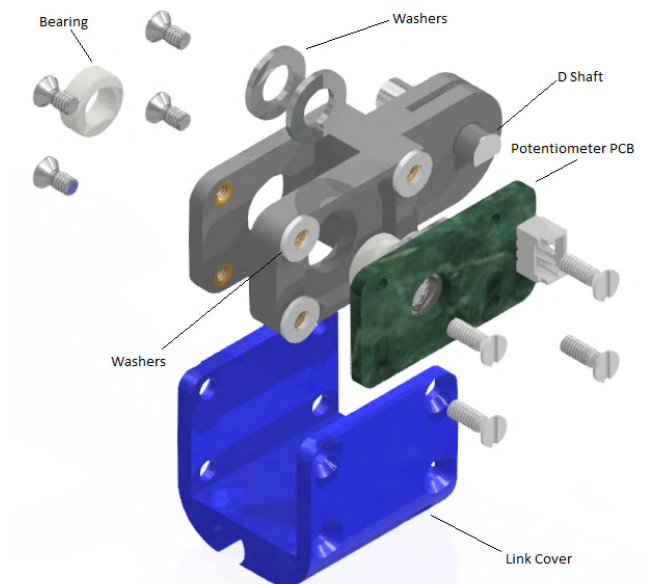


Fig. 18. Diagram showing an exploded link assembly (further explanation needed)

Continuing from previous designs, each link has a male and female side which allow these links to be connected in serial through the same interface.

Each link consists of two 3D printed parts, the Link Body and the Link Cover. It also includes a potentiometer as discussed in section II-H which is mounted onto the PCB seen in Fig. 28. A D-Shaft is fixed onto the male side of the link, which is used as the axle for the joint within the female side, as well as driving the potentiometer. This PCB is placed between the link body and link cover, with the link cover going around the PCB and allowing 4 bolts per side to connect the cover to the PCB and then the link body. Two 2 mm washers are placed between the PCB and the link body to provide clearance space for the PCB which is needed for the surface mount pins.

The link cover also allows an elastic material to be attached to provide a resistive torque which is needed to get the proportional finger bending motion as desired. The elastic strip is placed between the link cover and the link body. The slot along the back of the link cover will permit for cable routing through the finger which can be seen visualised in Fig. 19.



Fig. 19. Render of hand showing how the cable routing would be performed through the robot hand as illustrated by the orange tubing

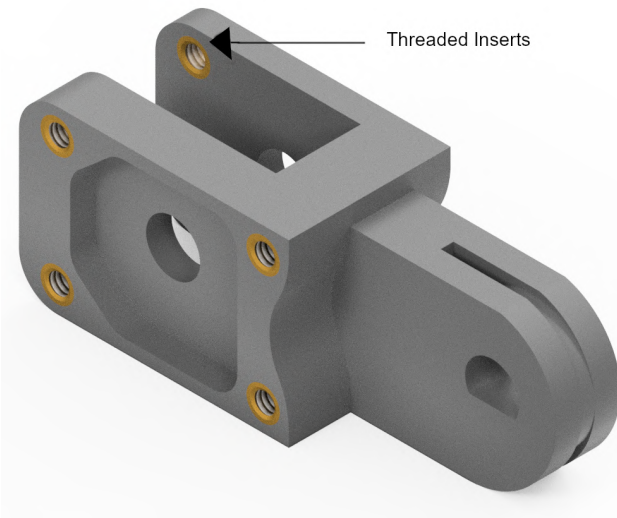


Fig. 20. Render of Link body showing the threaded inserts that are heat set into the plastic body

The bolts are fixed to the link body through brass heat set threaded inserts, which are embedded into the Link body by heating them and pushing them into the interference fit holes as seen in Fig. 20. While we could have tapped the holes within the body instead of using the inserts, which could have provided space savings, the threaded inserts provide a harder and more robust thread material which helps us meet our objective of an easy to repair design. The threaded insert is also easier to attach to the link body than threading each hole as a heating element such as a soldering iron can rapidly heat the insert, allowing it to embed within the thermoplastic body.

Two ball bearings are used within the female side of the link to provide a low friction interface between link and the axle as discussed in section II-D2.

*1) Modularity in Design:* To achieve our aim of modularity, we have implemented a few design choices within our link design. We have already discussed the modular

approach to links with all links having the same interfaces which enables consistency in results and manufacturing.

The components for the link are identical across all links with the only difference being the length of the middle section of the link body as seen in Fig. 21. This length was set to match the lengths specified in section II-K. To allow for easy creation of modifiable links, the following steps were taken.

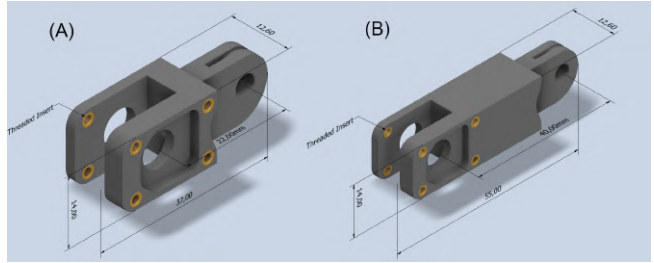


Fig. 21. The Link Body which is optimised for FDM 3d Printing can be seen here. The link body has 4 holes per side to allow for the heat-set threaded inserts, with a hole in the middle for a bearing/shaft. The shape of the potentiometer is inlaid into the link body to minimise space use and provide support. (A) shows the smallest configuration of this link, with a total length of 37mm with a kinematic length of 22mm. (B) shows a possible configuration of the link with the kinematic length adjusted to 40mm. The length of the link can be changed anywhere above 22mm using parameters within the CAD files, with the total link length being Kinematic Length + 15mm.

Firstly, the link parts and more specifically the link body were created with a strong focus on the use of user parameters within the CAD software (Autodesk Inventor). Parameters are variables that can either be independent such as the outer diameter of the bearing used, or can be dependant on other variables. This has enabled the creation of a CAD file which is based on the input user parameters, which could adapt the design to a new parameter automatically if a part matching the specifications set can't be found or to accommodate for manufacturing tolerances.

Parameter Name	Consumed by	Unit/Type	Equation	Nominal Value	Tol.	Model Value	Key	Comment
<i>User Parameters</i>								
isoleLength	wingLength_d11...	mm	14 mm	16.000000	0.000000	16.000000	□	□
isoleThickness	d15_d13_isole...	mm	2 mm	2.000000	0.000000	2.000000	□	□
isoleWidth	isoleWidth...	mm	1.0 mm	1.000000	1.000000	1.000000	□	□
isoleWidth	wingSideWidth...	mm	(isoleThickness * 2 * u) + cableWidth	5.000000	5.000000	5.000000	□	□
isoleLength	d29	mm	SectorLength - wingholeDistance - 10 mm	10.000000	0.000000	10.000000	□	□
isoleLength	d22	mm	isoleLength	16.000000	0.000000	16.000000	□	□
LivingThickness	d18	mm	bearingThickness	2.000000	0.000000	2.000000	□	□
RivetThickness	d19	mm	bearingThickness + sensorDepth	4.000000	0.000000	4.000000	□	□
bearingThickness	RivetThickness...	mm	2 mm	2.000000	0.000000	2.000000	□	bearing thickness
sensorDepth	d141_d85_d51...	mm	1 mm	2.000000	0.000000	2.000000	□	potentiometer thickness
wingSideWidth	d21_d20	mm	isoleWidth + (2 * u * washerThickness)	6.600000	0.000000	6.600000	□	□
washerThickness	wingSideWidth	mm	0.8 mm	0.800000	0.000000	0.800000	□	Washer thickness of plain bearing
sectorLength	isoleLength	mm	22 mm	22.000000	0.000000	22.000000	□	Kinematic Length of Link
wingholeDistance	isoleLength_d59...	mm	6 mm	6.000000	0.000000	6.000000	□	□
isoleWidth	isoleWidth_d59...	mm	14 mm	14.000000	0.000000	14.000000	□	□
bearingOD_Diameter	d200_d94_d88...	mm	7 mm	7.000000	0.000000	7.000000	□	□
bearingID_Diameter	d37	mm	4 mm	4.000000	0.000000	4.000000	□	□
ShaftDiameter	d85	mm	10 mm	10.000000	0.000000	10.000000	□	□
pulleyDiameter	d106	mm	1.2 mm	1.200000	0.000000	1.200000	□	□

Fig. 22. Parameters page within inventor showing all the set parameters which could easily be modified based on improvements or component availability, which automatically modify the part

This has enabled the creation of iPart and iAssembly files for the Links. The iPart file enables the user to place a finger link body part and adjust the kinematic length as a parameter when placing. This would enable someone to rapidly create their own version of the hand with different link lengths or a different scale quite easily as they can simply place each link body and adjust the length within the assembly rather than copying the part and then modifying each individual file manually.

This was then extended to create an iAssembly for the entire link which utilises the same system as used in the iPart but allows the placement of an entire link assembly with all the necessary parts at the desired kinematic length. This could therefore be used automatically with a spreadsheet to rapidly create the links for an entire hand by importing a table of desired kinematic lengths above the minimum (22 mm) such as the one referenced in section I.

#### F. Distal Link - Ahmed Sami Deiri

For the distal phalanges a modified version of the Link Body was made as seen in Fig. 23. To create this link, the female side (side containing the potentiometer) was removed from the link body and the length of the link was minimised to allow the fingertip to be mounted. The design has a minimum kinematic length of 12.5mm, however it was made thicker to accommodate for the fingertip mounting holes which are used to connect the fingertip assembly to the L3 link body. Two holes in the center of the part provided a path for the string tendons, where the string would be knotted and held against the hole. As with the previous link design, the length of the link can be varied as an iPart which allows it to confirm to whatever length is needed as specified in section II-K.

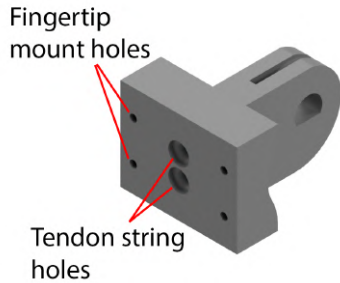


Fig. 23. Render of the L3 Link Body which makes up the bottom part of the Distal Link. This part contains two holes for the string tendon to pass through and for the knots to sit in. 4 holes along the sides allow for connection of the fingertip assembly discussed in section II-A.

#### G. 2nd Flexion/Extension DOF at the Index and Middle finger - Ahmed Sami Deiri

To achieve the desired range of motion for our in hand manipulation goals, we found the use of a single degree of freedom provided insufficient levels of control. This is due to the finger flexing either sequentially, with the fingertip joint (J3) reaching the maximum bending first. This is followed by the J2, and then J1. The addition of resistance at the joints through elastics, or tightening the bolts used as axles during testing, provided more uniform flexion along the finger. However, this resulted in a need to design the hand for a particular flexion/extension pattern which could not be changed without physical modification to the hand or change in springs/elastics.

To mitigate this, we explored the techniques discussed in the SOTA revolving around the selective increase/decrease in joint resistance and therefore vary the actuation

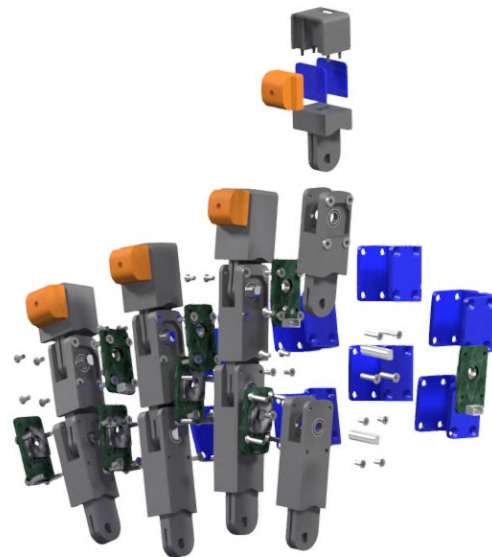


Fig. 24. Exploded Render of the fingers showing an exploded index finger

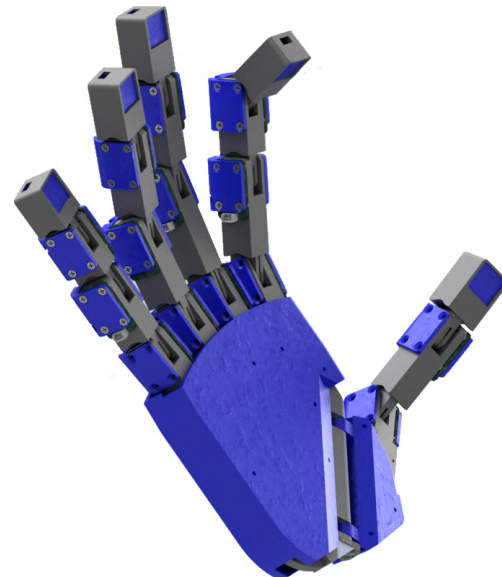


Fig. 25. Palm and finger assembly of final hand design using the final link designs discussed.

behaviour of each link. An example is the use of pneumatic chambers with selective pressurising of joints to stiffen them. These systems add complexity in terms of control and modelling, and requiring a source of pneumatic pressure, regulators/valves, and routing along the fingers to each joint. They are also more complex in terms of design and manufacture than alternatives. Ease of manufacture was considered to be a key objective, which pushed us to search for alternative design that could achieve our desired actuation capabilities.

To mitigate this, we explored the techniques discussed in the SOTA revolving around the selective increase/decrease in joint resistance and therefore vary the actuation behaviour of each link. An example is the use of pneumatic chambers with selective pressurising to selectively stiffen

joints [13]. These systems add complexity in terms of control and modelling, and require a source of pneumatic pressure, regulators/valves, and routing along the fingers to each joint. They are also more complex in terms of design and manufacture compared to alternatives solutions. Ease of manufacture and repairability were considered to be a key objectives, which pushed us to search for an alternative design that could achieve our desired actuation capabilities.

By optimising the number of DOF to our desired dexterity and grasping outcomes, a second actuated degree of freedom was applied around J1 for the index and middle finger performance needed for high dexterity grasping techniques (see section IV-A).

The design for this extra DOF can be seen in Fig. 27, which shows a comparison of a cross section cut for the L1 Link on the ring finger(a) and index finger(b). The index finger's L1 has an extra set of cable routing holes that allow for two tendons to provide flexion/extension around J1 as seen in Fig. 26. Due to the extension/flexion provided around the J1, the flexion/extension for the finger was determined to be impacted as rotation around J1 would cause the entire finger to also flex/extend. The cables extending to the fingertip would need to both extend and shrink when J1 is actuated due to the cable routing lengths. To compensate for this, we would need to have a way of adjusting the total length of the cables extending to the fingertip in the index and middle finger. Solutions such as the use of springs to maintain tension within the palm while allowing it to actuate were discussed. The final design utilised an extra motor/pulley actuation system for these fingers, which can independently act as antagonistic actuators when actuating the finger, but can independently adjust the length of each tendon when actuation around J1 is required.

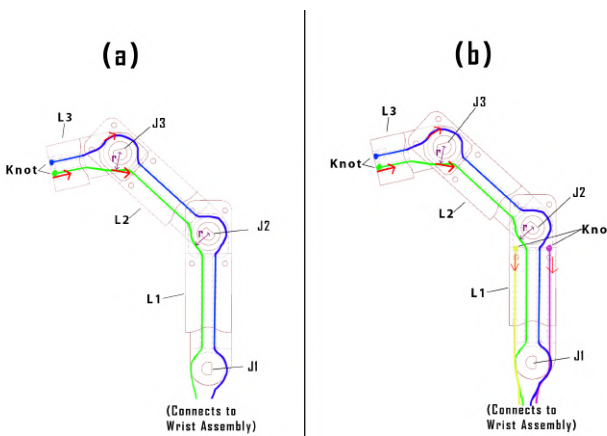


Fig. 26. Diagram showing the cable routing structure along the finger. As you can see, the two cables are routed through the finger links, with a "pulley" on each link providing leverage due to it providing a larger moment force (larger distance). (a) Shows this system implemented on the 1DOF joints such as the ring and little finger, while (b) shows the cable routing through the index and middle finger with the two added cables through L1 illustrated.

Therefore, to achieve the 2 DOF on the index and middle fingers, 3 motor and pulley actuation systems were required. 1 motor would provide antagonistic actuation around L1/J1 (ie both flexion and extension). The second

motor would be used for the flexion to the fingertip, with the third providing extension to the fingertip. The motor choice of the Dynamixel AX-12A provides us with a good platform to enable this type of control. The motors allow for relatively accurate motion with velocity control, but also allow us to set the torque of the motor and compliance. This would provide a system that would compensate for errors if the control model for the cables is not fully implemented.

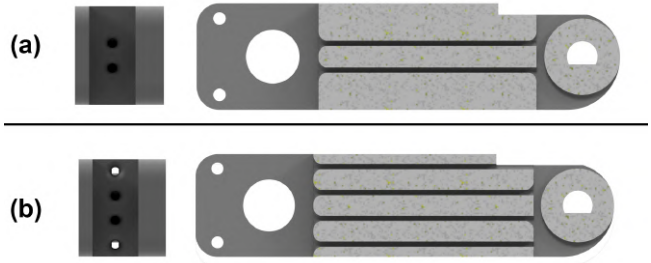


Fig. 27. Figure showing the cross sectional diagram of how the wire routing is preformed inside each link, with (a) showing the Link body back view, and cross section side view, with the two antagonistic cables routing through the middle in two slots to reduce the effect of any one cable on the other. (b) shows the Link Body side back view, and cross section side view of the Index and Middle finger L1 Link, which has 4 cable routings to provide an added flexion extension around J1.

#### H. Proprioceptive Sensing - Ahmed Sami Deiri

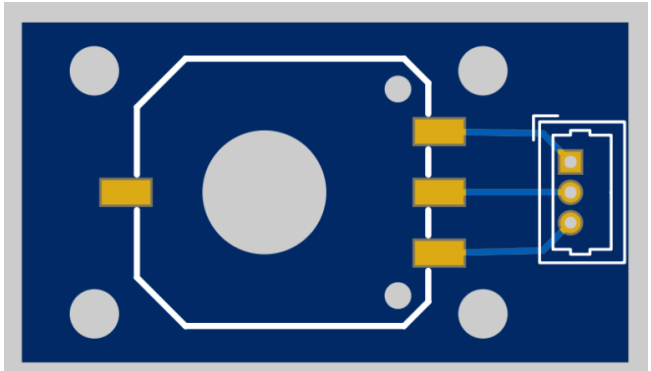


Fig. 28. The PCB design used for the potentiometer. The PCB here shows the surface mounts for the SV01 Potentiometer [14] outlined on the left, with 4 holes at the corners for mounting of the PCB. The 3 pins at the bottom of the potentiometer are connected to a Molex PicoBlade 3 Pin PCB header [15].

Proprioceptive sensing along the fingers was made possible using potentiometers placed at each joint within the finger Link Body. The potentiometer used is a Murata SV01 series STM through hole potentiometer [14]. The potentiometer is surface mounted onto a custom designed PCB seen in Fig. 28. This provides a method of mounting the potentiometer, and connecting to it using the Molex PicoBlade 3 Pin PCB header [15]. The potentiometer has a D shaped slot. A D-shaft is used to connect the child link to a parent link along the chain as seen in Fig. 29a. The D-shaft slots into the potentiometer and will therefore vary the resistance of the potentiometer based on the angle  $\theta_i$  of the Link  $L_{i+1}$  relative to the link  $L_i$ . The links are connected in an open kinematic chain structure, where

the links are connected in series as seen in the kinematic model in Fig. 29b. This could then be used to maintain an awareness of the fingertip position relative to the hand using a forward kinematic of the hand with relative ease (as seen in section II-I).

The kinematic model structure for the hand can be seen in Fig. 29. The potentiometer was chosen over other methods of encoding due to its ability to provide absolute encoding in a simple and cost effective way.

### I. Kinematic Modelling of the Fingers - Ahmed Sami Deiri

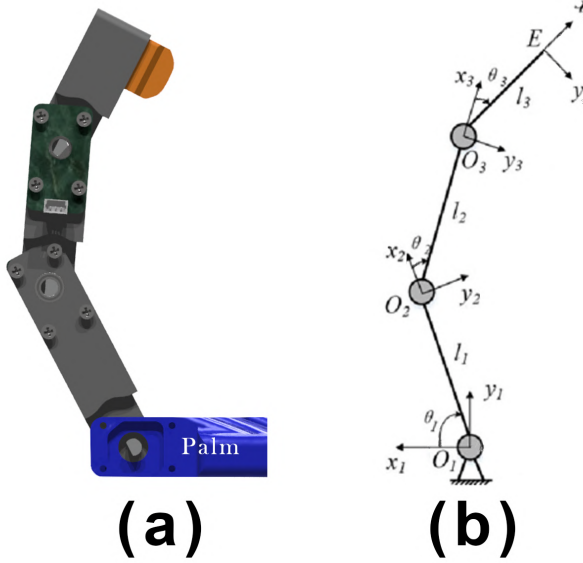


Fig. 29. (a) Shows the robot palm and a single finger, and (b) shows a model following the Denavit-Hartenberg (DH) convention.

Each finger can be represented as an open kinematic chain structure [16]. The Denavit-Hartenberg convention is used to create a transformation matrix for each link as seen in equation 1. This matrix defines the relationship between links i and i-1.

$$T_i^{i-1} = \begin{bmatrix} \cos \theta_i & -\cos \alpha_i \sin \theta_i & \sin \alpha_i \sin \theta_i & l_i \cos \theta_i \\ \sin \theta_i & \cos \alpha_i \cos \theta_i & -\sin \alpha_i \cos \theta_i & l_i \sin \theta_i \\ 0 & \sin \alpha_i & \cos \alpha_i & d_i \\ 0 & 0 & 0 & 1 \end{bmatrix} \quad (1)$$

Applying this to the DH-model shown in Fig. 29 provides the following three transformations matrices for O2 with respect to the origin O1 (palm) in T01, O3 with respect to the coordinate frame O2 in T12, and the end effector E with respect to the coordinate frame O3 in T23. Since the finger only performs flexion/extension and does not have any abduction/adduction capabilities, we can set  $d_i$  and  $\alpha_i$  to zero.

$$T_1^0 = \begin{bmatrix} \cos \theta_1 & -\sin \theta_1 & 0 & l_1 \cos \theta_1 \\ \sin \theta_1 & \cos \theta_1 & 0 & l_1 \sin \theta_1 \\ 0 & 0 & 1 & 0 \\ 0 & 0 & 0 & 1 \end{bmatrix} \quad (2)$$

$$T_2^1 = \begin{bmatrix} \cos \theta_2 & -\sin \theta_2 & 0 & l_2 \cos \theta_2 \\ \sin \theta_2 & \cos \theta_2 & 0 & l_2 \sin \theta_2 \\ 0 & 0 & 1 & 0 \\ 0 & 0 & 0 & 1 \end{bmatrix} \quad (3)$$

$$T_3^2 = \begin{bmatrix} \cos \theta_3 & -\sin \theta_3 & 0 & l_3 \cos \theta_3 \\ \sin \theta_3 & \cos \theta_3 & 0 & l_3 \sin \theta_3 \\ 0 & 0 & 1 & 0 \\ 0 & 0 & 0 & 1 \end{bmatrix} \quad (4)$$

These equations can be combined to create a representation of the fingertip with respect to the origin(wrist) as  $T_3^0 = T_1^0 T_2^1 T_3^2$ .

$$T_3^0 = \begin{bmatrix} \cos \sum_1^3 \theta_i & \sin \sum_1^3 \theta_i & 0 & l_1 \cos \theta_1 + l_2 \cos \sum_1^2 \theta_i + l_3 \cos \sum_1^3 \theta_i \\ \sin \sum_1^3 \theta_i & \cos \sum_1^3 \theta_i & 0 & l_1 \sin \theta_1 + l_2 \sin \sum_1^2 \theta_i + l_3 \sin \sum_1^3 \theta_i \\ 0 & 0 & 1 & 1 \\ 0 & 0 & 0 & 1 \end{bmatrix} \quad (5)$$

This allows us to represent the fingertip coordinates Ex and Ey with respect to the origin O1 (Fig. 29) and the coordinate frame y1 and X1 using the following equations.

$$\begin{aligned} E_x &= l_1 \cos \theta_1 + l_2 \cos \sum_1^2 \theta_i + l_3 \cos \sum_1^3 \theta_i \\ E_y &= l_1 \sin \theta_1 + l_2 \sin \sum_1^2 \theta_i + l_3 \sin \sum_1^3 \theta_i \end{aligned} \quad (6)$$

Ez = 0 as the finger is not moving within the z axis relative to the origin coordinate frame O1.

In our hand design, the lengths for the links L1, L2, L3 are seen in table I. The angle  $\theta$  is the angle of the link as measured by the provided potentiometers at each link.

The transformation matrix for the fingertip wrt. J1 (ie  $T_3^0$ ) could be used to describe each finger with respect to a shared origin and coordinate frame along the palm or wrist assembly. To do this, a simple rigid body transformation can be used.

In terms of the thumb kinematics, the thumb has a similar kinematic structure as the other fingers (Fig. 29b), with an added revolute degree of freedom located along the link L1, with the axis of rotation (z) falling perpendicular to the link L1. This model was not created as I expected to utilise the URDF exported model to generate a forward and inverse kinematic model, however due to difficulties experienced in that section I began making this model but could not complete due to time constraints.

In terms of inverse kinematics, an accurate model of the inverse kinematics could not be obtained due to the under-actuated degree of freedom around J2 and J3 (and J1 on the ring and little finger). To model the hand a control loop using the potentiometers and the motors could be used to actuate until a position condition is met (or deemed impossible). On the index and middle finger, the extra flexion/extension DOF around J1 could be controlled directly and the proportional bending afforded by an elastic material/spring could be modelled mathematically as bending in the ratio of their respective resistive torques.

### J. Link Manufacturing optimisation - Ahmed Sami Deiri

Considering the design was to be FDM 3D printed, all manufactured parts were designed and optimised with the

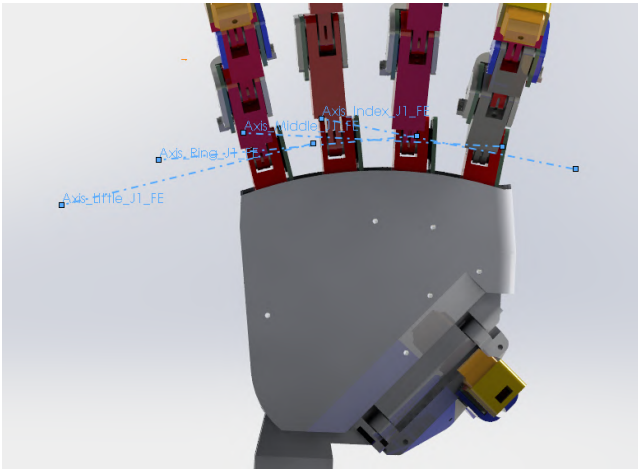


Fig. 30. Render of robot hand showing the J1 axis of rotation for index, middle, ring and little finger highlighted in blue.

manufacturing in mind. This means that our design should not require any/minimal supports to be printed, and should have sufficient bed adhesion to be printed without the use of bed adhesion. This should mean that parts can be removed and implemented within the product without any manual work required.

FDM 3D printing is a layer by layer additive manufacturing process. To achieve the desired result, the part needed to have an orientation that was flat with no overhangs which could be placed along the bed. Any holes/extrusions within the part were designed with consideration of the printing process. The final result can be seen in Fig. 31. The part is placed flat on the the bed with no large overhangs. The circular profile of the holes allows them to be printed without much support as it doesn't have any large overhangs, with the printer slowly printing progressively further rather than attempting a large overhang. The extruded cut for the center was more difficult to print, but the addition of fillets to the corners allowed this part to be consistently printed without any issues even with the 6.7 mm overhang.

By printing the finger link in this orientation we mitigate the risk of the part failing as FDM 3D printed parts are most susceptible to failure on shear forces applied along the layer lines.

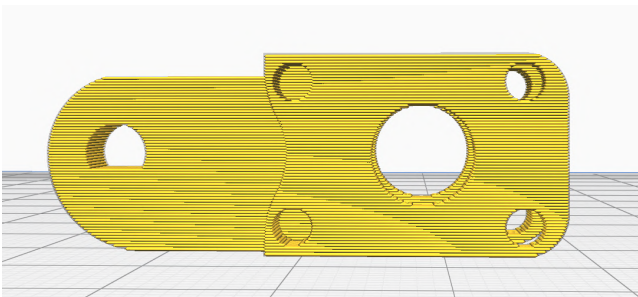


Fig. 31. Image of the printing orientation of the finger link for printing, showing the printing layers in the FDM slicing software Cura.

Overall, this part was a success with a printing time of 24-34 minutes per finger depending on the length.

### K. Link Lengths - Kai Page

As mentioned in our previous literature review, one critical aspect to designing the fingers were to justify the lengths each finger link should be designed to. Humanoid robot hands are designs so that they are modelled against a human hand regarding their appearance and their ability to move [17]. Therefore, our model has replicated the components of a human hand by consisting of 3 links (3 bones): proximal phalanx (L1), middle phalanx (L2) and distal phalanx (L3). Thanks to Kim's model of the Biomimetic Optimisation for the Sizing of Humanoid Robot Fingers (BOSHRF) algorithm [18], we were able to base our link lengths to this model and size each of our links (bones) specifically from the smallest link length that could be made with our design. The lengths are measured from joint to joint to create a kinematic model. The phalangeal parameters produced from [18] had been optimised by this algorithm with the interphalangeal joint coordination (0.62) of a human finger from the biomimetic viewpoint.

<i>i</i>	Finger	Length of phalanx (m)			Size (m)	Remarks
		$l_{1i}$	$l_{2i}$	$l_{3i}$		
1	Index	0.050	0.0389	0.0304	0.1193	Fig. 5
2	Middle	0.058	0.0441	0.0361	0.1382	Fig. 6
3	Ring	0.055	0.0430	0.0333	0.1313	Fig. 7
4	Little	0.045	0.0355	0.0270	0.1075	Fig. 8

Fig. 32. Phalangeal parameters of humanoid robot fingers optimised by the BOSHRF algorithm with interphalangeal joint coordination of 0.62 [18].

To begin calculating the links of each phalangeal parameters, the smallest link length that was possible for our design was determined as the smallest link of the smallest finger ( $L_{3i}$ ); the distal phalanx of the little finger. From there, the ratio was calculated based of the example lengths in [18] and multiplied with  $L_{3i}$ . This formulation is shown in Fig. 33A are examples of how some of the lengths highlighted in Table I are calculated. By following Fig.33A, all L3 of each fingers can be computed by simply replacing the respective given L3 lengths of each finger.

The next step taken is shown in Fig.33 B to determine L2 lengths of all the fingers. The example highlights the calculation for L2 Little finger where L2 of other fingers can be calculated by replacing the ratio of L2/L3 of their respective fingers taken from [18] and then multiplying with also their respective L3 lengths. This method is repeated to calculate L1 lengths of all the fingers but by replacing the ratio with L1/L3 as shown in Fig.33C.

Lastly, the calculations for the parameters of thumb required a different method as Kim's [18] analysis did not include the thumb. Due to this, the link lengths for the thumb is calculated based on parametric lengths of the whole hand from [19], where a design and analysis of a multi-fingered robot was illustrated. During this process, Kumar and Bhushan estimates measurements by using the Hand Length (HL). As our hand had already computed the other four fingers and palm, the HL could be determined

TABLE I

CALCULATED PHALANGEAL PARAMETERS OF THE DESIGNED FINGER LINKS WHICH WAS ACHIEVED BY USING THE SMALLEST POSSIBLE LINK DESIGN  $L_{3l}$ , TO SCALE UP USING [18] BOSHRF ALGORITHM. THE THUMB USED THE RESEARCH FROM [19] PAPER WHICH ANALYSED THE PARAMETRIC LENGTHS OF THE HAND. DUE TO THE THUMB HAVING TWO ADDITIONAL LINKS (THE PALM HINGE AND ADDUCTION/ABDUCTION LINKS), THE TWO LINK LENGTHS DISCUSSED HERE ARE THE L3 AND L4 LINKS RATHER THAN L2 AND L3. THUMB L4 REFERS TO THE THUMB FINGERTIP ASSEMBLY.

	<b>L1</b>	<b>Link Name</b>	<b>L2</b>	<b>Link Name</b>	<b>L3</b>	<b>Link Name</b>	<b>L4</b>	<b>Link Name</b>	<b>Total Length</b>
<b>Little</b>	37.717	$L_{1l}$	29.754	$L_{2l}$	22.630	$L_{3l}$			90.101
<b>Ring</b>	46.098	$L_{1r}$	36.040	$L_{2r}$	27.910	$L_{3r}$			110.049
<b>Middle</b>	48.613	$L_{1m}$	36.962	$L_{2m}$	30.257	$L_{3m}$			115.832
<b>Index</b>	41.907	$L_{1i}$	32.604	$L_{2i}$	25.480	$L_{3i}$			99.991
<b>Thumb</b>					42.460	$L_{3t}$	34.230	$L_{4t}$	76.690

Fig. 33. Examples of calculations taken to determine the link lengths shown in I. (A): Calculates the length of L3 Ring finger by deriving a ratio from Kim's [18] given lengths of L3 Ring and Little, then scaling with the known length of our design (L3 Little finger). L3 of different fingers can be calculated with the same method by using their respective ratios and then multiplying with the known L3 Little finger, (B): Calculates the L2 Little finger by deriving a ratio from Kim's [18] given lengths of L2 and L3 Little and then multiplying with the known L3 Little finger's length. This formula can be repeated for all L2 fingers by using their respective L2/L3 ratios and respective calculated L3 lengths, (C): Calculates the L1 Little finger by deriving a ratio from Kim's [18] given lengths of L1 and L3 Little and then multiplying with the known L3 Little finger's length. This formula can be repeated for all L1 fingers by using their L1/L3 ratios and calculated L3 lengths respectively.

as the longest length of the hand, measured from the tip of the middle finger to the bottom of where the palm ends. This allowed us to calculate both the proximal  $L_{3t}$  and the distal  $L_{4t}$  phalanges of the thumb. The calculated link lengths for the final design are highlighted in Table I.

#### L. Finger Performance and Behaviour - Ahmed Sami Deiri

Due to the COVID crisis and more specifically issues relating to ordering, we were unable to build this hand as per our design. To test the finger joint behaviour, a testing platform was created that utilises the original 3D printed parts for the palm assembly and the finger assembly.

Parts that could not be acquired were replaced or omitted. This included the PCB which was completely omitted, with the potentiometer being placed in the slot without being connected. The prototype finger could be seen in Fig. 35. The goal of this test was to evaluate behaviour of the finger, however, data regarding the torque

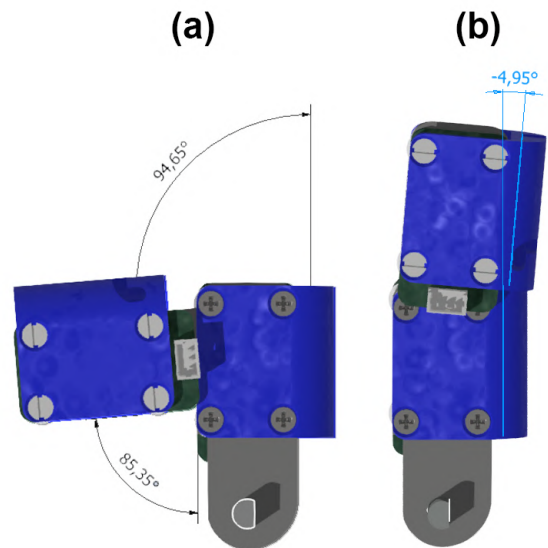


Fig. 34. (a) Shows the maximum bending capability of the links, with 0° being both links pointing directly upwards. (b) shows the maximum movement that can be achieved during extension, which is limited by the link covers. These link covers are placed there to limit the movement of the joints to prevent them from rotating backwards,

required to pull the finger could not be gathered due to the prototype lacking parts from the final construction of the finger. The finger was tested across both degrees of freedom, with full finger actuation seen in Fig. 37, and the actuation at J1 from the tendons in L1 shown in Fig. 37.

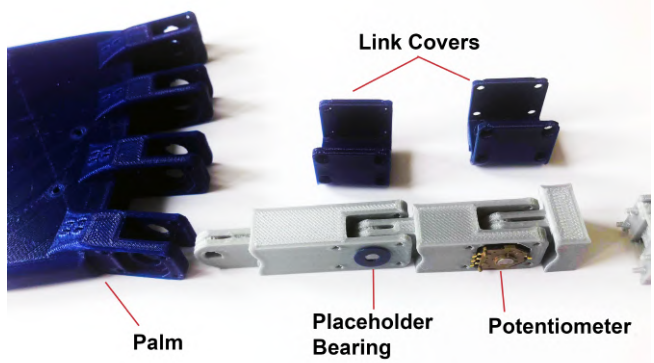


Fig. 35. Image showing the prototype finger assembled for use

The desired motion was successfully achieved from L1, with the antagonistic actuation functioning as intended. The full finger actuation was also operational, however

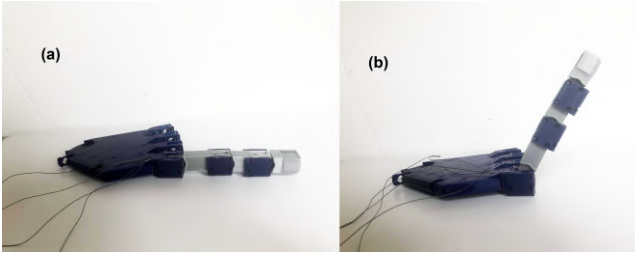


Fig. 36. Images showing the real finger at different stages of flexion due to tension along L1. (a) shows the neutral state with no flexion tension. (b) shows the finger with flexional tension applied along

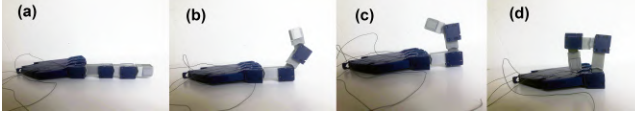


Fig. 37. Images showing the real finger at different stages of flexion due to tension along the entire finger. (a) shows the neutral state with no flexion tension. (b) shows

we established that the finger will bend from the joint with the lowest friction/resistance. If all the joints have approximately the same resistance the finger will bend from the fingertip inwards. This reinforces the need for springs/elastic materials to be attached to the finger. While this will introduce some added resistance to rotation, it will allow the fingers to move simultaneously with the correct resistance ranges, by providing a linear relationship between joint angle and resistance induced.

In terms of manufacturing, the finger was able to be printed fully without needing any supports or brim/raft, and could be taken from printing to assembly without requiring any post processing. One thing that could need changing would be the size of the holes, as the hole for the D-shaft was found to be too small at the normal printing size of 4 mm diameter. This was mitigated by increasing the hole diameter to 4.2 mm. This could be tweaked for individual manufacturing tolerances based on the manufacturing process/device used.

#### *M. Weight Reduction in the Finger link - Ahmed Sami Deiri*

In terms of link design, the Link Body could be made thinner, especially in the middle which is currently larger than required to accommodate for easy modification and embedding of sensors. A link body as seen in Fig.38a, can be used in place of the current link body design as seen in Fig.38b depending on user preferences. While this would decrease the weight and size of the fingers, it would provide a much less customisable and manufacturable link body design due to the complex geometries. This was found to reduce the weight from 5 g average for link bodies to 4 g. While this could be seen as a 20% decrease in weight reduction in terms of this part, it poses an approximate 14g decrease in weight over the entire hand. Therefore, the primary advantages of this implementation would be size. This size reduction could be furthered by reducing the number of holes through the center of the link to 1 hole, and relying on carbon tubing with a pulley and potentiometer mount on either side. This improvement

could pose a manufacturability improvement if required, however, the customisability would suffer as any further attachments would need to be mounted onto carbon tubing rather than printed in place.

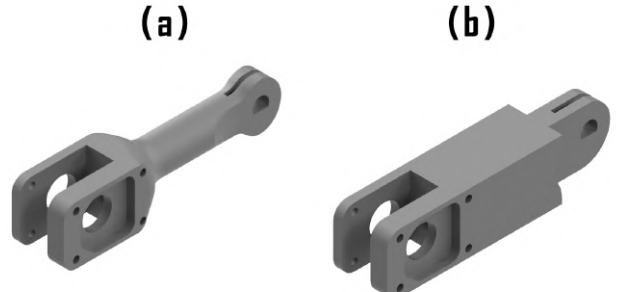


Fig. 38. Render of minimised finger link body (a) and the current link body (b).

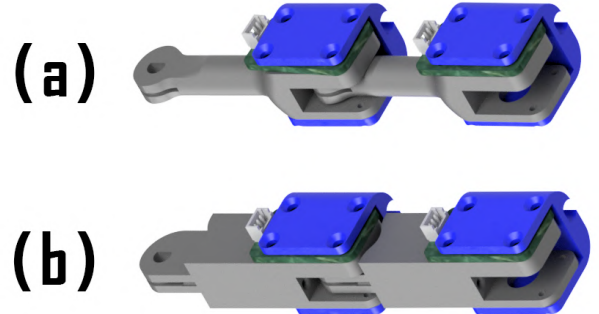


Fig. 39. Render of minimised finger link body (a) and the current link body (b) within a 2 link assembly.

#### *N. Palm Design and covers - Talha Tailor*

The palm was designed in order to support the structure of the fingers and thumb as well as provide a routing path for the tendons and the sensor wiring. The palm structure dimensions were obtained from the average human male palm size which is approx 101mm by 88 mm [20]. Due to the palm structure being SLA printed the thickness was kept at 10mm to ensure stability of the structure. The back surface of the structure was kept flat with minimal grooves to allow for ease of printing. A palm design with all fingers parallel to one another was replaced with a curved hand approach. The palm was designed to have fingers at slight angles from one another to allow for a more cohesive grasp, particularly of objects with non-uniform shapes, thus allowing fingers to point inwards- see Fig. 40.

The structure and all internal components are enclosed by SLA printed hard covers which are designed to screw into the main structure. 5mm thread inserts can be placed at either end of the main structure, with the covers screwed in from both sides- see Fig.40. The covers can then be removed easily for any adjustments to the tendon routing and wiring as well as maintaining modularity. The hard covers provide a supporting structure, shelter the internal

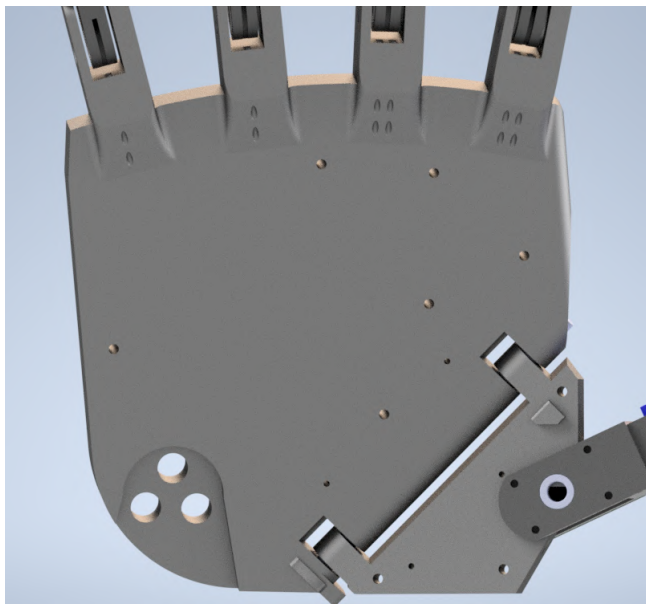


Fig. 40. Overview of complete palm- not including tendon routing

components as well as provide a surface for allocation of sensors at various regions of the palm. The palm structure can be seen in the following section where tendon routing is discussed.

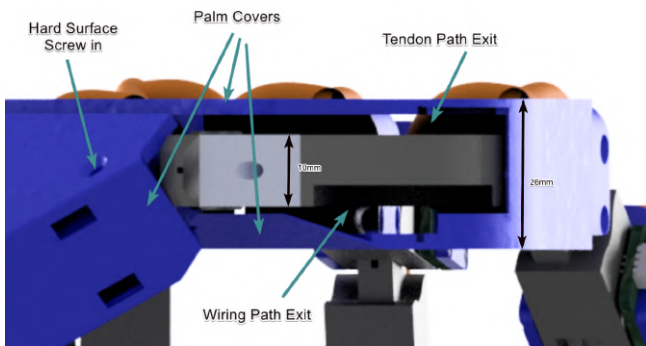


Fig. 41. Figures shows a side view of the palm, presenting the palm structure sandwiched by the covers and exit paths of the tendons and wiring.

The hard covers were designed to provide a 5mm gap at front side and 4mm gap at back region with the covers themselves being 1mm thick (resulting the the whole hand structure having a width of 21mm)- see Fig. 41. The purpose of having this region of space at the back as well as the front is for clearer tendon routing and wiring. 1.2mm thick rectangular rib supports were added after the initial print after noticing structural weaknesses (see Fig. 42). Tendons are all routed to the the front of the palm with all sensor wiring routed to the back. This allows for ease of replacement, again maintaining the overall modularity and leaving space for more components and sensors if needed in the future.

*1) Tendon and wire routing - Talha, Bashar:* During testing and prototyping it was understood the tendons could not be routed generally through a printed path on palm. There are two main reason for why this system would be inefficient and impractical. The first being fric-

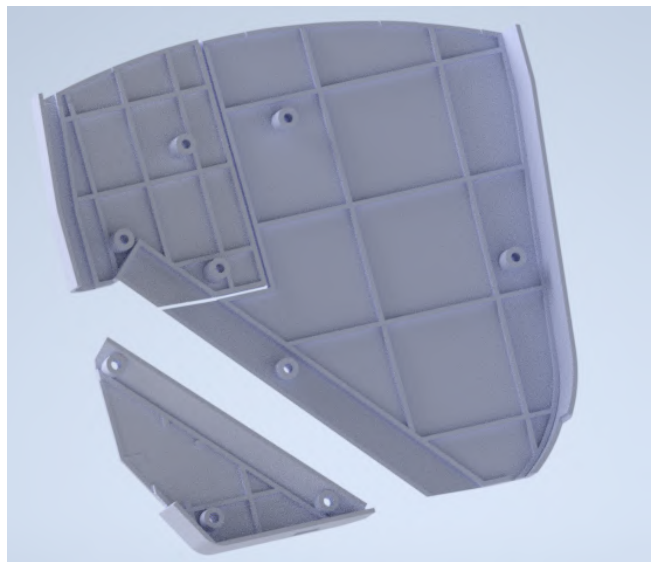


Fig. 42. Supporting rib for the hard cover structure ensuring cover remain rigid on contact.

tion between the tendon wiring and the plastic SLA print. Having multiple printed routing system would significantly increase the required torque from the motor. The second reason is the general wear the tendon wire will have on the plastic. The tendon, though very strong and durable, may eventually give out against the surface of the plastic, or worse permanently damage the printed tendon routing due constant wear- resulting the whole palm needing to be replaced.

A total of 18 tendons require routing at the front region of the palm. Two tendons each from the little and ring fingers, four each from the middle and index and six from thumb structure.

In order to provide a more efficient tendon routing system, set placed 2mm diameter stainless steel pins were fixed on specified areas of the palm. Pin placement is displayed in Fig. 43. The pins of 6mm length can be inserted rigidly into the wholes made into the palm. This would allow the tendon to be guided to the correct areas rather than hard rooted (which was done in the previous design). It also allows for simplicity and modularity in the overall design, particularly in the testing stage- pins can be slotted in various regions to determine their optimum locations. The pin placement positions however, could not be tested and optimised due the covid-19 situation.



Fig. 43. The figure presents inserted pin into the palm structure for ease of tendon routing.

The wiring for each finger is as follows. Hall effect Sensors: Live wire, Ground wire, SCL, SDA. Rotational Potentiometer: Live wire (Vref), Ground, Output. Wires are soldered and combined at specified regions with required slack to maximise space and avoid twisting and getting caught at joint regions. All wires are then crimped and connected via small junction connectors at the back region of the palm and fed to the motor housing box. Live wires for Hall sensors and potentiometers are separately connected in parallel with the ground wire shared between all sensors. Hall-effect SLA and SDA are also connected in parallel with the potentiometers each having their own separate output voltage wires.

#### O. Thumb design - Talha Tailor

*1) Design constraints:* The thumb is an important part of the robotic hand and if not designed correctly can lead to significant issues later on during the testing and improvement stages. Many robotic hand designs have very intricate and complex thumb joint mechanisms (such as the DLR-HIT Hand II [21]) in order to comply with their grasping objectives. Our design will focus more on a modular design while maintaining the required performance objectives.

Our constraints relate to the design aims and objectives where in-hand manipulation and dexterous thumb movement is a requirement. The thumb must have the functionality to aid in performing the required precision grasps as well as be stable enough to fulfil the tripod and writing grasps. The thumb has a design requirement of 3 DoF which includes one actuated abduction/adduction movement and two flexion/extension movements each actuated separately. As explained in the SOTA this was believed to be the simplest and most effective way in meeting our design aims. A few simple thumb design concepts were originally produced and tested before deciding on the final design. These preliminary designs were SLA printed and assembled to understand functionality and integration to the overall hand. The initial designs are displayed on Fig. 44.

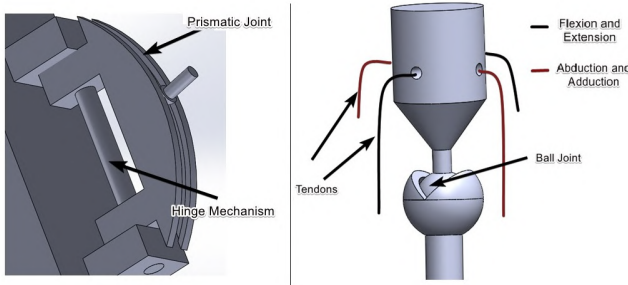


Fig. 44. Preliminary thumb designs. Prismatic thumb design on left, ball joint design on right

*2) Prototype I, II:* The prismatic joint design (Fig. 44), was the first design to be tested. The prismatic joint allowed for the abduction/adduction movement with following flexion movements using a hinge joint design. This design was flawed primarily due to its limited rotation due to the potential space it would take within the palm

as well as the potential frictional issues which would lead the joint to get stuck. Thus, in order for the design to function correctly it must be fabricated from a different material with higher accuracy- defeating the point of one of the objectives of the design, and increasing the overall cost.

The second joint design (right of Fig. 44) was the ball joint design. The movement through the use of tendons are illustrated, where the required flexion/extension can be completed at the MCP area and abduction and adduction are limited within the design to the required 90 degrees of rotation. This design was inspired by many ball joint thumb models presented in the SOTA, particularly the Etho dexterous hand [22].

Once printed and tested it was decided that this design would not be used over the current design. The ball joint itself would need to be purchased or produced by other than SLA. Frictional complications were present between the two plastic surfaces which was helped via lubrication but the issue of wear and tear would need to be solved- due to the plastic to plastic contact. The outer region which held the ball joint was also vulnerable and kept primarily in place by the attached tendons. Improving this region would lead to a considerably bulkier model and potentially limit the modularity of the design (where the ball joint is attached).

*3) Prototype III & Final Design:* The final design consists of a palm hinge design. This design was influenced by many of the designs stated in the SOTA including the FTN robot hand and Gifu hand III designs [23] [24]. The first tested prototype can be seen in Fig. 45, and final design structure in Fig. 46.

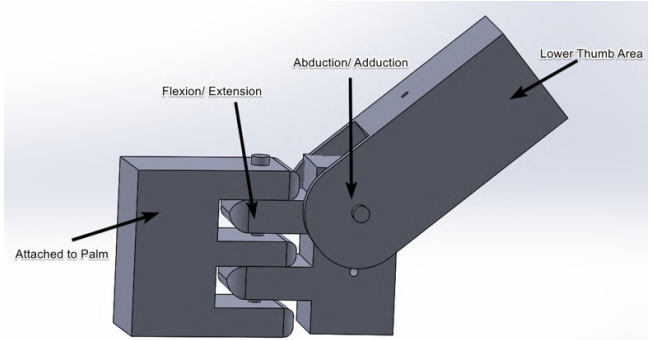


Fig. 45. Final design concept of thumb for flexion and abduction

Abduction/adduction occurs around the outer region of the palm with flexion/ extension of the palm hinge imitating that of the TMC joint and opposition of the thumb. Flexion/extension surrounding the MCP and PIP of the thumb are designed in a similar manner to the fingers discussed in Section on Finger-links. Joint angles, similar to those of the fingers, are measured through the use of angular potentiometers and PCB's. The potentiometer used for the palm hinge is connected to a shaft linear to the hinge with wiring going through the palm structure to the backside. Abduction/ adduction of the thumb is measured with the potentiometer and PCB connected directly to the side of the joint.

Many robot hands do not account for the full movement of the TMC joint and focuses further on flexion and

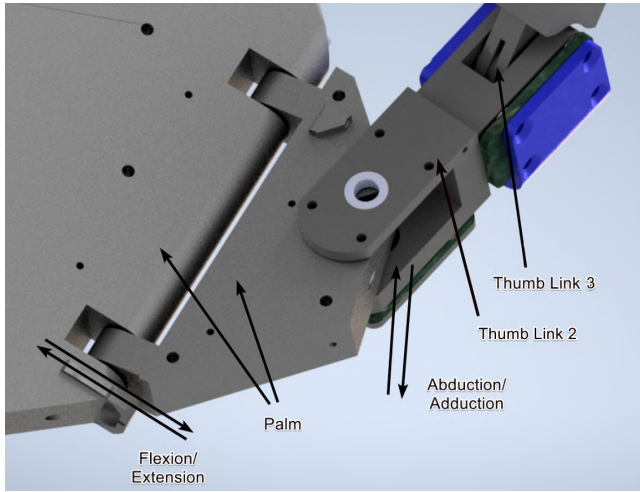


Fig. 46. The final thumb joint structure including the palm-hinge joint

extension around the MCP joint primarily- this can be seen in robot hands such as the Ethohand and the Robocasa [25] [22]. As stated in R.Chi et al, a paper surrounding the kinematic design optimisation for a robot hand, the opposition achieved by the TMC joint of the thumb to other fingers is critical when trying to mimic the dexterity of the human in hand manipulation [26]. Many robot hands do achieve the required motions (such as the DLR hand II [21]) but as discussed in the SOTA, have complex mechanical structure that cannot be implemented in our design due to the time and cost constraints that surrounds them.

In order to achieve the opposition mechanism that is unique to the thumb, which the TMC joint plays a fundamental role, the palm hinge was selected to be the best choice when considering our design constraints. The likelihood of this design to adequately preform the Schaeffer's test through opposition (movement of the tip of the thumb to the tip of the little finger) is also greater than the previous design models [27]. This palm arch (visible in Fig. 46) would also enable the hand to perform more dexterous in-hand manipulation of complex objects [22].

Prototyping the joint structure you see in Fig. 46, the tendon system need configuring to ensure actuation of the tendon controlling opposition did not affect the movement of the other joints (and vice-versa). Each joint motion needed to move independently from one another to ensure valid control. Therefore, cavities were designed within the palm structure for tendons to be inserted and re-routed. This was done for the flexion/ extension tendons at the MCP joint and adduction tendon of the thumb only. These movements would be then guided from the right palm structure, preventing any additional thumb motions other then those specified through actuation.

#### P. Wrist Design - Mohammed Al Bashar Khan

The wrist is designed as a box with maximum dimensions of 186.5 mm by 213.844 mm by 195.4 mm (height by width by depth). The wrist features different sections, designed specifically to work with components such as the Dynamixel motors and the F12 cooling fan. The wrist also has 2 levels, where the motors and electronics

are strategically placed for optimum performance. All of the plates described in this section were to be produced through 3D printing.

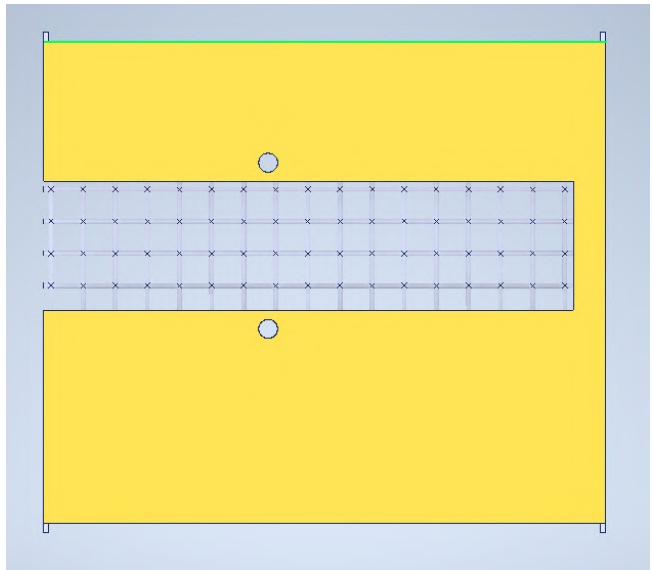


Fig. 47. The top plate of the wrist. Some of the features that can be seen in the image include the 2 M6 bolt holes for the hand mounting piece. the corners of the top plate also have tabs, which slot into connecting pieces

The Image in Fig. 47 features the top plate section of the wrist. The thickness of this plate is 10mm, and it consists of the mesh gap, for the tendons to pass through and the bolt holes, with which the hand can be attached to the wrist. The meshed gap in the top plate serves the purpose of providing space for the tendons to reach the motors. The mesh is there to help in keeping the tendons from getting tangled.

Furthermore, the diameter of the mesh bars is 1.5mm, and the area between bars is  $72.25\text{mm}^2$ . This results in a larger space for the tendons to freely go through the gap, which lower the chance of the tendons physically coming into contact with the bars. This is desired due to the fact that the tendon would be hindered by the friction effects from rubbing against the bars, which would in turn have a negative effect on the performance of the hand. The mesh gap is 165 mm by 40 mm, large enough that the tendons for 8 different motors can pass between hand and motor and reach the components that are on different levels of the wrist.

The image in Fig. 48 features the base plate for the top level in the wrist. This level will hold 6 motors and the power board. The mounting area for the power board can be seen in the top left of the base plate, where 4 motherboard standoffs have been placed, alongside a wiring hole which will feed the cable down to the lower level. The base plate also features 12 slots for the rails for the motors, 2 rails for each motor. Each of the rail slots has been placed so that the motors are close the mesh gap on the top plate, and also so that the pulleys attached to the motors will not come into contact, affecting the performance of the hand.

On the bottom right hand of the base plate, a long rectangular hole can be seen. This hole is right next to

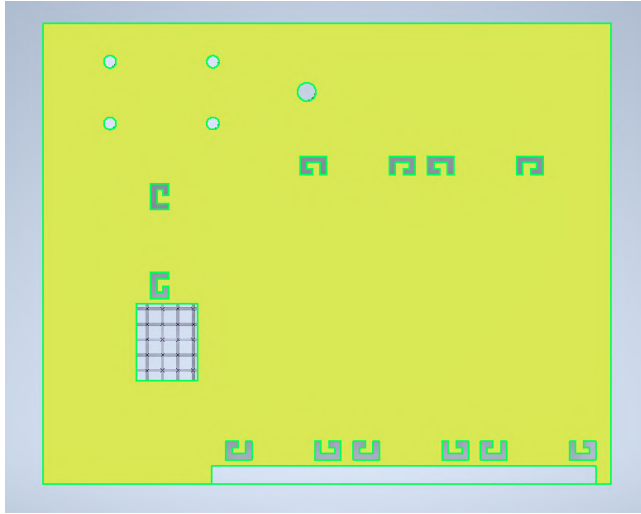


Fig. 48. The base plate of the wrist. The Rail slots shown in this image are 10mm deep, so that the rail is held in the base and does not slip out easily. The base plate will slot into the side walls of the wrist, rather than being bolted on

where three of the motors will be placed and serves as the feed hole for the motor power cables. The meshed gap on the bottom left side of the base plate is the gap through which the tendons for the motors on the lower level of the wrist will go through. This meshed gap has also been placed so that it is close enough to the meshed gap on the top plate. This results in free space through which the tendons can go through, without being impeded by the wrist structure. The mesh bars on this gap have a diameter of 1mm, with a  $16\text{mm}^2$  space between bars. Like with the top plate, this results in a larger space for the tendons to freely go through the gap, which lower the chance of the tendons physically coming into contact with the bars.

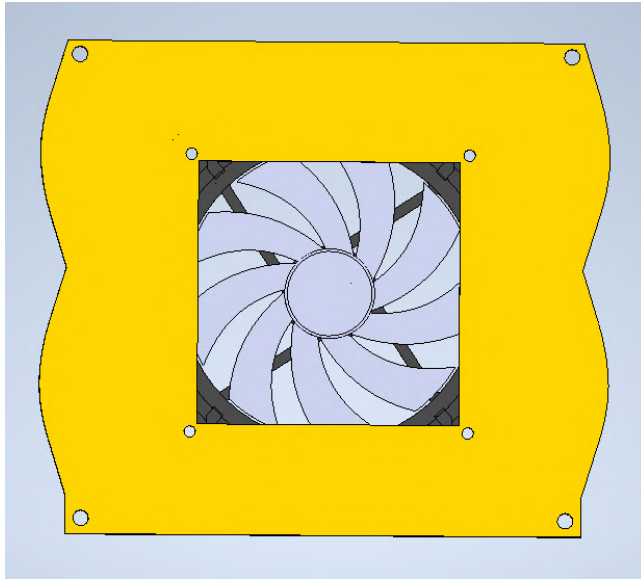


Fig. 49. The fan plate of the wrist, with the fan. The corners of this plate feature M6 holes, through which threaded rod can be placed to hold the whole wrist unit together

The images in Fig. 49 and Fig. 50 show the fan plates. In this wrist, it was decided to use a fan for cooling, as there

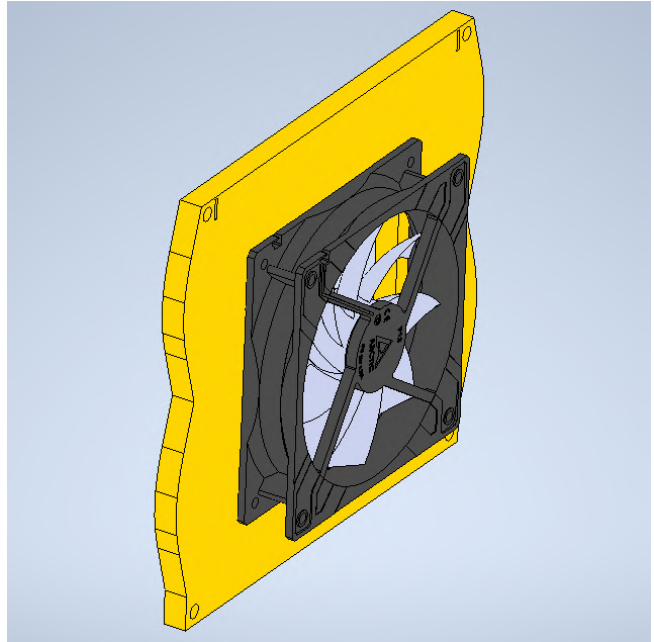


Fig. 50. The side view of the fan plate of the wrist, with the fan

was a large amount of high torque motors placed in a small area, which would inevitably result in overheating. The design of the fan plates is such that fan can slot into the wrist and then be fixed in place with screws. The cold air is blow through the fan plate, into the wrist and subsequently exiting the wrist through the opposite wall shown in Fig. 51.

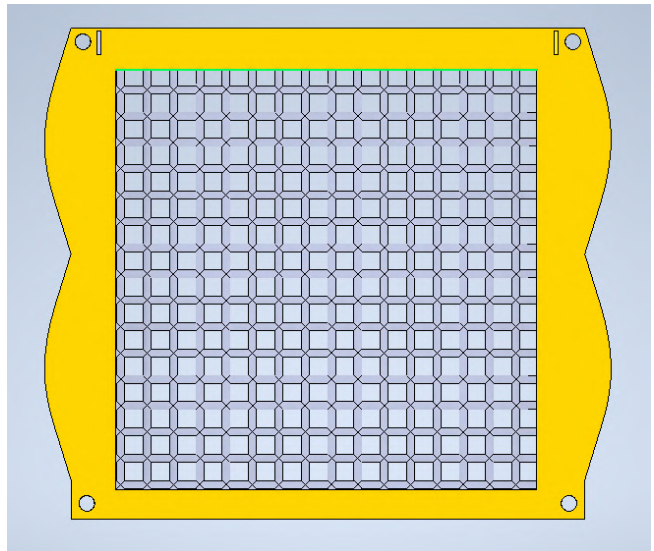


Fig. 51. The outer meshed plate of the wrist. Because this is an outer plate, the corners of this plate feature M6 holes, through which threaded rod can be placed to hold the whole wrist unit together

The opposite wall is meshed all the way through, to serve two purposes. Firstly, the meshed wall allows the air from the fan to escape the wrist. Secondly, the meshed wall can also be used to feed electrical cables through into the wrist, directly to the electrical components. The bars of the mesh have a diameter of 3mm, and there is a  $49\text{mm}^2$  gap between bars, which will allow wires and connectors through.

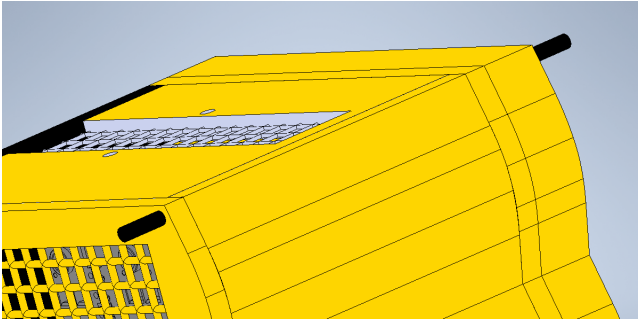


Fig. 52. The image shows how the threaded rod would fit through the M6 holes on the outer plates to hold the wrist together

*Q. Motor Placement - Mohammed Al Bashar Khan*

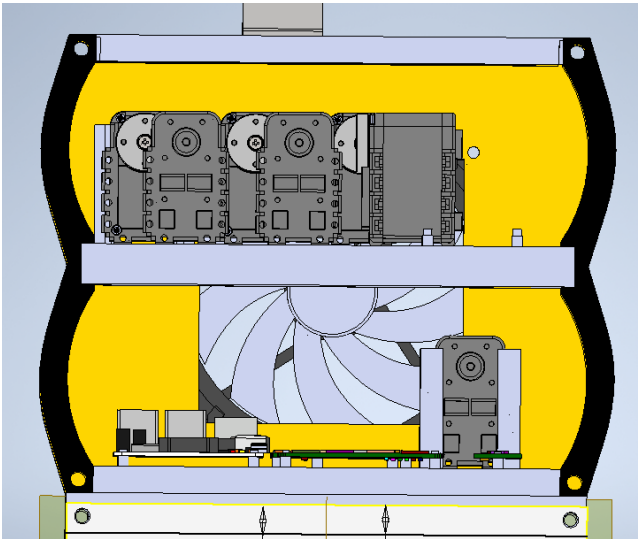


Fig. 53. The inside view of the wrist. the Components can be clearly seen to be spaced out and all be in close proximity to the cooling fan

The image in Fig. 53 shows the inside of the wrist with the motors. In total there are 8 motors in the wrist, with 6 on the top level and 2 on the bottom level. The 6 motors on the top level are for the pinky, ring, middle and index finger functions, and the remaining motor on the top level controls the palm flexion function.

The image shown in Fig. 54 shows how the motors in the top level of the wrist are arranged. The five motors at the top of the image, that face each other are connected to the fingers, and control the flexion and extension of those fingers. The lone motor at the bottom that is perpendicular to the rest is for the palm flexion, and is oriented that way due to the way the tendons are routed from the hand for palm flexion. The hand uses pins either side of the palm to route the tendons, so the motor for the palm will need to pull and release tendons from either side of the hand.

The image in Fig. 55 shows the view from the top of the wrist. As stated in the wrist design section, the meshed gap in the top plate allows the tendons through to all the motors, including the ones on the lower level of the wrist. The two motors on the lower level of the wrist are for the thumb flexion and abduction/adduction functions. These two motors have been kept at a greater distance from the

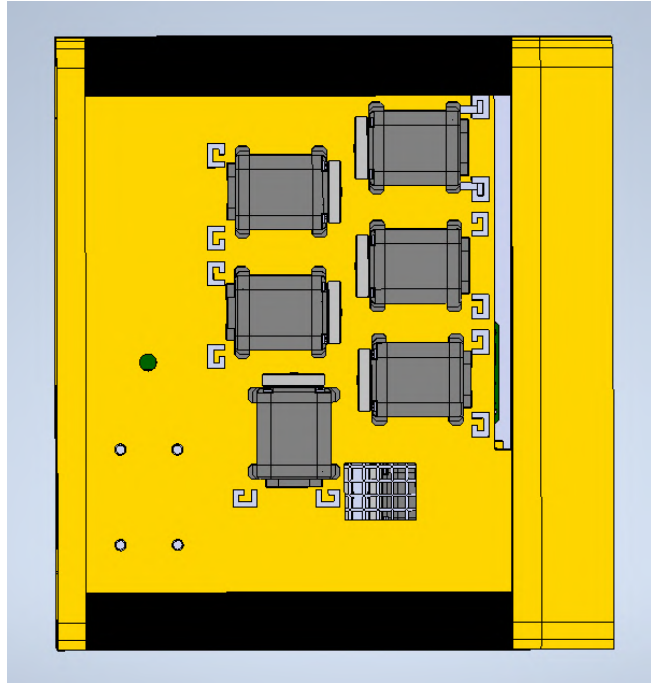


Fig. 54. The overhead view of the top level of the wrist

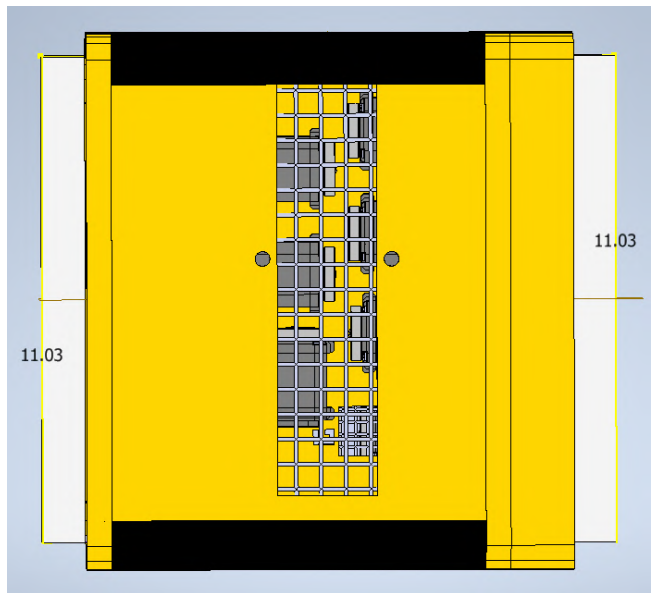


Fig. 55. The overhead view of the wrist

hand than the rest of the motors due to the palm flexion function.

The section of the palm that contains the fingers is fixed, therefore the tendon path and length for the fingers is fixed. This is why the motors for the fingers are simply directly below the hand. But the thumb is connecting to the section of the palm that moves. This results in the tendon path and length for the thumb abduction/adduction and flexion to change as the palm position changes. By increasing the distance of the motors from the hand, and therefore the length of the tendon, the effects from the change will be felt less in the hand performance.

*1) Tendon routing material - Mohammed Al Bashar Khan:* The image shown in Fig. 43 in section II-N shows

some of the 2mm diameter pins used in the hand to route the tendon cable to the wrist. These cables will then go through the meshed gaps through to the motors below. Whilst these feature have been specifically designed so that the tendons can have limited interactions with the different surfaces (and therefore have less friction affect the function of the tendons), further efforts need to be made to minimise friction between tendon and hand/wrist surface.

The best way to decrease the friction between the tendons and the hand/wrist surfaces is to introduce material with low friction coefficient to the palm pins and the mesh in the wrist. An issue with this method is that the friction coefficient is measured between two materials, as they interact. Therefore, for conclusive results, physical testing would be required. As this option is not currently available, possible materials can only be discussed in terms of manufacturability and availability.

Since the tendons are already decided, and are made of a mixture of materials, the values for friction coefficient cannot simply be found on the internet. Therefore, common low friction materials like metals will need to be considered in the hope that they are a safe enough choice that they fulfil the criteria required of them. A possible solution would be to use tape made of a plastic with low friction (e.g. electrical insulation tape). This could be cut to size, and would be adhesive from the outset, so wouldn't require the spending of more money on adhesives. This solution would work well with the 3D printed mesh bars on the wrist.

However, after considering the size of the pins (2mm diameter), it would not be possible to create durable parts using 3D printing. Therefore the pins themselves would need to be bought. The chosen items were M2 X 6mm Round Head Groove Pins (DIN 1476) - A1 Stainless Steel. These were considered for the pins as they were the Right size, and they were also made of stainless steel. Stainless steel is good for this application as it strong enough to rout the tendons without failure, and as a metal it will have a low friction coefficient, which will improve the function of the tendons.

#### R. Wrist Electronics - Mohammed Al Bashar Khan

The image in Fig. 56 shows the electronics placed in the lower level of the wrist. By keeping the electronics within the wrist, the only thing connected to the wrist will be the power cables. Furthermore, by keeping the electronics within an enclosed space, the component will be less at risk of getting damaged. By keeping most of the components within the wrist, the design will also be more aesthetically pleasing.

The placement of the electronics has been done keeping in mind the requirements of each of the electrical components in the wrist. The raspberry pi unit that can be seen in the top of the image has been placed so that the connecting wires are easily placed, and the surrounding components are close by so that there aren't too many wires exposed near the motors. All the PCB's on this level are also set upon motherboard standoffs. These pieces will be bolted onto the standoffs, which is why a reasonable amount of

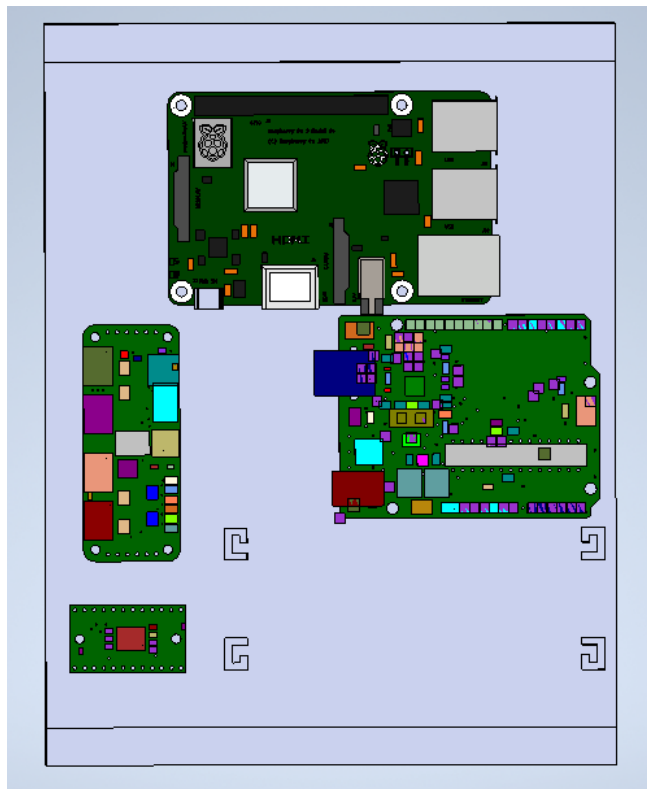


Fig. 56. The lower level of the wrist, where the electronics, excluding the power board, are kept. starting from right going Anti-clockwise, the Arduino unit, Raspberry Pi unit, Adafruit PCA9685 and the Adafruit TCA9548A

space has been left above the component on both levels of the wrist, so that the whole assembly need not be taken apart to replace or remove items.

#### S. Pulleys - Mohammed Al Bashar Khan

The pulleys are the component that will be attached to the motor and the tendons and will be used by the motors to pull the tendon. This will drive the motion of the fingers and palm on the hand. Preliminary testing of the fingers found the size requirement of the pulleys to be 22mm in diameter. Subsequent testing or progression was not made due to the COVID-19 situation. The other requirements for the pulley are that they be thick enough that the tendons can be successfully wound around them. The tendons will then be knotted through the pulley, so the design will also need to have the appropriate holes in place to accommodate for the tendon knotting.

Furthermore, as the pulleys will be attached to the motors there will need to be the appropriate holes to accommodate the screws that will attach the pulleys to the motors. Since the pulleys will need to have precise geometry features at the right locations, the pulleys will be 3D printed.

#### T. Motor Rails - Mohammed Al Bashar Khan

The image in Fig. 57 shows the method of fixing the motors to the bases of the wrist. The yellow fixtures shown in the image are the rails, which slot into the holes shown in fig middle base plate. These rails will have pins (shown

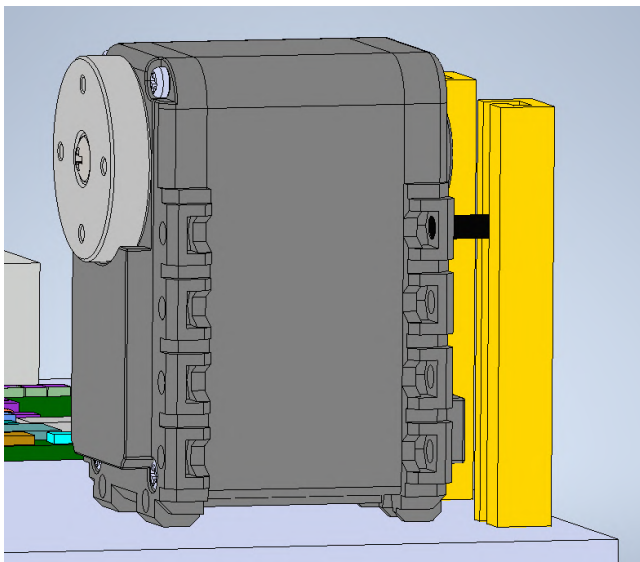


Fig. 57. The motor and rail setup. The motor is attached to the yellow rail by the black pin, which allows the motor to be raised or lowered as required.

in black in the image) which fit snugly into them. The pins in turn will slot into the attachment holes for the motors, which will allow the motors to be raised and lowered as desired. This is especially necessary when considering the fit of the tendons to the motors. The rails and pins are to be produced by 3D printing them.

#### *U. Mounting Bracket - Mohammed Al Bashar Khan*

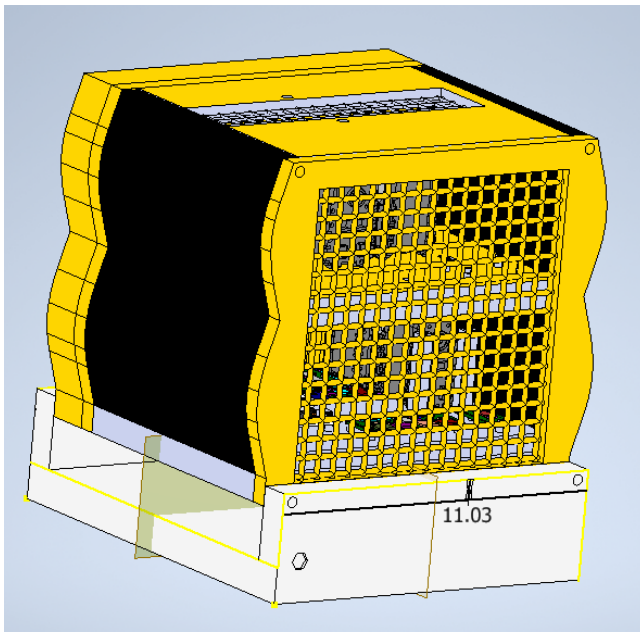


Fig. 58. The mounting bracket, attached to the wrist. the bracket has the appropriate holes for it to be screwed into a UR5 robot arm, which helps fulfil one of the objectives of this project.

The image in Fig. 58 shows the wrist attached to the mounting bracket (shown in white at the bottom of the image). The bracket has maximum dimensions of 60mm by 195mm by 230 mm (height by width by depth) and has been designed so that it can be fixed to the outside

of the wrist. This has been done so that the method for attaching and removing the bracket is to simply remove 2 of the threaded rods from the bottom of the wrist, rather than removing multiple components.

#### *V. Electric Power Enclosure - Jamie Sengun*

A separate enclosure for the power supply and power breakout board was required to house the main wiring loop from the power supply and provide a safe environment that isolates the user from potential high voltage connections. Without this the user and other individuals will be exposed to high voltage equipment that contains partially exposed contacts. This part is shown in Fig 59.

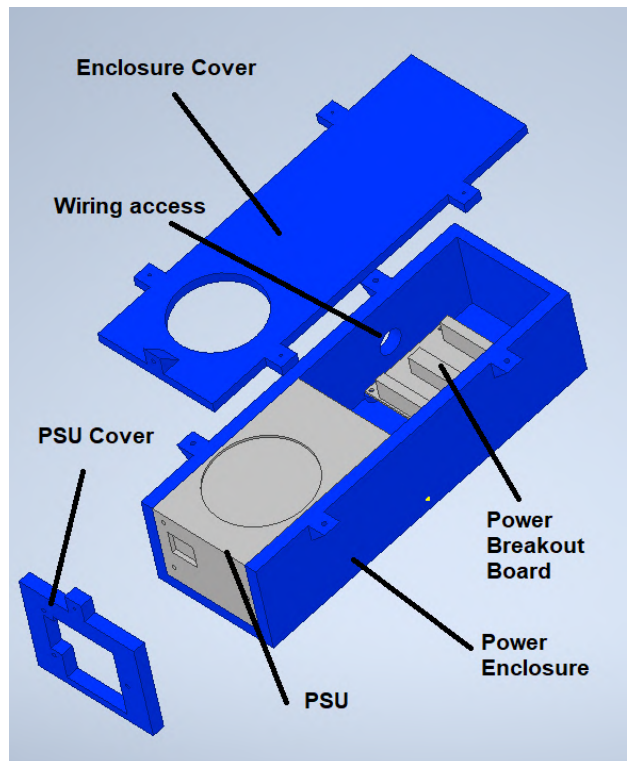


Fig. 59. Power enclosure overview - provides a isolated environment for high voltage electronic equipment by housing the PSU and power breakout board

The box has been initially designed to be 3D printed using an FDM printer and PLA plastic like the other components. The enclosure has been designed with 10 mm wall thickness throughout, so there is potential to upscale the production of these parts by utilising prefabricated 10 mm plastic sheets and laser cut them into the desired shapes. This would require more manual assembly and some consumables in terms of creating the enclosure and would require the purchase of a laser cutter or a contractor. Laser cutters can be automated and is magnitudes faster at creating simple geometrical parts compared to 3D printing. By swapping over to this production method for this part it would free up 3D printing resources for other components. This would greatly reduce the initial fixed costs in purchasing 3D printers as less would be required for the same production output. Alternatively, the wall thickness could be reduced between 5 mm to 10 mm to improve print speed and reduce filament usage; however,

this wall thickness was chosen for extra structure rigidity and strength as it was designed to be handled, moved around and support its own weight.

The dimensions for the individual parts from Fig 59 are shown in the associated engineering drawings located in the appendix. With a 20% infill the estimated weight of this component without the PSU and power breakout board is 573g. The power breakout board can be mounted on stand offs that contain M3 x 3 mm thread inserts for the PCB to be securely attached. The enclosure cover can be bolted onto the power enclosure for easy accessibility via the use of M2 x 12 mm bolts that attach into M2 x 5 mm thread inserts located in the extruded tabs of the power enclosure. The PSU cover can be attached to the three PSU mounting holes that are provided with the PSU. The PSU cover can then be attached to the enclosure cover with one M2 x 12 mm bolt that attaches into M2 x 5 mm thread inserts located in the vertical extruded tab of the enclosure cover. These connectors are not shown in the image for illustration purposes. A wire access port has been included besides the power breakout board to allow for wire management.

### III. MUJOCO SIMULATION - TALHA TAILOR

Mujoco is a physics engine with various uses in the development and research of robotic/ bio-mechanics simulation. The engine can be used for the purpose of model based optimisation and testing. In our case where fast and accurate simulation is needed the physics simulator can be used to produce measurements and data which could be replicated in a controlled environment- with similar tests completed with a real model. In order to simulate the hand and understand potential grasping and forces for specified motor tendon linkage a Mujoco model was created and simulated [28].

#### A. Model Creation - Talha Tailor

A Mujoco model was defined in a XML file, written in the MJCF file format (MuJoCo's XML modelling format). Various regions of the hand were created with components reflecting the approximate measurements used in the real hand design. The geometry used for the simulation of the basic hand structure were Mujoco supported primitive shapes, primarily the use of capsules and boxes. These are 3d shapes rigidly attached to specified coordinate frames (geoms). The dimensions of these structures closely replicated those of the real model, though more rudimentary. Thus, the inertia's and masses are inferred from geoms rather than explicitly stated. Though this a more simplistic version of geometry, data collected can still be extrapolated to reflect a real model (of slightly differing geometry). A more complex model has also been produced via the use of STL model files and explicitly stated inertia values [28].

For simplicity all joints are simulated as hinge joints, with multiple hinge joints used in regions of multiple degrees of freedom (i.e. the thumb region). The range of the joints and axis of movement have been explicitly stated with all finger flexion at 90 degrees and 60 degrees for

abduction of the thumb (the rotations capable from real hand model).

Locations of Mujoco 'sites' (region of interest within the model body frame which can be used to specify spatial properties) were selected in relation to the potential positioning of sensors in the actual model. Therefore, site locations were present at the finger-tips and upper regions of the palm in order to measure Mujoco sensory output. Mujoco has a wide range of sensor output that can be simulated within the engine, the selection of these were generally to ensure the model functioned in cohesive manner as well as produce data that could possibly be replicated in real world environment. Position/ velocity joint and actuator sensor were added to for all joints and actuators. Force sensors were placed in specified area for testing and data collection.

Tendons were also modelled for all applicable joint regions and connected to their respective models. Tendons connecting the ring and little finger were coupled as to reflect the real hand model.

An estimation of motor gain was provided within the model with all tendon compliant flexion fingers given a Kp value of 10, the Palm hinge flexion was given a Kp value of 15 and abduction/adduction of the thumb a Kp value of 20. The gear in relation to the motor pulley used for the tendons were also added to the simulation.

#### B. Simulation Data

The following simulation surrounds sensor placement. Site locations are placed at various regions of the palms and finger and force data is collected with the hand performing grasps for objects of various sizes and shapes. These force reading are taken to measure which contact areas are affected most by particular grasps. The data is then compared in order to understand the best practical sensor placement positions as well as further testing which may need to be carried in the real hand model. Various aspects of sensor testing could not be completed with the full hand configuration due to the Covid-19 situation. The Mujoco simulation would provide an insight into the sensing, performance and testing side that otherwise could not done.

1) *Minimum grasping force:* The following sets of data were produced in relation to the Mujoco model.

Force sensor outputs were recorded from the finger tip when the model grasps a spherical object. The diameter of the object was gradually decreased to the point at which the hand encapsulated the object (see Fig. 60)- mass was inferred proportionally from object diameter. Outputs were recorded at each stage in order to observe the minimum grasping force at the finger tip. The hand (and grasped object) was faced towards the ground with gravity simulated, thus the grasped hand is only preventing the object from falling. The sensor outputs three numbers, which were the interaction force between a child and a parent body, expressed in the site frame defining the sensor.

Fig. 61 presents the x and Y force data collected. As expected the minimum grasping force required by the finger decreases with the diameter of the sphere. Force

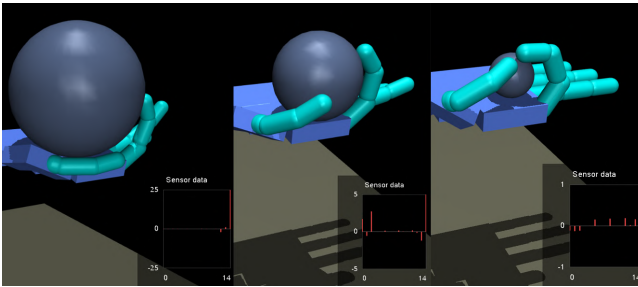


Fig. 60. The MuJoCo model grasping a sphere of varying dimensions, displayed via MuJoCo OpenGL visualiser.

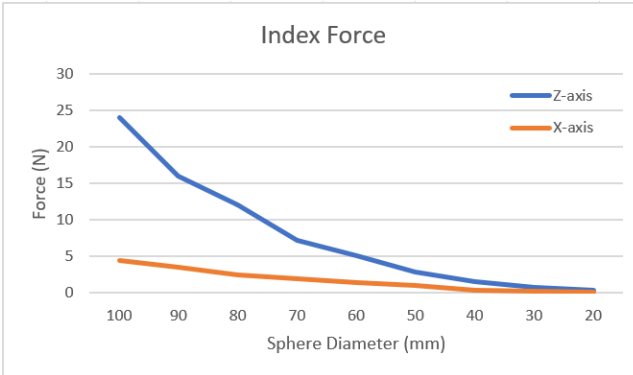


Fig. 61. Figure shows the Data extracted from the MuJoCo model grasping a sphere. Forces in the X and Z direction presented on graph (z-axis normal to the contact surface and x axis tangential)

decrease is not linear but with a curved slopes which may present the greater force required due to slipping of large objects. Sufficient grip force normal to the surface of the object must be applied through the index finger to overcome the load force tangential to the surfaces that acts on the sphere due to gravity and inertia. Though the simulation was not made to measure slip, it helps understand suitable frictional testing required to be done on the real robot hand (also more practical to be done on the real model due to inexact frictional constraints presented in the simulation.). [29]

2) *Tripod grasping*: The following simulation completed surround precision grasping of a pen-like object. A tripod grasp is performed with the object at varying angles.

Sensors reading have been simulated on the right edge of the index and palm. In order to do this small separate dummy geom were created for the area. This can be seen with the extruded site positions on Fig. 62. The force readings were then measured at these specific location for differing tripod grasps-see Fig. 63. Data collected can be seen on the bar chart below presenting readings at these specified sites - all forces are measured in the Z direction and presented as positive (force vector of thumb being opposite to index when performing the grasp).

When the whole hand is rotated 90 degrees, the object (representing a pen) remains in a resting position with minimal forces present at the tip of the index and thumb to maintain it in place. However, when positioned to other regions, near L1 of the index or thumb, a greater force can be seen (see Fig. 64) from the finger and thumb tip

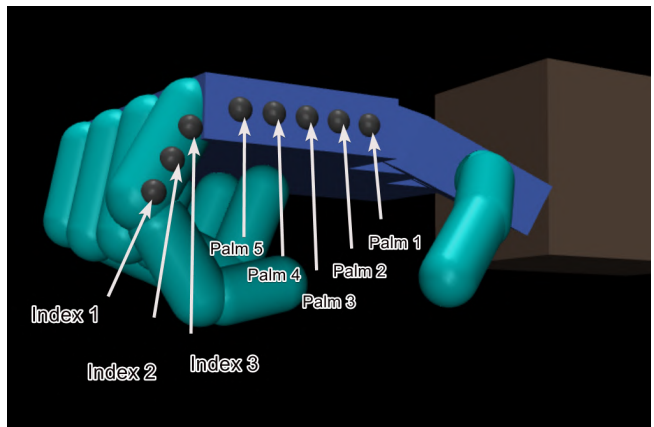


Fig. 62. The figure present the location for sensors sites on the side of the index and palm which have been added to XML files to be simulated for grasp readings.

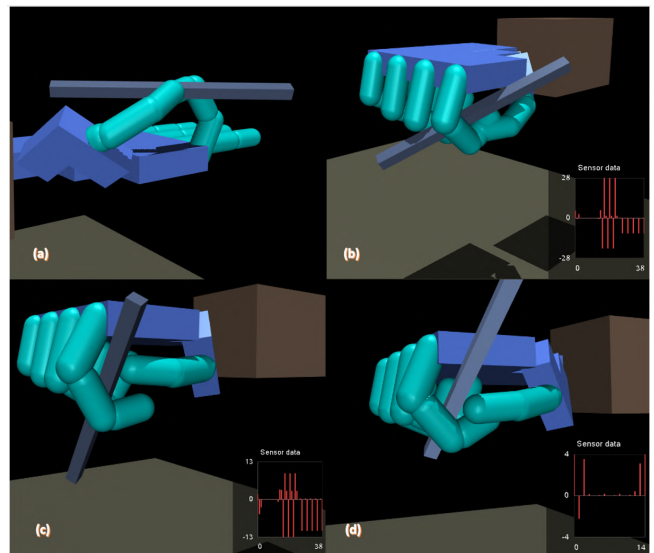


Fig. 63. The figure presents the pen grasps performed by the MuJoCo model, displayed via MuJoCo OpenGL visualiser. (a) Prismatic two finger grasp (b) Tripod grasp object or pen positioned towards thumb L1, (c) Tripod grasp object positioned towards index L1, (d) Tripod grasp object at a central tripod position.

regions for the position to be held. In order for controlled movement, the pen must be held by the tips of the index/thumb rather than simply resting in between the index and thumb fingers.

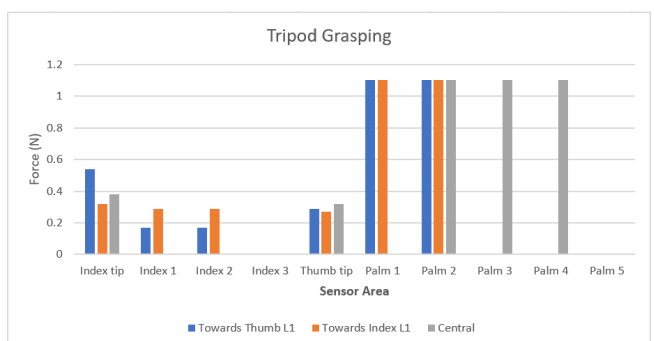


Fig. 64. The bar chart presents force reading taken from the MuJoCo simulation for the sensor site location shown in Fig. 62. Index and thumb tip reading are included.

From the data its can be made clear which sensor positions would provide useful data if tested with the real model. Positions index 3 and palm 5 provided no data for the three tripod positions shown in Fig. 63. The sensor position which provided data for all three sites, excluding the index and thumb tips, was Palm 2 position. Placing a hall sensor in this position, even 1D, may deliver useful positioning output data when testing the tripod grasp with the real hand model. Though not tested, but made apparent from Fig. 63, an additional sensor maybe applicable for the right side region of the middle finger, where the pen rests against. This may be something to consider for the future work and improvements.

From the tripod grasp test, one thing is made particularly clear, abduction/adduction of the index would aid considerably on achieving the tripod grasp. Movement of the object while in the grasp via the finger and thumb (in-hand manipulation) is possible, but very difficult due to the limited degrees of freedom in the index and middle fingers. Though due to the covid-19 situation the abduction/adduction of the index could not be completed, this addition actuated degree of movement would allow for the lateral movement of the grasped object.

### C. Sensor Placement Analysis - Talha Tailor

The placement position of sensors on the hand, as discussed in the SOTA, was based upon K. Murakami et al 2010 [30]. The paper surrounds the placing tactile sensing element on a sensor glove for recognition of varying grasps. The intention was to place 3D Hall effect sensor on the index, middle and thumb tips, with these locations being primary areas used in in-hand manipulation and precision gasping. Due to cost constraints the placement of these sites were limited and cannot be allocated to all regions of the fingers and palm.

The above data from both grasping test also present similar findings. Locations which produced the most amount of usable data were the tips of these respective fingers. The sides of the palm and fingers were also simulated presenting data that would support the addition of sensors in these locations. As mentioned previously these palm-side sensors were not added to the design due the COVID-19 pandemic. Data was therefore, extracted from Mujoco to present findings that could no longer be produced with the real model.

3D Hall sensors were also intended to be placed on the palm, below Link 1 of the index and middle fingers. This would provide data for other grasps as well as possible in-hand manipulation testing. These sensor placements were no longer feasible due to the cost constraints of the project, thus a trade-off was necessary, ensuring key location took priority (i.e. the finger tip regions).

### D. Validity and Accuracy - Talha Tailor

The largest factor effecting the validity of data is modelling of friction. Though every joint region in the real model is present with bearings which significantly reduce friction, friction will still be present particularly with tendon contact with the links and routing system. Friction was still simulated at a constant value of [1 0.005

0.001]N within the model, the accuracy of this value can be questioned with friction varying in different regions within the real model, particularly where a greater number of routing pins are needed.

## IV. WORKING PRINCIPLE

### A. Degree of Freedom (DoF) - Kai, Talha

Another vital decision made while designing the robotic hand is the number of degrees each specific finger would have and the total number of DoF for the whole hand. Biological research has been done into the human hand revealing that it has 27 DoF [31]; 4 DoF in each finger, 5 DoF in the thumb, which leaves 6 DoF for the wrist. However, when trying to achieve this much DoF, a compromise between the complexity of the robot and it's dexterity must be made. As we know, the biomechanics of the human hand is proven to be very dexterous, but having 27 DoF would require a lot of actuation, motors and complexity that it would make it very challenging, costly and time consuming. Therefore, by using the Principle Component Analysis (PCA) it can create simplified hand models by investigating the essential grip behaviours and variables required to represent a fully working hand. Here, Cobos, Ferre and Aracil [32] describes simplified hand models consisting of 1-3 DoF that are only capable of performing circular power grasps and 4-6 DoF hands performing circular and prismatic power grasps, see Fig.7. This denotes that to be able to achieve precision grasps, more than 6 DoF hand model is necessary so that robotic hands can implement dexterous manipulations.

Therefore, our hand has been designed to have a total of 9 degrees of freedom with a total of 8 actuators- an under-actuated hand design. One flexion/extension motion from each of the little and ring fingers, two flexion/extension for the index and the middle fingers, one flexion from the palm hinge, along with one flexion from the links 1 and 2 of the thumb and one final DoF via abduction/adduction of the thumb. The little and ring fingers have been coupled to allowing for one actuated degree of freedom but two overall DoFs. This is because the ring and little fingers are proven to provide stability in the grasping compared to the rest of the 3 fingers that are known to assist more dexterous manipulations [6]. Therefore, actuating these fingers separately would unnecessarily increase the overall cost and weight of the hand particularly when considering our design objectives- hand dexterity over grasping power.

The lowest joints of the middle and index finger are actuated independently (independent L1 movement) with the rest of the links (L2 and L3) connected via tendons and actuated together- see Fig. 65. The reason for this independent actuation of the lower link is for increased dexterity and actuated control of the precision grasping fingers. During prototyping and testing, these fingers were tested without this addition DoF. The model did not provide the desired motion. The improvement can now allow for full independent 90 degree rotation of the L1 (MCP joint).

### B. Differential pulley - Talha Tailor

As discussed in the previous section the little finger and ring finger are coupled, and thus actuation for both

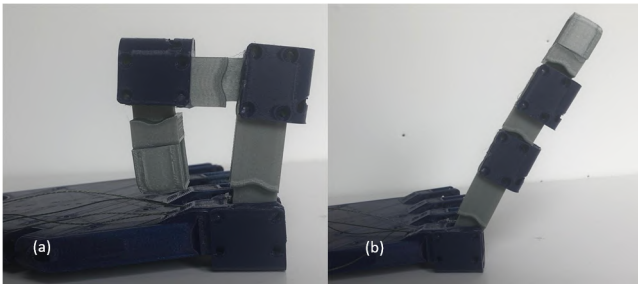


Fig. 65. Prototype model displaying movement of the index finger. (a) 1 actuated DoF via tendon linkage (b) independent actuation of L1

occurs through the use of a single motor. Issues may arise when coupled fingers grasp an object, particularly when the object is uneven or asymmetric. When one of the finger's motion is halted due to contact with the object, the other fingers movement will also stop, even if space still exist between one of the finger grasping object. This prevents the hand reaching a complete grasp.

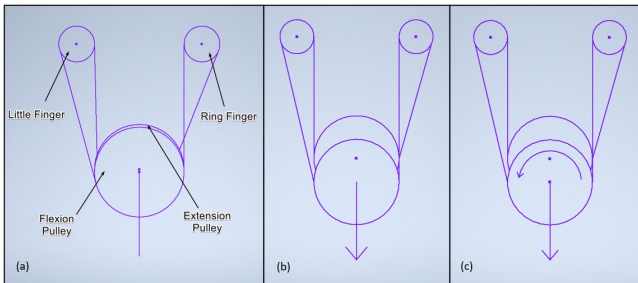


Fig. 66. Diagram displays the motion of the differential pulley system for illustrative purposes. (a) pulley system at rest with annotations, (b) tendon connected to flexion pulley engaged (c) Ring finger obstructed, the pulley moves towards free finger- actuation continues.

For this reason a differential pulley system has been used. The integration of this system would allow the coupled fingers to continue motion even after the one finger's movement is restricted (without an additional actuator). In order for the system to be functional the pulley is required to be larger than the width between the two fingers- thus a 40mm diameter pulley was selected.

Two pulleys are used in order for the system to work correctly, one for flexion of the fingers and the other for extension. The pulleys are placed in parallel and separated by a thin sheet to avoid tangling and reduce friction. When flexion is necessary the pulley is dragged lower by the connected tendons. If one of the finger's movement is restricted, the pulley would compensate for this by rolling slight to the free finger. The free finger can then continue to flex. This is displayed more clearly in Fig. 66. The opposite would occur with extension, with the second pulley system being in use.

## V. SOFT SKIN TACTILE SENSING - KAI PAGE

To experimentally test the MLX90393 3D sensors, we were lucky enough to be able to mould the silicone as shown in Fig.12. Due to this, an investigation was carried out as follows to test which designs of the soft skins would suit better for when normally displaced. Due to the current Covid-19 situation, we were unable to have the correct

facilities and equipment to test how the shapes of the soft skin would react to shear forces in the x and y direction. Therefore, masses were added directly on top of the soft skin and data was collected from the sensor output. Firstly, Finite Element Magnetic Model was simulated to compare and contrast against the experimental data to evaluate the magnetic field and its corresponding displacement.

### A. Finite Element Magnetic Model (FEMM) - Kai

Preliminary testing on FEMM was first carried out to decide an appropriate thickness for the silicone skins. The reason for this was that as the magnet is embedded at the surface of the silicone, the compromise to having the magnet far enough from the sensor so that when displaced by normal force it doesn't exceed its min/max range of detection. As the hall effect sensor works by measuring the magnetic field from magnet displacement, we can work out the magnetic flux density varies around the magnet and its behaviour. To generate this simulation, the following steps and conditions were followed by creating a Magnetic Problem:

- i) When opening a new simulation, the problem settings are set at Axisymmetric and the units to work with are chosen (mm)
- ii) Nodes are then operated to draw the size of the magnet that is axisymmetrical about the centre coordinates (0,0). The N42 neodymium has 2mm diameter with a 1 mm thickness; hence drawing a 1 mm x 1 mm.
- iii) Then, define the material's name and properties for N42. The relative permeability in cylindrical coordinates 1.05 [33] and the coercivity as 915000A/m [34]. The rest of the settings can be kept as default.
- iv) After add labels to the blocks and define the inside as the N42 (which was defined in the previous step) and air as the outside. This is with the assumption that the other materials used surrounding the magnet does not have any magnetic permeability and can be treated as air.
- v) Define the boundary as open and insert the required radius of the boundary. In this case, the radius was modelled as 15mm as the soft skin designs were moulded at a thickness of 10mm  $\pm 2$  mm.
- vi) Finally, generate mesh, run activity and then view result to see the density plot of the generated model in Fig. 67. To improve results, the mesh density can be increased.
- vii) To analyse results in the z direction shown in 67, the generated magnetic flux density values with their corresponding distance from the magnet is copied into Excel.

Therefore, when tested at 10mm  $\pm 2$  mm thickness, it proved to provide a magnetic flux density well within the magnet range detectable by the sensor. Though the FEMM provides data from the centre of the magnet to the boundary, the graph from Fig. 68 is filtered from the magnetic density of 9649.51  $\mu\text{T}$  which corresponds to 3.821 mm. This was done in order to amplify the data

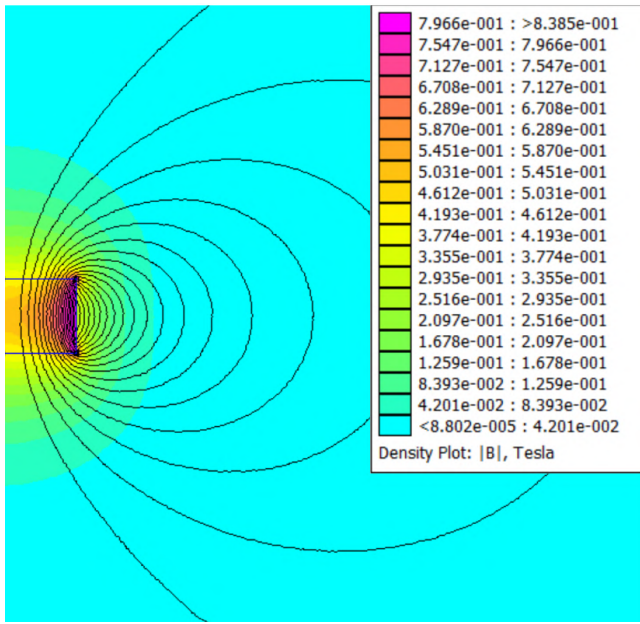


Fig. 67. A density plot of the FEMM simulation modelled for the N42 neodymium magnet's properties.

more appropriately as the graph approaches exponential. This range was calculated from the chosen sensor settings where the 3D hall effect sensors provides variable gain & resolution and sensor range data sheets [35] which can also be found in Table XVIII and XIX in the Appendix. To begin with, Gain (*Gain\_Sel*) was then set at 7 and the Resolution (*RES*) set at 0. This was chosen as it gave the sensor its highest level of sensitivity with the maximum resolution. According to our FEMM model that highlights magnetic sensitivity with distance, Fig. 68 (right) shows that the thickness of our silicone dimension and the distance of the magnet to the sensor is sufficient that we are able to increase its sensitivity. However, if this experiment was to be repeated with a softer material or one with a thinner dimension which forces the magnet to be significantly closer towards the sensor, then it would be critical to change the Gain and RES settings to that of Fig. 68(left). The settings used for *Gain\_Sel* = 0 and *Res* = 1 ultimately allows the magnet to be as close as 1.611 mm to the sensor before reaching the magnetic saturation. This saturation is reached when the sensor's detectable magnetic flux density is maximised so that if the magnet comes closer than this range, the sensor cannot produce data.

From the current settings and analysing the data from FEMM, the silicone is able to displace (in the z direction) up to  $\approx$  5.8 mm from the resting position, before the saturation distance is met. The results and conclusion on which design of the silicone skin produced is the most suitable for this particular robotic hand is discussed in the results V-B3 section.

#### B. Experimental Testing - Kai

This project started out with the aim of achieving a manufactured robotic hand from the ground up, the current global situations with Covid-19 prevented us from doing so. Therefore, while working remotely from University's

facilities, simulations and experiments carried out from home were improvised. This involved testing the moulded silicone fingertips with the 3D MLX90393 hall effect sensors on some 3D printed PLA fingertips. The desired outcome from this experiment was to analyse some data produced to improve understanding on what features and shapes of the designed soft skins will fit best for this purpose. However, since this had to be done remotely without proper equipment, the testing for the sensor could only be done more accurately for the normal displacement as it is easier to do a repeatable test on normal forces only. However, this will still not be perfect as measuring mass on a home baking scale would not be as accurate as scientific measuring scales. The measurements of paper pieces were also calculated based on the dimensions of the pieces to the provided mass of the whole pack. Hence, the weight of the calculated masses could be made more accurate with proper equipment. A simple test rig was designed to hold the fingertip in place when all the apparatus is set up. This was arranged as we found that once the wired sensor is placed inside its compartment of the fingertip, the wires may cause movement to the fingertip and create error data sets. Therefore this was designed so the fingertip can temporarily glued down and held in place. As the sensitivity is triggered by any movement, it was important to ensure there were no other displacement apart from the one being tested. The setup to the experiment can be seen in Fig. 69.

1) *Hypotheses*: Some hypotheses that were made before the start of this experiment include:

- The accumulation of mass on the silicone experienced by the sensor, will result in higher magnetic field due to deformation, as the embedded magnet is displaced closer to the sensor. Hence a correlation of increasing mass with sensor displacement.
- The thinner walled square silicone designs will result in a higher displacement of the magnet with force as they are softer.

These hypotheses will be tested using the described Methodology and explored in Results & Discussion.

2) *Methodology*: A crucial factor to look out for is with the handling of the sensor as the PCB is very small and fragile. If not careful, the soldering could come off, as well as the microchip that is attached to the PCB, leading to breakage of the PCB. Additionally, the weights that are placed onto the silicone must all be equal so that the displacement can be accurately highlighted at equal intervals. This way we can further investigate the sensitivity of the sensor as well as its detection rate. When adding weights, it is crucial to make sure they line up on top of each other precisely so that the direction of the displacement can be controlled. In this case, since we are investigating the normal displacement, making sure that the coins and the paper are stacking on top of each other flatly in the middle of the silicone is vital.

To be able to add a known mass in the top of the silicone; using some 5p coins and a square piece of paper with a known mass was cut to an appropriate dimension. 5p coins weight 3.25g, and using up to a total of 10 x 5p coins summed up to 32.5g [36]. The decision to use 5p was that they were the smallest diameter out of all coins.

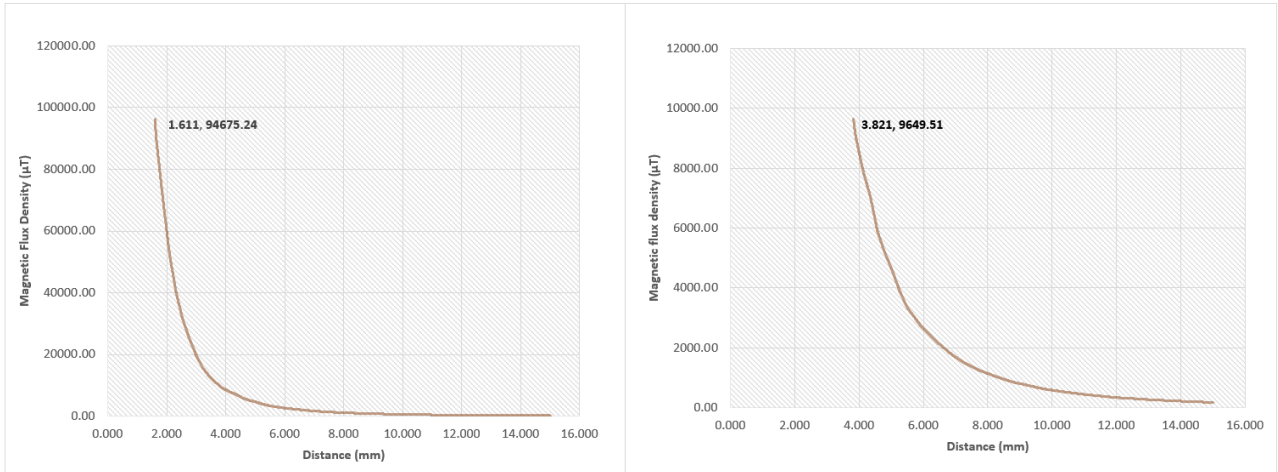


Fig. 68. Graphs derived from FEMM modelling of how the magnetic flux density changes with increasing distance of the magnet from the sensor, (left): using decreased settings of GAIN\_SEL = 0 & RES = 1 which are the lowest resolution settings to denote the distance at which magnetic saturation will occur (1.611 mm), (right): using the current settings of the sensor of GAIN\_SEL = 7 & RES = 0 which is the highest resolution settings to denote the distance at which magnetic saturation will occur (3.821 mm)

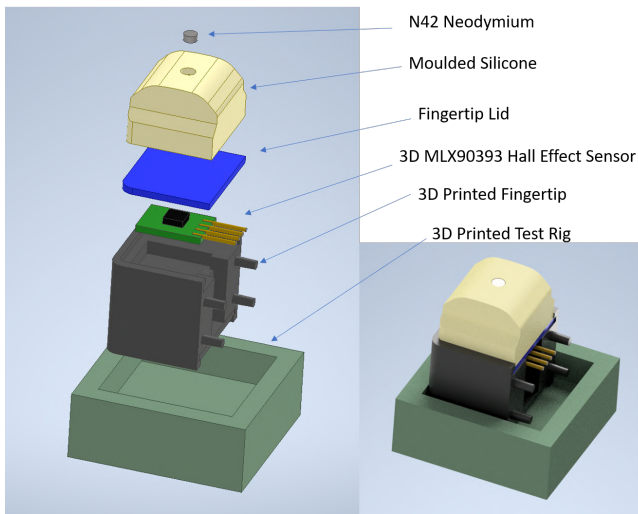


Fig. 69. Sensor testing setup, (left): exploded view of the apparatus set up with labels, (right): none exploded view setup.

Resuming the experiment at home meant being limited to equipment such as scientific scales. Therefore the solution was to gather some objects with known mass that were easily obtainable in large amounts. The also had to be able to stack up on top of each other so that the mass can be accumulated.

Another apparatus used as mass are the Q-Connect Record Cards of 127 mm x 76 mm. These were then cut into small square pieces with 18 mm sides so that identical pieces would have the same mass when added on top of each other. To work out the mass of each pieces of paper squares, a simple ratio calculation is worked out from the mass of each 127 mm x 76 mm card. This resulted in 0.0503g for each small square [37] with a total of 25 x 0.0503g summed up to 1.258g. By being able to test small masses, we are able to identify whether small forces can displace the magnet in the silicone. If this was the case, it would prove sensitivity of the sensors as when the hand is assembled, when grasping or manipulating objects,

whether it is light or heavy, it will cause detection. As each mass is added at regular intervals, the total mass is accumulated and the results will highlight how a greater mass causes a higher magnetic field as the magnet is displaced closer to the sensor.

The steps described below are carried out in order:

- i) Place all parts in position as seen in Fig. 69.
- ii) Connect the other side of the wires as explained in Section VII, making sure that it is connected properly. The real life set up is shown in Fig. 70 where the sensor is connected to the Arduino, and then the Arduino to a PC.
- iii) Then, connect the USB into a computer and upload the Arduino script in the Appendix C. Generate the 'Scatter Monitor'.
- iv) If the connections are working, the serial monitor displays continuous values in the x, y and z direction. If there is normal displacement, the negative values ( $\mu\text{T}$ ) decreases.
- v) Add 5p coins directly onto the centre of the flat silicone surface in regular intervals; keeping an eye on the serial monitor for any unexpected changes (Fig. 71).
- vi) Once all the weights have been added, copy the data from the scatter monitor into excel for data analysis.
- vii) Repeat steps iii to vi when changing the type of weights or the silicone part (Fig. 72). This is to make sure that the Arduino refreshes properly and that the collected data is reliable.

*3) Results & Discussion:* The magnetic field output measured form the sensor readings were first exported into Excel for data analysis. Firstly, only the displacement in the z plane was recorded to illustrate how the measured magnetic field changes when mass is placed onto the soft skins. As each mass was added at equal intervals, discrete data of the magnetic field was required to compare this value to that of the FEMM simulation to denote its respective distance from the sensor. By doing this, the

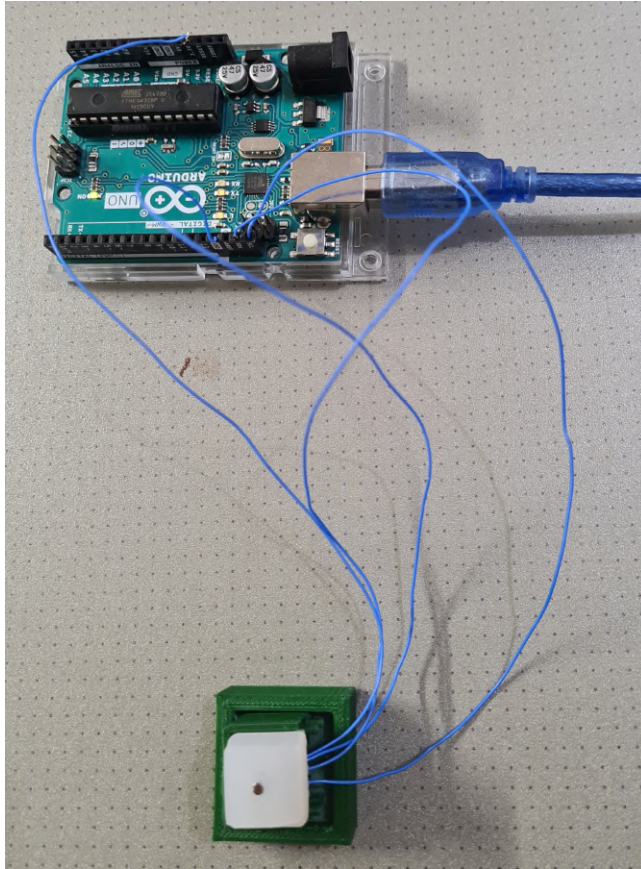


Fig. 70. The experimental set up of the arduino, 3D printed fingertip, 3D printed test rig and the silicone moulded soft skin

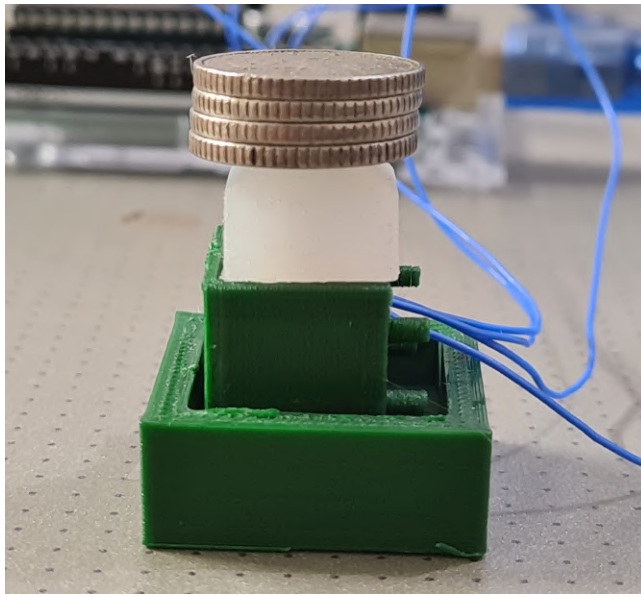


Fig. 71. Experimental set up of how the coin masses are stacked up on top of the soft skin while the sensor is running measurements

distance at which a specific magnetic density is met can be denoted. This method was repeated for all intervals of mass for the sensor readings and the magnetic flux density was averaged. Finally, from the inferred distances, the data is then normalised to give the displacement of the sensor with each addition of mass (Fig. 73).

The output from the sensor is formatted and presented

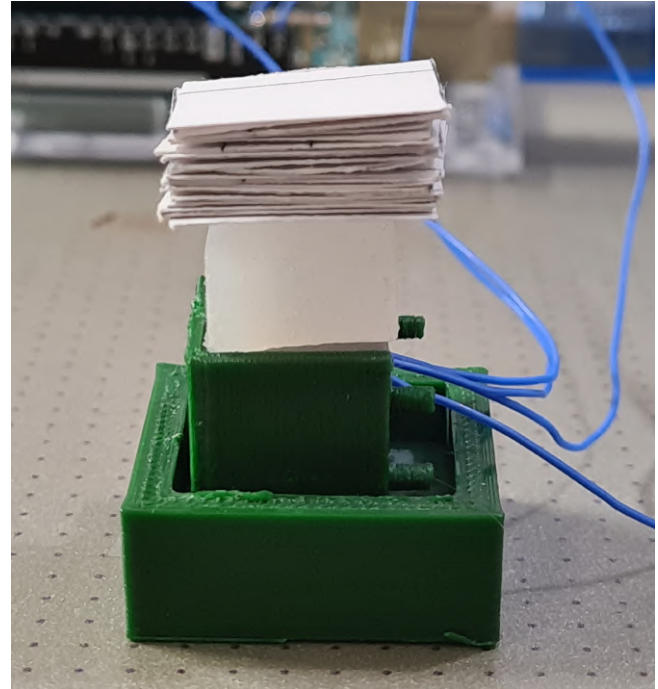


Fig. 72. Experimental set up of how the coin masses are stacked up on top of the soft skin while the sensor is running measurements

as scatter graphs to compare how the the magnetic field strength changes as the sensor is displaced in its normal direction by known masses.

From the principles of a hall effect sensor, it allows for the measurement of the strength of the magnet's field through its displacement in each axis [38]. However, in this investigation, due to the limitation of remote working and equipment availability, only the displacement in the z axis were witnessed. We can assume that the mass added to the soft fingertip is the force that the fingertip may experience, with another assumption that that acceleration will be the same for all mass added. This means that as the mass increase, the force experienced on the soft silicone parts will also be greater.

The graphs seen in Fig. 73 compares the changes in the displacement of the soft skin when mass is added to the different shaped silicone. The trend line is included with its equation to highlight how the change in mass affects the change in the displacement. The results illustrates that a gradual increase in the magnetic field is correlated to the magnet in the soft skin moving closer to the MLX90393 sensor. This trend was both demonstrated in theory by the FEMM simulations as well the experimental results. This results satisfied the hypothesis where the addition of more mass created a higher displacement in the z plane.

The line of best fit is plotted into the scatter graph with its equation to highlight quantitatively how the change in displacement is varied for different wall thickness of the same silicone shape. This analysis satisfied the second hypothesis where the thinner walled silicone (2mm) produced the highest gradient (Fig. 73) and the non-hollow design with the smallest gradient. This meant that though the addition of each mass caused gradual displacement towards the sensor, the softer skins were also able to gather bigger displacement with the same mass. Therefore, the

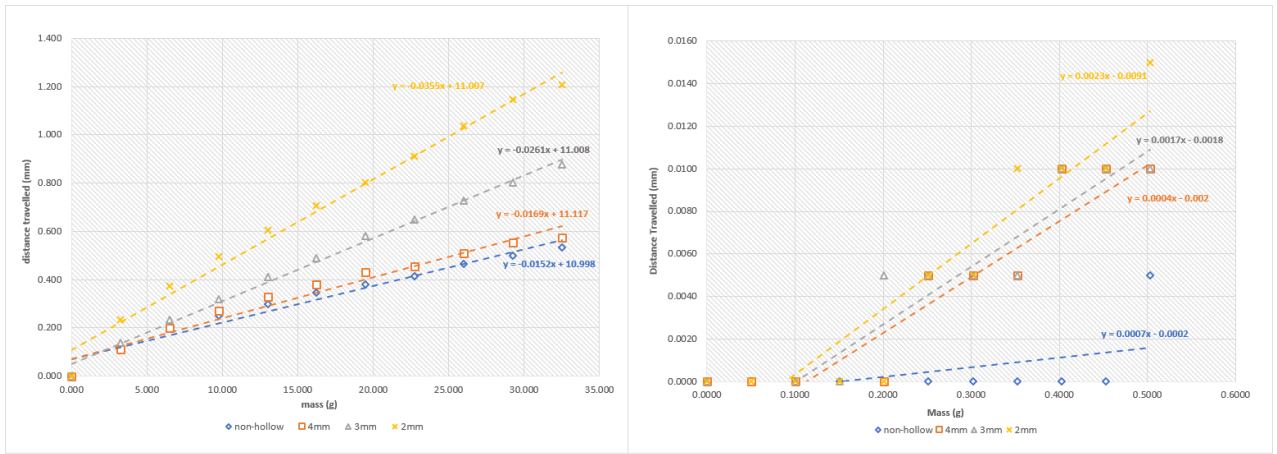


Fig. 73. Graphs showing the displacement of the embedded sensor with the addition of each interval mass, (left): The displacement of the sensor on embedded in the soft skins with varying wall thickness by the addition on 3.25g mass intervals, (right): The displacement of the sensor on embedded in the soft skins with varying wall thickness by the addition on 0.0503g mass intervals.

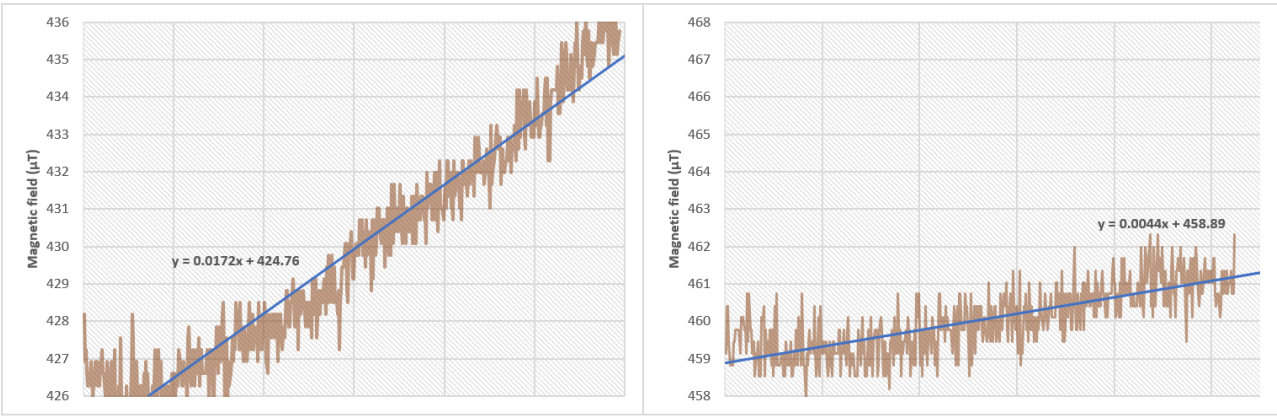


Fig. 74. Graphs comparing the magnetic flux output from the MLX90393 sensor of a 2mm walled silicone soft skin (left) and a non-hollow silicone soft skin (right) while adding a mass of 0.0503g per interval.

2mm walled silicone shape can be considered the least stiff.

Fig. 76 highlights how changing the shape of the fingertips (not just the thickness of wall) contributes to how well the 3D sensor will perform. The original plan was to be able to test (for all soft skins) in all x, y and z directions as the 3D sensor is able to detect these changes. However, due to the unforeseeable limited resources, the effect of different shapes to the sensor can only be obtained in the z direction under normal displacement. This has shown that the circle shaped skin was the most compliant to the same mass compared to the square curved or the non-hollow square one. This might be caused by the fact that the circular shape was reduced in volume, making the material more compliant.

Secondly, the results from testing very small mass such as a tiny paper weighting  $\approx 0.3\text{g}$  individually prove that the settings from the sensor and the strength of the magnet used is sensitive enough to detect change with a minuscule amount of displacement (Fig. 74). The same positive correlation experienced with a much heavier mass is mirrored even when the force is decreased drastically. However, in Fig. 74, one noticeable difference between the experiment with a 2mm wall thickness and a non-

hollowed one is that the data is more condensed in the 2mm walled skin, as the force displaces the soft skin and changes the magnetic field. Whereas, with the non-hollowed shape, since this is thought to be the stiffest, the change in the magnetic field is minuscule with small force which also highlights high fluctuation. One explanation for this is that because the force caused by placing 0.0503g is so small, the background noise is also detected as the values increase with the addition of more paper. Due to this reason, the non-hollowed shape can be depicted as being the least suitable design if required to sense small forces. On one hand, it would be wrong to rule out this design completely in the future as the total mass used in the paper test was only  $\approx 1.26\text{g}$  which is relatively light compared to objects that the fingers could come into contact with.

Comparing the tested results to the ones produced from FEMM simulations will help us determine which design of the soft fingertip will be the most suitable. As the FEMM simulation modelled the current magnetic field used, the data obtained from this helped us approximate the range of detection. As highlighted in Section V-A, the closest distance that the magnet can be within the sensor before it reaches saturation level is 3.821 mm. This meant that with the current settings, it would not be ideal to use a

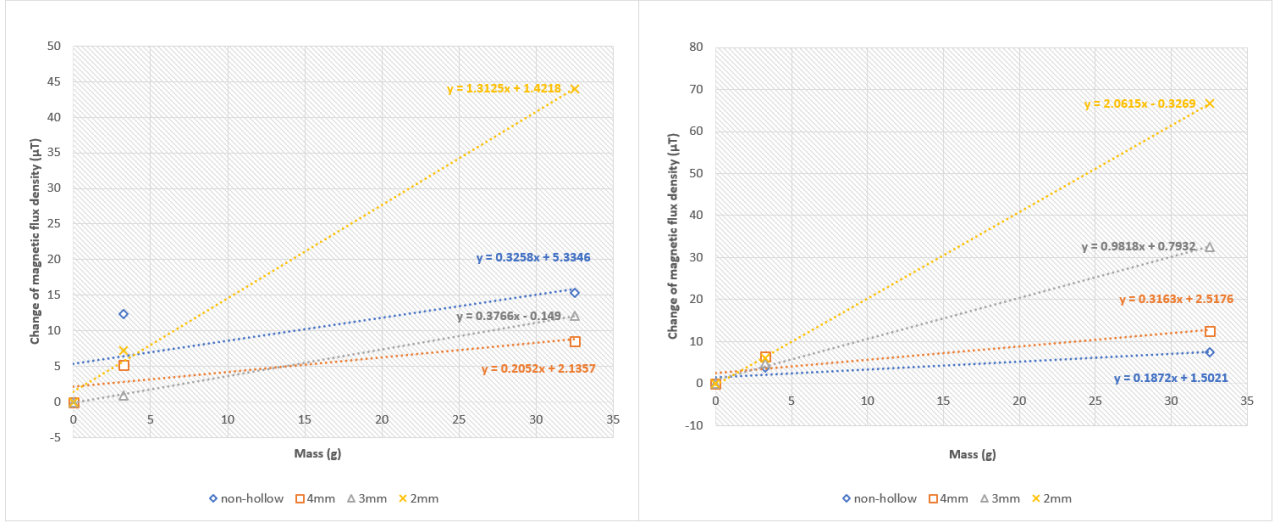


Fig. 75. Graphs highlights how normal force in the z plane affects the magnetic fields in the x (left) and y (right) planes. Three different intervals of 0g (no mass), 3.25g and 32.5g were added and its corresponding x and y magnetic field values are recorded.

design that is easily compliant and will displace to force easily. If the soft fingertip was to displace and reaches the saturation range easily, it makes the hand difficult to grasp heavier/bigger objects that will result in detecting larger forces impossible as the force is reliant on the soft skin displacement.

Moreover, the attempt to denote how the soft skins will react to normal placement in the x and y directions are investigated. This is suggested in Fig. 75 where the sensor readings are taken at 3.25g and then added 29.25g more, totalling to 32.5g. By analysing the graph, there seems to be a correlation with respect to the change in magnetic field in the y plane where the softer silicone skins showed a greater change in the magnetic field with increased mass. This meant that as displacement is experienced in the normal direction, there are also some shift in the y direction, where a softer skin creates more shift. However, this is not mirrored in the x plane, as the gradient on the non-hollowed silicone came out second highest; denoting that apart from the 2mm wall thickness soft skin, the non-hollow skin had the second greatest change in the magnetic strength with displacement in the z axis.

The testing to measure how x and y directions change with z displacement is very futile as it is crucial to calculate the displacement of x and y with respect to z. Just by looking at the change in the magnetic field, it cannot tell us whether some shapes will experience more movement in the x and y direction due to z displacement. Adding on, the magnetic field values generated from FEMM cannot be translated to displacement distance in the x and y as FEMM was modelled axisymmetrically to generate z coordinates. More calculations are required to convert this magnetic change from the x and y axis to its corresponding z axis so that the distance can be translated.

Lastly, the main ideology behind designing different fingertip shapes (apart from wall thickness) was to inspect how the soft skin would act in all x, y and z direction. The plan for different shapes was to test the shear displacement in x and y direction. The shape in Fig. 12C was designed

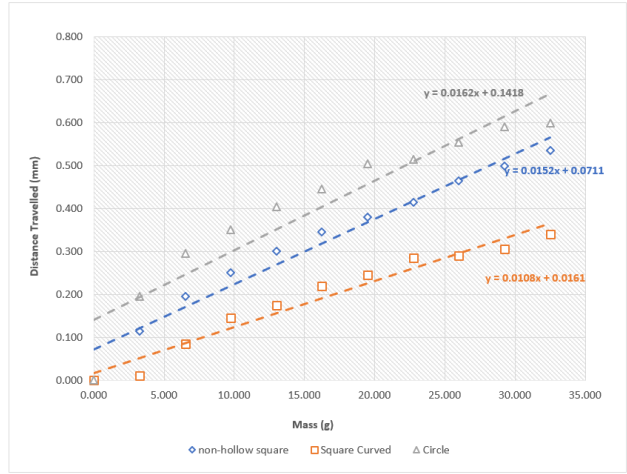


Fig. 76. Comparing the displacement of different moulded shapes with increasing mass at 3.25g intervals. The line of best fit added suggests the gradient of each set of scatter plots. The different moulded shapes are shown in Fig. 12 with A: circle, B: square curved and C: square(non-hollow)

mainly to decouple the x and y displacement from z; with the addition of air gaps (Fig. 12D, E, F) similar to [3] to limit crosstalk. However, with the current results produced, it has summarised how stiff each soft skin design is and how it deforms under force. From Fig. 76, the circle design experienced the highest displacement with known mass and the square curved shape the least.

From all the analysed results, it can be summarised that as more mass is added, the sensor embedded in the soft skin is shifted towards the sensor. It has also shown that, a mass as small as 0.3g can be detected by the sensor at a distance of  $\approx 10\text{mm}$ . However, from combining the results from FEMM simulations and the experimental results, since the sensor will reach a level of magnetic saturation if the sensor is displaced to within 3.81mm. Therefore, this information helps us decide which stiffness and design of the soft skin would be more ideal than others. Also, a

main objective was to test different shapes of the soft skin to decouple displacement in the 3 axis by investigating the effect of shear force on the soft material. However, since this had not been carried out, results to these extent were not gathered. However, from Fig. 75, it provides a rough idea of how stiff a design should be (by comparing the same shape with different wall thickness) and the resulting magnetic strength in the x and y direction.

To conclude, since the softest skin would not be ideal as it would be susceptible to high displacement of the sensor with high force, the 2mm wall thickness silicone would be ruled out. The non-hollow silicone would also not be ideal as the noise signalling causes heavy fluctuation when investigating very light mass as seen in Fig. 74. Hence, the 4mm thick walled silicone would be a better pick as it would give enough leniency to high forces displacing the sensor to the magnetic saturation level, but also providing the softness for very light forces to cause measurable displacement. Having an air gap would also avoid incompressibility in the soft skin and may avoid the need for calibration of the sensor which can be long and complex. Therefore, these designs attempts at decoupling the axis measurements of the sensor measurements and include different stiffness to test which design would suit the chosen sensor settings best.

### *C. Limitations - Kai*

One limitation of using hall effect sensors with magnets is that this puts a limitation on ferromagnetic objects it is able to grasp. Therefore, any grasped object that is also magnetic will cause a change in the magnetic field of the magnet embedded in the soft skin and the sensor. This also includes any external magnetic fields that would interfere with the sensing, hence the results are likely to be affected and inaccurate.

Additionally, the process of silicone mould is much less quality than that of the elastic resin which could've been printed by the SLA printer. These quality problems arise when the moulded parts are pulled out of the mould, which requires force and delicacy so that the silicone would not tear or deform permanently. This creates the resulting product to not have a good finish. Also, since the silicone liquid is pours from the top of the mould, when removing the mould, it requires the removal/cutting of the excess silicone that could be stuck to the useful parts. By cutting these off, it could form some detriment to the size of the silicone than that of the created CAD model. These small changes cause a large detriment in the magnetic field readings. Also, during the methodology, we did not use any vacuum degassing methods to remove air bubbles or curing to make the parts stiffer. Lastly, if silicone moulding is proved to create a more ideal soft skin, it would be necessary to improve the manufacturing process and the moulding tools so that better quality parts are produced. This is so that, it will not result in dimensional difference between the CAD models and the moulded silicone.

Due to the covid-19 situation, we were not able to test forces in all 3 dimensions on how the soft skin would react to normal and shear displacements. Therefore, there is a limitation in my conclusion about what design would

make for the best results. Hence, if in real life, the design concluded with a 4mm wall thickness working the best for normal displacement, and not shear forces, it would be a solution to calibrate the Hall effect sensors.

Lastly, if silicone moulding is proved to create a more ideal soft skin, it would be necessary to improve the manufacturing process and the moulding tools so that better quality parts are produced. This is so that, it will not result in dimensional difference between the CAD models and the moulded silicone. Further improvements to the testing and developing of the soft skin is included in section XI.

## VI. FEM ANALYSIS OF FINGERTIP - MOHAMMED AL BASHAR KHAN

In this section, the behaviour of the synthetic soft skin that makes up the fingertips of the hand will be analysed, as it experiences normal and shear forces. This will be achieved by simulating the process using finite element methods through the use of Abaqus software. In a human hand the fingertip is one of the most sensitive sections and send information to the brain regarding various features of the objects that it comes into contact with. This information results in the understanding of the temperature and weight of the object, and also the discrimination of the texture and shape. In the design produced for this project, the fingertips of the thumb, index and middle fingers will utilise 3D Melexis MLX90393 sensors. the ring and little fingers on the other hand will utilise 1D Honeywell SS495A sensors which consist of a magnet and sensing chip either end of the silicone skin. Then when the fingers lift the payload, the weight of the payload, and the forces exerted by the fingers will cause the skin to undergo compression. This results in the distance between the magnet and the sensing chip to decrease, which in turn results in information being sent to the computer, showing the forces being applied. So, because of this, the simulations being carried out for this section will focus the deformation of the fingertip when experiencing pressure forces. This part of the investigation will primarily be carried out to analyse how the performance of the 1D sensors can be optimised, as the 3D sensors are sensitive enough that small displacements are not an issue. Furthermore, the stresses the skin experiences, and the locations of the stress will be analysed, to help ascertain the suitability of the material and the optimum location of the sensor components. This is necessary for this project, as one of the objectives of this project was to employ tactile sensors to sense the shear and normal forces along the fingertips. By carrying out this investigation into the performance of the fingertips skin in relation to the sensors, the objective can be achieved.

### *A. Finite Element method (FEM) - Mohammed Al Bashar Khan*

FEM is a numerical method which allows for the approximation of real-life engineering problems, using factors like load, material properties and geometry. Typically, FEM is used when a solution to an engineering problem cannot be found analytically, or when a complex geometry

requires a numerical method such as FEM. The finite element method approximates a function by discretizing the whole domain of a body into a finite number of elements. The size and number of these elements can be varied by changing the mesh width, shape and/or the order of the polynomial (Constant, Linear, Quadratic or Cubic) in the simulation. For the simulations in this project, the chosen properties for the elements were Quadratic Tetrahedral, with a mesh width of 0.5.

#### B. Geometry - Mohammed Al Bashar Khan

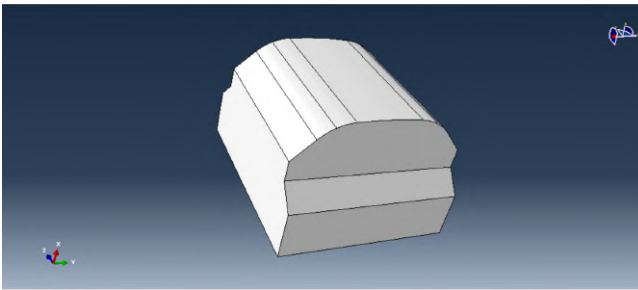


Fig. 77. The CAD design of the fingertip that will be used in the Abaqus simulation

The volume of the fingertip was 1466.557mm<sup>3</sup> and the maximum dimensions of the fingertip used in the simulations were a maximum thickness of 20.732mm, a maximum height of 14.7mm and maximum width of 13mm.

The figures below show the location of the three different sections of the fingertip where normal pressure forces will be simulated to study the effect on the fingertip.

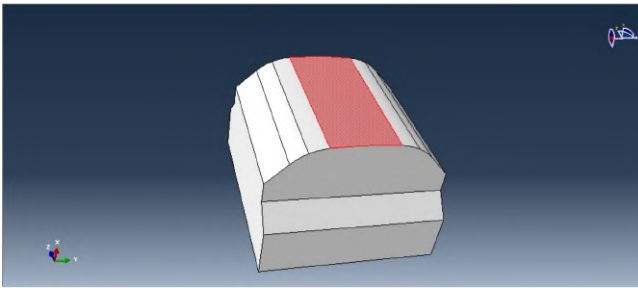


Fig. 78. The central strip area of the fingertip that will experience load in the Abaqus simulation

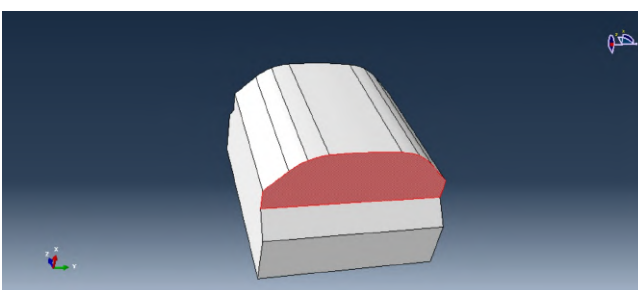


Fig. 79. The top area of the fingertip that will experience load in the Abaqus simulation

These three areas of the fingertip that will directly experience pressure forces that are dependent of the area

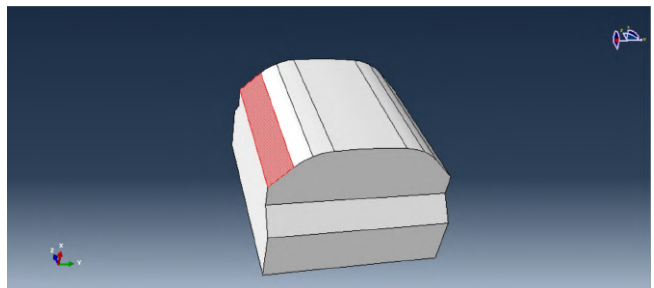


Fig. 80. The side area of the fingertip that will experience load in the Abaqus simulation

of each individual section. The areas of these sections are shown in table VI-B.

TABLE II  
AREAS OF THE FINGERTIP THAT WILL DIRECTLY EXPERIENCE PRESSURE FORCES

Fingertip Section	Area (mm <sup>3</sup> )
Centre Strip	58.540
Top	24.918
Side	46.688

#### C. Materials - Mohammed Al Bashar Khan

The material chosen for this simulation was actually two different materials; Silicone, phenyl-type (PVMQ, heat cured, 10-30% fumed silica) and Silicone (VMQ, heat cured, low hardness, 5-15% fumed silica). The first type of silicone mentioned, phenyl-type (PVMQ, heat cured, 10-30% fumed silica), will be used as the standard material used throughout the stress and displacement analysis part of the investigation. This is due to the fact that in this part of the investigation, the focus will be on the performance of the fingertip geometry more than on the material being used. Then, in subsequent parts of the investigation, the second type of silicone, (VMQ, heat cured, low hardness, 5-15% fumed silica), will be used. The simulations run using the second material will have the same load and boundary condition settings as the simulations for the first material, thereby providing results which will allow for the comparison between the two types of silicone.

These two types of silicone have been selected from the CES database specifically because of the physical and mechanical properties. The first type of silicone, phenyl-type (PVMQ, heat cured, 10-30% fumed silica), is amongst the densest and stiffest types of silicone available in the CES database. The second type of silicone, VMQ, heat cured, low hardness, 5-15% fumed silica), is conversely amongst the least dense and most compliant of the silicones available in the CES software. By having these two extremes in terms of materials, the aim is to be able to ascertain through simulations exactly how stiff the fingertip skin need be.

Table VI-C contains some of the most significant material properties for both types of silicone to be used the Abaqus simulations for this project. Whilst the values for the density and Poisson's ratio for both material are not so different, the same cannot be said for the Youngs modulus, the tensile strength and the compressive strength. As

TABLE III  
COMPARISON OF SILICONE PROPERTIES

	Material	
	Silicone, (PVMQ)	Silicone, (VMQ),
Density	1.230tonne/mm <sup>3</sup>	1.070tonne/mm <sup>3</sup>
Youngs Modulus	50 MPa	0.215 MPa
Poisson's Ratio	0.47	0.47
Tensile Strength	10.5 MPa	2.13 MPa
Compressive Strength	12.6 MPa	2.56 MPa

mentioned previously, this large discrepancy in stiffness will help to pinpoint the type of material that would be best for the requirements of the project.

In terms of the Abaqus simulation, the only material characteristics that will be used are the density, the Youngs modulus and the Poisson's ratio of each material.

#### D. Load - Mohammed Al Bashar Khan

[39] estimates that the maximum force (press) exerted by a single digit in a human hand to be  $40 \pm 15.2$  N. The maximum force (Pull) was estimated to be  $53.9 \pm 21.6$  N. To keep within the range of these estimated maximum values, the various loads that the fingertip would experience in the simulation were set at 1, 5, 10, 20, 30, 40 and 50 Newtons.

These load would be experienced by the fingertips as pressure forces, since in real life situations, the payloads are of various shapes and sizes so would come into contact with various sections of the fingertip. Therefore, in addition to being pressure forces, the loads would affect different parts of the fingertip, as detailed in the geometry section.

In the first part of the Abaqus investigation, the centre strip will experience various loads from 1 newton to 50 newtons. The material in this part will be Silicone, phenyl-type (PVMQ, heat cured,10-30% fumed silica).

The image below shows the load as it is displayed in the Abaqus programme.

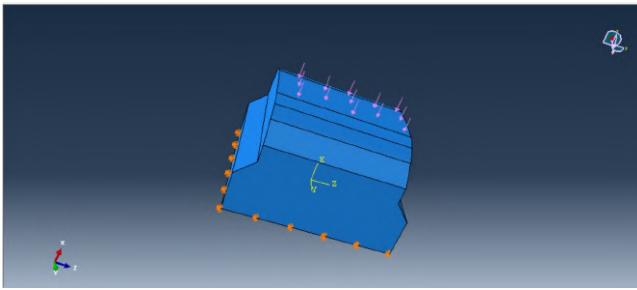


Fig. 81. The load as displayed in the Abaqus simulation. In This image the load is a pressure force affecting the centre strip of the fingertip

The next parts will be the side section of the fingertip experiencing 50 N load, and then the top section of the fingertip experiencing the same 50 N load. This part will also still be using the material Silicone, phenyl-type (PVMQ, heat cured,10-30% fumed silica).

Then, the next part will change the material to Silicone, VMQ, heat cured, low hardness, 5-15% fumed silica), and the centre and side sections will both be experiencing 50 N loads. Table VI-D displays the pressure forces of each load type as it entered into the Abaqus program.

#### E. Boundary Condition - Mohammed Al Bashar Khan

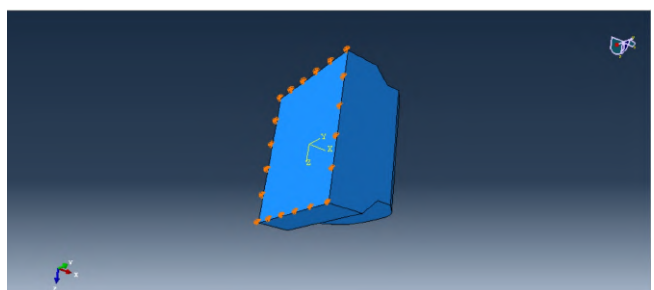


Fig. 82. The Boundary Condition as displayed in the Abaqus simulation.

The image in Fig. 82 shows the boundary conditions for the fingertip as it is displayed in the Abaqus programme. Since the purpose of the simulation is to see how the fingertip behaves and deforms as it comes under load form various angles, the boundary conditions need to be set at the back of the fingertip, where it would be connected to the finger. By allowing zero displacement in this section, the fingertip will deform under the pressure, as it is designed to do.

#### F. Mesh - Mohammed Al Bashar Khan

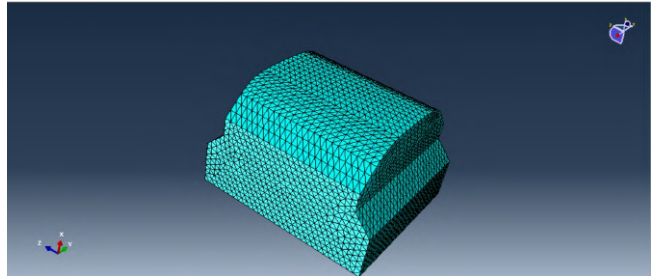


Fig. 83. The tetrahedral 0.5 width mesh as displayed in the Abaqus simulation.

The image in Fig. 83 shows the mesh for the simulation. The mesh had characteristics quadratic tetrahedral, with mesh width at 0.5. These characteristics were chosen as quadratic tetrahedral meshes would give the most accurate results as they would have most elements relative to mesh width. The mesh width was set at the value of 0.5 as that was the most refined mesh possible, due to technological limitations.

TABLE IV  
PRESSURE FORCES OF EACH LOAD TYPE AS ENTERED INTO THE  
ABAQUS PROGRAM

Load (N)	Pressure (MPa)		
	Centre	Side	Top
1	0.017	-	-
5	0.085	-	-
10	0.171	-	- 43
20	0.342	-	-
30	0.512	-	-
40	0.683	-	-
50	0.854	2.007	1.071

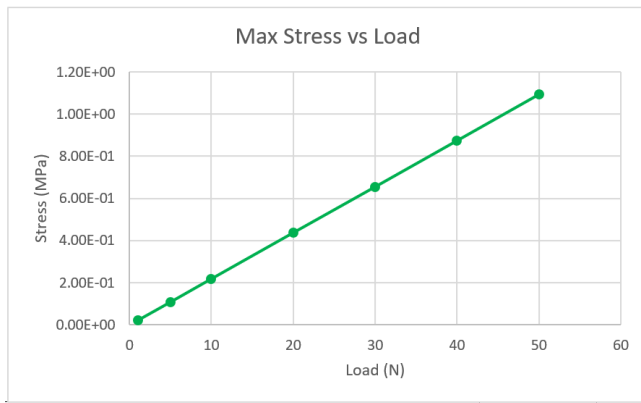


Fig. 84. Graph of the maximum stress vs the load

#### G. Analysis of fingertip response to normal force - Mohammed Al Bashar Khan

As mentioned in previous sections, in this part of the investigation, the fingertip (with the first type of silicone) is made to experience normal force at the central strip. The load will vary in magnitude from 1 Newton to 50 Newtons. Table 3 shows the values for the maximum stresses and displacements.

TABLE V

Load	Stress (MPa)	Displacement (mm)
1	2.18E-02	2.41E-03
5	1.09E-01	1.21E-02
10	2.19E-01	2.42E-02
20	4.38E-01	4.85E-02
30	6.55E-01	7.26E-02
40	8.74E-01	9.68E-02
50	1.09E+00	1.21E-01

From the values in the table it is clear that as the load increases the values for stress and displacement consistently increase. The value for maximum stress experienced stays far below the compressive and tensile strengths of the silicone used, which shows that the fingertip and its design is easily capable of enduring the forces that it has been subjected to. In terms of the displacement values, they are very small, which is a point of concern for the 1D sensors, whose sensitivity may not be small enough to register the small changes in displacement, and therefore wont calculate the changes in load as accurately as desired.



Fig. 85. Graph of the maximum Displacement vs the load

The graphs shown in Fig. 84 and Fig. 85 are of the Maximum stress vs Load and the Maximum displacement vs Load. As with the table, both the stress and the displacement are shown to increase with load, with linear correlation. For more specific data on the stress and displacement in the fingertip when it is experiencing load, it would be better to look at the contour plots for the von mises stress and the displacement, as they will show both the magnitude and location of the different stresses and displacements.

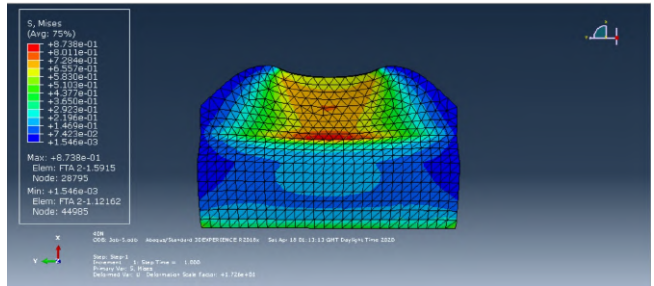


Fig. 86. Contour plot displaying the von mises stress for the simulation with normal force from a load of 40 newtons, for material 1

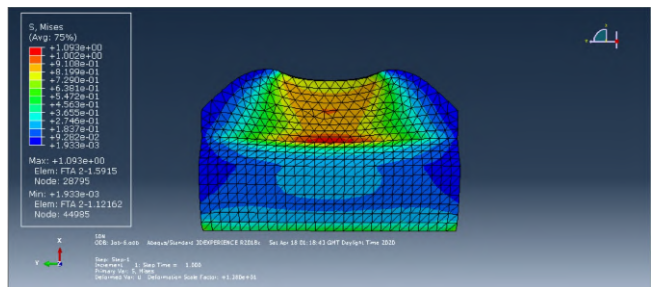


Fig. 87. Contour plot displaying the von mises stress for the simulation with normal force from a load of 50 newtons, for material 1

1) *Stress:* The images shown in Fig. 86 and 87 display the contour plots of the Von Mises stress when the fingertip is experiencing loads of 40 and 50 Newtons respectively. As mentioned previously, the maximum value of stress can be seen to increase with the load. What can also be seen however, is that the precise region where the stress is highest is the same in every single contour plot.

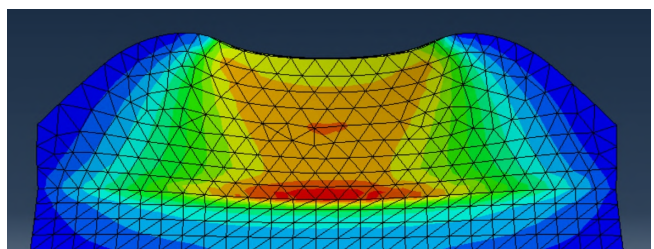


Fig. 88. A closer look at the Contour plot displaying the von mises stress for the simulation with normal force from a load of 50 newtons, for material 1

This high stress zone is situated just below the location of the area where the pressure force affects the surface of the fingertip and goes all the way to the centre of the fingertip. The concentration of the stress at this region indicates that the placement of the sensor components,

such as the magnet would be preferable in any of the sections of the fingertip marked blue green or yellow. This is due to the fact that the lower stresses in these areas would result in less damage to the sensor components.

In terms of the material however, the highest load in the simulation produces a maximum Von Mises stress of 1.093 MPa. When considering that the compressive strength of Silicone, phenyl-type (PVMQ, heat cured, 10-30% fumed silica) is 12.6 MPa, it can be concluded that the material is at least strong enough to endure the forces applied when handling payloads.

Apart from the region closest to where the fingertip experiences the pressure force, the stress in all of the contour plots is very low, save for the base of the fingertip. The higher stress at this region was to be expected, as that is the section of the fingertip where there was a boundary condition placed in the Abaqus simulation.

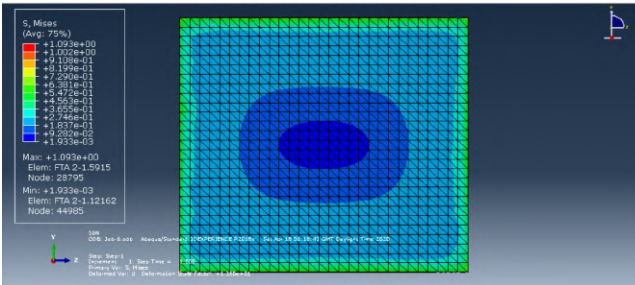


Fig. 89. A view of the base of the fingertip in the Contour plot displaying the Von Mises stress for the simulation with normal force from a load of 20 newtons, for material 1

When taking a closer look at the base of the fingertip shown in Fig. 89, it can be seen that the stress is higher only around the edges of the fingertip, whereas at the very centre of the base, the stress is at its lowest. It is at this central position then where a component for the force sensors could be safely placed, without great risk of damage.

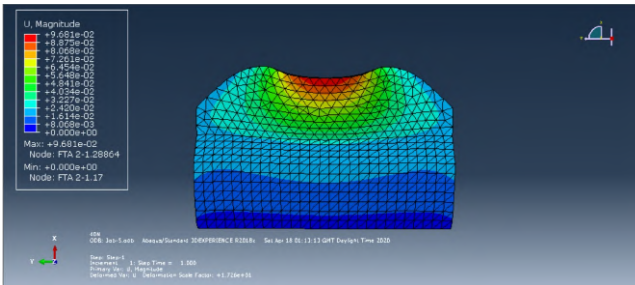


Fig. 90. The Contour plot displaying the Displacement magnitude for the simulation with normal force from a load of 40 newtons, for material 1

**2) Displacement:** The images shown in Fig. 86 and 87 display the contour plots of the displacement magnitude when the fingertip is experiencing loads of 40 N and 50 N respectively. As with the stress in the previous section, the maximum value of displacement magnitude can be seen to increase with the load. Also similar to the stress, the precise region where the displacement is highest is the same in every single contour plot.

From the contour plots shown above, it seems clear that the displacement is uniformly highest where the load is.

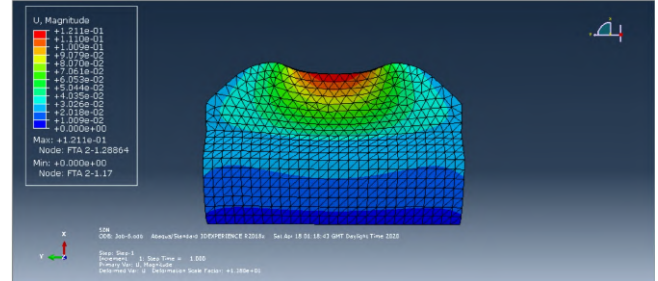


Fig. 91. The Contour plot displaying the Displacement magnitude for the simulation with normal force from a load of 50 newtons, for material 1

However, the figure below showing the contour plot from an overhead view proves otherwise.

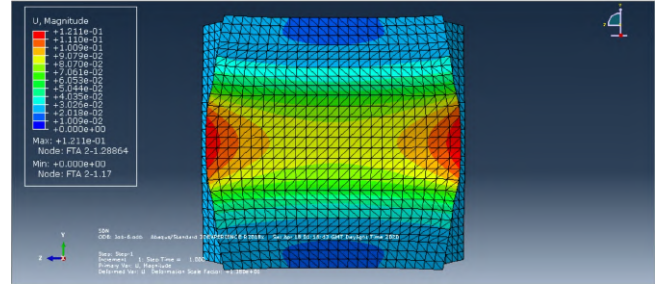


Fig. 92. Overhead view of the Contour plot displaying the Displacement magnitude for the simulation with normal force from a load of 50 newtons, for material 1

From the figure shown in Fig. 92, it can be seen that the locations of the maximum displacement are solely at the sides of the fingertip, even though the force was equal all across the centre strip area. This has occurred due to the material being used for the fingertip being compliant. The material deforms and therefore the displacement from a uniform pressure force produces a non-uniform displacement across the centre strip area of the fingertip. This may be a cause for concern for the ring and little fingers which will utilise 1D sensors.

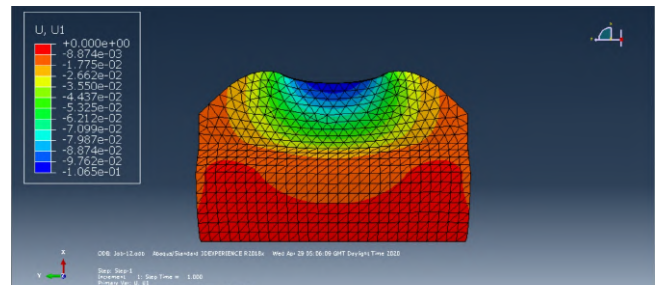


Fig. 93. The Contour plot displaying the Displacement in the x direction for the simulation with normal force from a load of 50 newtons, for material 1

The image in Fig. 93 shows the side profile of the fingertip for the 50 N load simulation, only this time the displacement shown is in the x direction. This is significant for the ring and little fingers, as that is the direction in which the 1D sensor would be measuring the displacement. The 3D sensors on the other fingers on the other hand, would consider the directions of the dis-

placement and of the force automatically. The maximum displacement value that can be seen in the legend shows a displacement of 0.1065mm. When comparing this value to the maximum displacement magnitude at the same load (0.1211mm), the difference is not so large. The image in Fig. 94 displays the side profile of the fingertip for the 50-newton load simulation, only this time the displacement shown is in the y direction. The maximum value for the displacement in the y direction is 0.02616 mm, which is 24.6% of the value in the x direction.

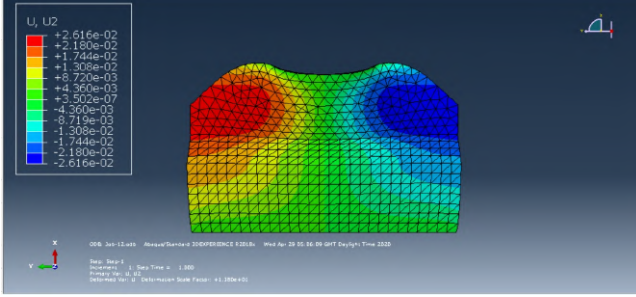


Fig. 94. The Contour plot displaying the Displacement in the y direction for the simulation with normal force from a load of 50 newtons, for material 1

The image in Fig. 95 shows the overhead view of the fingertip, showing the displacement in the z axis. The maximum value for displacement in this direction is 0.05756 mm, which is 54.0% of the value in the x direction. All this indicates that the design and material of the fingertip causes it to deform far more in the y and z direction than desirable for the fingertips that will utilise 1D sensors. By optimising the design of the fingertip, it could be possible that the deformation upon normal forces interacting with the fingertip could be as biased to the x axis as possible. That way the ring and little finger would not have issues sensing forces, thereby causing issues when grasping he payloads. This is significant as those two fingers are important for a hand when holding an object.

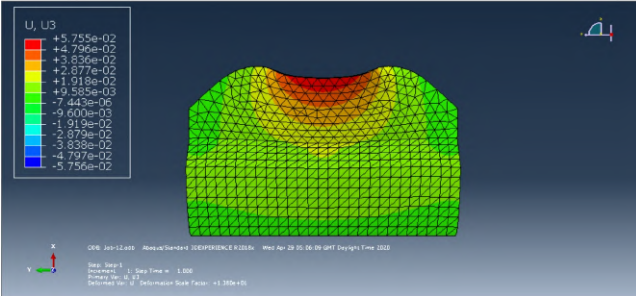


Fig. 95. The Contour plot displaying the Displacement in the z direction for the simulation with normal force from a load of 50 newtons, for material 1

#### H. Analysis of fingertip response to shear force - Mohammed Al Bashir Khan

1) Load from the top: The images shown in figures 96, 97 and 98 display the von mises stress contour plots for Silicone, phenyl-type (PVMQ, heat cured,10-30% fumed silica), with the  $load = 50\text{ N}$ . In this case the pressure

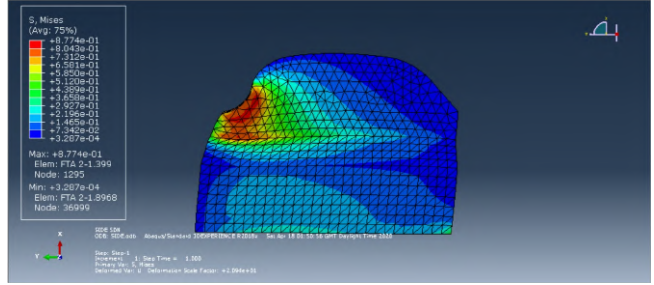


Fig. 96. The Contour plot displaying the von mises stress for the simulation with shear force on the top side, from a load of 50 newtons, for material 1

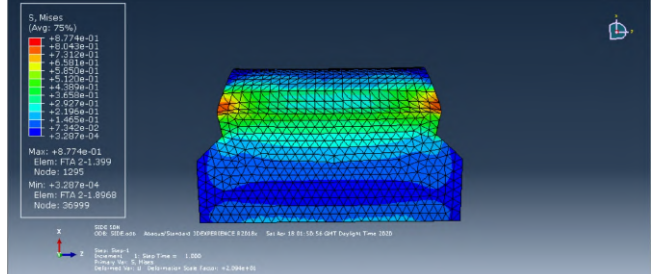


Fig. 97. Side view of the Contour plot displaying the von mises stress for the simulation with shear force on the top side, from a load of 50 newtons, for material 1

force interacts with the fingertip from the top side. In the first contour plot the xy view of the fingertip can be seen, and similar to the stress contour plots for normal force, the region of maximum stress is close to where the force interaction area is. However, at 0.8774 MPa, the value of the maximum stress for this shear force simulation is less than the 1.093 MPa of the previous stress contour plot. Furthermore, although the load is equal, the proportion of the fingertip that is experiencing high stress is lower than that of the normal force simulation.

The figures shown above display the displacement magnitude stress contour plots for Silicone, phenyl-type (PVMQ, heat cured,10-30% fumed silica), with the  $load = 50\text{ N}$ , where the pressure force interacts at the top side of the fingertip. Like the previous displacement magnitude contour plots for the normal force simulation, the highest displacements occur where the force interacts with the fingertip surface. Also, as can be seen from the overhead view contour plot, the maximum displacement magnitude only occurs on the sides of the area where the pressure force acts.

In the normal force the displacement magnitude was 0.1211 mm, whereas the displacement magnitude is much lower at 0.08673 mm. This is despite the fact that the load is equal, and the area that the shear force acts upon is smaller, causing the pressure to be higher.

The image in Fig. 101 shows the side profile of the fingertip, with the displacement contour fore the x direction. The contour shows that the largest value for displacement in the x direction is 0.03433 mm. At 39.6% of the displacement magnitude for this simulation, the displacement is far lower than the 87.9% the x direction displacement in the normal force simulation produced. This has occurred due to the fact that the pressure force

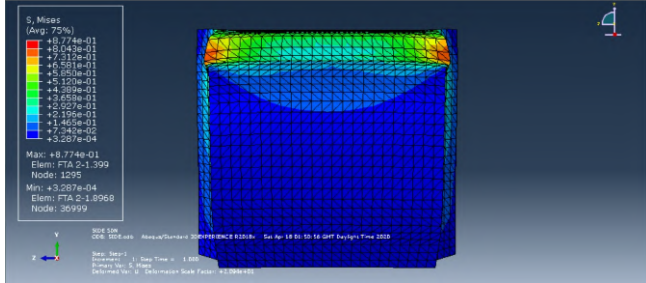


Fig. 98. Overhead view of the Contour plot displaying the von mises stress for the simulation with shear force on the top side, from a load of 50 newtons, for material 1

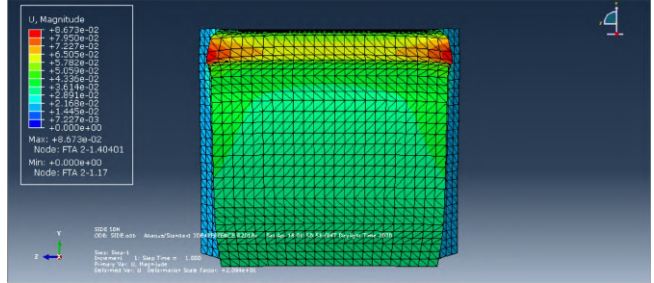


Fig. 100. Overhead view of the Contour plot displaying the Displacement magnitude for the simulation with shear force on the top side, from a load of 50 newtons, for material 1

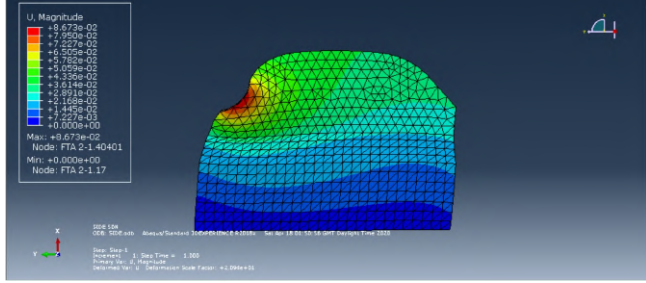


Fig. 99. The Contour plot displaying the Displacement magnitude for the simulation with shear force on the top side, from a load of 50 newtons, for material 1

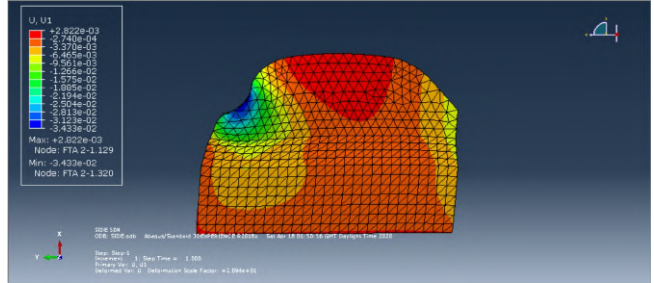


Fig. 101. The Contour plot displaying the Displacement in the x direction for the simulation with shear force on the top side, from a load of 50 newtons, for material 1

was acting at an angle, unlike the normal force which was purely acting in the x direction.

Fig. 102 shows the contour plots for the displacement in the y direction. The maximum displacement magnitude in this direction is 0.07019 mm and that account for 80.9% of the displacement magnitude for the simulation. Furthermore, the contour plots for the y direction shows a clear variation of displacement throughout the fingertip, whereas the x direction contour plots shows a small area at the contact point where there is some displacement variation, and the rest of the fingertip is displaced by a measurement that is at best 4 thousandths of a millimetre. This alone shows a significant limitation of the 1D sensors to be used in some of the fingertips, as the sensors will only be able to measure displacement in one direction. Furthermore, because of the small measurements in the x direction contour plots, it is clear that only a sensor with very high sensitivity (like the 3D sensors) will be able to compute the minute differences in displacement.

Fig. 103 shows the contour plots for the displacement in the z direction. The maximum displacement magnitude in this direction is 0.03793 mm and that account for 43.7% of the displacement magnitude for the simulation. This contour plot is similar to the x direction plot in that the regions of high displacement are limited, in this case to the sides of the contact area. Otherwise, the z direction displacement in the rest of the fingertip is relatively low.

2) *Load from the Side:* The images shown in figures 104, 105 and 106 display the von mises stress contour plots for Silicone, phenyl-type (PVMQ, heat cured, 10-30% fumed silica), with the  $load = 50N$ . In this case the pressure force interacts with the fingertip from the side of the fingertip. In the first contour plot the xy view of the fingertip can be seen, and there are two separate

regions of high stress. One is close to the region where the force interaction occurs, and the other is at the base of the fingertip where the fingertip is fixed to the finger. At 2.206 MPa, maximum von mises stress in this simulation is higher than for bot the normal force and other shear force simulation at the same load. This is due to the fact that the force in this simulation works on smaller area and in one direction in this simulation.

The images shown in figures 107, 108 and 109 display the displacement magnitude stress contour plots for Silicone, phenyl-type (PVMQ, heat cured, 10-30% fumed silica), with the  $load = 50 N$ , where the pressure force interacts at the side of the fingertip. As can be seen from the displacement magnitude contour plots, the highest displacement occurs in the region closest to the area where the force interacts with the fingertip. Furthermore, the maximum displacement magnitude in this simulation is far higher than for the normal force and other shear force simulation. This can be assumed to happen due to the same reason that the stress in this simulation is higher than for the others.

However high the displacement magnitude is, it is clear from looking at the side of the displacement magnitude contour plot that the deformation of the fingertip has caused the most significant displacement to occurs in the z direction, as can be seen more clearly from the figures shown below.

Figs 110 and 111 show the contour plots for the displacement in the x direction. The maximum displacement in the x direction is 0.1112mm, which is 37.3% of the maximum displacement magnitude for the simulation. The displacement in the x direction being so low was to be expected since the initial pressure force acting on the fingertip only acted in the z direction.

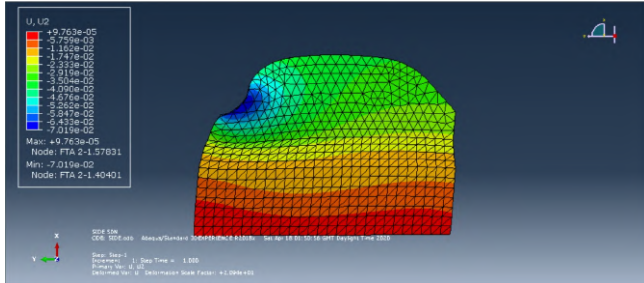


Fig. 102. The Contour plot displaying the Displacement in the y direction for the simulation with shear force on the top side, from a load of 50 newtons, for material 1

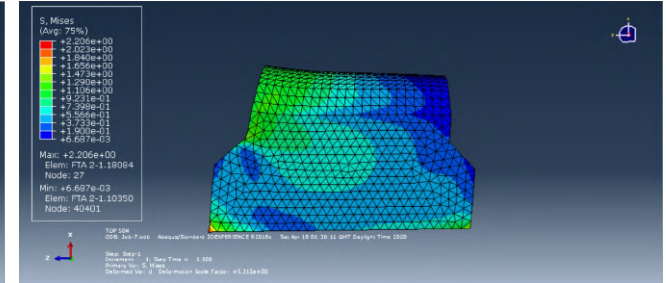


Fig. 106. Side view of the Contour plot displaying the von mises stress for the simulation with shear force on the side of the fingertip, from a load of 50 newtons, for material 1

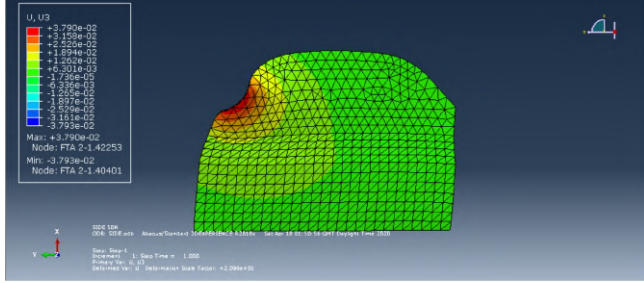


Fig. 103. The Contour plot displaying the Displacement in the z direction for the simulation with shear force on the top side, from a load of 50 newtons, for material 1

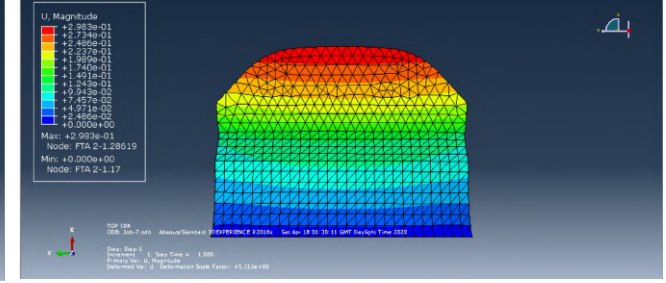


Fig. 107. The Contour plot displaying the Displacement Magnitude for the simulation with shear force on the side of the fingertip, from a load of 50 newtons, for material 1

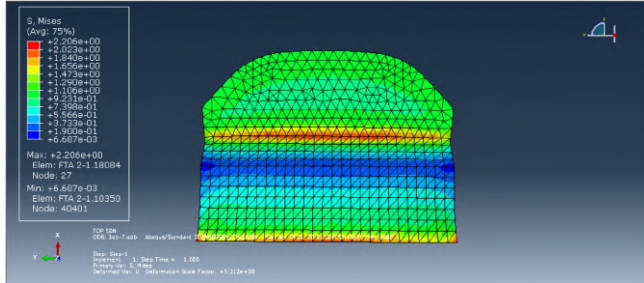


Fig. 104. The Contour plot displaying the von mises stress for the simulation with shear force on the side of the fingertip, from a load of 50 newtons, for material 1

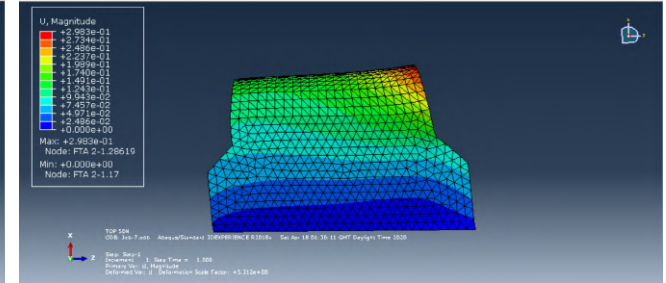


Fig. 108. Side view of the Contour plot displaying the Displacement Magnitude for the simulation with shear force on the side of the fingertip, from a load of 50 newtons, for material 1

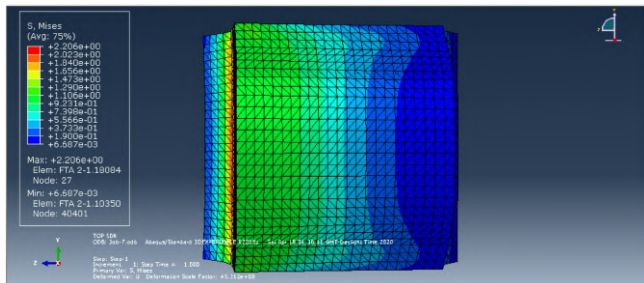


Fig. 105. Overhead view of the Contour plot displaying the von mises stress for the simulation with shear force on the side of the fingertip, from a load of 50 newtons, for material 1

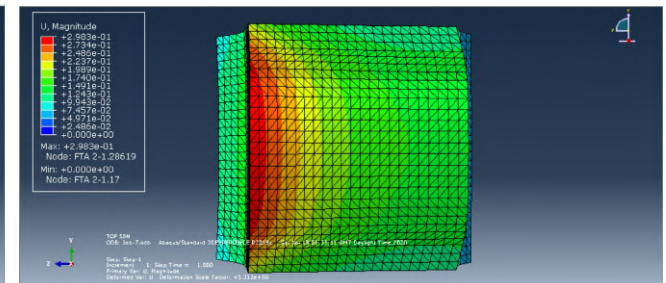


Fig. 109. Overhead view of the Contour plot displaying the Displacement Magnitude for the simulation with shear force on the side of the fingertip, from a load of 50 newtons, for material 1

Similarly, the contour plots for displacement in the y direction show the same discrepancy between displacement and displacement magnitude. In this case the displacement is 0.03513 mm, which is only 11.8% of the displacement magnitude.

Finally, figures 114 and 115 show the contour plots for the displacements in the z axis. The maximum dis-

placement value here is 0.2767, which is 92.8% of the displacement magnitude for the simulation. As expected, the displacement caused by a force4 acting in the z direction, is greatest in the z direction. This is an issue as the finger that utilise 1D sensors for the fingers are limited to measuring the displacement in only the x direction (of the simulation, z direction in real life). Therefore, there

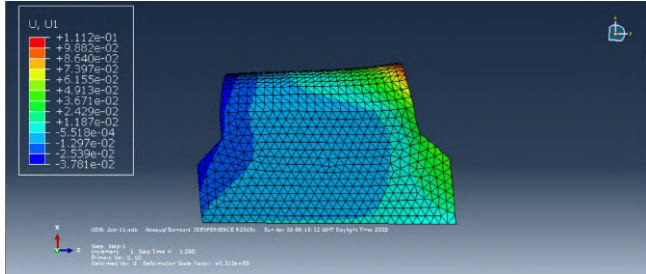


Fig. 110. Side view of the Contour plot displaying the Displacement in the x direction for the simulation with shear force on the side of the fingertip, from a load of 50 newtons, for material 1

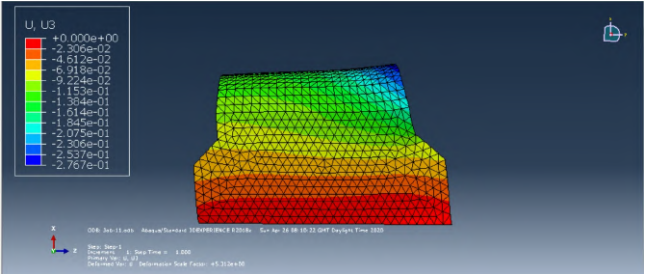


Fig. 114. Side view of the Contour plot displaying the Displacement in the z direction for the simulation with shear force on the side of the fingertip, from a load of 50 newtons, for material 1

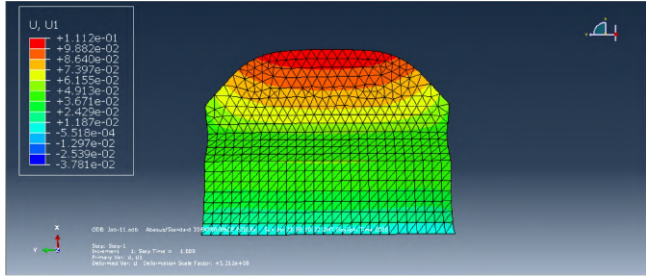


Fig. 111. The Contour plot displaying the Displacement in the x direction for the simulation with shear force on the side of the fingertip, from a load of 50 newtons, for material 1

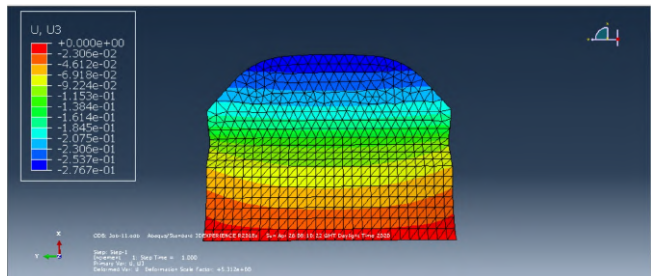


Fig. 115. The Contour plot displaying the Displacement in the z direction for the simulation with shear force on the side of the fingertip, from a load of 50 newtons, for material 1

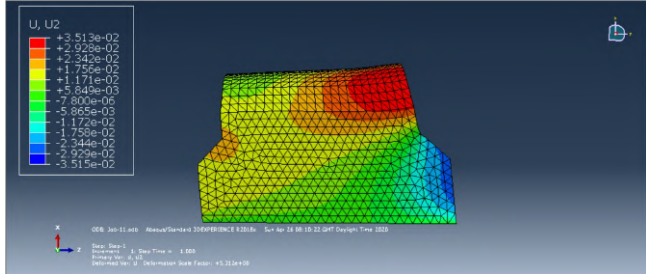


Fig. 112. Side view of the Contour plot displaying the Displacement in the y direction for the simulation with shear force on the side of the fingertip, from a load of 50 newtons, for material 1

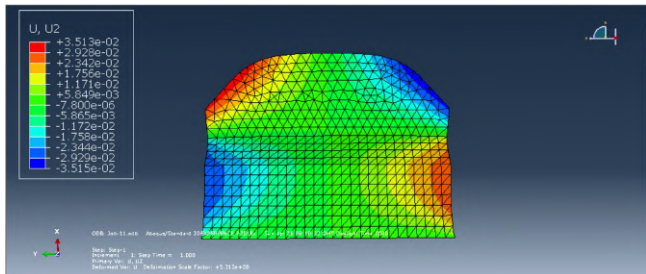


Fig. 113. The Contour plot displaying the Displacement in the y direction for the simulation with shear force on the side of the fingertip, from a load of 50 newtons, for material 1

must be changes made to the fingertip, to ensure that the fingers that use 1D sensors can provide useful information.

#### I. Analysis of fingertip reaction with different material - Bashar

One possible solution to this issue is to use a material for the fingertip that will have greater deformation under equal load. This way the displacement would be greater in

general, which would result in shear forces causing more displacement in the x direction of the fingertip. This in turn would result in the force sensors being able to measure the larger displacement, and then producing force readings. The new material to be used is Silicone, VMQ, heat cured, low hardness, 5-15% fumed silica), which Is much more compliant than the Silicone, phenyl-type (PVMQ, heat cured, 10-30% fumed silica) that has been used so far in this investigation.

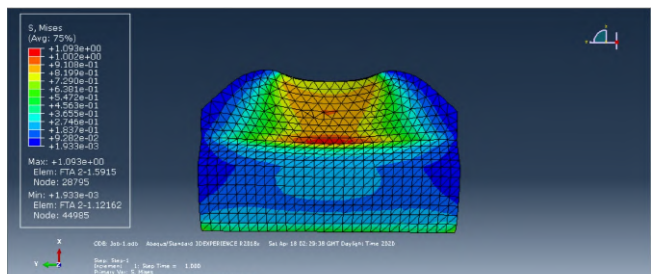


Fig. 116. The Contour plot displaying the von mises stress for the simulation with normal force on the centre of the fingertip, from a load of 50 newtons, for material 2

*1) Normal Force:* The images in Figures 116, 117 and 118 display the Von Mises stress contour plots for Silicone, VMQ, heat cured, low hardness, 5-15% fumed silica), with the *load* = 50 N. In this case the pressure force interacts with the fingertip from the centre strip, normal to the fingertip. As can be seen from the contour plots, the location of the high stress regions in the fingertip for this material, is almost exactly the same as for the material used in the previous simulations. It would be expected then that the difference would be in the maximum values for the stress. However, this is not so, as the maximum stress

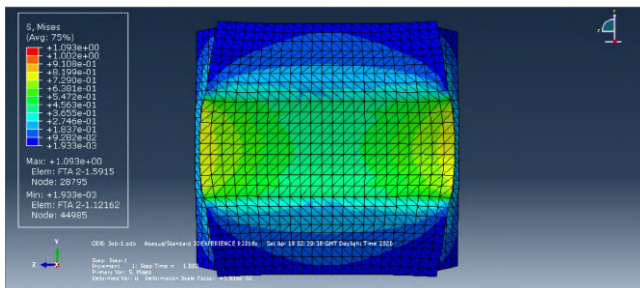


Fig. 117. Side view of the Contour plot displaying the von mises stress for the simulation with normal force on the centre of the fingertip, from a load of 50 newtons, for material 2

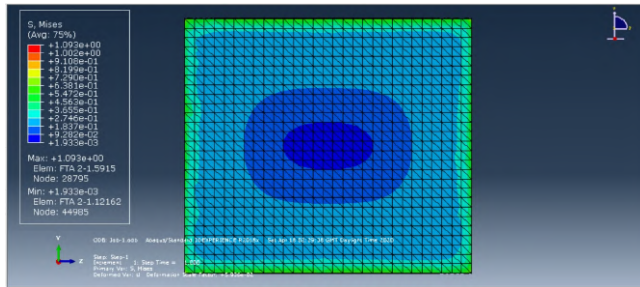


Fig. 118. Base view of the Contour plot displaying the von mises stress for the simulation with normal force on the centre of the fingertip, from a load of 50 newtons, for material 2

value for the second material is equal to that for the first material under the same conditions, at 1.093 MPa.

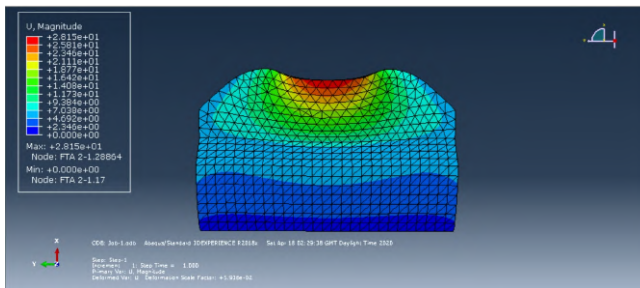


Fig. 119. The Contour plot displaying the Displacement Magnitude for the simulation with normal force on the centre of the fingertip, from a load of 50 newtons, for material 2

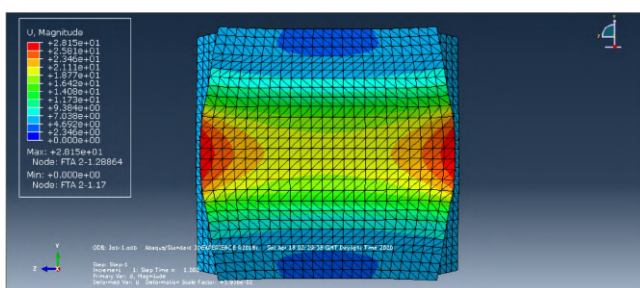


Fig. 120. Side view of the Contour plot displaying the displacement magnitudes for the simulation with normal force on the centre of the fingertip, from a load of 50 newtons, for material 2

The images shown in figures 119 and 120 display the displacement magnitude contour plots for the normal force simulation for material 2. Like the normal force contour plots for material 1, the displacement is highest near

the force contact area, and the maximum displacement magnitude regions lie near the sides of the fingertip. However, the displacement magnitude produced from 50 Newtons of load with this material is 28.15mm, which is much higher than the 0.1211 mm from the simulations using the first material.

The issue that 28.15 mm is greater than the thickness of the fingertip, which indicates that with the material, the fingertip would fail at such high load. However, the result has proved that the choice of a more compliant material does indeed increase the displacement, with normal force at least.

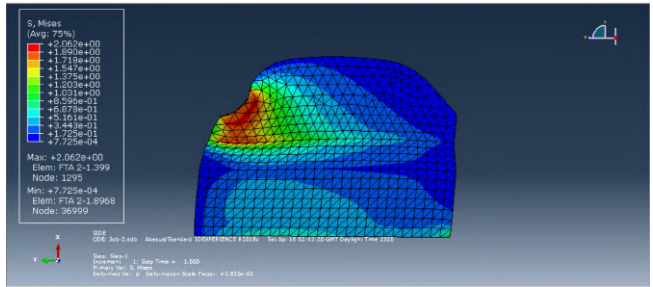


Fig. 121. The Contour plot displaying the Von Mises stress for the simulation with shear force on the top of the fingertip, from a load of 50 newtons, for material 2

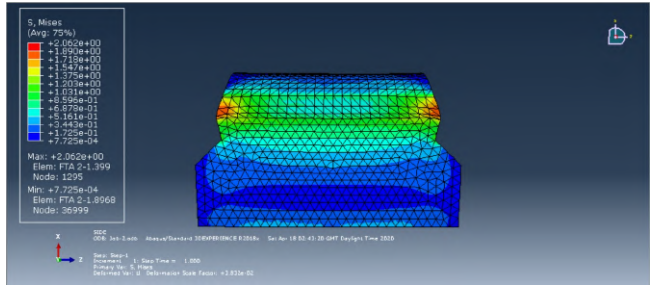


Fig. 122. Side view of the Contour plot displaying the Von Mises stress for the simulation with shear force on the top of the fingertip, from a load of 50 newtons, for material 2

**2) Shear Force:** The images in Figures 121 and 122 display the Von Mises stress contour plots for Silicone, VMQ, heat cured, low hardness, 5-15% fumed silica), with the *load* = 50 N. In this case the pressure force interacts with the fingertip from the top of the fingertip. As can be seen from the contour plots, the location of the high stress regions in the fingertip for this material, is almost exactly the same as for the material used in the previous shear force simulations. the value of maximum displacement on the other hand is different, at 2.062 MPa. This is in stark contrast to the shear force simulation for material 1, which produced a maximum stress of 0.8774 MPa. This is also in contrast to the two normal force simulations for the two materials at 50N load, which produced the exact same maximum stress value.

The images in Fig. 123 and Fig. 124 show the displacement magnitude contour plots for material 2 when experiencing shear force from the top of the fingertip. Much like the simulation with material 1, the location of maximum displacements is near the contact area, towards the edges of the fingertip. The value of the maximum

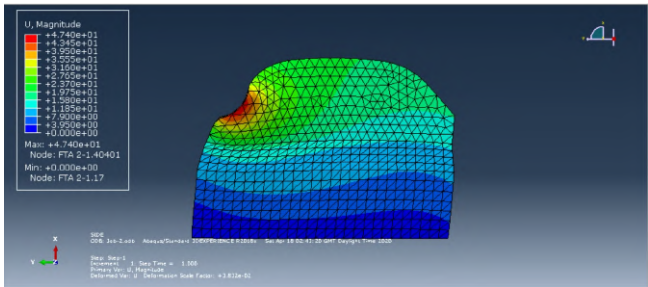


Fig. 123. The Contour plot displaying the Displacement magnitude for the simulation with shear force on the top of the fingertip, from a load of 50 newtons, for material 2

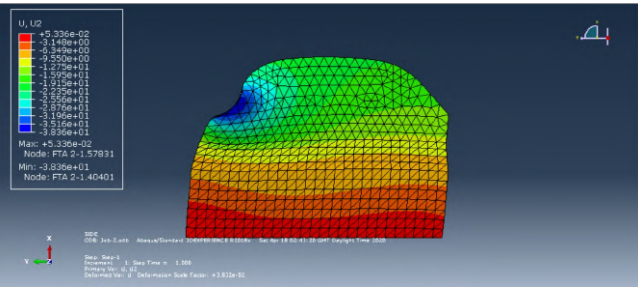


Fig. 126. The Contour plot displaying the Displacement in the y direction for the simulation with shear force on the top of the fingertip, from a load of 50 newtons, for material 2

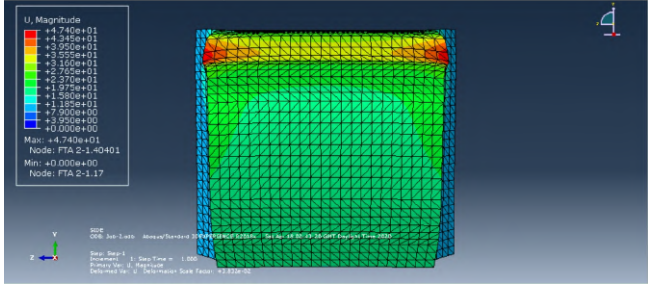


Fig. 124. Overhead view of the Contour plot displaying the von mises stress for the simulation with shear force on the top of the fingertip, from a load of 50 newtons, for material 2

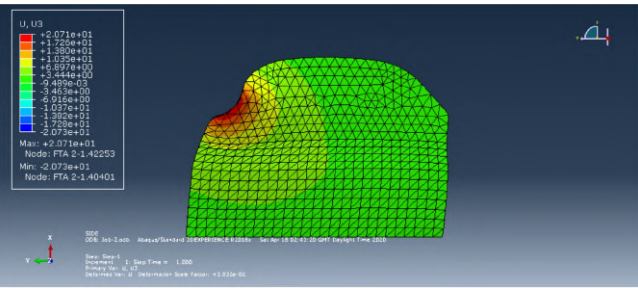


Fig. 127. The Contour plot displaying the Displacement in the z direction for the simulation with shear force on the top of the fingertip, from a load of 50 newtons, for material 2

displacement magnitude, however, is far larger than for the previous simulation at 47.40mm. This, like the contour plot for the normal force acting on the same material, obviously indicates that the material has failed at this load. However, it is promising in that where material 1 failed to produce enough displacement in the x direction from shear force, this material may yet succeed.

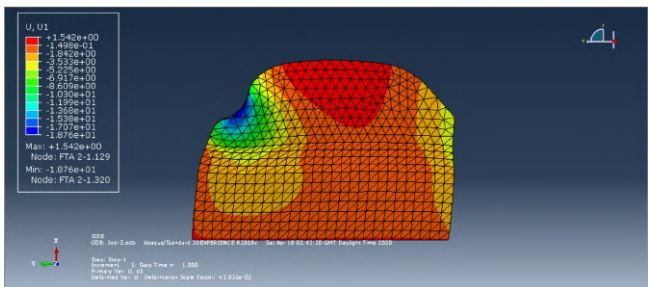


Fig. 125. The Contour plot displaying the Displacement in the x direction for the simulation with shear force on the top of the fingertip, from a load of 50 newtons, for material 2

Figures 125, 126 and 127 show the Displacement contour plots showing displacement in the X, Y and Z direction respectively. Like with the simulation for material 1, the contour plots generally have the regions of maximum and minimum displacement in the same location, to the point where the contour plots look the same. However, as can be seen from the table 5, displaying the maximum displacements in each direction, the change in material has caused the displacements to increase massively. Where in the first simulation with material 1, the displacement in the x direction was 0.03433mm, with material 2 the displacement is 18.76mm.

Whilst this material has proven itself to be far too

compliant to handle the loads it needs to; it has provided proof that the change of material help to overcome limitations with sensors. The next steps in terms of materials will be to find a type of silicone with material properties within the values of the two types of silicone tested in this investigation. That way it will be possible to have a soft skin that can help with force detection, without being damaged in the process.

#### *J. Analysis of results and design improvements - Mohammed Al Bashar Khan*

**1) Hollow Fingertip:** The previous sections have analysed the effect that a change in materials can have on the displacement produced from the load acting on the fingertip. It was found that a material that is more compliant will produce more displacement, due to it deforming more than the stiffer material under the same load. In this section, the effect of using a hollow fingertip will be analysed to see if that will result in greater displacement in the x direction. As shown in the previous sections, the displacement in the x direction from shear force acting on the fingertip has caused less displacement than desired. Therefore, the effect of shear force from the top of the fingertip on the deformation will be analysed to assess whether hollowing out the fingertip is a good way to optimise the fingertip that will be used with 1D force sensors. The material will be the stiffer silicone used in the first part of the study, as the investigation carried out on material 2 proved that it deformed too much.

The previous simulation that used the shear force on the top of the fingertip produced the maximum displacement values shown in VII.

TABLE VI

	Displacement (mm)
X	18.76
Y	38.36
Z	20.73

TABLE VII

Displacement Type	Displacement Value (mm)
Magnitude	0.08673
U1 (X Direction)	0.03433
U2 (Y Direction)	0.07019
U3 (Z Direction)	0.03793

If the hollow fingertip is successful, the displacements from the same 50N load will be much larger, which will make sure that they are measured by the 1D sensors.

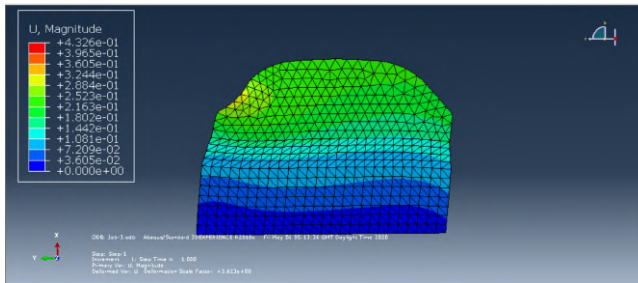


Fig. 128. The Displacement magnitude contour plot for the hollow fingertip

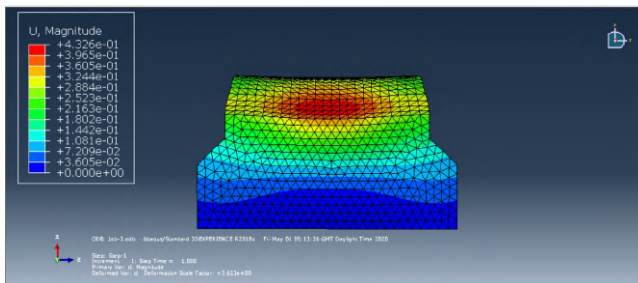


Fig. 129. Side view of the Displacement magnitude contour plot for the hollow fingertip

The images shown above in figures 128 and 129 show the displacement magnitude contour plots for the hollow fingertip. The first thing that is apparent from the contour plot is that the maximum displacement areas are not to the sides of the fingertip but are instead in the middle of the contact area, closest to where the hollow region is. Secondly, the maximum displacement magnitude is much higher for this fingertip, with a value of 0.4326 mm. This indicates that the hollow fingertip has achieved its objective of increasing the displacement. However, because the sensors are 1D sensors, the displacement in the x direction needs to be analysed to make sure that a large enough displacement is produced.

Fig. 130 shows the contour plot for displacement in the x direction. The maximum displacement in this contour plot is 0.1566 mm, which is almost 4.56 times higher than the x direction displacement from the standard fingertip simulation. Therefore, the hollowed-out fingertip has

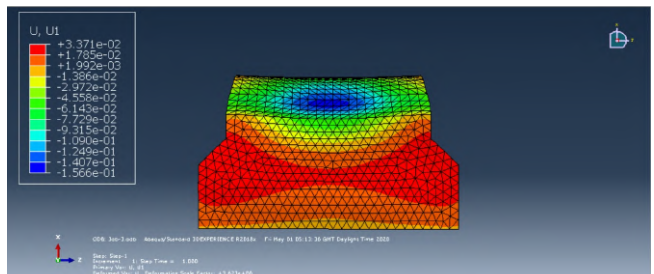


Fig. 130. Side view of the x direction Displacement contour plot for the hollow fingertip

enabled the fingertip, even with a very stiff material to produce significant enough displacement, that even the limited 1D sensors will be able to measure.

*2) Mesh Convergence:* One of the decisions taken for this investigation was to have the mesh width at 0.5 for all of the simulations that were run. The reasoning behind this was due to technological limitations that caused issues when the mesh was refined any further. Considering that the mesh was compromised by the limitations to mesh refinements, the accuracy of the results needs to be analysed. This can be done by carrying out a mesh convergence study.

Multiple simulations were run to find the values for maximum stress and displacements for a single simulation with a load of 75N and where the mesh was varied from 3.5 to 0.5 in intervals of 0.5. A graph was then plotted of the stress or displacement against the number of elements to find whether the graphs of stress or displacement converged as the mesh was refined further.

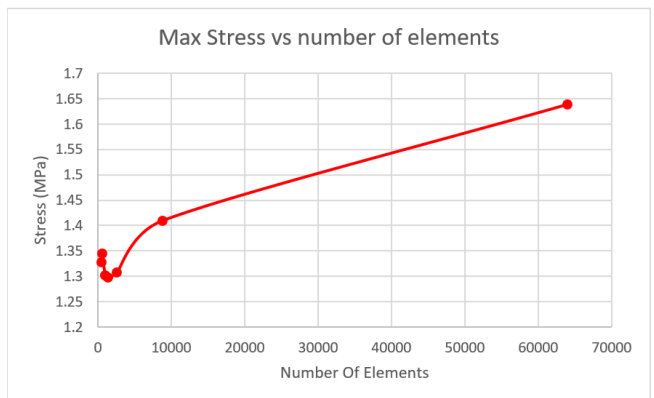


Fig. 131. Graph of maximum stress vs number of elements for load=75N

The graph shown in Fig. 131 displays the maximum stress against the number of elements. Whilst the graph does show the gradient of the line decreasing as the number of elements increases, at the final point the graph clearly has not converged. This is due to the mesh not being refined enough, and because of this the reliability of the results for the von Mises stress must be called into question.

The graphs shown in figs 132 and 133 display the maximum displacement against the number of elements. Unlike the stress graph, this one does converge, albeit in the final two points. However, considering that the gradient

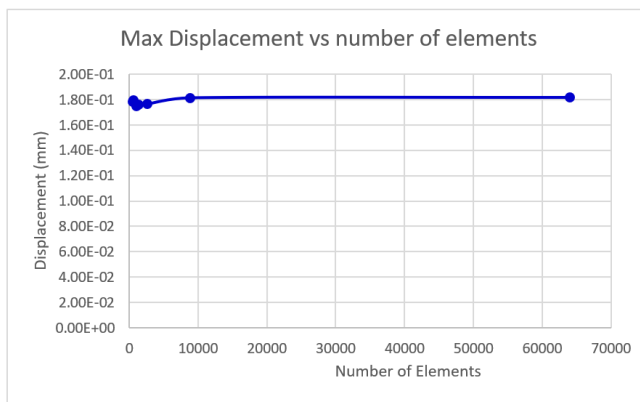


Fig. 132. Graph of maximum displacement magnitude vs number of elements for load= 75N

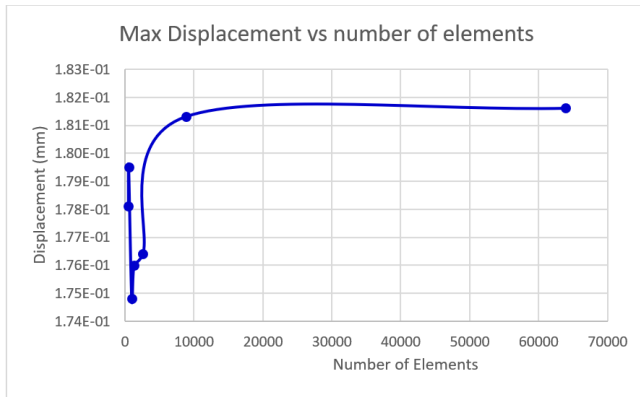


Fig. 133. Zoomed in graph of maximum Displacement magnitude vs number of elements for load= 75N

of the line at the final point is so low, it can be considered to have converged. Despite this, the simulation could do with further mesh refinement, which would provide more points on the graph at which it would have converged to a value.

In future attempts, where there will not be the same technological limitations, the mesh should be refined further until it can be confirmed that both the graphs for stress and displacement against number of elements have converged.

#### K. Fingertip Material - Mohammed Al Bashar Khan

The soft skin is a very important component to choose a material for, as the material itself defines the performance of the soft skin. A material that is too stiff will have small displacements under load, which is fine for the 3D sensors, but disastrous for the 1D sensors as they are not as sensitive. On the other hand, a material that is too compliant will not be able to handle large loads and will either deform too much or fail completely. The method of producing the skin for this hand was decided to be moulded silicone, however the type of silicone has not yet been confirmed. The FEA analysis that has been carried out in this report concluded that the silicone used have a young's modulus between 0.215 MPa and 50MPa. The result of the maximum load on the softer silicone can be seen in 119. The image shown in Fig. 134 shows the

displacement magnitude contour plot for 1N normal load on the fingertip for the stiffer silicone.

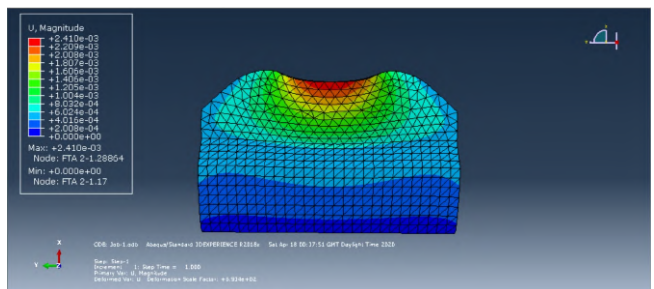


Fig. 134. The contour plot displaying the displacement magnitude for the 1N normal load on the fingertip made of material 1

The maximum displacement in this simulation was 0.00241 mm. A small displacement such as this may be measurable for the 3D sensors on the Thumb, index and middle fingers, but the 1D sensors on the ring and pinky fingers will not be able to sense such a small displacement. The two silicones used in the simulations were Silicone (VMQ, heat cured, low hardness, 5-15% fumed silica) and Silicone, phenyl-type (PVMQ, heat cured, 10-30% fumed silica), where the latter was the stiffer material. One of the types of silicone already procured for this project is Ecoflex™ 00-50, which has properties similar to the softer silicone. This will result in a skin that can sense small loads like 1N but will be damaged by larger loads.

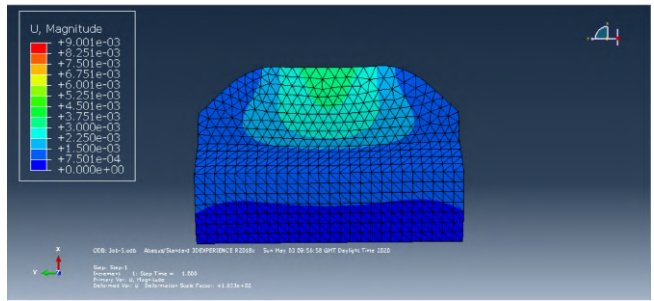


Fig. 135. The contour plot displaying the displacement magnitude for the 1N normal load on the hollow fingertip made of material 1

The image in Fig. 135, shows the displacement magnitude contour plot for Silicone, phenyl-type (PVMQ, heat cured, 10-30% fumed silica), under 1N of normal load. However, this simulation uses the hollow fingertip described in section hollow fingertip section. By including a hollow section in the fingertip (giving the fingertip 2mm thick walls) and changing nothing else, the displacement from 1N of load has been increased by 273%. With a material that is a little more compliant, the deformation of the fingertip could be changed enough so that all the sensors used in the fingertips could perform properly. One of the materials that could be used for this purpose includes Silicone (VMQ, thermally conductive, 40-70% mineral), which has a young's modulus of 18 MPa and compressive strength of 4.32 MPa.

#### L. Result Analysis - Mohammed Al Bashar Khan

The mesh convergence study carried out for this report found that whilst the displacement did converge, the stress

did not. This is due to the fact that mesh refinement used for the simulations in this investigation was not refined enough. The COVID-19 situation led to remote access being required to access the Abaqus software used for the study. The technological limitations as a result of this was the reasoning behind the mesh not being refined further, and in future attempts at similar simulations, the mesh must be refined to the point where the convergence study produces converging graphs for both stress and displacement. Another issue caused by the COVID-19 situation, was that physical testing was not possible.

A significant issue with FEM simulation is that by entering a limited amount of variable into the programme, results are produced without considering other factors. For example, the simulations in this report used models that only considered the density and simple elastic properties like Youngs modulus and Poisson's ratio. This means that the compressive and tensile strengths were not considered. Without physical testing, the results of the simulation cannot be verified, and the conclusions of this investigation can only be taken as indications of what to do next.

## VII. COMPONENT JUSTIFICATIONS & BILL OF MATERIALS

### *A. Bill of Materials - Jamie Sengun*

The costs shown in the bill of materials is the total cost per parts for one unit of the complete robot hand and wrist assembly and does not take into account costing or savings due to bulk purchases. For example, only the length of wire used per unit with respect to the total spool length is shown. Mass manufacturing unit cost varies depending on the scale of manufacturing and is not evaluated in this report. The complete bill of materials for parts, materials and components is shown in Table VIII. The current unit cost of the complete robot hand and wrist assembly is £1153.70. The bill of materials for the consumables, tools and tooling required for manufacturing is shown in Table IX. The current cost of tooling is £49.96; however, this is variable depending on the supply needed to meet manufacturing demands.

The following section will initially outline justifications for major parts and a general overview of how the parts function and interact with the complete assembly. Minor parts like bolts, washers etc will not be discussed here but may be referenced in their respective design section. This is then followed with a section that outlines the bill of materials and finance for the parts and tooling required for the complete assembly. Components costs will represent the retail price in January 2020 and are not optimised for the lowest cost, but were optimised to reduce the number of required retailers for the prototyping phase due to ordering limitations imposed by the University finance team.

### *B. Component Justification*

*1) Dynamixel AX-12A motors - Jamie Sengun:* This item supports objectives 5.1, 5.2, 5.3. Dynamixel AX-12A servo motors were chosen over conventional analog/digital PWM servo motors due to several beneficial programmable features that provide the user with the ability

to fine tune the setup performance and safety capabilities for the robotic hand. A list of beneficial features are listed below:

- Toggle motor torque on/off while powered on
- Position, velocity, acceleration, voltage, current and temperature sensing with the ability to plot with respect to time and export to a CSV file. Can utilise the torque toggle to orientate the motors manually while recording motor sensor data and then use it to make pre-programmed poses or motions more rapidly compared to manually defining the motor angle sequence with respect to time. This is particularly useful for rapid testing for specific grasp types and dexterity testing.
- Modifiable rotational speed, torque, compliance and starting position. Compliance is defined as the relationship between the motor output torque relative to the magnitude of the error between the desired and current value. With an outsourced control method, this variable can theoretically allow for on-demand optimised grasping forces and manipulation capabilities per finger for the hand with various objects of differing fragility. All the other variables also have potential to be changed on-demand using functions in a majority of programming languages, using the ROBOTIS U2D2 controller and the ROBOTIS SDK software [40]. These two components are discussed later in the section.
- Programmable auto-shutdown and error reporting for reaching a defined temperature, voltage, current and torque limit. This is particularly useful to prevent any events that could lead to a damaged motor, particularly in the scenario of prolonged object grasping with potentially incorrect compliance or maximum torque settings. Conventional servo motors have a tendency to burn out and damage themselves in these scenarios as there is no fail-safe to prevent it other than the user proactively reducing the potential maximum load or torque on the motors with a safety buffer so that it is less probable.
- 300° rotation with a resolution of 0.29° due to 10-bit controller implementing 1024 steps. This range is sufficient and can be limited per motor to prevent any scenarios where the user may accidentally ask the motor to move outside the range potentially damaging components on the hand, as is the case with PWM control on conventional servo motors where a software solution is used. For the AX-12A motors, if the user calls the motor to move outside of its programmed range then it will not acknowledge the command and act as a failsafe.

The Dynamixel AX-12A motors utilise a serial data channel instead of the conventional PWM for control. They use a 3 pin proprietary connector to allow for motors to be daisy-chained to distribute power and serial connections. Each motor has a programmable ID number between 0-253 that can be used to directly address a motor in the daisy-chain; or alternatively, a group of motors can be controlled simultaneously. We were unable to validate the real world performance of the AX-12 motors compared

TABLE VIII

BILL OF MATERIALS OF ALL PARTS, MATERIALS AND COMPONENTS REQUIRED FOR THE ASSEMBLY OF THE COMPLETE ROBOT HAND AND WRIST.

Product Name	Type	Manufacturer ID	Cost (£) Per unit or per [m] or per [kg]	Number of units or [m] or [kg]	Total Cost per part (£)
Honeywell Ratiometric Hall Effect Sensor switching current 1.5 mA supply voltage 4.5 → 10.5 V dc	1D sensor	SS495A	2.69	2	5.38
Custom Melixis MLX90393 3D hall effect PCB	3D sensor		50.00	3	150.00
Araldite Araldite 2011 Epoxy Paste 200ml Cartridge (£ per mL)	Adhesive		0.19	20	3.80
Velleman Analogue Input Board Arduino™ Board KA12	Analog Shield	KA12	14.96	1	14.96
SV01A103AEA01B00 - Rotary Positon Sensor, SV01 Series, SMD, Centre Hole for Shaft, 10 kohm, 2%, 2 mN-m, 5 Vdc	Angular Sensor	SV01A103AEA01B00	1.74	16	27.84
Arduino Uno Rev3 MCU Development Board A000066	Arduino	A000066	19.73	1	19.73
4mm Radial Ball Bearing 7mm O.D	Bearings	DDL-740ZZH3P25LY121	3.74	30	112.20
Molex PicoBlade Female Connector Housing, 1.25mm Pitch, 4 Way, 1 Row	Connector	510210400	0.24	5	1.20
Crimp Connector Housing: 0.1 inch pitch 1x3-Pin 25-Pack	Connector	CRIMPHOUS3	0.03	37	1.07
Molex KK 254 171857, 2 Way, 1 Row, Right Angle PCB Header	Connector	1718573002	0.16	1	0.16
Arctic F12 12cm Quiet Case Fan with Fluid Dynamic Bearing	Fan	AFACO-12000-GBA01	4.49	1	4.49
Akasa Aluminium for 120mm Fan filter	Fan Filter	GRM120-AL01-BK	2.48	1	2.48
TCA9548A I2C Multiplexer	I2C multiplexer	2717	6.91	1	6.91
MIKROE-512, 10 piece Breadboard Jumper Wire Kit	Jumper cable	MIKROE-512	0.29	4	1.16
Pack of 50, 2mm dia x 1mm thick N42 Neodymium Magnet - 0.11kg Pull	Magnet	F321-50	0.08	5	0.41
4mm diameter, 1m long circular rod - pack of 5 [Meter]	Metal Rod		3.20	0.2867	0.92
6 Port AX/MX Power Hub	Motor power/signal	IL-3PHUB	6.40	1	6.40
ROBOTIS U2D2	Motor programmer	902-0132-000	46.50	1	46.50
Robotis Dynamixel AX-12A (Single Buy)	Motors	902-0003-001	41.80	12	501.60
RS PRO, M1.6 Countersunk Head, 3mm Stainless Steel Slot A2 304	nuts/bolts/washers	179-5641	0.18	116	21.02
Nickel Plated Brass Plain Washer, 0.8mm Thickness, M4	nuts/bolts/washers	483-0653	0.02	30	0.54
Knurled Threaded Insert, M2 x 3mm (L) x 3.2mm (OD) Female Thread Brass Embedment Nuts, Pack of 100	nuts/bolts/washers		0.06	116	7.53
Knurled Threaded Insert, M2 x 5mm (L) x 3.5mm (OD) Female Thread Brass Embedment Nuts, Pack of 100	nuts/bolts/washers		0.04	23	0.99
Knurled Threaded Insert, M3 x 3mm (L) x 5mm (OD) Female Thread Brass Embedment Nuts, Pack of 100	nuts/bolts/washers		0.06	4	0.24
M2 X 12mm Full Thread Cap Head Screws (DIN 912) - A2 Stainless Steel	nuts/bolts/washers		0.20	5	1.00
Chrome Plated Steel Plain Washer, 0.5mm Thickness, M4	nuts/bolts/washers	4979874451774	0.02	6	0.12
M2 X 10mm Socket Countersunk Screws (DIN 7991) - A2 Stainless Steel	nuts/bolts/washers		0.41	18	7.38
EASYFIX CARBON STEEL HEX FLAT NUTS M6 100 PACK	nuts/bolts/washers		0.02	8	0.18
EASYFIX BZP STEEL THREADED RODS M6 X 300MM 5 PACK	nuts/bolts/washers		0.68	4	2.71
M2 X 6mm Round Head Groove Pins (DIN 1476) - A1 Stainless Steel	nuts/bolts/washers		0.20	13	3.60
Rotational potentiometer PCB - Double layer pcb with holes pre-drilled not assembled 25 x 14 mm x1.6mm	PCB		0.60	15	9.07
RS PRO DC Power Plug Rated At 5A, 12 V, Cable Mount, length 23.6mm, Nickel Plate	Power Connector	487-858	1.20	1	1.20
Electronics-Salon 24/20-pin ATX DC Power Supply Breakout Board Module	Power Distribution		12.99	1	12.99
RS PRO Male Micro USB B to Bare Wire, 0.5m USB Cable	Power Distribution	173-3530	1.91	1	1.91
iHaospace PCA9685 16 Channel PWM Servo Driver IIC interface for arduino Raspberry Pi Shield Module Servo Shield	Power Distribution		3.99	1	3.99
3D FilaPrint Finest Traffic Blue PLA 3D Printing Filament 1.75mm 1kg (Cost per kg - 20% infil) [kg]	Printing Filament		25.20	2.121	53.45
3D FilaPrint Finest Traffi Grey PLA 3D Printing Filament 1.75mm 1kg (Cost per kg - 20% infil) [kg]	Printing Filament		25.20	0.104	2.62
Seasonic 300W PC Power Supply, 100 → 240V dc Input, -12 V dc, 3.3 V dc, 5 V dc, 12 V dc Output	PSU	SSP-300TBS	36.53	1	36.53
Raspberry Pi 3 Model B+	Raspberry Pi	Raspberry Pi 3 Model B+	34.07	1	34.07
Ecoflex™ 00-50 Trial kit: Cost per kg [kg]	Silicone		36.27	0.01	0.36
PowerPro Braided Line - 135m - Moss Green 40kg (0.41mm) [Meters]	Tendon		0.15	7.426038	1.10
MPT 0.5/12-2.54 - Wire-To-Board Terminal Block, 2.54 mm, 12 Ways, 26 AWG, 20 AWG, 0.5 mm², Screw	Terminal Block	MPT 0.5/12-2.54	4.39	2	8.78
Molex PicoBlade Female Crimp Terminal Contact 26AWG 50079-8000	Terminal Connector	50079-8000	0.04	68	2.72
1.25mm Pitch, PicoBlade Male Crimp Terminal, Tin (Sn) Plating, 26-28 AWG, Bag	Terminal Connector	501258000	0.04	68	2.72
Female Crimp Pins for 0.1" Housings 50-Pack	Terminal Connector	CRIMPPINS	0.05	108	5.05
1.25mm Pitch, PicoBlade PCB Header, Single Row, Vertical, Through Hole, Tin Plating, Friction Lock, 3 Circuits, Tray, 2.30mm PC Tail Length	Terminal Connector	53047-0310	0.17	16	2.78
RS PRO USB 2.0, Male USB A to Male USB B, 0.5m USB Cable	USB	182-8547	2.34	1	2.34
(Male Housing) 1.25mm Pitch, PicoBlade Plug Crimp Housing, Single Row, Friction Lock, 4 Circuits, Natural	Wire Connectors	510470400	0.24	5	1.20
(Male Housing) 1.25mm Pitch, PicoBlade Receptacle Crimp Housing, Single Row, Friction Lock, 3 Circuits, Natural	Wire Connectors	510210300	0.24	16	3.84
RS PRO Orange, 0.13 mm² Hook Up Wire, 100m	Wiring	873-9920	0.04	3	0.13
3 core Servo Cable	Wiring	SERVOCABLE	0.79	16	12.64
RS PRO Blue, 0.08 mm² Equipment Wire, 50m	Wiring	801-5013	0.29	18	5.25
<b>Total Cost (£)</b>					<b>1153.70</b>

TABLE IX

TABLE OF THE CONSUMABLES, TOOLS AND TOOLING REQUIRED FOR THE MANUFACTURE OF THE COMPLETE ASSEMBLY OF THE ROBOT HAND AND WRIST

Product Name	Type	Retail Cost (£)	Amount required	Cost Per unit or Cost per meter (£)
10pcs 900M-TSeries Copper Base Lead-free Electroplating Iron and Nickel Replaceable Solder Iron Tips Set Low Temperature Soldering Station Tool Shape I, SI, B, K, 1.2D, 2.4D, 3.2D, 2C, 3C and 4C	Soldering stuff	6.29	1	0.63
Hakko T18-D16 T18 Series Chiseled Soldering Tip, 1.60mm	Soldering stuff	9.34	1	9.34
PA-09 CRIMPING TOOL (MICRO & MINI CRIMP PINS)	Tool	39.99	1	39.99
<b>Total Unit Cost (£)</b>				49.96

to typical servo motors for our robot hand and it's use case as we were unable to program or test them in this project due to the inability to build the robot hand due to the COVID-19 situation.

2) *ROBOTIS U2D2 Controller - Jamie Sengun:* The ROBOTIS U2D2 controller was required to control and programme the AX-12A servo motors using the ROBOTIS SDK [40] and Dynamixel Wizard 2.0 [41]. This controller can be connected to the Raspberry Pi via the USB port and to the daisy-chained motors. Note the U2D2 does not provide power, only the serial connection. 6-port AX/MX power hubs were used to distribute the serial connection, ground and 12 V power from the ATX connector power breakout board to the motors. This was decided as a precaution since there were no technical specifications for the maximum current that could pass through the daisy-chained motors.

3) *Adafruit TCA9548A I2C Multiplexer - Jamie Sengun:* Adafruit TCA9548A is a I2C multiplexer that was chosen to expand the number of addressable I2C components up to 8 devices that may or may not have identical physical I2C addresses. This was primarily required because of the limited four I2C addresses that the 3D hall effect sensor PCBs has when more than four of them were required - this is discussed in the following paragraph. The use of the TCA9548A was beneficial in providing a small simple PCB for grouping the SDA and SCL I2C connections together for input into their respective Arduino ports. Note, we designed the robot hand to utilise three 3D hall effect sensors and theoretically do not reach the limit of four; however, the TCA9584A allows the expansion the number of I2C components in the future should the user wish to. The eight addresses of the TCA9548A can be addressed individually by using a few simple lines of Arduino code to provide a left shift in the 8-bit integer input into the TCA9548A; where the default I2C address of the TCA9584A is 0x70 in hexadecimal as shown in Listing 1 - this code was later implemented into the Arduino code (**arduino\_sensors.ino**) for the reading of the Melexis MLX90393 sensors. The default I2C address for the TCA9548A can be changed by shorting either of the **A0**, **A1**, **A2** pins to the **Vin** pin to change addresses from 0x70 to 0x77 as per the manufacturer's instructions allowing for up to 64 I2C devices with the same physical I2C address.

```
#define TCAADDR 0x70

void tcaselect(uint8_t i) {
    if (i > 7) return;
```

```
Wire.beginTransmission(TCAADDR);
Wire.write(1 << i);
Wire.endTransmission();
}
```

Listing 1. Example Arduino code for TCA9548A I2C port selection [42]

4) *Melexis MLX90393 - Jamie Sengun:* This item supports objective 3.2, 4.2. The 3D hall effect sensors are Melexis MLX90393 chips mounted on a custom rigid PCB that can use the SPI and I2C protocols for addressing the sensors. The hall effect is a phenomena where a voltage can be measured across a electrical conductor surface when subjected to a passing current and is perpendicular to a magnetic field. Due to the availability of the I2C protocol on Arduino boards it was decided to use this for addressing multiple devices on a shared digital serial bus. They use an input voltage of 2.2 V to 3.6 V, can operate between -20 °C to 80 °C, consume approximately 3 mA under normal working circumstances and have a dynamic magnetic field density range between 5 mT to 50 mT. However, this comes with limitations as a compromise must be achieved between magnetic field density range and sensitivity. For the sake of clarity, the mechanics of the sensor will be mentioned here instead of in the Software/Libraries section.

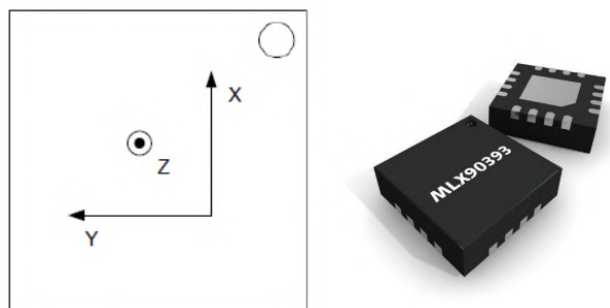


Fig. 136. MLX90393 magnetic field density axis definitions. [35]

The sensor is able to output magnetic flux density measurements in micro-Tesla (µT) in three dimensions along with temperature measurements (°C). The magnetic flux density axis definitions are illustrated in Fig 136. The sensitivity of the magnetic flux density measurements are reliant on two variables: resolution (*RES*) and analog gain (*GAIN\_SEL*). The MLX90393 datasheet defines how the sensitivity (µT/LSB) changes with respect to these two variables and how the range varies with respect to the

chosen *RES*, as shown in the appendix, Table XVIII and Table XIX respectively.

When using these tables it is best practice to identify the desirable characteristic for the sensor for the use case. In this case hypothetically, high sensitivity would be ideal to detect small changes in the displacement of the magnet relative to the sensor; which ultimately represents a small applied force when the magnet is embedded within a deformed soft skin material. Additionally, a wide range of magnetic flux density would be beneficial as it could allow for large magnetic displacement ranges and a wider range of potential magnet choices sizes and strengths. Lastly, the use of magnetic flux density measurement temperature compensation (*TCMP\_EN*) is beneficial to reduce temperature dependent drift to obtain more accurate readings. However, enabling *TCMP\_EM* limits the user to *RES=0* and *RES=1* only, which is satisfactory as it allows the use of the full dynamic range up to the magnetic saturation onset of  $\pm 50$  mT for the X, Y, Z axes. The magnitude of the maximum magnetic flux density in  $\mu\text{T}$  is calculated using (7); where  $SENS_i$  is the sensitivity of either [X,Y] or [Z] axes and  $R$  is the range as defined in Table XIX as shown in the appendix; which is  $\pm 2^{15}$  when *TCMP\_EN* is enabled.

$$|B_{\max}| = \frac{SENS_i \cdot R}{1000} \quad (7)$$

The most sensitive setup of  $0.161 \mu\text{T}/\text{LSB}$  for the X,Y axis sensitivities ( $SENS_{XY}$ ) and  $0.294 \mu\text{T}/\text{LSB}$  for the Z axis sensitivity ( $SENS_Z$ ) can be achieved using *RES=0* and *GAIN\_SEL=7*. This provides a magnetic flux density range of approximately  $\pm 5.275$  mT and  $\pm 9.634$  mT for  $SENS_{XY}$  and  $SENS_Z$  respectively for 16 bit data. To achieve this level of sensitivity would require the use of a magnet that is able to provide the magnetic flux density changes in the vicinity of its respective MLX90393 based on the designed soft skin displacement range. Research was conducted into simulating magnets using Finite Element Method Magnetics (FEMM) software [33] in conjunction with real-world experimental testing to determine suitable displacement ranges relative to the soft skin deformation capabilities to ensure magnet flux density detection and to avoid sensor output saturation as discussed in section V-A.

Additionally, the MLX90393 is able to provide variable sample rates by utilising combinations of internal digital signal filtering (*DIG\_FILT*) and oversampling rate (*OSR*) varying from 4.5 Hz to 716.9 Hz as shown in Table XX in the appendix. The default I2C address of the MLX90393 on the PCB is 0x0F in hexadecimal but can be changed to one of four addresses locally by shorting connection pads **A0** and **A1** as described in Table X and shown in Fig.137. However, this was not necessary with the introduction of the TCA9584A multiplexer. A PCA9685 PWM servo driver was used to distribute ground and 3.3 V connections from the Arduino to the three MLX90393 PCBs as it can fulfill the current requirements to their low 3mA consumption. The PCA9685A was chosen as it was already in our possession, can cost a little as £4 and can supply parallel power and ground connections to 16 channels with 0.1" or 2.54 mm pitch pins. Alternatively two common connection

terminal blocks would be required for the same effect; one for 3.3 V and one for ground.

TABLE X  
CUSTOM PCB MLX90393 PHYSICAL I2C ADDRESSES

Address	A1	A0
0x0C	GND	GND
0x0D	GND	VCC
0x0E	VCC	GND
0x0F	VCC	VCC

The MLX90393 chip has the dimensions of 3 mm width, 3 mm length and 1 mm thickness. The custom rigid PCB; including the MLX90393, designed by Pedro Ribeiro at INESC MN in Portugal has the dimensions of 7mm width, 9.7 mm length, 2 mm thickness and is shown in Fig.137. The dimensions of this custom PCB are small relative to commercial retail PCBs that incorporate the MLX90393. For example, the Sparkfun MLX90393 board has a 26 mm width, 26 mm length and 2 mm thickness, while the Adafruit MLX90393 board has a 23 mm width, 19.2 mm length and 2.8 mm thickness. Using a PCB with the smallest dimensions was critical for reducing the minimal dimensions of the fingertips, where the commercial options proved to be abnormally large for embedding in the palmar side of the fingers. The MLX90393 chip itself is on average £2 per chip from online retailers at the time of writing; however, the proposed custom PCB current costs approximately £50 each due to low quantity manufacturing when compared to the Sparkfun and Adafruit variants at £15 and £11 respectively. There is potential in the future to reduce the cost of this custom PCB significantly with a greater production scale using a 3rd party manufacturer.

5) Honeywell SS495A - Jamie Sengun: yThis item supports objective 3.2, 4.2. A cheaper alternative to the 3D MLX90393 hall effect sensors is the Honeywell SS495A Ratiometric 1D hall effect sensor which can detect normal displacements only; with no shear displacement detection and does not require soldering to a PCB. This was utilised in areas of the hand that were determined less feasible due to a reduced need for full 3D sensing capabilities and sensitivity in some areas of the hand relative to the cost of implementing 3D sensors in all proposed locations - This was particularly important to minimise costs to fulfil our 'low-cost' aim at £2.69 per unit. Additionally, this sensor is no larger than the dimensions of the 3D sensor custom PCB and requires an input voltage of 4.5 V to 10.5 V, has an operating temperature range of -40°C to 150°C, consumes approximately 6 mA under normal working circumstances and is able to detect magnetic flux density range of  $\pm 67$  mT. The low 6mA current consumption is ideal for direct power of the Arduino Uno through the KA-12 analog shield. The sensor has a reported sensitivity of  $3.125 \pm 0.125 \text{ mV/G}$  with a supply voltage of 5V and an output voltage range of 0.2 V to 4.8 V. While the sensor has a voltage range of 4.5 V to 10.5 V, typical analog to digital converters on boards like Arduino typically work with a maximum 5 V or 3.3 V for some variants and have a maximum resolution of 10-bit or 1024 steps. Due to this the sensitivity of these sensors

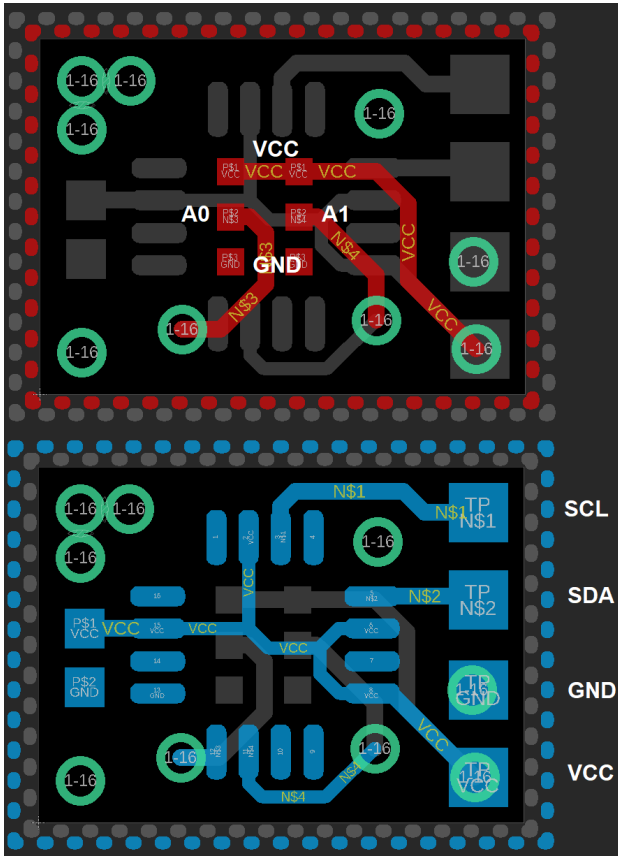


Fig. 137. Electrical schematic for the Custom 3D Melexis MLX90393 rigid PCB created by Pedro Ribeiro at INESC MN in Portugal. Top picture is the top layer of the PCB and the bottom picture is the bottom layer of the PCB.

are limited - The 4.6 V output range would be limited to approximately 942 of those 1024 steps over the full 5 V range which equates to an approximate sensitivity of 142.25  $\mu\text{T}/\text{LSB}$ . This level of sensitivity should be sufficient for areas of the hand that are less critical to the overall dexterity and object manipulation capabilities of the hand; for example, these sensors would be deemed sufficient for the ring and index finger as these fingers typically just provide support and have less contribution towards dexterous manipulation of an object. Unlike the MLX90393 sensors, the SS495A does not have built-in temperature compensation and can have systematic measurement errors caused by temperature fluctuations. The SS495A has a linearity between -0.5% of span for -40°C to -1.5% of span for 125 °C, and has a null drift of  $\pm 0.06\%/\text{°C}$  and sensitivity drift of between -0.01%/°C to +0.005%/°C from the reference 25°C value. Due to the magnetic flux density dependence on the temperature of the SS495A and no internal temperature compensation, it is recommended to validate the code that converts the voltage readings into  $\mu\text{T}$  using a 3rd party tool with a known reliable calibration to identify and include any necessary corrections to the conversion with respect to the typical operational temperatures of SS495A in the robot hand under typical use as discussed in section.

6) *MagnetExpert N42 2 mm diameter, 1 mm thick cylindrical magnets - Jamie Sengun:* Magnets were required to be embedded within the soft skin material to

be displaced when a force is applied to the soft skin. This displacement causes a change in the magnetic flux density at the hall effect sensor located directly beneath magnet. Due to the dimension constraints on the links for the fingertip and subsequently the soft skin, the magnets chosen had to be sufficiently small enough to be fixed in place within the top surface of the skin. Having the magnet in this position removes the event that any initial skin deformation that does not displace the magnet when a force is initially applied. The retailer MagnetExpert was chosen due to their range of manufactured magnets. Neodymium magnets were chosen due to the fact that the smallest magnets were only available with this material. Neodymium magnets can range in their performance and are rated based off their maximum energy product with commonly used ranges between N35 to N52. N42 2 mm diameter, 1 mm thick cylindrical magnets were chosen for initial testing as were readily available by our project supervisor. Initial testing of these magnets with simulation software (FEMM) in section V-A and with a test material of similar dimensions to the designed soft skin in section V-B provided satisfactory results with a fully detectable range.

7) *Molex Picoblade Connectors & Wire - Jamie Sengun:* An alternative solution to using singular wires to bridge the connections between the I2C and power connections for the MLX90393 sensor PCBs and the microcontroller PCBs was required. This was due to the MLX90393 having fragile connection pads that could break off if the soldered wires were tensioned or pulled; which is very plausible. Molex Picoblade connectors and housings (Molex 51047-0400 & Molex 51021-0400) with 4 circuits and a 1.25 mm pitch were chosen due to their small dimensions 6.75 mm width, 8 mm length and 3.2 mm height allowing for the connector to be rigidly mounted within the fingertip structure providing a disconnect allowing for no tension on the wires between the MLX90393 PCB and the connector housing. A 50 m length spool of 0.62 mm insulation diameter 28 AWG wire was purchased for the Picoblade connectors due to the 1 mm insulation diameter size limit of the PicoBlade crimping terminals (Molex 50079-8000 & Molex 50125-8000) for the connectors. These crimping terminals are designed to be used with the Molex hand crimp tools (Molex 2002182000) to produce the best results according to Molex; however, they retail for £250+ each and are more suitable for large quantity batch usage to provide quick and repeatable crimps. For these reasons the use of these would be recommended in the manufacturing of large quantities of the final commercial product; however, for prototyping we purchased an alternative third party hand crimping tool called the Engineer PA-09 for £39.99 that is compatible with the PicoBlade crimp terminals used in this project.

8) *Murata SV01A103AEA01B00 - Jamie Sengun:* This item supports objective 3.1, 4.1. An axle based rotational potentiometer sensor was required to measure the rotational displacement changes of each joint on the robot hand for potential control and modelling use in RoS or however the user wishes. The desired sensor was specified to be sufficiently thin and similar in dimensions to the finger links to ensure that their implementation does not

drastically impact the overall design by creating links that were too thick or wide for the desired use case. Research into the current market did not show up many viable rotational potentiometers with replaceable axles that were within the desired dimensions; however, we found a suitable solution with the Murata SV01A103AEA01B00. Notable features are listed below:

- 4 mm diameter D-shaped thru-hole axle rotor. This enabled us to design and fabricate shafts for the sensors and the links to allow for a rotation coupling.
- Analog voltage output, readable by analogRead() on the Arduino or using an analog port expansion shield like the Velleman KA-12.
- Rotational displacement range of  $\pm 160^\circ$  with guaranteed linearity.
- Rated voltage input of 5 V. Easy to electronically integrate due to common voltage.
- Rated for a life cycle of 1 million rotation cycles.
- 12 mm length x 11 mm width 2.1 mm thickness.
- -40°C to +85°C operating temperature range
- Operational current draw of 0.5 mA. This low current draw enables the option for powering them via the Arduino 5 V output through the Velleman KA-12 Analog shield as discussed below.

The main disadvantage with this sensor was the surface mountable terminals that are too fragile for directly soldered wires and should be soldered to a rigid PCB. To overcome this issue an electronic PCB with stronger wire terminals was designed by us for fabrication by a 3rd party vendor as shown in section II-H. We looked into finding suppliers for standard length D-shafts that could be bulk purchased; however, we were unable to find any suppliers in the UK that were able to provide the lengths (As discussed in the design section). There were potential suppliers from China that could potentially be utilised in the final commercial design; however, due to prototyping time restrictions we decided to utilise the MakerSpace and workshop facilities at University to outsource the machining work required to make 4 mm D-shafts out of 4 mm Silver steel rods that were already in the possession of the MakerSpace. Silver steel is defined in BS 1407 (British Standards Institute) [43] as a high carbon steel that is typically used for tool parts due to its ability to be easily machined and shaped while providing high levels of wear resistance. Alternative steels or metal choices could be optimised in the future for the final commercial product. FDM 3D printed 4mm D-shafts were also trialled as they could provide potential time and cost savings; however, the printing tolerances on the available 3D printer proved insufficient for the design tolerances of D-shafts due to the small dimensions of the parts. The main issue with this method was the geometry distortion of the 3D printed shafts due to the fact that the printer was unable to print reliably at a sufficiently small resolution for this use case.

9) *Arduino Uno, Velleman KA-12 & Wiring - Jamie Sengun:* This supports objective 4.3. An Arduino was required for the 3D hall effect sensors as they utilise Arduino based libraries for their operation. An alternative solution was required since neither Arduino or Raspberry Pi boards can provide the 20 analog inputs required for

the rotational potentiometers and 1D hall effect sensors. Upon researching solutions we found more solutions for the Arduino in the form of self contained IO shields that could provide 20+ analog inputs, ground and 5 V power connections. The Velleman KA-12 analog input Arduino shield was chosen for exactly these reasons as it could provide 24 analog input ports using 4 Arduino pins (**D5, D6, D7, A0**) and was controllable using an Arduino library [44]. The provided pins on the KA-12 use the standard 0.1" or 2.54 mm pitch size. Due to this reason, 3 circuit 2.54 mm pitch connectors and crimping terminals were purchased to allow for custom length wiring using 26 AWG servo cable for improved cable management. It is known that there are other non-Arduino micro controllers on the market that utilise the Arduino IDE; however, there was no need or justification for using them as only basic functionality in the form of I2C and 20+ analog ports were required. The Arduino Uno was chosen as it was the smallest and cheapest Arduino option that could allow for the use of an analog IO shield and I2C ports as other features were not required. The analog input ports on the Arduino provide sufficient resolution as they have a 10-bit analog to digital converter which can provide 1024 steps ranging from 0 V to 5 V [45].

10) *Raspberry Pi 3B+ - Jamie Sengun:* This supports objective 4.3. A Raspberry Pi 3B+ using the Raspbian Linux distribution was chosen as the centralised controller for obtaining and processing all sensor data using Python scripts. The 3B+ was chosen over the Raspberry Pi 4, due to its support with ROS installations and having the next best technical specifications. Additionally, the included Wi-Fi and Ethernet provide good connectivity for a stand-alone solution that can be connected to remotely over a network. The USB is useful for connecting the ROBOTIS U2D2 for the AX-12A motor control, in addition to running the Linux variant of their Dynamixel Wizard 2.0 for programming the AX-12A motors.

11) *TFX Power supply unit & Power breakout board - Jamie Sengun:* A 300 Watt computer TFX DC power supply was chosen for the power distribution for this prototype as it is able provide multiple 3.3 V, 5 V and 12 V output up to a maximum current of 18 A to 20 A per channel. This current limit was sufficient for most current demanding scenario, where the 12 AX-12A servo motors could be loaded simultaneously between the standby and max draw currents of 50 mA and 900 mA respectively. These output voltage ranges were ideal for the project as all the electronics could utilise either one of these outputs directly. For example, the Arduino and Raspberry Pi required a 5 V DC input and the Dynamixel AX-12A servo motors required a 12 V DC input. This solution when combined with the Electronics-Salon 24/20 pin TFX power breakout board provided a cost effective solution that is versatile and can provide the end-user with several future power expansion options. The power breakout board is able to withstand up 24 A of current per PCB path and the screw terminal blocks allow for quick modifications to wiring. This avoids needing expensive external bench power supplies or several power supplies of different voltages or voltage regulators which are typically current limited and require extra wiring.

*12) PowerPro Braided Line 40kg (0.41 mm) - Jamie Sengun:* The main criteria for tendon choice for this project was:

- Capable of knots that are sufficiently strong and stable over a period of time.
- Sufficiently large breaking load strength
- Sufficiently thin diameter to be routed internally within the links.
- Low abrasion, as it will may rub in areas of the assembly; where long term exposure could cause damage to the structure of the hand or the tendon.

The PowerPro braided line was chosen as the tendon for our project due to its advertised 'near zero' (2% - 3% elongation) stretch and it's ability to create compact, high strength knots; depending on the knot style used. Additionally, a breaking load of 40kg was chosen to provide a safety margin over the capability of AX-12A motors that have a rated holding torque of 15 kg·cm, where spikes in the torque due to fast movements while handling an object could cause weaker tendons to break.

*13) Artic F12 120 mm Fan, Dust filter - Jamie Sengun:* A fan was required for providing a level of cooling to the wrist which houses all the AX-12A motors and various electronics and PCBs. A 120 mm Arctic F12 fan was chosen as it was cheap and could easily be powered by the Raspberry Pi 5 V output due to its low 0.1 A consumption. A dust filter was added to prevent internal dust build up that could hinder the cooling performance over time.

*14) Ecoflex Silicone Rubber - Kai:* This silicone was chosen to use as a material for the soft parts of the robot hand. The main reasons behind this choice is to pick a product that is easily producible and would be compliant to a certain degree to use as the soft skin for embedding the magnet. This had a shore hardness of 00-50 which allowed for a soft material that is still yet stiffness to not deform on its own. From research, the same product was tested which proved to work well in a similar circumstance [3]. The Ecoflex made it early producible as it requires a relatively short cure time, also allowing to cure at room temperature. Since this project has limited facilities, we were not able to vacuum degas or cure the silicone after moulding. In hindsight, this would have allowed for the material to be stiffer and not deform as much under force. It also has its advantages in a high tensile strength of 315 psi and the elongation at break percentage of 980%. This aids in provided a design that is able to withstand high tension under high load and stress.

*15) Araldite 2011 - Adhesive paste - Kai Page:* The Araldite was chosen as the adhesive to combine the soft skin with the fingertip parts. One of the crucial properties of the adhesive must be able to have high shear strength and high tensile strength. The shear strength is extremely important in gluing the soft skin, where the objects in manipulation may add shear force to the soft skin and cause movement. The data sheet in [46] shows that the adhesive has many advantages such as long working life, high lap shear strength with high strength and toughness. These qualities makes the Araldite suitable for this application. Moreover, the fact that this adhesive is able to cure in a short time (increasing cure time will result in higher lap shear strength) with an easy mix ratio of 1A:1B.

Hence, this allows for easier handling and preparation time, making the process easy and less time consuming.

*16) 3D Printing Material for Links, Palm and Wrist - Mohammed Al Bashar Khan:* Another of the aims and objectives for this project, was to produce a robot that was 3D printed. Therefore, the links, the palm and the wrist of the robot were all designed on cad, so that they could be printed out to the exact specifications. However, when choosing the material for 3D printing, the other limiting factors had to be considered. As mentioned previously, the robot was required to be low cost. Also, the weight of the robot needed to be kept low (less than 5Kg), to fulfil the objective of making it mountable onto a UR5 robot. This means that the material properties to be considered for the 3D printing materials are specifics stiffness and price. Since price is one of the features that needs to be considered, SLA printing needs to be discounted as an option. Whilst SLA printing does produce more refined results than FDM printing, the manufacturing costs are also much higher. With a material volume of 2879399.98 cubic millimetres in the wrist alone, the price of the material used must be kept as low as possible. Some of the FDM printing materials considered were ABS and Nylon. However, the final choice for the 3D printing material was PLA.

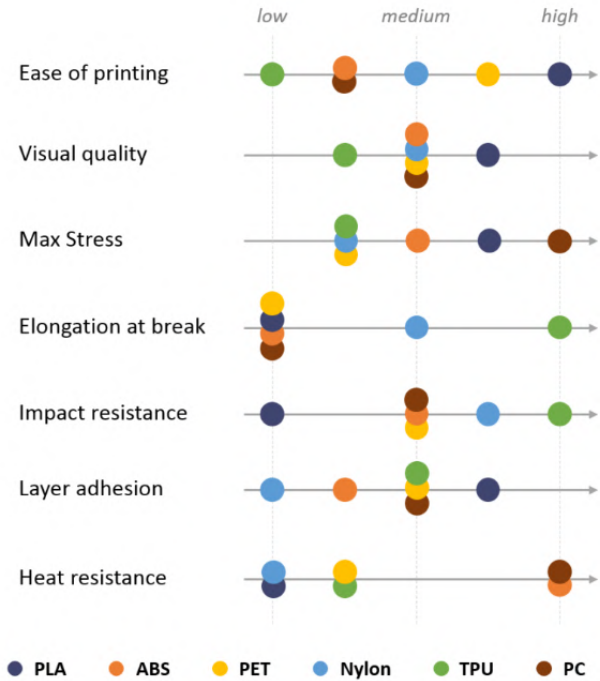


Fig. 138. Graph of different materials used in FDM printers and their ranking in terms of properties [47]

The image in Fig 138 shows the property comparison of different FDM printer materials. Of the materials that were considered, PLA consistently has the more desirable properties, such as max stress (which implies that the material is stronger and stiffer than the rest), layer adhesion (which produces a result of higher quality), and ease of printing (which is very important as there are so many components to be printed separately).

Table XI shows some of the properties of the different material being analysed [ [48][ [49]][ [50]].

TABLE XI  
THE DIFFERENT MATERIALS BEING CONSIDERED FOR 3D PRINTING,  
AND THEIR RELEVANT MATERIAL PROPERTIES

Property	Material		
	ABS	Nylon	PLA
Tensile Strength (MPa)	43.6	50.4	46.6
Elongation (%)	34	5.8	2.1
Elastic Modulus (MPa)	2030	510	3973

From the values shown in table XI, PLA is clearly the stiffest of the materials in consideration. Whilst the nylon has a greater tensile strength, the elastic modulus of PLA is much higher. Furthermore, most of the stress any of the components of the hand will endure is going to be compressive stress. Due to all these reasons the material used to 3D print the Components of the hand with is PLA.

### VIII. ELECTRONICS SCHEMATIC - JAMIE SENGUN

A general overview of the electronic schematics of the complete robot hand power and data connections is shown in Fig.139.

The size and weight of electronic components like the 300 Watt power supply and ATX power breakout board do not contributed to the overall weight of the hand & wrist combination as it can be placed remotely in an electronic enclosure that does not need to be mounted on the wrist. The wrist supports the hand structure and houses the AX-12A motors, Raspberry Pi, Arduino, TCA9548A I2C multiplexer, PCA9685A servo driver and 6 port AX/MX power hub.

### IX. ROBOT MOTOR & SENSOR SOFTWARE/LIBRARIES - JAMIE SENGUN

From this point onwards any mention of Raspberry Pi inherently means the Raspberry Pi 3B+. The Raspberry Pi was updated with NOOBS (New out of the box software) version 3.3.1 that uses Raspbian Buster (13/02/2020) [51]. Raspbian is a compiled version of the Debian Linux distribution optimised for the Raspberry Pi hardware.

The Arduino IDE on the Raspberry Pi was updated to Linux ARM 32-bit version 1.8.12 [52] as the Raspbian operating system is currently distributed in 32-bit variants despite the processor having 64-bit capabilities.

Python version 3.8.2 [53] was installed to the Raspberry Pi to allow for it to behave as the master controller for the entire system. The reasoning for using the Raspberry Pi as the master controller was two-fold. Firstly, it allows for the installation of RoS to create a centralised software solution for the software control and implementation of all motors and sensors to provide the end-user with a large potential for customisability and controllability. A direct benefit of this is the ability to implement Python scripts and functions directly into RoS for specific robot tasks like the sensor processing and motor control. Secondly, it provides a stand-alone solution that requires no external computer or controller and can be remotely accessed over a network connect using ethernet or Wi-Fi to allow for the user update software etc.

Dynamixel Wizard 2.0 software [41] was used on Microsoft Windows 10 to configure the Dynamixel AX-12A servo motors; however, there are Mac or Linux based variants available. Using the software, each motor was given a unique ID number between 1 to 12. The previously mentioned Dynamixel AX-12 settings were not changed from their default values as we did not construct the robot due to the COVID-19 situation. It is recommended to set the voltage limit to 12 V. The rotational displacement, rotational speed, maximum torque and compliance should be limited with functionality testing of the constructed hand with objects.

A folder hierarchy was created on the desktop of the Raspberry Pi to store all Python and Arduino code:

- Control\_code
  - Python
  - AX-12
  - Sensors
- Arduino
  - Arduino\_Sensors

The reader should note that all code created by the author has not been tested on the actual robot hand components as it was not possible to assemble and test it due to the quarantine issues surrounding the COVID-19. The code was designed with care taken in not introducing coding bugs; however, minor bugs may still exist and require further analysis in the future when the robot hand can fully be tested.

This supports objective 4.4, 5.1. Python scripts were created to control the servo motors using either user operable sliders for real-time manual position manipulation or individual scripts to control various motor parameters from other control software means like RoS. This script utilises libraries from multiple sources. The Zip file of the Dynamixel SDK from ROBOTIS-GIT at <https://github.com/ROBOTIS-GIT/DynamixelSDK> [40] was used to build a Python Linux based library as per the installation instructions found in [54] as shown below.

- 1) Download & extract the Zip file from <https://github.com/ROBOTIS-GIT/DynamixelSDK>
- 2) Navigate to the extracted **DynamixelSDK/python** folder and run the file **setup.py** using Python.

This step was completed first as it is a prerequisite for the Dynamixel AX12 control library created by Aary Kieu (ckkieu) at [https://github.com/ckkieu/dxl\\_control](https://github.com/ckkieu/dxl_control) [55] that utilises the Python language. The Zip file was downloaded and extracted into **Control\_code/Python/AX-12** folder. The variable on Line 10 **DEVICENAME='COM3'** within the file **Ax12.py** in the **Control\_code/Python/AX-12/dxl\_control** folder directory was changed to represent the serial port ID of the Robotis U2D2 device when it is connected to in the USB port of the Raspberry Pi. This serial port ID can be found using a variety of methods that are easily searchable on the internet and will not be listed here. This step is required for the AX-12 library to be able to connect with the Robotis U2D2. The sample code in the **dxl\_test.py** file was used as a reference point for creating the final six motor control Python scripts aimed at use within RoS. It was decided to create numerous scripts that each do specialised functions instead of having one

# Electrical Schematic - Overview

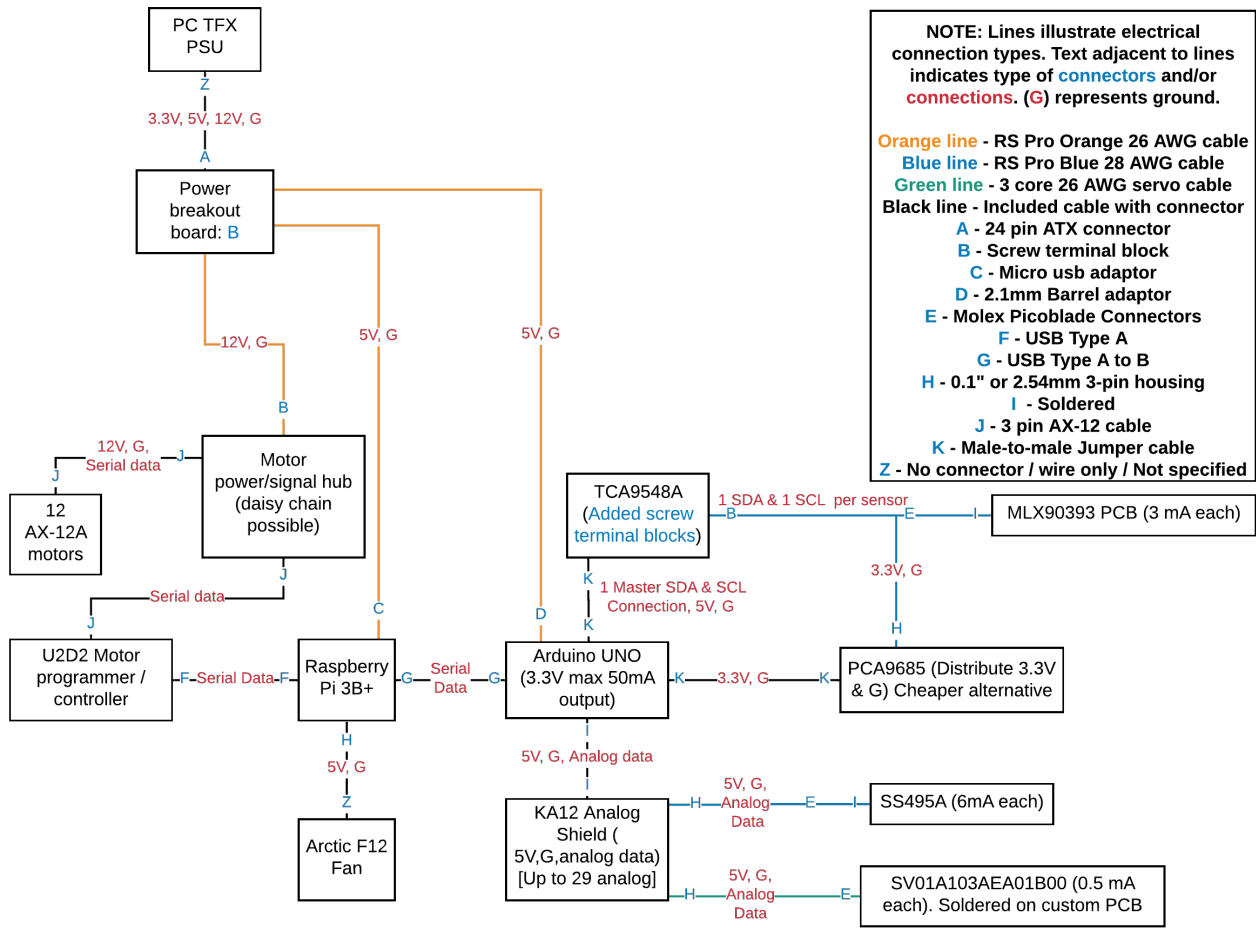


Fig. 139. Electrical schematic overview for the complete robot hand power and data connections

script with multiple functions for a number of reasons. Firstly, this level of modularity can be beneficial for future development, testing and reuse in other projects. Lastly, it allows the user to utilise virtual inputs and outputs in RoS for simulation and control at various levels of operation. The six motor control scripts created by myself as defined below are shown in listings located within the appendix. These six scripts were developed upon by Sami to finalise RoS implementation as discussed in section X.

- Connect all motors on the defined serial port. Connects to the Robotis U2D2 using the default serial port in Ax12.py using the motor default 1000000 baud rate. (Listing 3 - **(ax12\_open.py)**)
- Disconnect all motors on the defined serial port. (Listing 4 - **ax12\_close.py**)
- Enable motor torque on a user specified motor ID. (Listing 8 - **ax12\_enable\_torque.py**)
- Disable motor torque on a user specified motor ID. (Listing 7 - **ax12\_disable\_torque.py**)
- Individually set (Listing 5 - **ax12\_move.py**) and get the position (Listing 6 - **ax12\_getpos.py**) of each motor via the motor's ID and an angle in degrees between 0° to 300° mapped between 0 to 1023 to match the AX-12 library syntax - This range can and will be limited for each motor to prevent undesired

rotating that may cause damage to components. A default limited displacement of 90° from the resting position was chosen as a realistic estimate, however, pulley designs and values were not completely tested for as it was not fully built due to the COVID-19 situation. If a value outside of the limited range of the motor is request it is setup to do nothing by default until it receives a valid position.

Alternatively, **motorsliders.py** was created with manual user operation of the joint angles in mind. This script utilises the same AX control library as the previous six scripts. It creates a GUI with 12 sliders that can be moved from 0 to 1023; where the value of the slider is used to update the respective motor angle. This script is particularly useful for quickly testing grasps with manual manipulation rather than using ROS. This script is shown in more detail in Listing 9 in the appendix.

Arduino IDE libraries for this project were imported into Arduino using their respective Zip files. This was done by opening the Arduino IDE and navigating to the toolbar at the top and using **Sketch-Includelibrary-Add-Ziplibrary** to import the Zip files for each of the libraries.

The Velleman KA-12 Arduino library was downloaded from the manufacturer at [https://www.velleman.eu/downloads/files/downloads/velleman\\_ka12.zip](https://www.velleman.eu/downloads/files/downloads/velleman_ka12.zip) [44] and

imported into the Arduino IDE. This library provides the ability to analog read up to all 24 analog devices connected to the KA-12 shield.

The Melexis MLX90393 Arduino library developed by Theodore Yapo (Tedyapo) was downloaded from <https://github.com/tedyapo/arduino-MLX90393> [56] and imported into the Arduino IDE. This library is capable of implementing the majority of the features outlined in the MLX90393 datasheet [57]. For example, variable sensitivity ( $\mu\text{T}/\text{LSB}$ ) through variable analog gain (*GAIN\_SEL*) and resolution (*RES*). Additionally, temperature compensation (*TCMP\_EN*) is available and variable rate sampling is possible through variable oversampling (*OSR*) and signal filtering (*DIG\_FILT*). However, increases in rate sampling provide increases in noise in an exponential manner as the conversion time approaches 0 ms from positive duration. Details on how these variables work exactly are discussed in section VII-A and can be found in more detail listed in the MLX90393 data sheet for reference [57]. Unfortunately, we were unable to optimise the sensor settings and test the performance of the MLX90393 on the final prototype robot hand with the soft skin due to the COVID-19 situation. We were able to initially test the MLX90393 with a soft material with an embedded magnet to familiarise with the features of the sensor. We found that settings in listing 2 provided a sufficient sample rate of 50 ms or 20 Hz and sensitivity with minimal signal noise. However, it is probable that this will need further analysis in the future with the completed prototype to reach an optimised compromise between the noise and sample rate for implementation into future control algorithms.

```
mlx.setGainSel(0); //GAIN_SEL, change
    analog gain
mlx.setResolution(0, 0, 0); //x, y, z
    , RES, alters the resolution
mlx.setOverSampling(1); //OSR ,
    alters the oversampling rate
mlx.setDigitalFiltering(7); ///
    DIG_FILT, alters the digital
    filtering severity
mlx.setTemperatureCompensation(1);
    //TCMP_EN, Enables or disables
    temperature compensation on
    magnetic flux readings
```

Listing 2. MLX90393 settings for the Arduino code

This next section supports objective 3.5, 4.2, 4.4. The Arduino IDE code for the 3D hall effect MLX90393, rotational potentiometers and the 1D Honeywell hall effect sensor is shown within Listing 10 in the appendix. This code utilises the Velleman KA-12 and MLX90393 Arduino libraries to loop periodically to group the sensor output data into a string and forward it to the serial output for the Raspberry Pi when requested to complete further data processing. The user will need to specify how many analog sensors and I2C sensors are present by changing the variables *num\_ana* & *num\_3d* in the code **Arduino\_Sensors.ino**. For continuity between the Arduino and Python code it is recommended that the rotational potentiometers should be wired and referenced

from analog port 1 on the KA-12 shield, followed by the analog 1D sensors and then by the MLX90393 sensors that use the TCA9548A I2C multiplexer while recording the exact order. An optional time delay has been added to the end of the loop should the user wish to limit the update rate of the sensors. It is currently unknown if there may be bandwidth issues utilising one Arduino to request data from 18 analog ports and 3 sets (X, Y, Z) of data from 3 I2C sensors due to not being able to build the full assembly and test its capabilities due to the COVID-19 situation. If it is found that the analog sensors are causing a bottleneck in the MLX90393 request rate with one Arduino then it is recommended to separate the MLX90393 I2C data gathering to a second Arduino to maximise the request rate should the Raspberry Pi be capable of facilitating that level of throughput. However, this is subjective and would require real-world testing with the assembled robot hand.

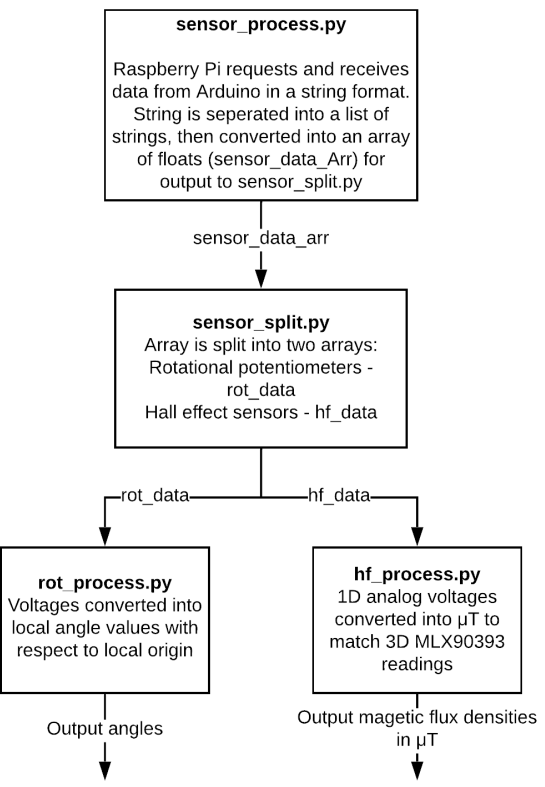


Fig. 140. Flow diagram of pseudo code representing the Python scripts for obtaining serial data from the Arduino and processing it for use in downstream control methods.

The flow chart shown in Fig 140 outlines the logic pathing for sensor data received by the Raspberry Pi from the Arduino. The code for each of the mentioned scripts is shown below in the defined listings in the appendix. These Python scripts were further developed upon by Sami to finalise RoS implementation as discussed in section X.

- sensor\_process.py** in Listing 11
- sensor\_split.py** in Listing 12
- rot\_process.py** in Listing 13
- hf\_process.py** in Listing 14

Upon calling **sensor\_process**, the script clears existing serial connections and opens a serial connection on a specified port to the Arduino. The default serial port

for line 36 and line 37 should be changed by the user to represent the serial USB port that the Arduino is connected to in a similar manner to the Robotis U2D2. It will then start the Raspberry Pi serial data request from the Arduino by utilising the internal function `ser_loop`. On line 40 there is a variable called '`csv_record`' that can be changed to either '`yes`' or '`no`' to enable or disable data logging to a CSV file in the My Documents folder without using RoS for logging. If neither of these variables are provided for '`csv_record`' then it will cease running the code. Additionally, there are variables '`num_rot`', '`num_1d`' and '`num_3d`' on lines 46, 47 and 48 respectively in `sensor_process.py` that must be changed to represent the number of rotational potentiometers, analog 1D hall effect sensors and MLX90393 3D hall effect sensors connected to the Arduino to match all other Python and Arduino scripts/code in `sensor_split.py`, `rot_process.py` & `hf_process.py`. These variables are used for data processing and error checking on the imported serial data to determine if all the sensor data is present to avoid incorrect data streams assignments for sensors that would create invalid readings for sensors. If the code receives an invalid number of data streams per request data string, the code will ignore it and continue requesting more data. For each data request loop, the Arduino is told to clear its buffer cache to prevent the build up of a set of older data outputs that were not forwarded to the Raspberry Pi due to the request rate being slower than Arduino sensor sampling rate. This means that the request rate limit is independent up to the maximise sampling rate of the Arduino for the sensors. The request rate should not be faster than the Arduino sampling rate in practice to avoid incomplete data; however, the error checking in the Python code will activate and ignore requests with no data. The request rate can be moderated by changing the '`time.sleep`' value on lines 59 and 63. It was set to 0.01 seconds for initial testing; however, it requires further testing with the constructed final product to find an optimised setting. Unfortunately, we were unable to build it due to the COVID-19 situation. The `sensor_process.py` script firstly converts the requested string of sensor values from the Arduino into a list of strings. The list of strings is then converted into an array of float values in an output variable called `sensor_data_arr` that can be forwarded to `sensor_split.py` to split the array into two separate arrays, one for all rotational potentiometers `rot_data` and one for all hall effect sensors `hf_data`. `rot_data` and `hf_data` are output to `rot_process.py` and `hf_process.py` respectively for converting the raw data voltage values from the analog sensors; rotational potentiometers and SS495A sensors into an angle in degrees and a magnetic flux density in  $\mu\text{T}$  respectively.

For `hf_process.py`, the output voltage values from the SS495A sensors between 0.2 V to 4.8 V (5 V supply) are mapped to the typical magnetic flux density output range between -67000  $\mu\text{T}$  to 67000  $\mu\text{T}$  as defined in the datasheet [58] as shown in the code in appendix Listing 14.

For `rot_process.py`, the output voltage values from the Murata SA01 rotational potentiometers between 0 V to 5 V (5V supply) are mapped to the reference angular range output between -166.65° to 166.65° as defined in the

datasheet [59]. The datasheet defines guaranteed linearity between  $\pm 160^\circ$ , so all angular displacement ranges for the joints on the robot hand were designed to operate within this limit.

KA-12 ports are as defined for rotational potentiometers (ROT), J1 is the base joint and J2 is the middle joint and J3 is the fingertip joint:

- Little finger link joints: J1=1, J2=2, J3=3
- Ring finger link joints: J1=4, J2=5, J3=6
- Middle finger link joints: J1=7, J2=8, J3=9
- Index finger link joints: J1=10, J2=11, J3=12
- Thumb opposable joint: J1=13
- Thumb AA joint: J2=14
- Thumb link joints: J3=15, J4=16

All joint angles for ROT 1 to 12 and 15 to 16 have a local coordinate frame that is defined when looking at the palmar side to be fully extended ( $0^\circ$ ) to fully flexed ( $90^\circ$  etc). The raw rotational potentiometer angles; fully extended to fully flexed respectively, shown in the list below are mapped to the defined local coordinate frame of fully extended ( $0^\circ$ ) to fully flexed ( $90^\circ$  etc).

- Left side raw potentiometers output for J2 on all fingers; not including thumb = fully extended ( $-90^\circ$ ) to fully flexed ( $0^\circ$ )
- Right side raw potentiometers output for J1 and J3 on all fingers and 2 thumb links = fully extended ( $90^\circ$ ) to fully flexed ( $0^\circ$ )

All 1 to 12 and 15 to 16 link rotational potentiometers are converted as they all start at  $-90^\circ$  or  $90^\circ$  as shown above, so the absolute values are the same as they approach  $0^\circ$ . Joints have been designed to have a max displacement range of  $90^\circ$ . The displacement range will be controlled by testing and programming the AX-12 motors. ROT 14 has a range of  $60^\circ$ , from potentiometer readings of  $30^\circ$  to  $-30^\circ$ , mapped between  $0^\circ$  to  $60^\circ$  respectively. ROT 13 has a range of  $90^\circ$ , from potentiometer readings of  $0^\circ$  to  $-90^\circ$ , mapped between  $0^\circ$  to  $90^\circ$  respectively.

It has been configured such that all potentiometers; except the Thumb AA joint will output either all positive or negative angles that are then converted to their absolute values. A displacement range greater than  $90$  degrees is not required for the desired functionality, so a more complicated solution involving both positive and minus values from a potentiometer was not required.

The maximum loop rate or polling rate of the `sensor_process.py` on the Raspberry Pi and `Arduino_Sensors.ino` on the Arduino Uno are not known as we were unable to fully test the final version of the code on the Raspberry Pi and Arduino Uno due to not being able to get access to them due to the COVID-19 situation. Estimations on the loop rate of the Python code on other hardware other than the Raspberry Pi is invalid due to the differences in hardware performance, and so it has not been estimated. Variables time delays have been added to these codes to allow for a customisable update rates at the user's discretion upon further testing.

## X. ROS PACKAGE - AHMED SAMI DEIRI

A Robotics Operating System (ROS) package was created to control the robot hand, providing an interface

between the ROS ecosystem and the physical hand. The programs within the package are either modified versions of the python scripts discussed in section IX or new programs. This package could be found at <https://github.com/sam-eee/jamkit>

The package aimed to encourage future development on the hand by providing a cohesive package that could be used to gather input data for processing, and/or communicating with the motors to provide actuation to the hand. The input data was processed within the script, however the strong focus on the use of a modular architecture allows a user to access data from the hand at various levels of abstraction for different applications. By focusing on modularity within the package we can ensure that future work can be easily implemented through the use of nodes and the various communication methods within ROS.

#### A. Generating the Simulation Model - Ahmed Sami Deiri

To import a kinematic and simulation model of the hand for use within ROS, it was necessary to generate a Unified Robot Description Format (URDF) model of the robot hand. URDF is an XML format used to represent a robot model. To do this I had 3 possible routes:

- Use a URDF export tool for Autodesk Inventor
- Manually develop the URDF Model.
- Use a URDF export tool for Solidworks

Initially I attempted to use the Autodesk Inventor URDF export tool RoboVerter [60] developed by EntelechySolutions. This tool did not work with the robot hand and was designed for much more simple models.

The next approach considered was creating the URDF and the meshes manually. This method was determined to be too time consuming given the number of degrees of freedom, and the curve along the palm and the finger mounting slots (see Fig. 30). The curve resulted in a model with a somewhat hard to define structure, and given the number of parts involved, the automatic nature of the solid works exporter was deemed to be preferable.

Therefore the next approach was to attempt using the the URDF exporter developed for the SolidWorks suite. There were difficulties experienced with moving the assembly from Autodesk Inventor to Solidworks as it had to be done manually. Initially I exported every link assembly as a single step file, however that appeared to break the assembly, however the .sat format appeared to maintain its structure when imported into Solidworks.

After re-creating the hand assembly and defining all the relevant mates and limits, the URDF exporter was used. The URDF exporter required declaration of parameters on the model. Firstly, the structure of the hand was declared through a set of parent-child relationships between the different links (ie parts/assemblies) as seen in Fig. 142. The joint relationship between each child and parent was then declared, specifying the type of joint, limits and maximum properties such as max velocity and mass of each link. After following the export process (and all the issues discussed in section X-B), the URDF model and mesh were generated. The URDF model can be seen visualised in Fig. 141. The model sets the bottom center of the wrist assembly as the base coordinate frame/origin. This enables

us to easily modify the model when its mounted onto a surface/robot arm for a new global coordinate frame if needed.

The URDF export add-in for Solidworks outputs the model as a ROS Package containing the URDF model, and the meshes for the robot hand (STL files for 3D modelling). The ROS structure using `rqt_graph` for this package can be seen in Fig. 143. The package is dependant on Gazebo, RVIZ and the `robot_state_publisher` and `joint_state_publisher` packages. The joint state when running a simulation is published onto the `joint_state` topic. In this configuration, the `robot_state_publisher` subscribes to the `joint_state` topic and publishes the 3D poses of the robot links.

#### B. Simulation of Model - Ahmed Sami Deiri

When exporting the robot hand the export would keep failing (see Fig. 144).

A lot of time was spent debugging this setup, with me manually checking all the URDF parameters, checking the assembly within Solidworks, inventor and trying to fix any possible issues that might arise. After days of debugging, the exported assembly was deemed to be a likely cause for these failures. I attempted techniques such as converting the link assemblies into single rigid parts, or exporting them as .STL files manually and manually adjusting the URDF to align the mesh correctly which did not work as there appeared to be an error with the exported mesh, however the error could not be narrowed down to its specific cause. The best output from this can be seen running in gazebo in Fig. 145.

After rebuilding the entire assembly from scratch within Solidworks, the URDF output was correctly representative of the robot hand, however, the mesh remained faulty when trying to re-assemble the model as seen in Fig 146. This process was very time consuming and resulted in a lot of wasted time which could have been spent implementing more scripts within the package, however, it was seen as a key target due to it contributing to the real time simulation of our hand within gazebo, as well as it being necessary to create the accurate Mujoco dynamic modelling and analysis. This failure and my attempts to fix that resulted in a relatively barren package due to time constraints.

This resulted in us not being able to continue with the following steps

- MoveIt Integration
- Joint limit analysis and fixing (the 0 degrees for each joint is not consistent)
- Integration of the model within the ROS package for modelling of the robot hand

#### C. Simulation of the Proprioceptive Values - Ahmed Sami Deiri

The link angle is collected using the potentiometers as discussed in section II-H. The potentiometer provides the position by varying the resistance and therefore the voltage value into the Analogue inputs on the KA12 Arduino Shield. The analogue voltage measurement can be used with an awareness of the resistance range of the potentiometer to determine the joint state. The python

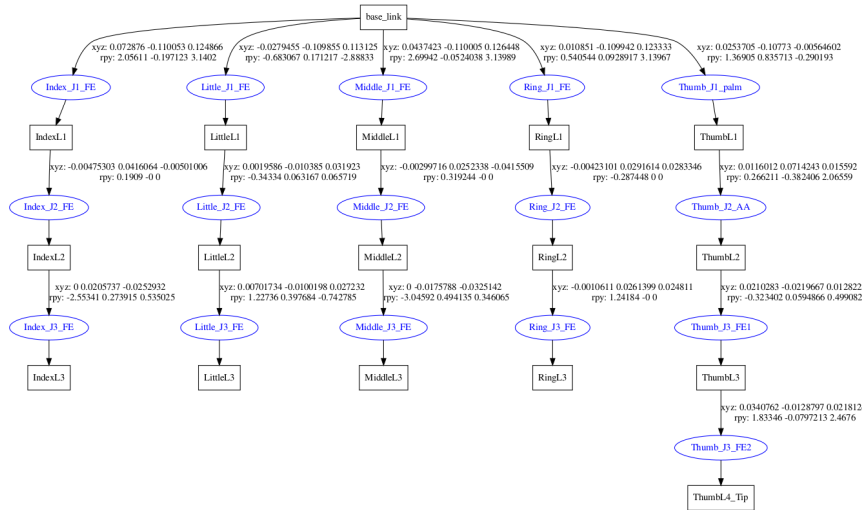


Fig. 141. Visualisation of the URDF model of the robot hand generated by the urdf\_to\_graphviz function. This diagram shows the hierarchy of the URDF model, with each finger shown as an open chain structure. Links are illustrated by the rectangular boxes, with the joints being represented by the circular boxes. The hierarchy starts at the base link which includes the palm and wrist assembly, which is connected to 5 child links for the first link of each finger. Each finger is made of three links, except for the thumb which has 4 links. The origin of this model is declared to be the bottom center of the wrist assembly.

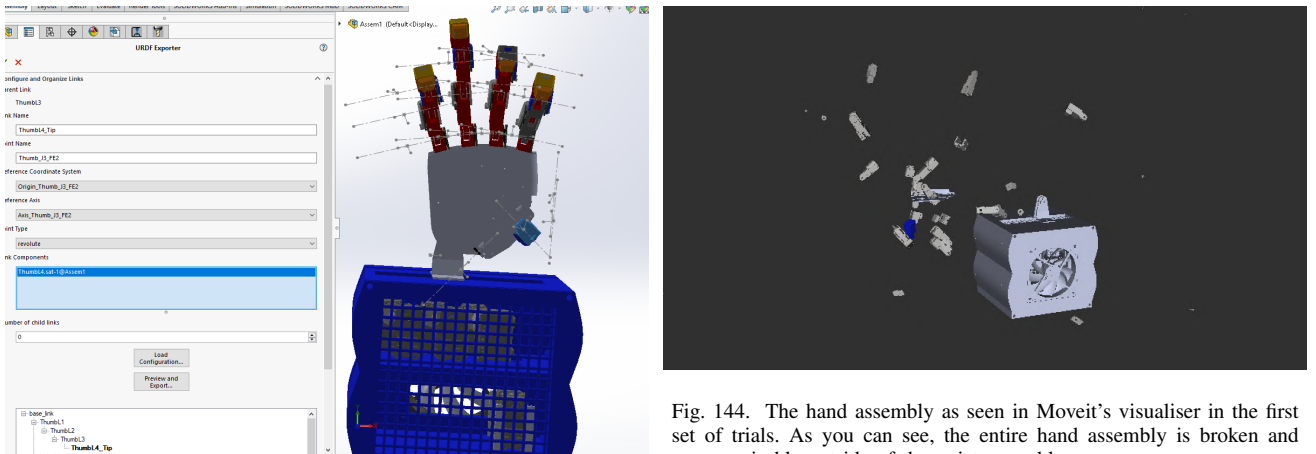


Fig. 142. Screenshot of Solidworks showing the joint axis, coordinate frames and the user interface provided for selecting the parent/child link structure

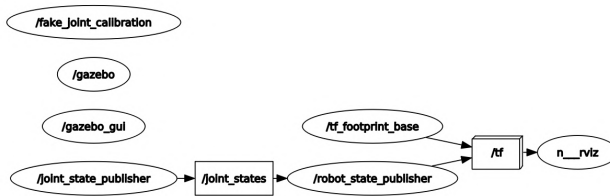


Fig. 143. Visualisation of ROS computation graph using rqt\_graph of the package created by the Solidworks export tool with both Gazebo and RVIZ running.

scripts discussed in section IX were modified to work within the ROS ecosystem. A node sensor\_process is initiated, which based on the sensor\_process.py developed by Jamie, aggregates the input voltage for the fingertip 1D sensors + potentiometers, and the digital sensor values from the 3-axis hall effect sensors. This is done in the

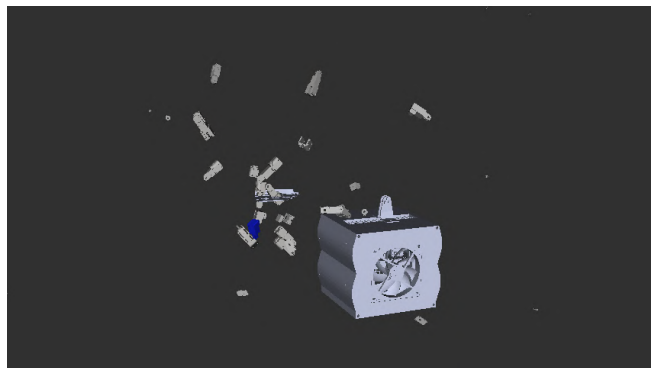


Fig. 144. The hand assembly as seen in Moveit's visualiser in the first set of trials. As you can see, the entire hand assembly is broken and unrecognisable outside of the wrist assembly.

form of a single float64 array containing the values for each sensor within a pre-set array position. This array is then published by the node onto the topic /hand\_sensing\_output.

The node sensor\_split receives an array containing all the sensor values as float64 values, and splits the sensor input value array into two arrays, one containing the fingertip sensor values which is published onto the topic /force\_raw, and the second array containing the recorded potentiometer values for all the joints: rotation\_raw. The nodes hf\_process and rot\_process subscribe to these topics respectively, and will process the values. The hf\_process node will receive the fingertip sensor values for processing, publishing them to topic /correctedfingertip, while the rot\_process will receive the pin values for the potentiometers and process the array, publishing the joint angles to the topic /correctedjointangle.

#### D. Controlling the Motors - Ahmed Sami Deiri

The ros package dynamixel\_motor was installed was installed. A program called motor\_ctrl.py was created

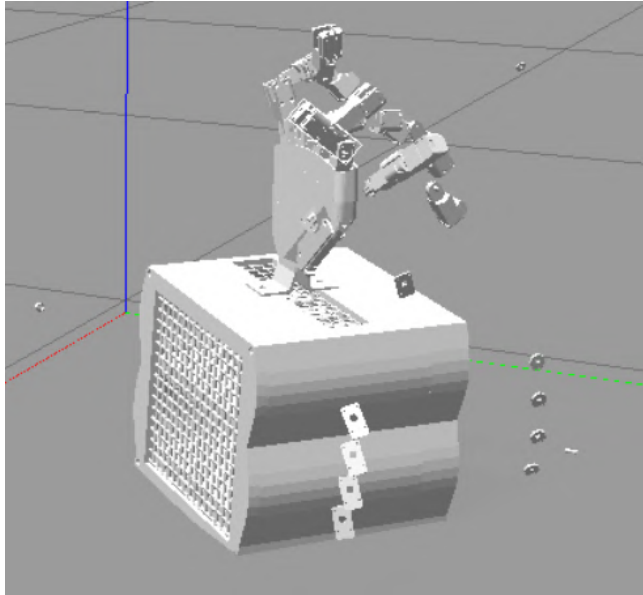


Fig. 145. Shows the imported model within gazebo after attempted rebuilding manually through modification of the URDF file and manual export of STL files for any broken link assemblies.

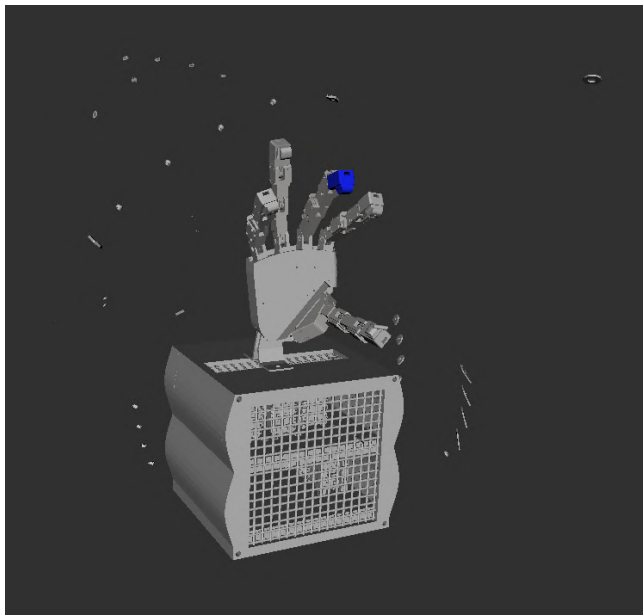


Fig. 146. Shows the best mesh and URDF export result achieved as a result of rebuilding the entire assembly within Solidworks. As you can see, the main link assemblies appear to be in the correct places, however there are still sub-parts such as washers that appear to not be fixed to the hand, and are scattered around instead.

to work in conjunction with a modified version of the motor control software developed by Jamie as discussed in section IX. Motor\_ctrl.py creates a node called motor\_ctrl which subscribes to the topic desired\_motor\_position. This could be used to provide simple motor control as the desired motor position could be output to the motor directly with the motor firmware handling the path to the goal.

A ROS service called motor\_utils was created which allows a node to request motor present values such as:

- Connection status
- Current position

- Speed
- Moving speed to goal
- Load on motor
- Motor Temperature
- Motor Voltage
- Torque Limit
- Current state of motor (moving or static)

#### E. Setting a zero position for the hand - Ahmed Sami Deiri

In traditional robotic systems, especially when calibrating the system without access to accurate absolute encoding, having a way to "zero"/calibrate the system is essential for the efficient performance of the system. This is often done by using limit switches or contact switches that will send a signal when a certain position is reached. The AX-12 motors have the ability to measure the load applied, which we can use to provide a method of calibration and setting our maximum and minimum rotations without manual intervention. A script called calibrate\_hand\_angles.py would be created.

The script would run when the robot hand is first powered on. Each motor would rotate causing the fingers to flex until a load threshold is met. Once this is met, the current position is set as the maximum flexion motor position. The motor then rotates in the opposite direction until it a threshold in load is met which indicates the finger is at maximum flexion. The motor is stopped and the position is saved as the maximum flexion position.

Given the design of the robot hand provides rigid limits at set angles (see Fig. 34, we are able to accurately determine the maximum flexion and extension positions at each link. This could be used to calibrate the new max/min values for each of the potentiometers. This can therefore correct for any inaccuracy in the resistance of the potentiometer due to manufacturing tolerances etc., as the new maximum and minimum input voltage could be used in conjunction with the known hand geometric limits to calibrate all the potentiometers.

## XI. EVALUATION & FUTURE WORK

The hand design could not be manufactured and tested through traditional means due to the COVID-19 crisis, and thus many objectives could not be physically tested. However we have tried to use alternative methods of testing or proof to try and meet them or reach some result regarding them. Most of these conclusions and discussion can be seen in section I-C.

### A. Manufacturing

We were able to carry out this project by utilising 3D printing for the main structure of the hand, wrist, power enclosure and moulds for the creation of silicone soft skin. The final hand was built with modularity in mind for easy maintenance part replacement. This was done by the achieving modularity through consistency in design of the fingertips, links and palm designs.

For the assembly, the design utilised easily accessible temporary joints such as bolts, with a minimal reliance on adhesives. The only parts utilising permanent adhesive for joints rather than temporary joints would be the



Fig. 147. (Will be replaced with rosgraph of final) Visualisation of the sensor processing structure using rqt\_graph.

silicone for the fingertips, which were adhered to the 3D printed fingertip assemblies using the two part epoxy resin Araldite® 2011.

All printed parts were also designed with the 3D printing process in mind. We achieved this by minimising or removing the need for support structures to reduce material cost, print time, post-processing and assembly time. The use of 3D printing does provide us with the ability to make rapid changes to the design; however, the production output of 3D printing is linear in the sense that to increase production more printers must be added.

Alternatively, some parts of the hand could be converted to be manufactured through injection moulding if a very large volume of parts was required; where the production rate can be exponentially increased. However, changes to parts would require retooling which is expensive and time consuming.

Alternative manufacturing processes discussed in the SOTA report, such as SLA or Direct Metal Laser Sintering (DMLS) would likely provide more interesting material choices with higher tolerances than FDM 3D printing, with DMLS allowing for metallic components. This could be an interesting process to explore further in future papers. However, this process was omitted primarily due to lack of availability and significantly higher costs involved.

SLA often utilises thermoset plastics where a resin is selectively cured, often using UV light. This can be used to provide more thermally stable parts with higher tolerances, surface finish, and resolution. However, use of this would result in issues such as the inability to heat weld the threaded inserts into the parts, longer manufacturing times, less material choices. The manufacturing process for SLA is also much more intensive in terms of labour, requiring post printing curing and cleaning. For our design FDM 3D printing was determined to be ideal for the links and body, however the use of SLA could allow for much more compact and complex design structures with the limiting factor being the components such as the potentiometers used.

Lastly, laser cutting out of preformed plastic sheets could be used to provide rapid cutting of simple shaped parts to reduce the demand of 3D printing usage; this could increase the production rate of these parts at a reduced fixed cost compared to 3D printing.

The power enclosure was designed with uniform wall thickness to be initially 3D printed for the prototype. However, utilising 3D printing for up scaled production rates to manufacture this part is not feasible due to the cost per part. Due to the simple geometry of this part, it could be segmented into laser cut parts and assembled manually. The use of a laser cutter or using a laser cutting service could rapidly increase the production rate of this

component and reduce costs if done in sufficiently large batches, although limitations may arise due to the 2D nature of laser cutters, so parts may have to be redesigned to accommodate for the process.

This could also be done to the link design, with the link body design being capable of manufacture through layers connected by a temporary or permanent joint such as a bolt or adhesives. This can be achieved as the design does not utilise many complex shapes along the horizontal plane. The issue with this in the current design is the inconsistent thickness, however, if a 0.8 mm plastic is used we could manufacture the same link body design with minor modifications.

For manufacturing of the soft skin we did initially look into SLA printing; however, the turnaround time of up two weeks and accessibility of the SLA printing facilities at Queen Mary University proved to be time inefficient after two attempts as the deadline was approaching in semester B. An alternative manufacturing method using silicone moulding was chosen to create the soft skins. The process requires mixing reagents, pouring in a mould and waiting for the cure time. This process can be scaled up easily by creating numerous mould blocks for making skins. However, this method requires a large amount of labour to remove the skins from the mould and post-processing to remove the flashing. SLA printing would provide additional benefits in making micro structures and geometries that would be impossible with the silicone moulding process, which could provide more complex behaviour that could be tweaked for the desired application.

1) *Weight*: The estimated weights of the different parts of the hand were calculated in Tables XIII, XIV, XV, XVI, XVII, with a summary seen in Table XII. The hand is comprised of a power enclosure which is mounted remotely as discussed in section II-V, and the wrist and hand assembly which is ideally mounted on the robot arm. The primary weight of concern is the weight that will be mounted on the robot hand, which is calculated to be 2.691 kg, which is predominantly the weight of the wrist assembly.

By looking at the weights within the wrist assembly as seen in Table XVI, we see 63% of the weight being formed by the 3D printed frame at 1.48 kg at 20% infill. The current design of the wrist contains large sections of 3D printed parts that should be optimised further to reduce the weight. FEM analysis may be required to optimise this structure further.

In terms of weight reduction within the hand itself, we could achieve a 14g reduction as discussed in section II-M. Due to the small structure of the fingers, optimisation performed within the fingers/wrist would provide relatively small improvements in weight capability. Due to

the parts being 3D printed, we could do an FEM analysis of these parts to optimise them for the expected loads and removing material where it is not needed, however this is not necessary due to the payload capabilities of the UR5 robot arm exceeding the weight of the hand and the likely maximum payload.

TABLE XII

CONTAINS THE ESTIMATED WEIGHTS FOR THE DIFFERENT PARTS OF THE ROBOT HAND, WITH MORE DETAILED BREAKDOWNS SEEN IN THE APPENDIX TABLES XIII, XIV, XV, XVI, XVII.

Part	Total Weight (g)
Fingers (excluding thumb)	202.32
Thumb Assembly	66.86
Palm Assembly	81.00
Wrist Assembly	2341.30
Power Enclosure	2033.57
Total Hand (Fingers+Palm)	350.18
Total Hand + Wrist	2691.48

To meet the weight conditions of the UR5 robot arm, we can look at Fig.148, which is taken from the manual for the UR5 robot arm. The diagram shows the maximum payload the robot arm can handle based on the displacement of the center of gravity of the end effector/payload. The entire mounted assembly (hand and wrist) has an approximate center of mass of 153.60 mm from the mounting plate. Our hand's grasping position is at approximately 355 mm from the mounting plate as illustrated in Fig.149. This means that we should be able to extract the full 5kg payload out of the UR5, leaving us with a an excess UR5 payload capability of 2.31 kg (as the hand weighs 2.69 kg). This exceeds the lifting capability of the hand and therefore we can ignore any limitations posed by the UR5's weight capability in our hand behaviour within that margin. Assuming the grasped load is at 2.31 kg at the 355 mm grasping distance, the center of gravity for the hand + load would still be 246.58 mm.

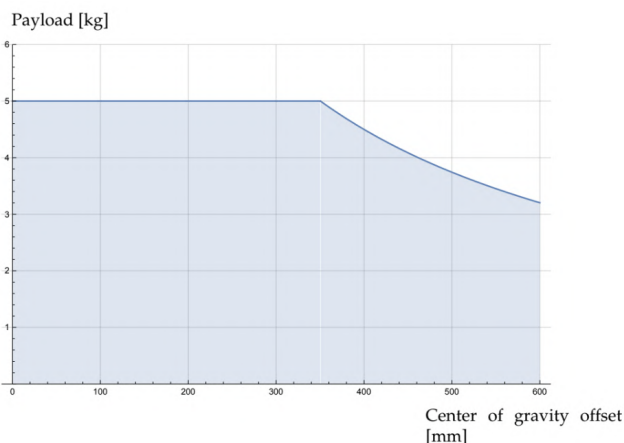


Fig. 148. Relationship between the maximum allowed payload and the center of gravity offset. Taken from the UR5 User manual [61].

2) **Size:** The robot hand has a maximum height of 500 mm when fully extended, with an approximate vertical distance between the mounting plate and the grasping position of 355 mm, as seen in Fig.149. The wrist box is 195.4 mm x 214.7 mm x 186.5 mm (D x W x H).

Attaching the mounting plate increases that to 230 mm x 214.7 mm 235.4 mm.

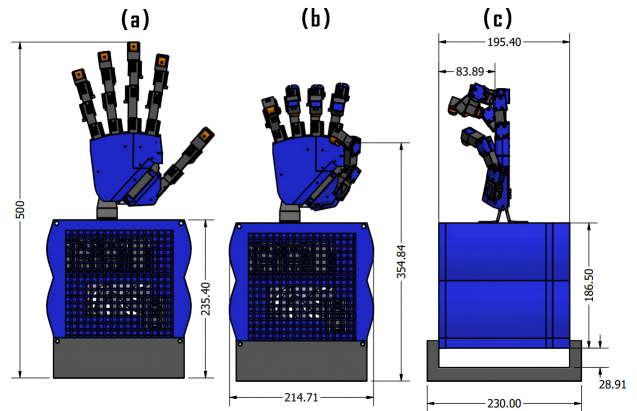


Fig. 149. Hand Dimensions.

The hand is able to mount onto the UR5 as seen in Fig. 150, however, due to the large size of the hand and wrist assembly, we do see limitations in terms of the movement of the robot arm as seen in Fig.151 and Fig.152. This results in a limited configuration space for the system compared to a UR5 robot arm, which could result in new singularity configurations that would need to be accounted for.

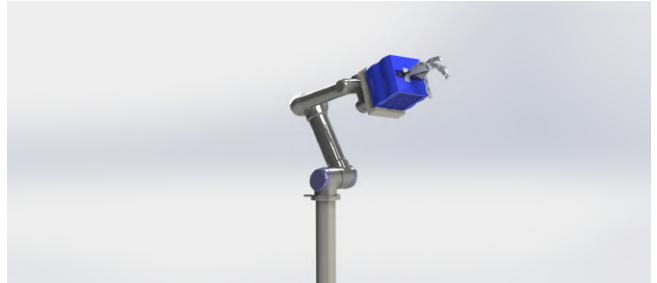


Fig. 150. Render of the developed assembly mounted onto a UR5 Robot arm.

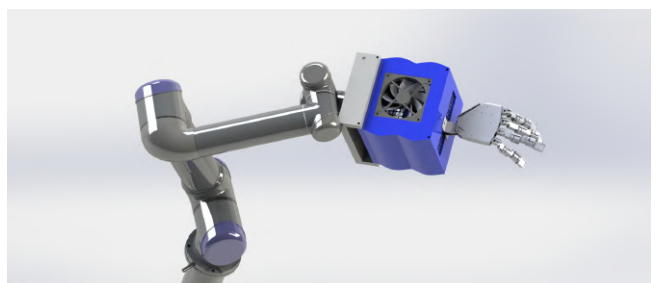


Fig. 151. Render of the robot hand assembly illustrating limitations in motion due to collision with the 4th link along the UR5 robot arm.

3) **Maintenance, Customisability and Repair:** The silicone fingertips while requiring moulding, were easily made through silicone casting in an FDM 3D printed mould. The silicone fingertip required minimal post processing before it could be adhered to the fingertip. While permanently jointed, the silicone fingertip is adhered to a small FDM 3D printed piece which could easily be remade and replaced for upgrades, or due to wear and tear.



Fig. 152. Render of the robot hand assembly illustrating limitations in motion due to collision with the 3rd link along the UR5 robot arm

For this prototype, the D-Shafts used within the finger link joints required the use of manufacturing equipment due to the lack of domestic availability of the part. However, this part is generally commercially available in larger quantities from suppliers such as AliExpress [62] for lower cost if manufacturing them is not a viable option.

#### B. Performance

In terms of performance, these metrics were difficult to evaluate through testing as the hand was not manufactured. The bio-mimetic aspect of the project had taken a decreased focus in comparison to the other performance metrics such as in hand manipulation, grasping and modelling/control capabilities. Bio-mimetic designs pose very interesting challenges for the design for artificial robot hands, but in order to balance our aims and objectives we disregarded highly bio-mimetic designs, and instead opted for a design that aims to optimise a robot hand for the types of movements performed within our other aims and objectives.

*1) Link Lengths:* An important aspect to note in the performance of the robotic hand is determination of the lengths of links, aiding to the lengths of the fingers and the overall hand. In this project, we evaluated the lengths of each link by using algorithms from previous literature and modelled it to perform in hand manipulation to achieve our aims and objectives. This has proved successful as the hand is able to manipulate power grasps as well as precision grasps. However, this approach can be limiting as the modelling of a robotic hand may perform in varying ways depending on its designs. Hence, in the future, it would be best to compare and contrast experimental results on how the fingers grasp objects with respect to different finger lengths. From this, it would be possible to gather more accurate lengths that would work specifically for the designed hand. Due to remote working, we were unable to perform any physical testing of the hand.

*2) Fingers and Palm:* The current thumb joint design has been successful in achieving the required 3 DoF-opposition, flexion and abduction movements. The initial prototyping stage displayed the palm joint adequately presenting the opposition motion. Prototyping results were also good for the two motions with abduction and flexion mechanisms trialled and improved. All areas of the design allowed for integration of rotational potentiometers including that of the palm hinge. The design could not progress to the improvement/testing stage due to the COVID-19 situation. Improvements that could be made include

amendments to the angle at which the palm joint is fixed. This would have been understood during testing particular grasping techniques in order for full functionality of the opposition joint. Amendments to the abduction/adduction joint area could also be made, for a more compact design, possibly through the use of smaller bearings or possible extruding the design further from the front of the palm surface.

The current palm and cover design has provided designated areas for tendon and wire routing and a suitable hard surface to protect and enclose all internal components. The modular design allows components to be replaced or amended with ease, without the full structure requiring disassembly. The major future improvement that will need is the positioning of the tendon routing pins. Due to the COVID-19 situation the preferred position of the pins could not be tested and thus the favoured positioning of the pins have only been estimated. The tendon routing for the thumb systems will also need further work for these reasons. Testing could not be carried out to determine the precise location routing, as well as which methods would be functional in ensuring the actuation of the flexion tendons do not affect the motion of the abduction joint. The current solution of feeding the tendon through the palm structure may not be suitable long term due to friction, and improvement may need to be made for large cavities within the palm structure to reduce friction. The angle at which the tendon slot through from the palm structure will need to be investigated.

*3) Wrist:* The design on the wrist allows for the mounting of 8 motors and control components, whilst at the same time incorporating a cooling system to maintain the motor temperature. The motors are strategically placed to minimise the amount of cable routing needed within the wrist, with the majority of the motors having direct access to the palm assembly without requiring any cable routing.

However, the design of wrist does require some improvements. The most important improvement that needs to be made is the accommodation for more motors. The wrist in this report was designed to hold 8 motors and the control components for the hand. The number of motors that were actually planned was 12. The motors that were abandoned were the ones that caused the adduction of the index and middle fingers. As the hand could not be physically tested to verify whether the 8 motors alone would work, the design of the wrist never progressed to the next stage with the extra motors. In a possible improved design for the wrist, the extra motors need to be added to the setup. Other improvements that could be made would be to mount the electronics to the side and top walls (upside down). This would lead to more space in the base areas for the extra motors. The cooling fan could also be removed from the wrist, to account for the extra weight of the new motors, thereby keeping the weight of the whole setup below the 5 kg maximum set by the objectives.

#### C. Grasping and manipulation

In terms of the hand's manipulation capabilities, the hand has 9 actuated degrees of freedom, with 3 DOF in the thumb, 2 DOF in the index and middle fingers, and 1 DOF

for the ring and middle fingers. The two flexion/extension degrees of freedom placed within the index and middle fingers have enabled the finger to perform the various grasps without needing to optimise the fingers' bending motion for the single grasping position. The coupling of the ring and little fingers in the design with the addition of the differential pulley system has allowed for an under actuated hand.

Grasping test could not be performed with the complete hand but were trialled through MuJoCo simulation. The simulated model performed well for all power grasps of large object, however, the precision grasping capabilities still require a few improvements. The model was capable in performing the tripod grasps as well as the two finger prismatic grasp, but it was clear from the model the grasping abilities would improve with the addition abduction/adduction in the index and middle fingers. These additional 2 DoF would also aid in the region of object in-hand manipulation; particularly when the hand is used to control a pen-like object. The true capabilities of the hand would only be determined through testing of the real hand in a controlled environment.

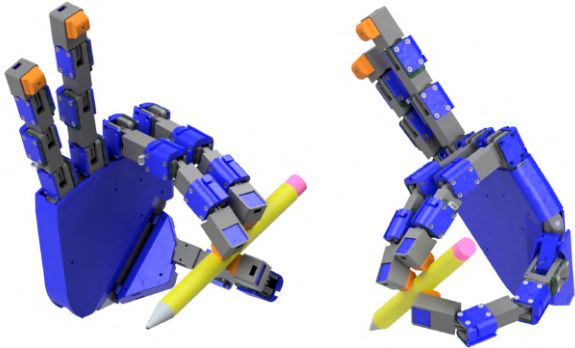


Fig. 153. Figure showing a prismatic 3 finger grasp preformed by the robot hand design within cad. This figure is used to illustrate a precision grasp our robot hand is capable of preforming.

#### D. Exteroception Sensing

Being able to test 3D sensing proved difficult under the COVID-19 situation. However, we were able to produce some results on how different soft skin silicone shapes would deform to a known mass and how that translates to the change in the magnetic field. The results from the experimental sensor testing is reinforced by the simulations of FEA proving that the designed soft skin sensing is adequate for loads ranging from 1 N to 50 N. It is also evaluated that using soft skin with a certain wall thickness is much more compliant than that of a solid bulk, as demonstrated in the experimental procedure with moulded silicone of different wall thickness. It is also advised against using solid bulk designs to ensure decoupling of the axis when using 3D sensors. Though shear testing was not done, previous research has proved that having air gaps minimised crosstalk and hence concluded that the solid bulk (non-hollow) silicone design is not ideal.

Another aspect that needs further work is the designing of the soft skin for the entire palmar side of the hand.

With more cost, more sensors can be added to the palm regions to improve force sensing capabilities using soft skin embedded tactile sensors. This can be extended further to the side of the fingers to increase friction and 3D sensing all over the hand, thus allowing for more detailed control algorithms for grasps and in hand manipulations.

Moreover, simple sensor placement testing was carried out through MuJoCo dynamic simulations. This provided an adequate replacement to previously intended real hand sensor placement testing which could not be carried out due to the COVID-19 situation. The model presented force sensor data to support many of the sensor placement positions previously suggested in the SOTA. This included the addition of 3D-hall effect sensors at the index, middle and thumb tips. Data collected also showed that sensors placed at the side of the index finger and side region of the palm should present useful data when the hand is performing the tripod grasp- previously presented in the objectives. Due to cost constraints, selective sensor positioning was necessary in the physical model due to the limited number of sensors available.

Another form of force detection is provided by the Dynamixel AX-12A motors. The motors are able to measure their present load, which can be used to calculate the force output by the finger on an object. This can be used as a secondary method of force exteroceptive sensing along the finger, which can be very useful in situations where the fingertip 3D magnetic field sensing would not be able to function (eg. ferrous materials).

#### E. Proprioception Sensing

In terms of proprioception, the hand relies primarily on the SV01 potentiometers utilised along every joint for absolute joint position, with secondary proprioception being provided by the Dynamixel AX-12A motors such as their current position, speed, load on motor, acceleration and state of the motor (among many others such as temperature and voltage). This information can be combined to provide a relatively detailed model of the current state of the hand. This information enabled the development of the models discussed for visualisation and control, with the ability to add even more features such as using the force sensing of the motors to determine when the limit positions have been reached which can be used to inherently home the hand position, as well as being used for exteroceptive sensing through the measurement of force from the motors.

The motor's ability to detect its current position could be used alongside its ability to disable its torque to manually adjust the finger positions into a desired pose and record the positions of the motors at that pose. This can therefore be used to provide learning through demonstration capabilities to the robot hand with minimal effort, although accurate repeatability may be difficult due to the under-actuated joints.

Other proprioception information is provided regarding the motor temperature directly from the motors which may not be necessary for the hand performance but could be important in ensuring the motors did not overheat within the wrist, with the possibility of implementing fan speed control based on motor temperature to reduce passive sound.

Other forms of proprioception could be implemented within the links if the discussed homing methods are not sufficient. This could include the use of cameras on the outside of the hand to provide visual servoing and grasp evaluation of the hand. However, this method is highly reliant on the absence of occlusion between the hand and the cameras, and requires complex multi-camera setups that are limited to a specified work space. Alternatively, leap motion control [63] and data control gloves [64] can be used in a master-slave relationship with custom made algorithms to map the sensed user's hand kinematics and motions to the robotic hand with the optional use of tactile feedback to inform the user when contact has been made.

#### F. Safety

If the hand was to be used within a laboratory environment or a manufacturing environment, it must adhere to strict health and safety regulation and special consideration both in terms of design and control must be taken to ensure the safety of the user as well as the robot hand.

Some safety considerations particularly involve the introduction of accidental forces onto the hand through due to other objects in the environment, or humans within the vicinity. One of the key methods of ensuring this safety is the Dynamixel AX-12A motor's ability to detect torques applied onto the hand. The Dynamixel motors provide the ability to set maximum parameters for the hand and an "alarm" state which will set the motor torque to zero, therefore providing the ability for the fingers to move freely rather than resisting the force. In theory this should be able to protect the fingers, and more specifically the motors from experiencing load that could damage the hardware.

This could however prove to be a detriment to the design as the failure mode of turning off the motors could prove to be dangerous in some applications if the safety procedure requires the hand to maintain its current state (eg. handling hazardous materials). This behaviour could easily be modified within the motor firmware, and more specifically utilising the ROS Package for the motor control to adjust these values, or adjusting the behaviour in the developed motor control nodes.

The maximum torque, voltage and temperature could be set to match the application, with the motor performing the Alarm routine as described in the documentation [65]. When any of these conditions are met, the motor raises a bit for the respective error. This could therefore be used to also trigger an emergency stop within the robot hand. An example of this is the UR5 safety I/O, which will perform a predetermined safety procedure if an input meets a certain condition (active high or low).

Another safety measure could be incorporated into the choice of tendon material. By choosing a tendon string that would fail at the maximum tension expected from an application, we could provide a point of failure that would avoid damage to the plastic and printed finger parts. The modularity of the design makes it relatively easy to replace the tendon cables making it an ideal planned failure point. However, this would need to take into account spikes in the maximum torque output from the AX-12A motors; where

they would need to be programmed to reduce large spikes that could surpass the max tendon load.

In terms of the hand design and mounting onto the wrist, the hand itself is assumed to be rigid. We would expect the robot arm/platform the hand is mounted onto to be able to detect forces along the wrist and palm, and have their own safety procedures in place. An example of this is the Robot Emergency Stop procedure on the UR5 robot arm which will lock the robot arm and disable motors if the experienced force exceeds a certain threshold.

If required, force sensors could be added onto the interface parts between the wrist assembly and the palm, providing increased proprioceptive awareness of the loads experienced by the hand. This could be used to trigger an emergency stop if the force exceeds a safety margin to prevent damage to the hand assembly.

The introduction of the power enclosure for the PSU and power breakout board keeps all exposed high voltage electrical equipment protected from individuals.

#### G. Comparison to State of the Art Technology

When comparing our Robot hand to those available in the market a few aspects need to be considered. Our hand was designed to be dexterous, low cost, 3D printable with embedded tactile sensors. The low cost and 3D printable aspects meant the hand must maintain a more simple and modular design while still maintaining dexterity. This hand cannot of course be compared to some of the more complex hands in the market such as the Shadow robot hand, or the Robonaut hand where large amounts of money and many years were invested in their creation [6] [11]. Our hand has been designed to have 9 DoF, 8 total actuators and a tendon transmission type. Comparisons of the hand can be made to other 3-D printed low cost hand such as the Lanigan and Tadesse (2017) providing a low-cost, tendon driven, 3D printed approach with addition of temperature and pressure sensing [66]. This hand however lacks the dexterous hand capability aimed for in our model. Dahiya el al (2019) employs a tactile sensing focused paper via 3D printed Soft Pressure Sensor [67]. A cost-effective fabrication method for tactile sensing, similar to our own, is provided in this approach. The most constructive comparison that can be made to our own model is Etho robot hand [22]. A tendon drive dexterous robot hand, with many aspects of the design involving 3D printed parts. The hand demonstrates dexterous grasping capabilities along with in-hand object manipulation. The hand however has considerably higher costs than our design, particularly due to the higher number of actuated degrees of freedom. Overall, the low cost, relative ease of manufacture and modularity of design makes our hand ideal for further development in the tactile sensing, dexterous robot hands sector. The hand provides prospect of providing a low-cost method of replicating human dexterity in robot form. The developed hand has potential application in both research (grasping and manipulation) and industrial fields, with long term expansion possible in the commercial (possibly in industry quality control and supervised manipulation sector).

## REFERENCES

- [1] Lorenzo Jamone, Lorenzo Natale, Giorgio Metta, and Giulio Sardini. Highly sensitive soft tactile sensors for an anthropomorphic robotic hand. *IEEE Sensors Journal*, 15(8):4226–4233, 2015.
- [2] Tito Pradhono Tomo, Wai Keat Wong, Alexander Schmitz, Harris Kristanto, Alexandre Sarazin, Lorenzo Jamone, Sophon Somlor, and Shigeki Sugano. A modular, distributed, soft, 3-axis sensor system for robot hands. *IEEE-RAS International Conference on Humanoid Robots*, pages 454–460, 2016.
- [3] Tito Pradhono Tomo, Alexander Schmitz, Wai Keat Wong, Harris Kristanto, Sophon Somlor, Jinsun Hwang, Lorenzo Jamone, and Shigeki Sugano. Covering a Robot Fingertip with uSkin: A Soft Electronic Skin with Distributed 3-Axis Force Sensitive Elements for Robot Hands. *IEEE Robotics and Automation Letters*, 3(1):124–131, 2018.
- [4] Sung Woo Park, Ji Hun Bae, Jae Han Park, and Moon Hong Baeg. Development of an anthropomorphic robot hand aimed at practical use for wide service robot application. *IEEE International Conference on Automation Science and Engineering*, pages 431–435, 2012.
- [5] Zhanat Kappassov, Juan Antonio, Corrales Ramon, Véronique Perdereau, Zhanat Kappassov, Juan Antonio, Corrales Ramon, and Véronique Perdereau. Tactile sensing in dexterous robot hands - Review To cite this version : HAL Id : hal-01680649. pages 195–220, 2015.
- [6] C S Lovchik, M A Diftler, and H A Aldridge. Design of the NASA Robonaut Hand. 1999.
- [7] SmoothOn. EcoflexTM Series. 2018.
- [8] Tito Pradhono Tomo, Massimo Regoli, Alexander Schmitz, Lorenzo Natale, Harris Kristanto, Sophon Somlor, Lorenzo Jamone, Giorgio Metta, and Shigeki Sugano. A New Silicone Structure for uSkin - A Soft, Distributed, Digital 3-Axis Skin Sensor and Its Integration on the Humanoid Robot iCub. *IEEE Robotics and Automation Letters*, 3(3):2584–2591, 2018.
- [9] Zhe Xu and Emanuel Todorov. Design of a highly biomimetic anthropomorphic robotic hand towards artificial limb regeneration. *Proceedings - IEEE International Conference on Robotics and Automation*, 2016-June:3485–3492, 2016.
- [10] Sang Hun Kim, Sunjong Oh, Kyu Bum Kim, Youngdo Jung, Hyunuei Lim, and Kyu Jin Cho. Design of a bioinspired robotic hand: Magnetic synapse sensor integration for a robust remote tactile sensing. *IEEE Robotics and Automation Letters*, 3(4):3545–3552, 2018.
- [11] Shadow Robot. Shadow Dexterous Hand E1 Series (E1M3R, E1M3L, E1P1R, E1P1L). (January):1–14, 2013.
- [12] Hand and Forarm – InMoov.
- [13] George P. Kontoudis, Minas Liarokapis, and Kyriakos G. Vamvoudakis. An Adaptive, Humanlike Robot Hand with Selective Interdigitation: Towards Robust Grasping and Dexterous, In-Hand Manipulation. In *IEEE-RAS International Conference on Humanoid Robots*, volume 2019-October, pages 251–258. IEEE Computer Society, 10 2019.
- [14] Murata Manufacturing Co. Rotary Position Sensors R51E.pdf. Technical report, 2017.
- [15] Molex. Molex 3 Pin PCB header PicoBlade.
- [16] Zhijie Tang, Jiaqi Lu, Zhen Wang, and Gaoqian Ma. The development of a new variable stiffness soft gripper. *International Journal of Advanced Robotic Systems*, 16(5), 2019.
- [17] G. Stillfried. Kinematic modelling of the human hand for robotics. 2015.
- [18] Byoung Ho Kim. Effective Length Design of Humanoid Robot Fingers Using Biomimetic Optimization. *International Journal of Advanced Robotic Systems*, 12(10), 2015.
- [19] Pramod Kumar Parida and Bibhuti Bhushan Biswal. Design and Analysis of a Multifingered Robot Hand. *IAES International Journal of Robotics and Automation (IJRA)*, 1(2), 2012.
- [20] Khaled E. Aboul-Hagag, Soheir A. Mohamed, Maha A. Hilal, and Eman A. Mohamed. Determination of sex from hand dimensions and index/ring finger length ratio in Upper Egyptians. *Egyptian Journal of Forensic Sciences*, 1(2):80–86, 2011.
- [21] H. Liu, K. Wu, P. Meusel, N. Seitz, G. Hirzinger, M. H. Jin, Y. W. Liu, S. W. Fan, T. Lan, and Z. P. Chen. Multisensory five-finger dexterous hand: The DLR/HIT hand II. *2008 IEEE/RSJ International Conference on Intelligent Robots and Systems, IROS*, pages 3692–3697, 2008.
- [22] Charalampos Konnaris, Constantinos Gavriel, Andreas A.C. Thomik, and A. Aldo Faisal. EthoHand: A dexterous robotic hand with ball-joint thumb enables complex in-hand object manipulation. *Proceedings of the IEEE RAS and EMBS International Conference on Biomedical Robotics and Biomechatronics*, 2016-July:1154–1159, 2016.
- [23] Mirko Raković, Govind Anil, Živorad Mihajlović, Srdjan Savić, Siddhata Naik, Branislav Borovac, and Achim Gottscheber. Fuzzy position-velocity control of underactuated finger of FTN robot hand. *Journal of Intelligent and Fuzzy Systems*, 34(4):2723–2736, 2018.
- [24] Tetsuya Moura, Haruhisa Kawasaki, Keisuke Yoshikawa, Jun Takai, and Satoshi Ito. Anthropomorphic Robot Hand : Gifu Hand III. pages 1288–1293.
- [25] Massimiliano Zecca, Stefano Roccella, and Giovanni Cappiello. *Romansy 16. Romansy 16*, (May 2014), 2006.
- [26] Won Suk You, Young Hun Lee, Gitae Kang, Hyun Seok Oh, Joon Kyue Seo, and Hyouk Ryeol Choi. Kinematic design optimization of anthropomorphic robot hand using a new performance index. *2017 14th International Conference on Ubiquitous Robots and Ambient Intelligence, URAI 2017*, pages 20–25, 2017.
- [27] K. Devi Sankar, P. Sharmila Bhanu, and Susan P. John. Incidence of agenesis of palmaris longus in the Andhra population of India. *Indian Journal of Plastic Surgery*, 44(1):134–138, 2011.
- [28] Emanuel Todorov, Tom Erez, and Yuval Tassa. MuJoCo: A physics engine for model-based control. *IEEE International Conference on Intelligent Robots and Systems*, pages 5026–5033, 2012.
- [29] Y. N. Turrell, F. X. Li, and A. M. Wing. Estimating the minimum grip force required when grasping objects under impulsive loading conditions. *Behavior Research Methods, Instruments, and Computers*, 33(1):38–45, 2001.
- [30] Kouji Murakami, Kazuya Matsuo, Tsutomu Hasegawa, and Ryo Kurazume. A decision method for placement of tactile elements on a sensor glove for the recognition of grasp types. *IEEE/ASME Transactions on Mechatronics*, 15(1):157–162, 2010.
- [31] George ElKoura and Karan Singh. Handrix: Animating the human hand. *Proceedings of the 2003 ACM SIGGRAPH/Eurographics Symposium on Computer Animation, SCA 2003*, 2003.
- [32] Salvador Cobos, Manuel Ferre, and Rafael Aracil. Simplified Human Hand Models Based On Principal Component Analysis. *Hand, The*, pages 610–615, 2010.
- [33] David Meeker. Finite Element Method Magnetics: HomePage, 2019.
- [34] NdFeB Magnets / Neodymium Iron Boron Magnets Datasheet. Technical report.
- [35] Melexis. MLX90393 Getting Started Guide Abstract MLX90393 Getting Started Guide Table of Contents - Rev 004, 2015.
- [36] Tony Clayton. Coins of England and Great Britain, 2019.
- [37] Supply My Office Limited. Q-Connect Record Card 127x76mm - KF35204.
- [38] Christoph Ledermann, Sascha Wirges, David Oertel, Michael Mende, and Heinz Woern. Tactile sensor on a magnetic basis using novel 3D Hall sensor - First prototypes and results. In *INES 2013 - IEEE 17th International Conference on Intelligent Engineering Systems, Proceedings*, 2013.
- [39] Angela Didomenico and Maury A. Nussbaum. Estimation of forces exerted by the fingers using standardised surface electromyography from the forearm. *Ergonomics*, 51(6):858–871, 2008.
- [40] ROBOTIS-GIT. GitHub - ROBOTIS-GIT/DynamixelSDK: ROBOTIS Dynamixel SDK (Protocol1.0/2.0).
- [41] ROBOTIS. DYNAMIXEL Wizard 2.0.
- [42] Adafruit. Wiring & Test — Adafruit TCA9548A 1-to-8 I2C Multiplexer Breakout — Adafruit Learning System.
- [43] BSI. BS 1407:1970 - Specification for high carbon bright steel (silver steel), 1970.
- [44] Velleman. Velleman KA-12 Arduino Library.
- [45] Arduino. Arduino Reference - Analogread().
- [46] Huntsman. Araldite ® 2011. (July):1–7, 2012.
- [47] 3D Matter. Fdm 3d printing materials compared, 2020.
- [48] 3D Filaprint. Filaprint abs x iron grey 1.75mm 750gms 3d printer filament, 2018.
- [49] 3D Filaprint. Nylon af80 aramid 3d printing filament, 2019.
- [50] 3D Filaprint. 3d filaprint satin champagne gold pla 1.75mm 3d printer filament, 2020.
- [51] Raspberry Pi. Download Raspbian for Raspberry Pi, 2020.
- [52] Arduino. Arduino - Software, 2020.
- [53] Python. Download Python — Python.org, 2020.
- [54] ROBOTIS. DYNAMIXEL SDK - Library Setup - Python Linux.
- [55] Aary Kieu. GitHub - cckieu/dxl\_control: Dynamixel Ax12 class using (dynamixelSDK) for easy, intuitive motor control.
- [56] Theodore Yapo. GitHub - tedyapo/arduino-MLX90393: Arduino library for MLX90393 magnetometer sensor.
- [57] Melexis. MLX90393 Triaxis Magnetic Node Datasheet - Revision 005 June 4, 2019. Technical report, 2017.

- [58] Honeywell. Solid State Sensors SS490 Series Miniature Ratiometric Linear Datasheet.
- [59] MuRata. Rotary Position Sensors, Revision - R51E.pdf, 2017.
- [60] entelechysolutions. entelechysolutions / robooverter — Bitbucket, 2018.
- [61] Universal Robots UR5/CB3 Original instructions (en). Technical report.
- [62] 10pcs D shaped shaft 4mm D shaped motor shaft stainless steel shaft spare parts for DIY models length 55mm 70mm—parts for—spare partsstainless steel shaft - AliExpress.
- [63] Jianshu Zhou, Xiaojiao Chen, Ukyoung Chang, Jia Pan, Wenping Wang, and Zheng Wang. Intuitive Control of Humanoid Soft-Robotic Hand BCL-13. *IEEE-RAS International Conference on Humanoid Robots*, 2018-Novem:314–319, 2019.
- [64] Stephen Arthur Powell. *A Review of Anthropomorphic Robotic Hand Technology and Data Glove Based Control Stephen Arthur Powell Thesis submitted to the faculty of the Virginia Polytechnic Institute and State University in partial fulfillment of the requirements for the degree of*. PhD thesis, Virginia Polytechnic Institute and State University, 2016.
- [65] AX-12A.
- [66] David Lanigan and Yonas Tadesse. Low Cost Robotic Hand that Senses Heat and Pressure. 2017.
- [67] Markellos Ntagios, Habib Nassar, Abhilash Pullanchiyodan, William Taube Navaraj, and Ravinder Dahiya. Robotic Hands with Intrinsic Tactile Sensing via 3D Printed Soft Pressure Sensors. *Advanced Intelligent Systems*, 1900080:1900080, 2019.

## XII. APPENDIX

### A. Weight Breakdown of the Hand - Ahmed Sami Deiri

TABLE XIII

TABLE CONTAINING THE WEIGHTS RELEVANT TO THE L1,L2,L3 LINKS FOR THE INDEX, MIDDLE, RING AND LITTLE FINGER.

<b>Finger Assembly (L1, L2, L3)</b>			
<b>Part</b>	<b>Weight (g)</b>	<b>Quantity</b>	<b>Total Weight (g)</b>
Mean Link Body Printed	5	1	5
Link Cover Printed	3	1	3
SV01 Potentiometer	0.36	1	0.36
Potentiometer pcb	0.5	1	0.5
Shaft	1	1	1
Bearing	2	2	4
bolts, washers, misc. (estimate)	3	1	3
		Total Per Link	16.86
		Total for 4 fingers	202.32

TABLE XIV

TABLE CONTAINING THE WEIGHTS RELEVANT TO THUMB ASSEMBLY.

<b>Thumb Assembly</b>			
<b>Part</b>	<b>Weight (g)</b>	<b>Quantity</b>	<b>Total Weight (g)</b>
Thumb Plastic	36	1	36
SV01 Potentiometer	0.36	1	0.36
Potentiometer pcb	0.5	1	0.5
Link Cover	3	1	3
Shaft	1	3	3
Long Shaft	2	1	2
Bearing	2	8	16
bolts, washers, misc. (estimate)	6	1	6
		Total for Thumb	66.86

TABLE XV

TABLE CONTAINING THE WEIGHTS RELEVANT TO THE PALM ASSEMBLY.

<b>Palm Assembly</b>			
<b>Part</b>	<b>Weight (g)</b>	<b>Quantity</b>	<b>Total Weight (g)</b>
Palm 3D Printed Parts	76	1	76
Palm Cable management	2	1	2
Palm bolts and inserts (estimate)	3	1	3
		Total	81

TABLE XVI

TABLE CONTAINING THE WEIGHTS RELEVANT WRIST ASSEMBLY, INCLUDING THE MOUNTING BRACKET.

<b>Wrist Assembly</b>			
<b>Part</b>	<b>Weight (g)</b>	<b>Quantity</b>	<b>Total Weight (g)</b>
Wrist 3D Printed Body	1480	1	1480
Motor per AX12	53.5	12	642
Artic 120mm case fan	108	1	108
TCA9548A I2C Multiplexer	1.8	1	1.8
Arduino uno	25	1	25
Raspberry Pi	50	1	50
6 Port AX/MX Power Hub	10	2	20
Adafruit PWM Driver	5.5	1	5.5
Robotis U2D2	9	1	9
bolts, washers, misc. (estimate)	10	1	10
		Total Wrist	2341.3

TABLE XVII  
TABLE CONTAINING THE WEIGHTS RELEVANT POWER ENCLOSURE ASSEMBLY

**Power Enclosure**

<b>Part</b>	<b>Weight (g)</b>	<b>Quantity</b>	<b>Total Weight (g)</b>
Seasonic 300W Power Supply	1360.77	1	1360.77
Power Supply breakout board	99.8	1	99.8
Plastic printed box	573	1	573
Total			2033.57

*B. Part List of all Designed Components - Kai Page*

Part/assembled Number	Drawing No.	Title	Subject	Author
RH-100	DWG-100-A	Fingertip Version 1	Fingertip	Kai Page
RH-100	DWG-100-B	Fingertip Version 1	Fingertip	Kai Page
RH-101	DWG-101-A	Fingertip Lid Version 1	Fingertip	Kai Page
RH-102	DWG-102-A	Fingertip Version 2	Fingertip	Kai Page
RH-102	DWG-102-B	Fingertip Version 2	Fingertip	Kai Page
RH-103	DWG-103-A	Fingertip Lid Version 2	Fingertip	Kai Page
RH-104	DWG-104-A	Fingertip Assembly	Fingertip	Kai Page
RH-105	DWG-105-A	2mm - Square Silicone	Soft Skin	Kai Page
RH-106	DWG-105-A	3mm - Square Silicone	Soft Skin	Kai Page
RH-107	DWG-105-A	4mm - Square Silicone	Soft Skin	Kai Page
RH-108	DWG-108-A	Circle Silicone	Soft Skin	Kai Page
RH-109	DWG-109-A	Square Curve Silione	Soft Skin	Kai Page
RH-110	DWG-110-A	1D Fingertip	Fingertip	Kai Page
RH-111	DWG-111-A	Non-Hollow Square Silicone	Soft Skin	Kai Page
RH-200	DWG-200-A	Link Body 1 - Index	Finger Links	Sami Deiri
RH-201	DWG-200-A	Link Body 1 - Middle	Finger Links	Sami Deiri
RH-202	DWG-200-A	Link Body 1 - Ring	Finger Links	Sami Deiri
RH-203	DWG-200-A	Link Body 1 - Little	Finger Links	Sami Deiri
RH-204	DWG-204-A	Link Body 2 - Index	Finger Links	Sami Deiri
RH-205	DWG-204-A	Link Body 2 - Middle	Finger Links	Sami Deiri
RH-206	DWG-204-A	Link Body 2 - Ring	Finger Links	Sami Deiri
RH-207	DWG-204-A	Link Body 2 - Little	Finger Links	Sami Deiri
RH-208	DWG-204-A	Link Body 2 - Thumb	Finger Links	Sami Deiri
RH-209	DWG-204-A	Link Body 2 - Little	Finger Links	Sami Deiri
RH-211	DWG-211-A	Link Body 3 - Index	Finger Links	Sami Deiri
RH-212	DWG-211-A	Link Body 3 - Middle	Finger Links	Sami Deiri
RH-213	DWG-211-A	Link Body 3 - Ring	Finger Links	Sami Deiri
RH-214	DWG-211-A	Link Body 3 - Little	Finger Links	Sami Deiri
RH-215	DWG-211-A	Link Body 3 - Thumb	Finger Links	Sami Deiri
RH-210	DWG-210-A	Link Cover	Finger Cover	Sami Deiri
RH-300	DWG-300-A	Palm Structure 1	Palm	Talha Tailor
RH-300	DWG-300-B	Palm Structure 1	Palm	Talha Tailor
RH-300	DWG-300-C	Palm Structure 1	Palm	Talha Tailor
RH-301	DWG-301-A	Palm Structure 2	Palm	Talha Tailor
RH-301	DWG-301-B	Palm Structure 2	Palm	Talha Tailor
RH-302	DWG-302-A	Thumb Body 1	Thumb	Talha Tailor
RH-303	DWG-303-A	Thumb Body 2	Thumb	Talha Tailor
RH-304	DWG-304-A	Palm Cover Front C8	Palm	Talha Tailor
RH-305	DWG-305-A	Palm Cover Front C7	Palm	Talha Tailor
RH-306	DWG-306-A	Palm Cover Front C6	Palm	Talha Tailor
RH-307	DWG-307-A	Palm Cover Back C8	Palm	Talha Tailor
RH-308	DWG-308-A	Palm Cover Back C7	Palm	Talha Tailor
RH-309	DWG-309-A	Palm Cover Back C6	Palm	Talha Tailor
RH-310	DWG-310-A	Routing Pin	Palm	Talha Tailor
RH-400	DWG-400-A	Side Plate	Wrist	Bashar Khan
RH-401	DWG-401-A	Outer Meshed Plate	Wrist	Bashar Khan
RH-402	DWG-402-A	Inner Fan Plate	Wrist	Bashar Khan
RH-403	DWG-403-A	Outer Fan Plate	Wrist	Bashar Khan
RH-404	DWG-404-A	Top Plate	Wrist	Bashar Khan
RH-405	DWG-405-A	Middle Base Plate	Wrist	Bashar Khan
RH-406	DWG-406-A	Floor Plate	Wrist	Bashar Khan
RH-407	DWG-407-A	Motor Rail	Wrist	Bashar Khan
RH-408	DWG-408-A	Motor Rail Pin	Wrist	Bashar Khan
RH-409	DWG-409-A	Mounting Bracket	Wrist	Bashar Khan
RH-500	DWG-500-A	Power Enclosure	Power Enclosure	Jamie Sengun
RH-501	DWG-501-A	Power Enclosure Cover	Power Enclosure	Jamie Sengun
RH-502	DWG-502-A	Power Enclosure Side	Power Encluser	Jamie Sengun

### C. Dynamixel Python Motor Control - ax12\_open.py - Jamie Sengun

```
from dxl_control.Ax12 import Ax12 #From https://github.com/cckieu/dxl_control by
    Aary Kieu

    Ax12.open_port() #Connects to the Robotis U2D2 using the default port in
        Ax12.py
    Ax12.set_baudrate() #Uses the motor default 1000000 baud rate.
```

Listing 3. Dynamixel Python motor control - open serial connection to motors

### D. Dynamixel Python Motor Control - ax12\_close.py - Jamie Sengun

```
from dxl_control.Ax12 import Ax12 #From https://github.com/cckieu/dxl_control by
    Aary Kieu

for x in range(11): #Disables torque for the 12 motors and disconnects them.
    my_dxl=Ax12(x+1)
    my_dxl.disable_torque()
Ax12.close_port()
```

Listing 4. Dynamixel Python motor control - close serial connection to motors

### E. Dynamixel Python Motor Control - ax12\_move.py - Jamie Sengun

```
from dxl_control.Ax12 import Ax12 #From https://github.com/cckieu/dxl_control by
    Aary Kieu
import numpy as np

#input
    #ID = motor ID
    #angle = motor angle in degrees

    #Motor angle function is between 0-1023 for the 300 degrees.
    #Requested motor angle in degrees is mapped between 0-1023
    angle=np.interp(angle,[0,300],[0,1023])

    motor_object= Ax12(ID)
    motor_object.set_position(angle)
```

Listing 5. Dynamixel Python motor control - Move specified motor to a certain angle between 0°to 300°

### F. Dynamixel Python Motor Control - ax12\_getpos.py - Jamie Sengun

```
from dxl_control.Ax12 import Ax12 #From https://github.com/cckieu/dxl_control by
    Aary Kieu
import numpy as np
#Get current position of a motor
#input
    #ID = motor ID

    motor_object= Ax12(ID)
    pos=motor_object.get_position()
    pos=np.interp(pos,[0,1023],[0,300])
    return pos

#output
    #pos
```

Listing 6. Dynamixel Python motor control - Get motor position for specified motor

*G. Dynamixel Python Motor Control - ax12\_disable\_torque.py - Jamie Sengun*

```
from dxl_control.Ax12 import Ax12 #From https://github.com/cckieu/dxl_control by
    Aary Kieu

#input
    #ID = motor id

    my_dxl=Ax12(ID)
    my_dxl.disable_torque()
```

Listing 7. Dynamixel Python motor control - Disable torque for a specified motor

*H. Dynamixel Python Motor Control - ax12\_enable\_torque.py - Jamie Sengun*

```
from dxl_control.Ax12 import Ax12 #From https://github.com/cckieu/dxl_control by
    Aary Kieu

#input
    #ID = motor ID

    my_dxl=Ax12(ID)
    my_dxl.enable_torque()
```

Listing 8. Dynamixel Python motor control - Enable torque for a specified motor

## I. Dynamixel Python Motor Control - Manual sliders. motorsliders.py - Jamie Sengun

```

from tkinter import *
import time
from dxl_control.Ax12 import Ax12 #From https://github.com/ckieu/dxl_control by
    Aary Kieu

#This code is designed to allow to user to move sliders to control the motors.
#It is recommended that either this method or direct function motor control is
    used
#as they cannot be used simultaneously by design.

Ax12.open_port() #Connects to the Robotis U2D2 using the default port in
    Ax12.py
Ax12.set_baudrate() #Uses the motor default 1000000 baud rate.

#Functions for changing servo angles, needed unique functions for the sliders
def F1(angle1):
    motor_object= Ax12(1)
    motor_object.set_position(angle1)

def F2(angle2):
    motor_object= Ax12(2)
    motor_object.set_position(angle2)

def F3(angle3):
    motor_object= Ax12(3)
    motor_object.set_position(angle3)

def F4(angle4):
    motor_object= Ax12(4)
    motor_object.set_position(angle4)

def F5(angle5):
    motor_object= Ax12(5)
    motor_object.set_position(angle5)

def F6(angle6):
    motor_object= Ax12(6)
    motor_object.set_position(angle6)

def F7(angle7):
    motor_object= Ax12(7)
    motor_object.set_position(angle7)

def F8(angle8):
    motor_object= Ax12(8)
    motor_object.set_position(angle8)

def F9(angle9):
    motor_object= Ax12(9)
    motor_object.set_position(angle9)

def F10(angle10):
    motor_object= Ax12(10)
    motor_object.set_position(angle10)

def F11(angle11):
    motor_object= Ax12(11)
    motor_object.set_position(angle11)

```

```

def F12(angle12):
    motor_object= Ax12(12)
    motor_object.set_position(angle12)

#GUI creation with sliders that control servos between 0-300 in steps 0-1023.
#Updates the sliders on initialisation to get current motor positions.
root =Tk()
time.sleep(1) #Pause for loading of GUI

w1=Scale(root,orient='vertical', command=F1, from_ =0, to=1023)
w1.set(ax.get_ax(1))
w2=Scale(root,orient='vertical', command=F2, from_ =0, to=1023)
w2.set(ax.get_ax(2))
w3=Scale(root,orient='vertical', command=F3, from_ =0, to=1023)
w3.set(ax.get_ax(3))
w4=Scale(root,orient='vertical', command=F4, from_ =0, to=1023)
w4.set(ax.get_ax(4))
w5=Scale(root,orient='vertical', command=F5, from_ =0, to=1023)
w5.set(ax.get_ax(5))
w6=Scale(root,orient='vertical', command=F6, from_ =0, to=1023)
w6.set(ax.get_ax(6))
w7=Scale(root,orient='vertical', command=F7, from_ =0, to=1023)
w7.set(ax.get_ax(7))
w8=Scale(root,orient='vertical', command=F8, from_ =0, to=1023)
w8.set(ax.get_ax(8))
w9=Scale(root,orient='vertical', command=F9, from_ =0, to=1023)
w9.set(ax.get_ax(9))
w10=Scale(root,orient='vertical', command=F10, from_ =0, to=1023)
w10.set(ax.get_ax(10))
w11=Scale(root,orient='vertical', command=F11, from_ =0, to=1023)
w11.set(ax.get_ax(11))
w12=Scale(root,orient='vertical', command=F12, from_ =0, to=1023)
w12.set(ax.get_ax(12))

Label(root, text="F1").grid(column=0,row=1)
Label(root, text="F2").grid(column=1,row=1)
Label(root, text="F3").grid(column=2,row=1)
Label(root, text="F4").grid(column=3,row=1)
Label(root, text="F5").grid(column=4,row=1)
Label(root, text="F6").grid(column=5,row=1)
Label(root, text="F7").grid(column=6,row=1)
Label(root, text="F8").grid(column=7,row=1)
Label(root, text="F9").grid(column=8,row=1)
Label(root, text="F10").grid(column=9,row=1)
Label(root, text="F11").grid(column=10,row=1)
Label(root, text="F12").grid(column=11,row=1)

w1.grid(column=0,row=0)
w2.grid(column=1,row=0)
w3.grid(column=2,row=0)
w4.grid(column=3,row=0)
w5.grid(column=4,row=0)
w6.grid(column=5,row=0)
w7.grid(column=6,row=0)
w8.grid(column=7,row=0)
w9.grid(column=8,row=0)
w10.grid(column=9,row=0)
w11.grid(column=10,row=0)
w12.grid(column=11,row=0)

```

```
root.mainloop()
```

Listing 9. Dynamixel Python motor control - manual sliders for motor angle control

*J. Arduino Sensors - MLX90393 & Analog sensors. Arduino\_sensors.ino - Jamie Sengun*

```
#include <Wire.h>
#include <MLX90393.h> //From https://github.com/tedyapo/arduino-MLX90393 by
Theodore Yapo
#include <Velleman_KA12.h> //From https://www.velleman.eu/downloads/files/
downloads/velleman_ka12.zip

int num_ana=18; //Change the number to suit the number of analog sensors, up to
24.
//Rotational sensors should be wired from port 1, followed by 1D hall effect
sensors.

int num_3d=3; //Change the number to suit the number of MLX90393 sensors, up to
8
int all[num_ana];
int sensor;

MLX90393 mlx;
MLX90393::txyz data; //Create a structure, called data, of four floats (t, x, y,
and z)

#define TCAADDR 0x70 //I2C address for the TCA9548A multiplexer

//Function to select the I2C ports on the TCA9548A.
void tcaselect(uint8_t i) {
    if (i > 7) return;

    Wire.beginTransmission(TCAADDR);
    Wire.write(1 << i);
    Wire.endTransmission();
}

void setup()
{
    Serial.begin(9600);
    Wire.begin();

    for(int i=0;i<num_3d;i=i+1) {
        tcaselect(i)
        byte status = mlx.begin(0,1);
        Serial.println();
        mlx.setGainSel(0);
        mlx.setResolution(0, 0, 0); //x, y, z
        mlx.setOverSampling(1);
        mlx.setDigitalFiltering(7);
        mlx.setTemperatureCompensation(1);
    }

    //See MLX90393.h and .cpp for additional functions including:
    //set/getOverSample, set/getTemperatureOverSample, set/getDigitalFiltering,
    //set/getResolution
    //set/getTemperatureCompensation, setOffsets, setWThresholds
}
```

```
ka12_init(); //Initialise the KA-12
}

void loop()
{
    ka12_readAll(all);
    String output="";
    for (int i=0; i < num_ana; i=i+1) {
        output=output+all[i]+", ";
    }

    //Output the MLX90393 x,y,z data from the TCA9584A port 0 ascending
    for(int i=0;i<num_3d;i=i+1){
        tcaselect(i);
        mlx.readData(data); //Read the values from the sensor
        output=output+data.x+", "+data.y+", "+data.z+", ";
    }
    output.remove(output.length()-1,1);
    Serial.println(output);
    //delay(0.1);
}
```

Listing 10. Arduino sensors data gathering and serial output

K. Python sensor data gathering for processing Sensor\_process.py - Jamie Sengun

```

import serial
import time
import csv
import sys
import numpy as np

#Function that pulls serial data and converts it to float array for processing.
#Function is called below.
def ser_loop(ser,num_rot,num_1d,num_3d):
    ser.flushInput()
    cc=ser.readline()
    cc=cc.decode('utf-8')
    sensor_data_list=cc.split(',',-1)
    #Error checking for number of expected number of sensor readings
    if len(sensor_data)!=num_rot+num_1d+num_3d*3:
        return

    #Convert imported split string values to float values.
    for k in range(0,len(sensor_data),1):
        try:
            sensor_data[k]=float(sensor_data[k])
        except ValueError:
            break

    #Convert list to array
    sensor_data_arr=np.array(sensor_data)
    return sensor_data_arr #Return one array of sensor data

#Set serial port variable for connected Arduino.

#Close any open connections and open a new serial connections to the Arduino
    serial.Serial.close(serial.Serial("COM4"))
    ser=serial.Serial("COM4", 9600,timeout=0.01)#Port, Baud rate, timeout

#Starts requesting serial data from the Arduino continuously
    csv_record='no' #set as 'yes' or 'no' for CSV recording in an Excel file.

    #Clear Serial cache on Arduino and idle time for completion.
    ser.flushInput()
    time.sleep(3)

    num_rot=16
    num_1d=2
    num_3d=3

#Rotational sensors should output first, followed by 1D hall effect sensors.(1
#      output each)
#3D hall effect sensors should output be last in the array. (3 outputs - X,Y,Z)
#This can be function expanded on depending on how the user wants the outputs
#done.
    if csv_record=='yes':
        while True:
            sensor_data_arr=ser_loop(ser,num_rot,num_1d,num_3d)
            with open("test_data.csv","a",newline='') as f:
                writer = csv.writer(f,delimiter=",")

```

```

        writer.writerow(sensor_data)
        time.sleep(0.01) #Time can be used to limit serial request rate to
                         match Arduino.
    elif csv_record=='no':
        while True:
            sensor_data_arr=ser_loop(ser,num_rot,num_1d,num_3d)
            time.sleep(0.01) #Time can be used to limit serial request rate to
                             match Arduino.
    else :
        sys.exit('Wrong_input_for_CSV_record') #if wrong then exit the program.

#OUTPUT sensor_data_arr to sensor_split.py

```

Listing 11. Python sensor data gathering for processing - output sent to sensor\_split.py

*L. Split raw sensor data array Sensor\_split.py - Jamie Sengun*

```

import numpy as np

#ADD INPUTS HERE. Fix accordingly
#Order of variables, Rotational potentiometers, 1D SS495A sensors, 3D MLX90393
sensor_raw=sensor_data_arr      #RAW SENSOR INPUT sensor_data_arr from
                                sensor_process.py

num_rot=16 #Number of rotational potentiometers
num_1d=2   #Number of 1D analog sensors
num_3d=3   #Number of MLX90393 I2C sensors


rot_data=sensor_raw[0:num_rot-1]      #rotational potentiometer data
hf_data=sensor_raw[num_rot:len(sensor_raw)-1] #1D then 3D hall effect sensors

return(rot_data,hf_data)
#OUTPUT DATA
#rot_data to rot_process.py
#hf_data to hf_process.py

```

M. Process raw rotational potentiometer data into angles rot\_process.py - Jamie Sengun

```

import numpy as np

#ADD INPUTS HERE. Fix accordingly
#import rot_data
#Data is in order of ports on KA-12 shield from port 1.

rot_data=rot_data
num_rot=16

#Defined KA-12 ports for rotational potentiometers, J1 is the base joint and
#J2 is the middle joint and J3 is the fingertip joint:
Little finger link joints: J1=1, J2=2, J3=3
Ring finger link joints: J1=4, J2=5, J3=6
Middle finger link joints: J1=7, J2=8, J3=9
Index finger link joints: J1=10, J2=11, J3=12
Thumb opposable joint: J1=13
Thumb AA joint: J2=14
Thumb link joints: J3=15, J4=16

#Guaranteed linearity is between +/- 160 degrees
#All link sensors for ROT 1 to 13 and 15 to 16 are orientated as defined when
    looking at the
#palmar side from fully extended (0 degree) to fully flexed (90 degree etc):
    #left side potentiometers output for L2 on all fingers; not including thumb
        #= -90 degree to 0 degree
    #right side potentiometers output for L1 and L3 on all fingers and 2 thumb
        #links = 90 degree to 0 degree

#All 1-12 and 15-16 link rotational potentiometers are converted as they all
    start at
#-90 degree or 90 degree as shown above, so the absolute values are
#the same as they approach 0 degree
#The other 2 thumb potentiometers are dealt separately.

#Joints have been designed to have a max displacement range of 90 degrees.
#The displacement range will be controlled by testing and programming the AX
    -12 motors
#Potentiometers do not travel greater than 90 degree from their
#starting position while staying within the range of +/- 166.65 degrees.

for i in range(num_rot-5):
    rot_data[i]=90-abs(np.interp(rot_data[i],[0,5],[-166.65,166.65]))

for i in range(num_rot-2,num_rot-1):
    rot_data[i]=90-abs(np.interp(rot_data[i],[0,5],[-166.65,166.65]))


#ROT 14 has a range of 60 degrees, from potentiometer readings of 30 degree
    to
#-30 degree, mapped between 0 degree to 60 degree respectively.
rot_data[num_rot-3]=30-np.interp(rot_data[i],[0,5],[-166.65,166.65])

#ROT 13 has a range of 90 degrees, from potentiometer readings of 0 degree
    #to -90 degree, mapped between 0 degree to 90 degree respectively.
rot_data[num_rot-4]=abs(np.interp(rot_data[i],[0,5],[-166.65,166.65]))

#It has been configured such that all potentiometers; except the Thumb AA joint
#will output either all positive or negative angles that are then converted to
    their

```

```
#absolute values. A displacement range greater than 90 degrees is not required
#           for
#the desired functionality, so a more complicated solution involving both
#           positive and minus
#values from a potentiometer was not required.

return rot_data
#OUTPUT rot_data array of potentiometer angles in an array.
```

Listing 13. Process raw rotational potentiometer data into angles

*N. Process raw hall effect data into magnetic density flux in  $\mu$ T units hf\_process.py - Jamie Sengun*

```
import numpy as np

#ADD INPUTS HERE. Fix accordingly
#input hd_data
#Order of variables, 1D SS495A sensors, 3D MLX90393 (x,y,z) readings per sensor

hf_data=hf_data
num_1d=2    #Number of 1D analog sensors
num_3d=3    #Number of MLX90393 I2C sensors

#Convert 1D voltage readings to MicroTesla as per typical values from SS495A
#datasheet.
#Assuming a 5V input voltage.
#May need calibration to validate readings
for i in range(num_1d-1):
    hf_data[i]=np.interp(hf_data[i],[0.2,4.8],[-67000,67000])

return hf_data
#OUTPUT DATA
#output hf_data array of hall effect sensor data in T units in an array.
```

Listing 14. Process raw hall effect data into magnetic density flux in  $\mu$ T units

*O. MLX90393 Sensitvity Parameters - from Datasheet - Jamie Sengun*

TABLE XVIII

TABLE OF MLX90393 X,Y AND Z DIRECTION SENSITIVITIES ( $\mu\text{T}/\text{LSB}$ ) WITH VARIABLE GAIN (*GAIN\_SEL*) & RESOLUTION (*RES*) [57]

<b>GAIN_SEL</b>	<b>RES = 0</b>		<b>RES = 1</b>		<b>RES = 2</b>		<b>RES = 3</b>	
	<b>SENS-XY</b>	<b>SENS-Z</b>	<b>SENS-XY</b>	<b>SENS-Z</b>	<b>SENS-XY</b>	<b>SENS-Z</b>	<b>SENS-XY</b>	<b>SENS-Z</b>
0	0.805	1.468	1.610	2.936	3.220	5.872	6.440	11.744
1	0.644	1.174	1.288	2.349	2.576	4.698	5.152	9.395
2	0.483	0.881	0.966	1.762	1.932	3.523	3.864	7.046
3	0.403	0.734	0.805	1.468	1.610	2.936	3.220	5.872
4	0.322	0.587	0.644	1.174	1.288	2.349	2.576	4.698
5	0.268	0.489	0.537	0.979	1.073	1.957	2.147	3.915
6	0.215	0.391	0.429	0.783	0.859	1.566	1.717	3.132
7	0.161	0.294	0.322	0.587	0.644	1.174	1.288	2.349

*P. MLX90393 Sensor Range - from Datasheet - Jamie Sengun*

TABLE XIX

TABLE OF SENSOR RANGE IN LSB FOR VARIOUS RESOLUTIONS (*RES*) WITH AND WITHOUT MEASUREMENT TEMPERATURE COMPENSATION (*TCMP\_EN*) [57]

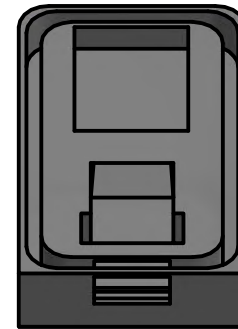
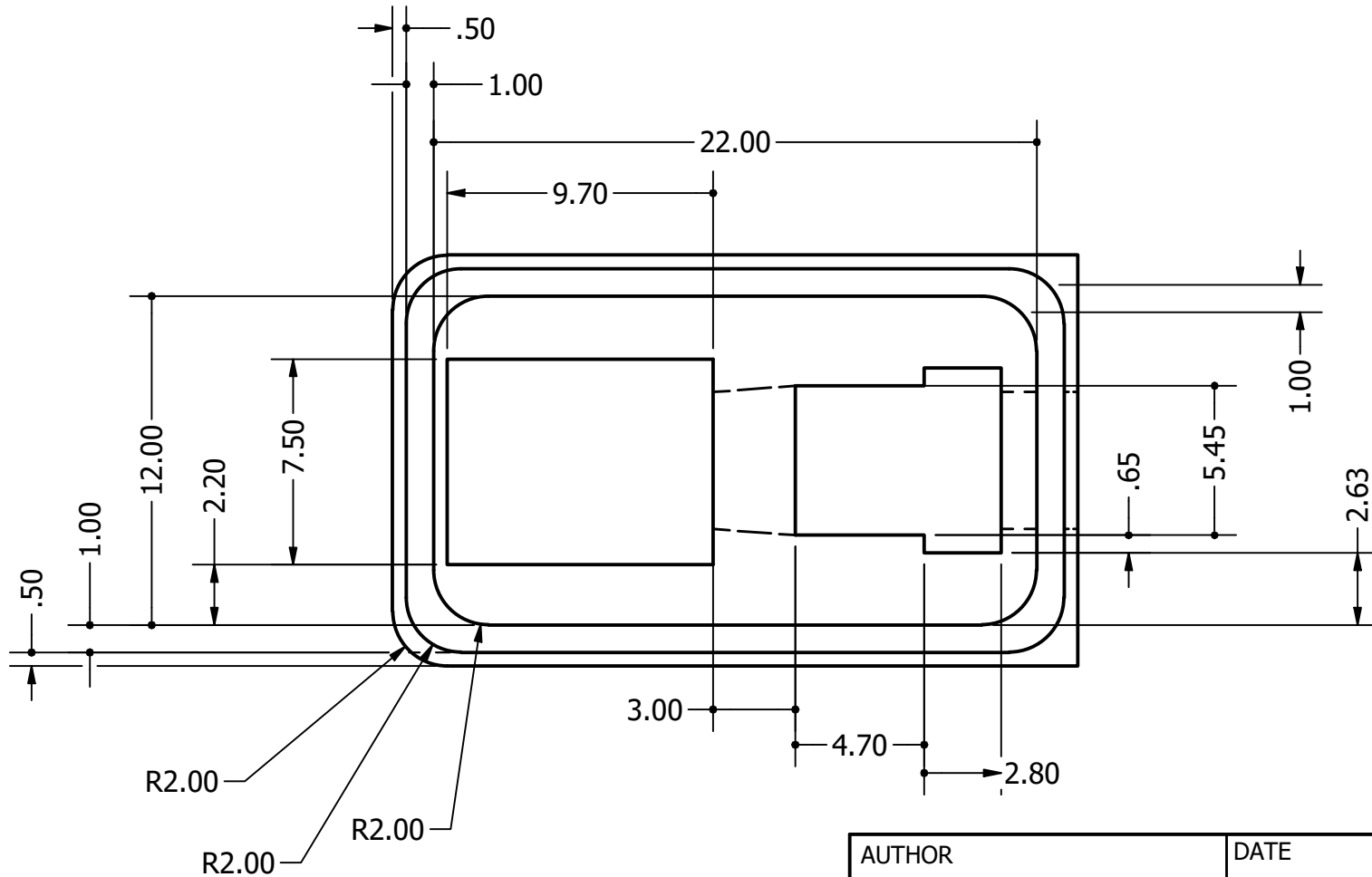
<b>RES</b>	<b>NO TCMP_EN</b>	<b>TCMP_EN</b>
	<b>RANGE</b>	
0	$\pm 2^{15}$	$\pm 2^{15}$
1	$\pm 2^{15}$	$\pm 2^{15}$
2	$\pm 22000$	N/A
3	$\pm 11000$	N/A

*Q. MLX90393 maximum output data rate (*ODR*) -from datasheet - Jamie Sengun*

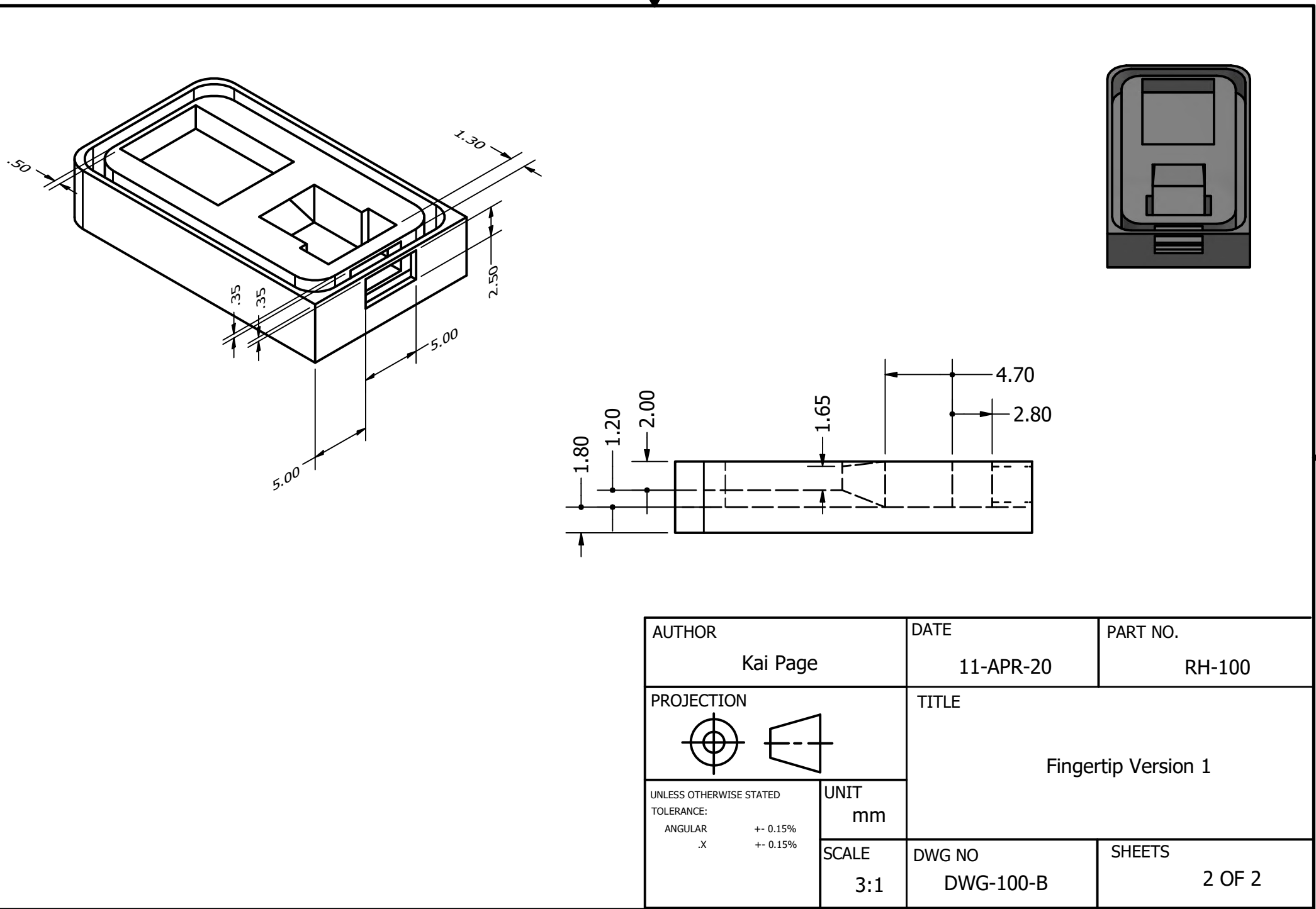
TABLE XX

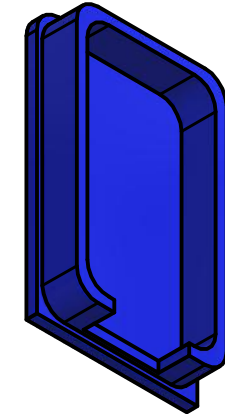
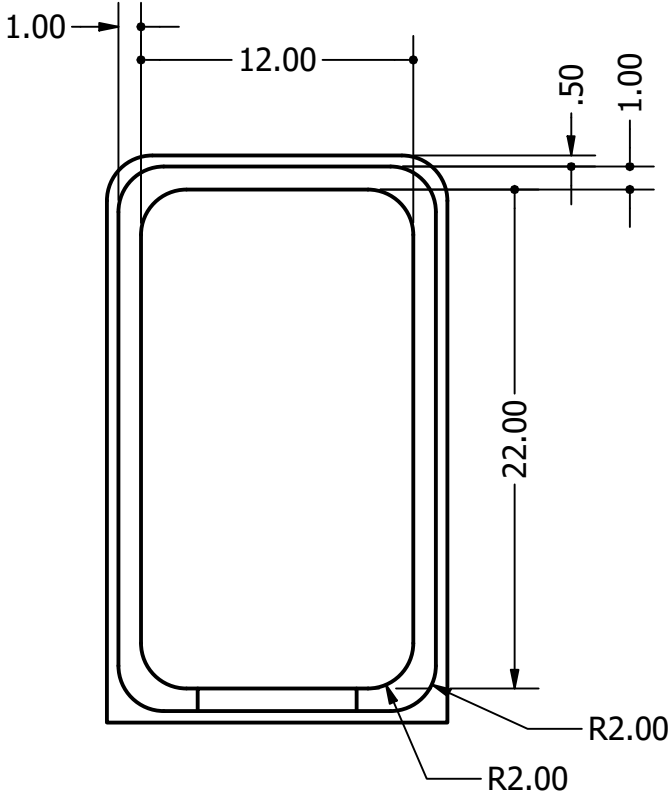
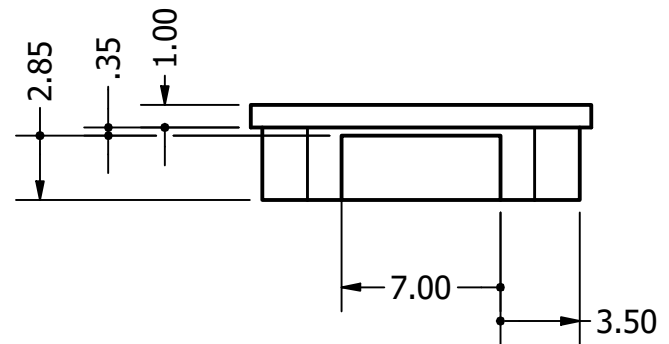
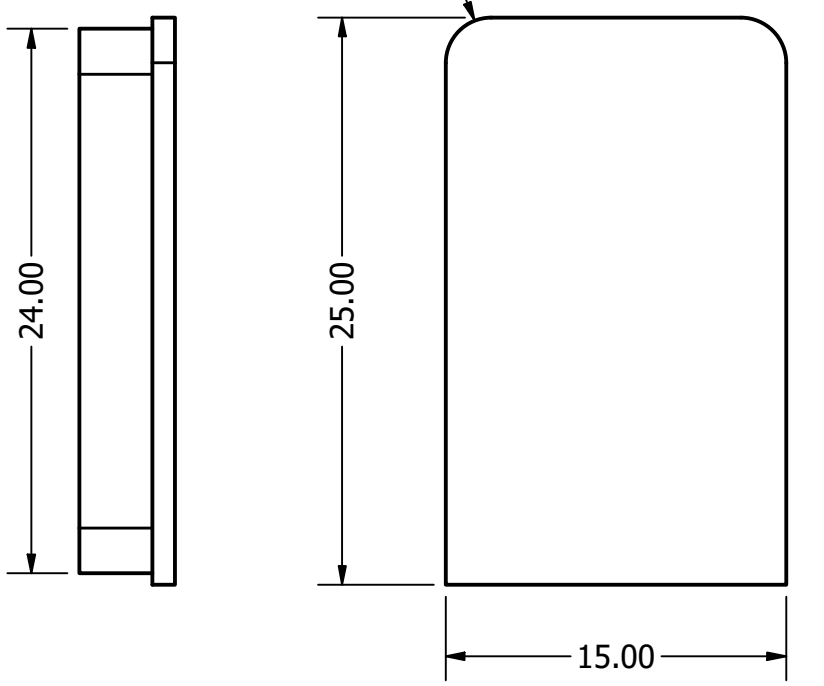
TABLE OF MAXIMUM OUTPUT DATA RATE (*ODR*) IN Hz AS A FUNCTION OF OVERSAMPLING RATE (*OSR*) AND DIGITAL FILTERING (*DIG\_FILT*) [57]

<b>DIG_FILT</b>	<b>OSR</b>			
	<b>0</b>	<b>1</b>	<b>2</b>	<b>3</b>
<b>0</b>	716.9	493.0	303.4	171.5
<b>1</b>	622.7	408.0	241.5	133.0
<b>2</b>	493.0	303.4	171.5	91.8
<b>3</b>	348.0	200.6	108.6	56.6
<b>4</b>	219.2	119.6	62.6	32.1
<b>5</b>	125.9	66.1	33.9	17.2
<b>6</b>	68.0	34.9	17.7	8.9
<b>7</b>	35.4	18.0	9.0	4.5

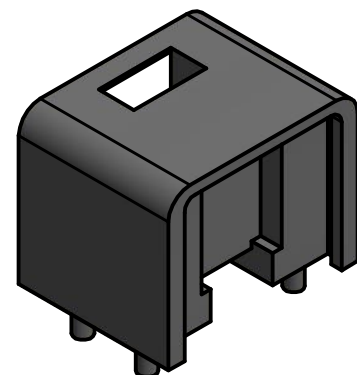
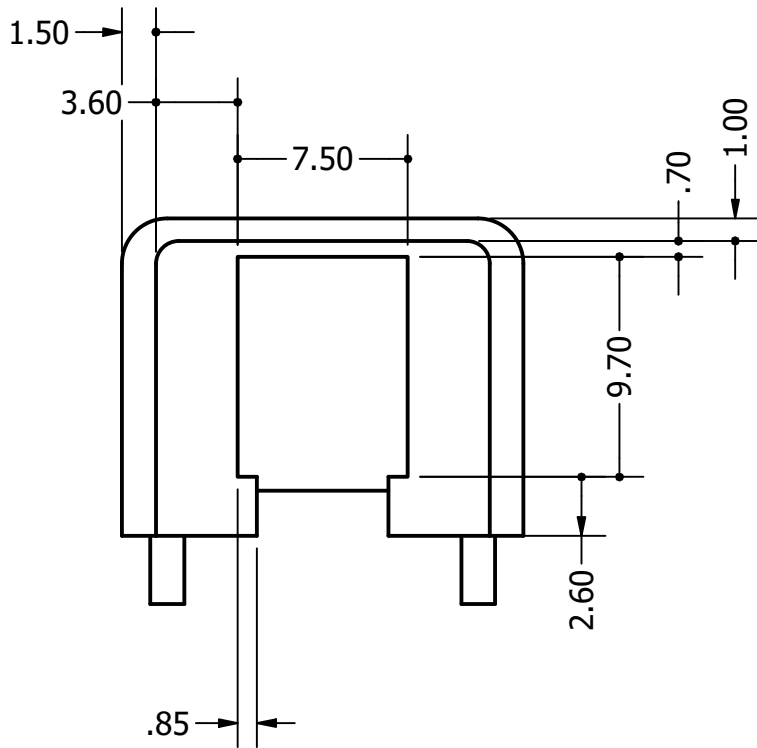
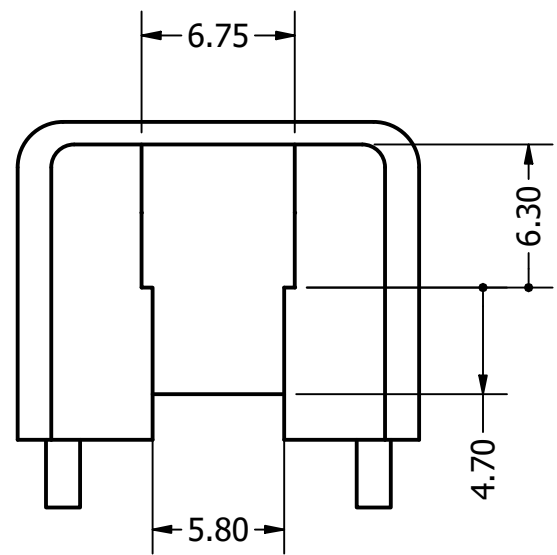
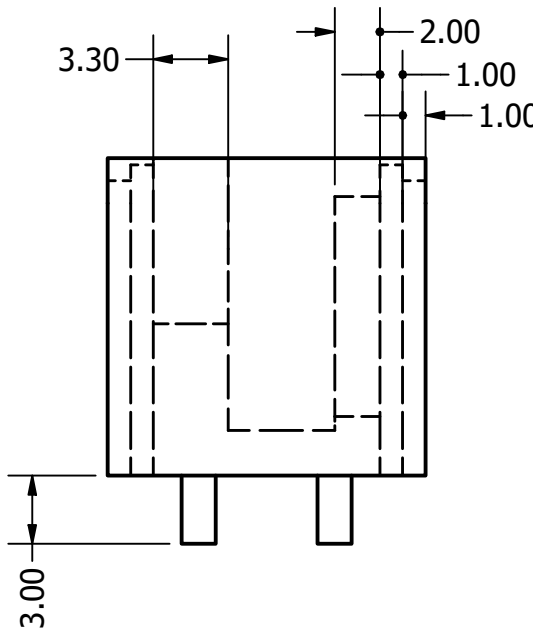


AUTHOR	Kai Page	DATE	11-APR-20	PART NO.
PROJECTION		TITLE	Fingertip Version 1	
UNLESS OTHERWISE STATED TOLERANCE: ANGULAR .X	$\pm 0.15\%$ $\pm 0.15\%$	UNIT	mm	
SCALE	3:1	DWG NO	DWG-100-A	SHEETS
				1 OF 2

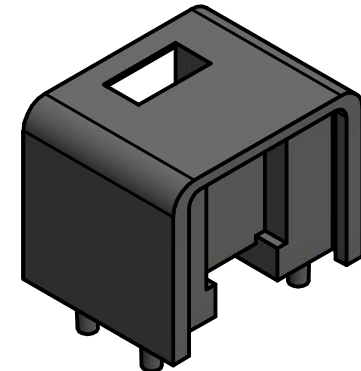
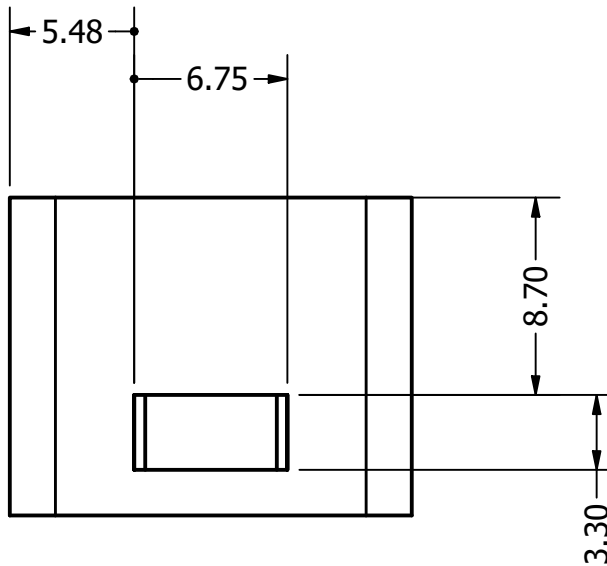
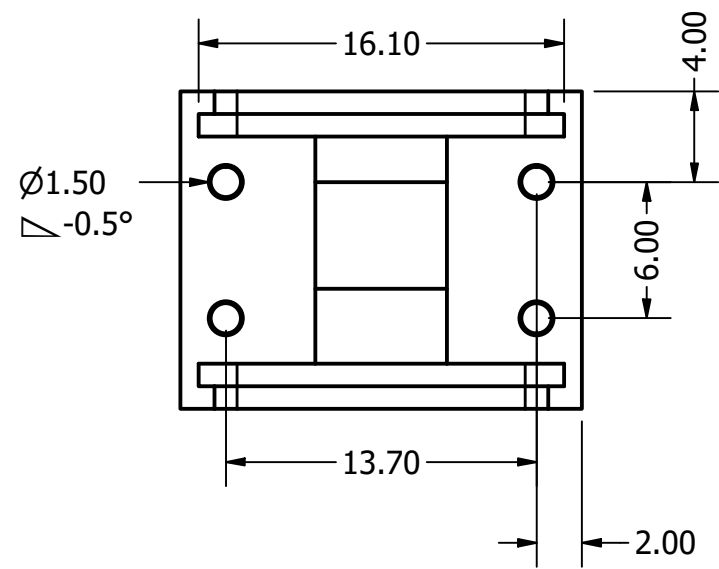




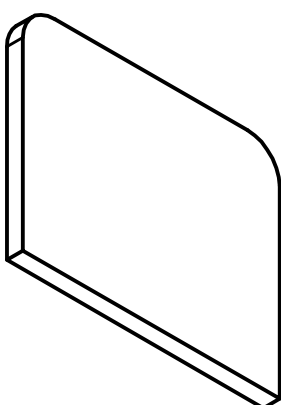
AUTHOR	Kai Page	DATE	14-APR-20	PART NO.	RH-101
PROJECTION		TITLE	Fingertip Lid Version 1		
UNLESS OTHERWISE STATED TOLERANCE: ANGULAR .X	$\pm 0.15\%$ $\pm 0.15\%$	UNIT mm	SCALE 3:1	DWG NO DWG-101-A	SHEETS 1 OF 1



AUTHOR	Kai Page	DATE	14-APR-20	PART NO.	RH-102
PROJECTION		TITLE	3D Fingertip		
UNLESS OTHERWISE STATED TOLERANCE: ANGULAR .X	$\pm 0.15\%$ $\pm 0.15\%$	UNIT	mm		
SCALE	3:1	DWG NO	DWG-102-A	SHEETS	1 OF 2

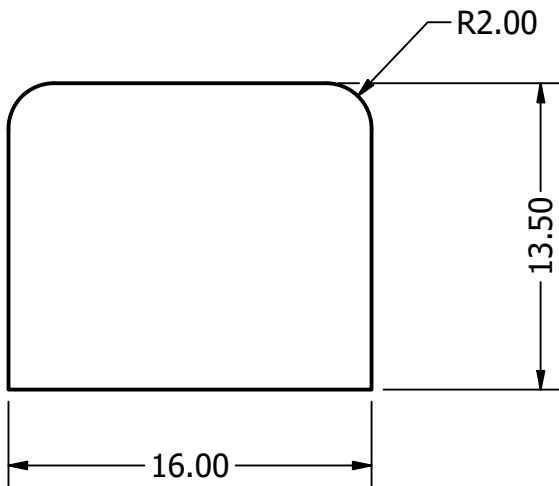


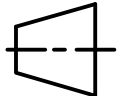
AUTHOR	Kai Page	DATE	14-APR-20	PART NO.	RH-102
PROJECTION			TITLE	3D Fingertip	
UNLESS OTHERWISE STATED TOLERANCE: ANGULAR .X	$\pm 0.15\%$ $\pm 0.15\%$	UNIT mm	SCALE 3:1	DWG NO DWG-102-B	SHEETS 2 OF 2

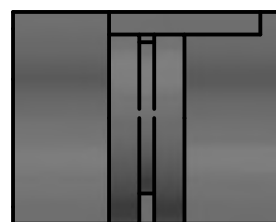
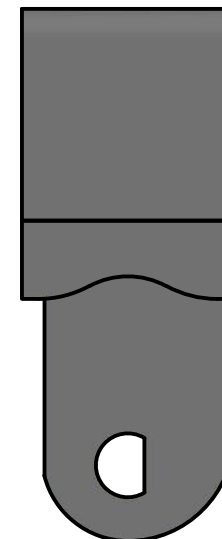
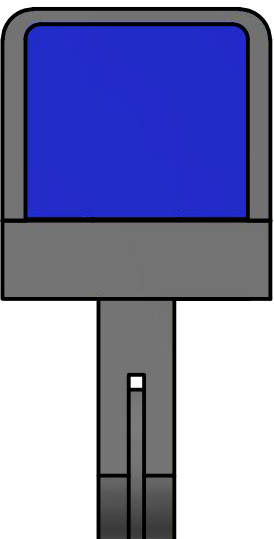
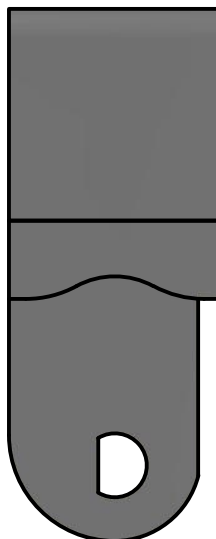


1.00

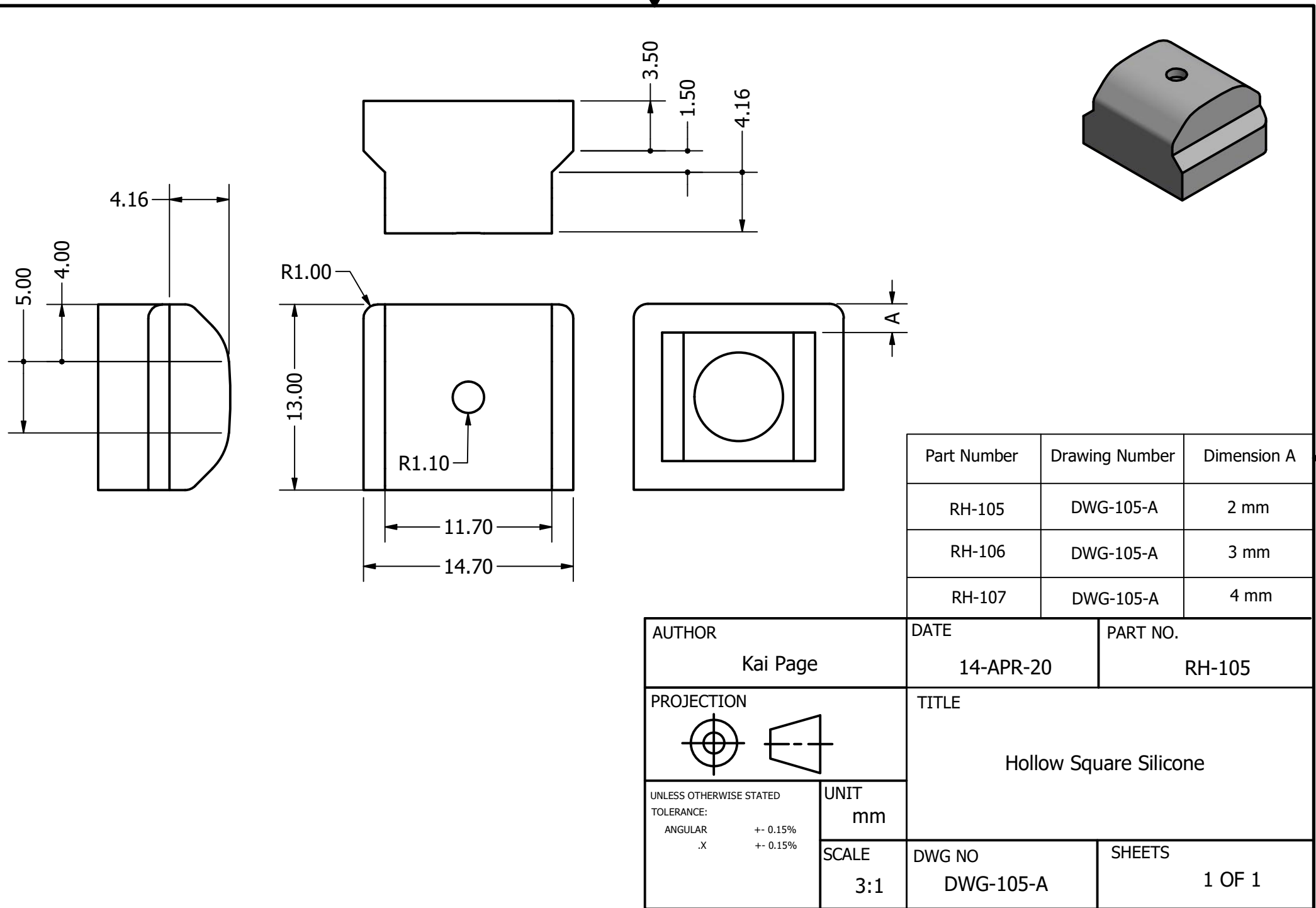
2.00

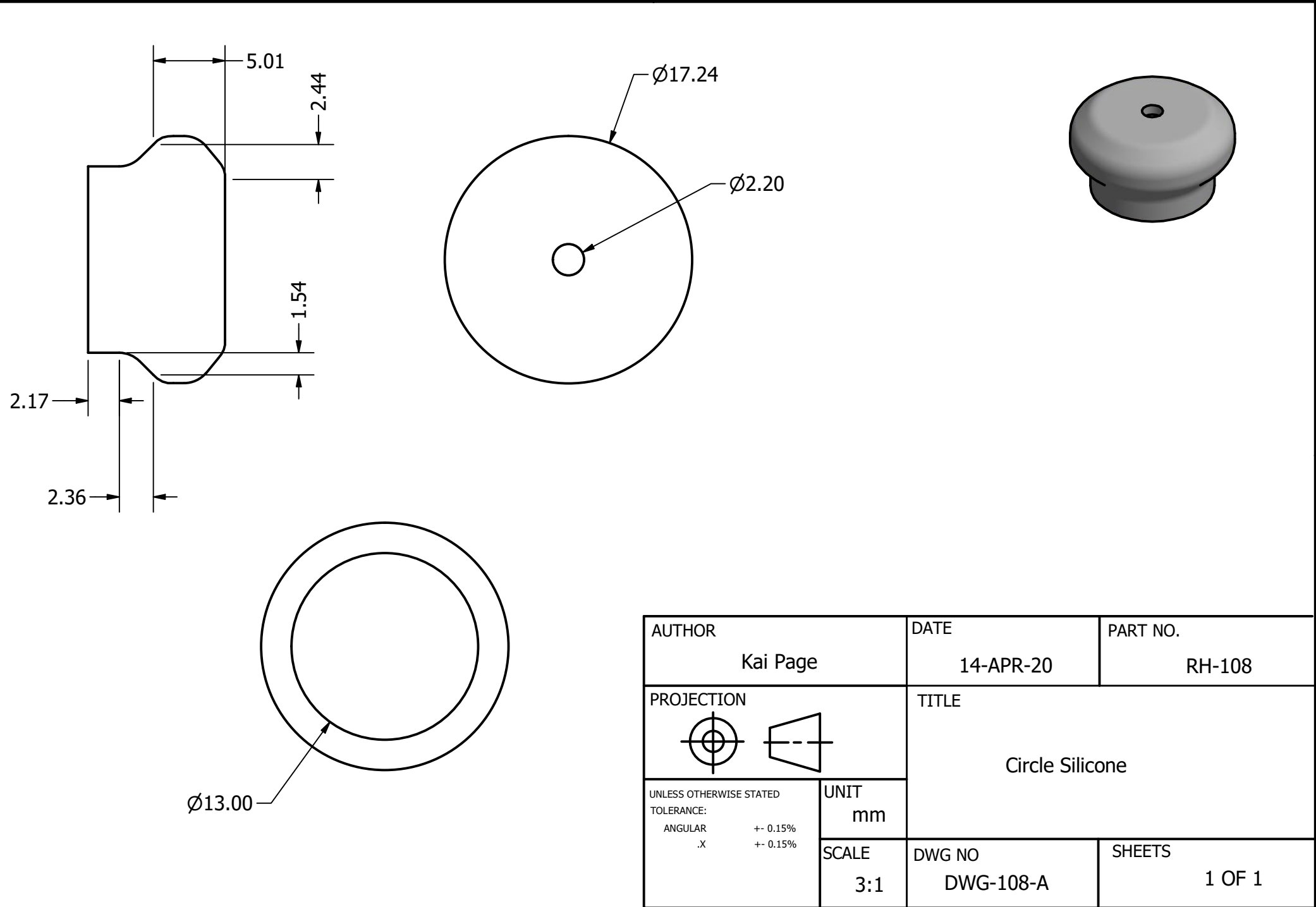


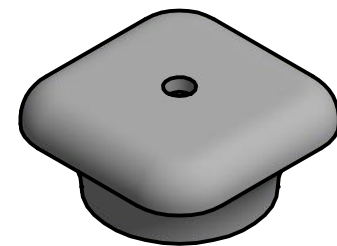
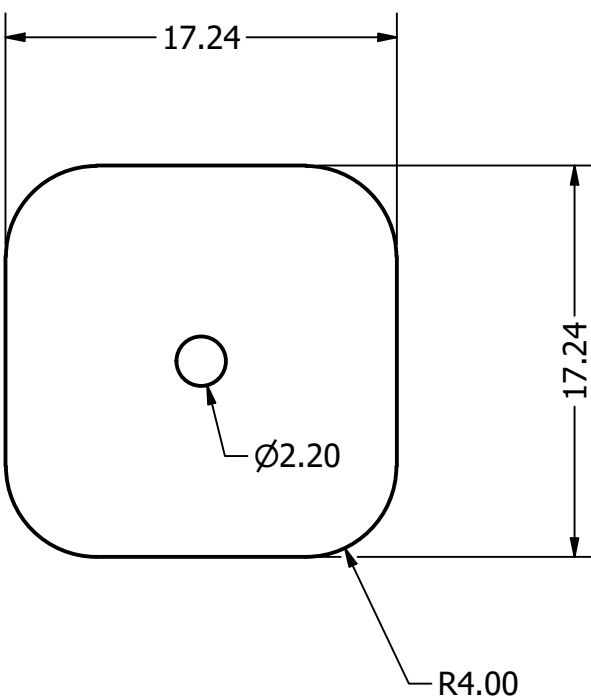
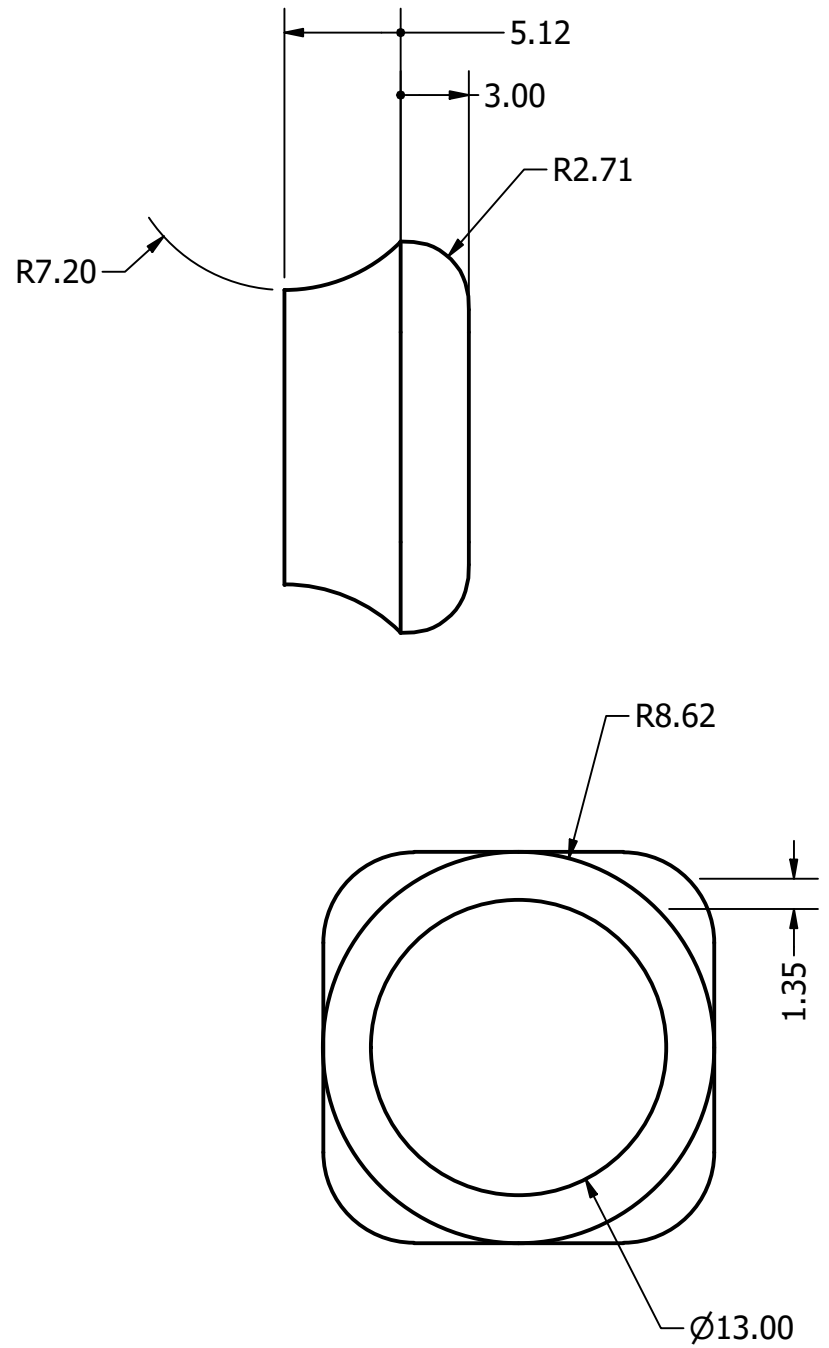
AUTHOR	Kai Page	DATE	14-APR-20	PART NO.	RH-103
PROJECTION	 	TITLE	Fingertip Lid		
UNLESS OTHERWISE STATED TOLERANCE: ANGULAR .X	$\pm 0.15\%$ $\pm 0.15\%$	UNIT	mm	SCALE	DWG NO DWG-103-A
		3:1		SHEETS	1 OF 1



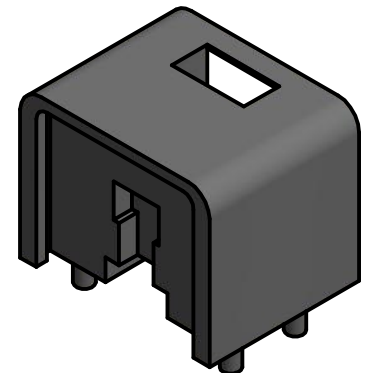
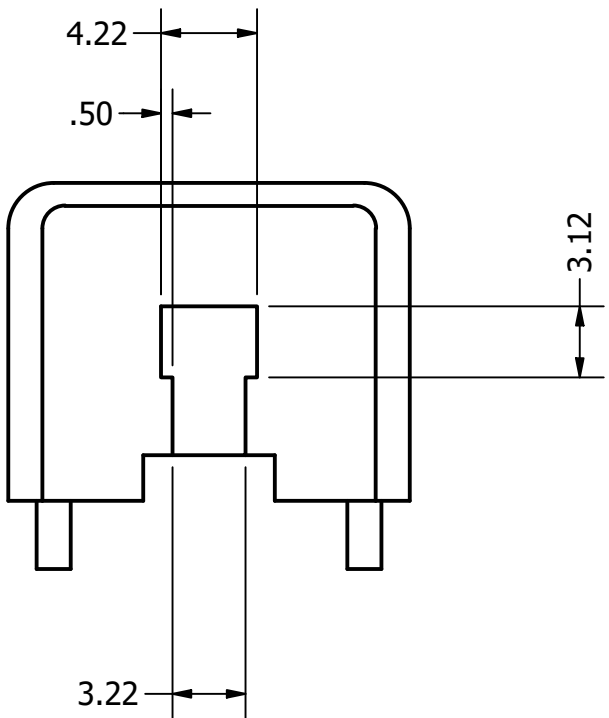
AUTHOR	Kai Page	DATE	14-APR-20	PART NO.	RH-104
PROJECTION	 	TITLE	Fingertip Assembly		
UNLESS OTHERWISE STATED TOLERANCE: ANGULAR .X	+- 0.15% +- 0.15%	UNIT	mm	SCALE	DWG NO DWG-104-A
		3:1		SHEETS	1 OF 1





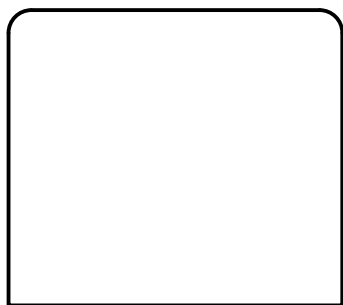
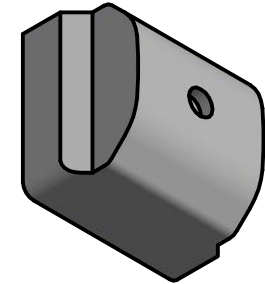
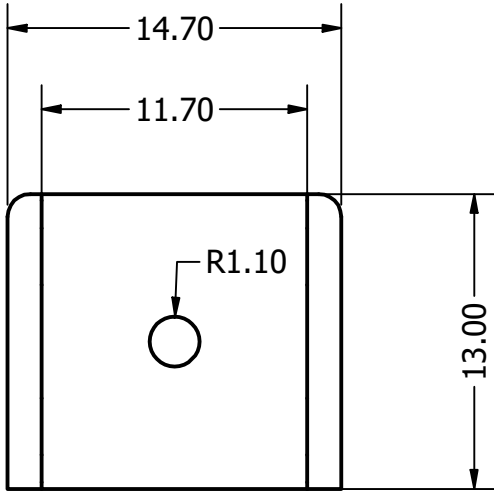
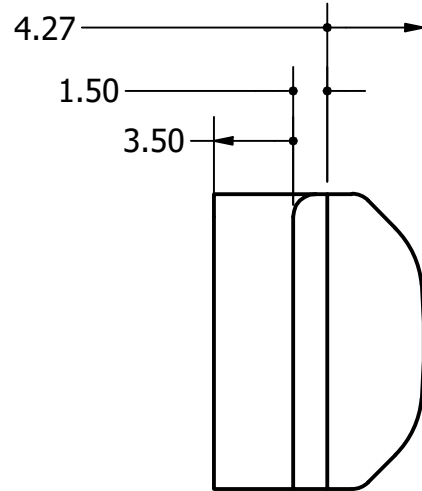


AUTHOR	Kai Page	DATE	14-APR-20	PART NO.	RH-109
PROJECTION			TITLE	Square Curve Silicone	
UNLESS OTHERWISE STATED TOLERANCE: ANGULAR .X	$\pm 0.15\%$ $\pm 0.15\%$	UNIT mm	SCALE 3:1	DWG NO DWG-109-A	SHEETS 1 OF 1

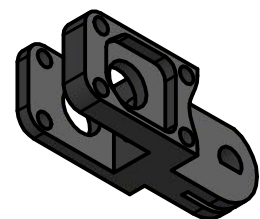
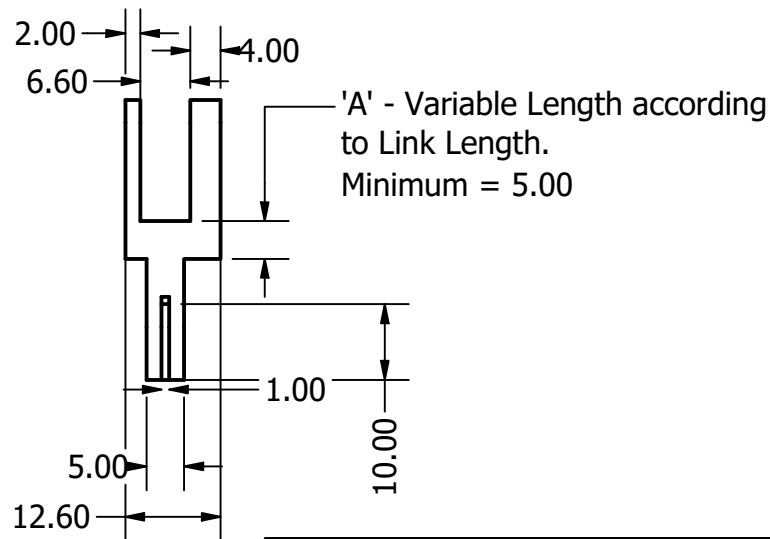
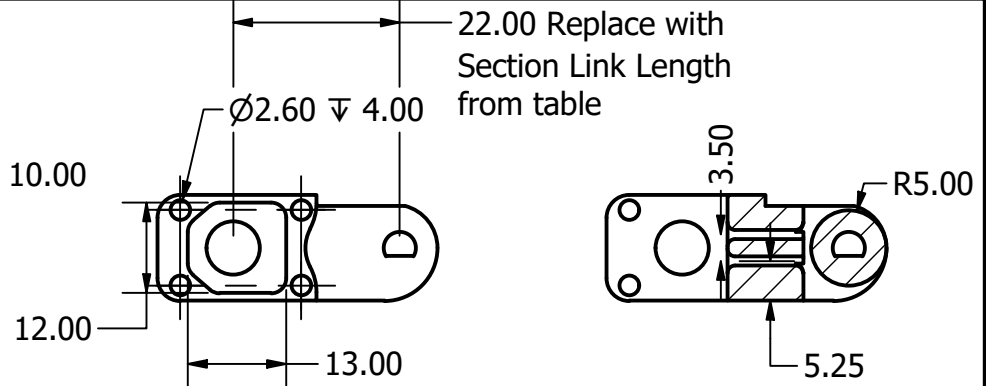
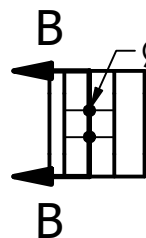
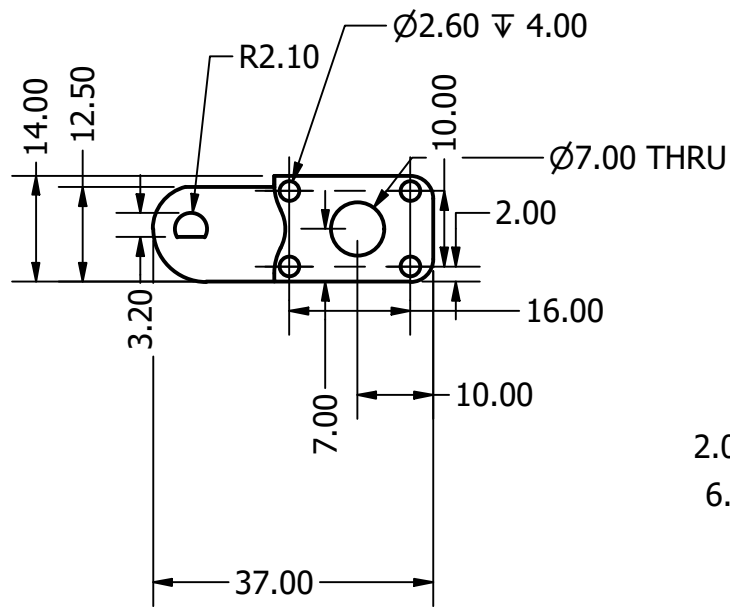


\*NOTE\*: All other dimensions remain the same as  
Part No. RH-102

AUTHOR	Kai Page	DATE	14-APR-20	PART NO.	RH-110
PROJECTION	 	TITLE	1D Fingertip		
UNLESS OTHERWISE STATED TOLERANCE: ANGULAR .X	$\pm 0.15\%$ $\pm 0.15\%$	UNIT	mm	SCALE	DWG NO DWG-110-A
				3:1	SHEETS 1 OF 1

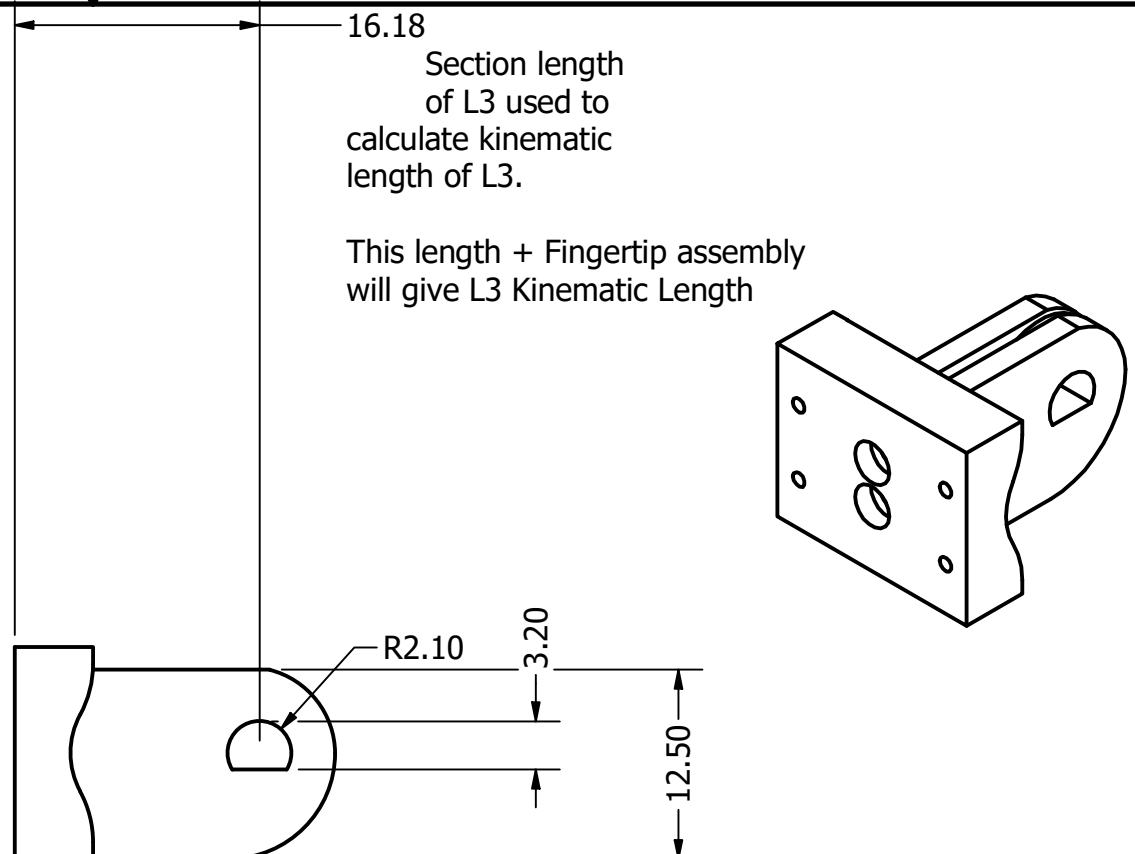
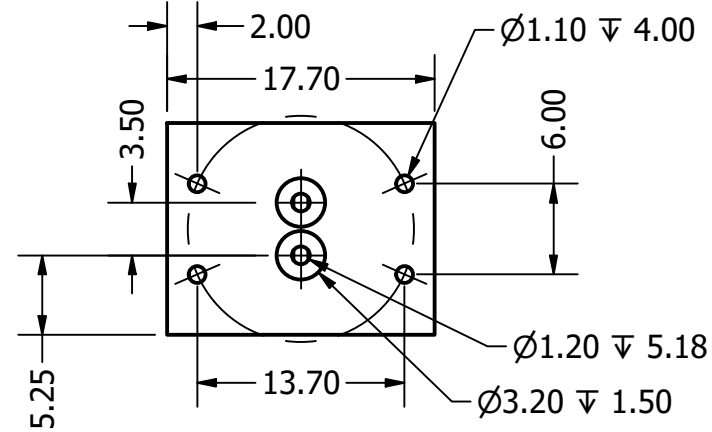
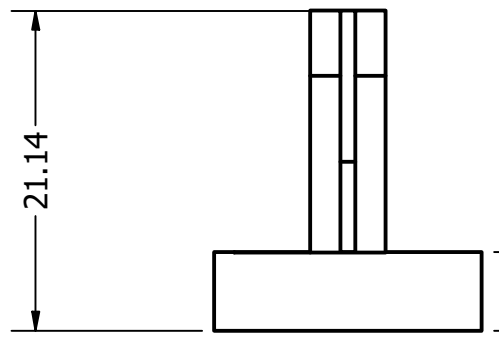


AUTHOR	Kai Page	DATE	14-APR-20	PART NO.	RH-111
PROJECTION			TITLE	Non- Hollow Square Silicone	
UNLESS OTHERWISE STATED TOLERANCE: ANGULAR .X	$\pm 0.15\%$ $\pm 0.15\%$	UNIT mm	SCALE 3:1	DWG NO DWG-111-A	SHEETS 1 OF 1

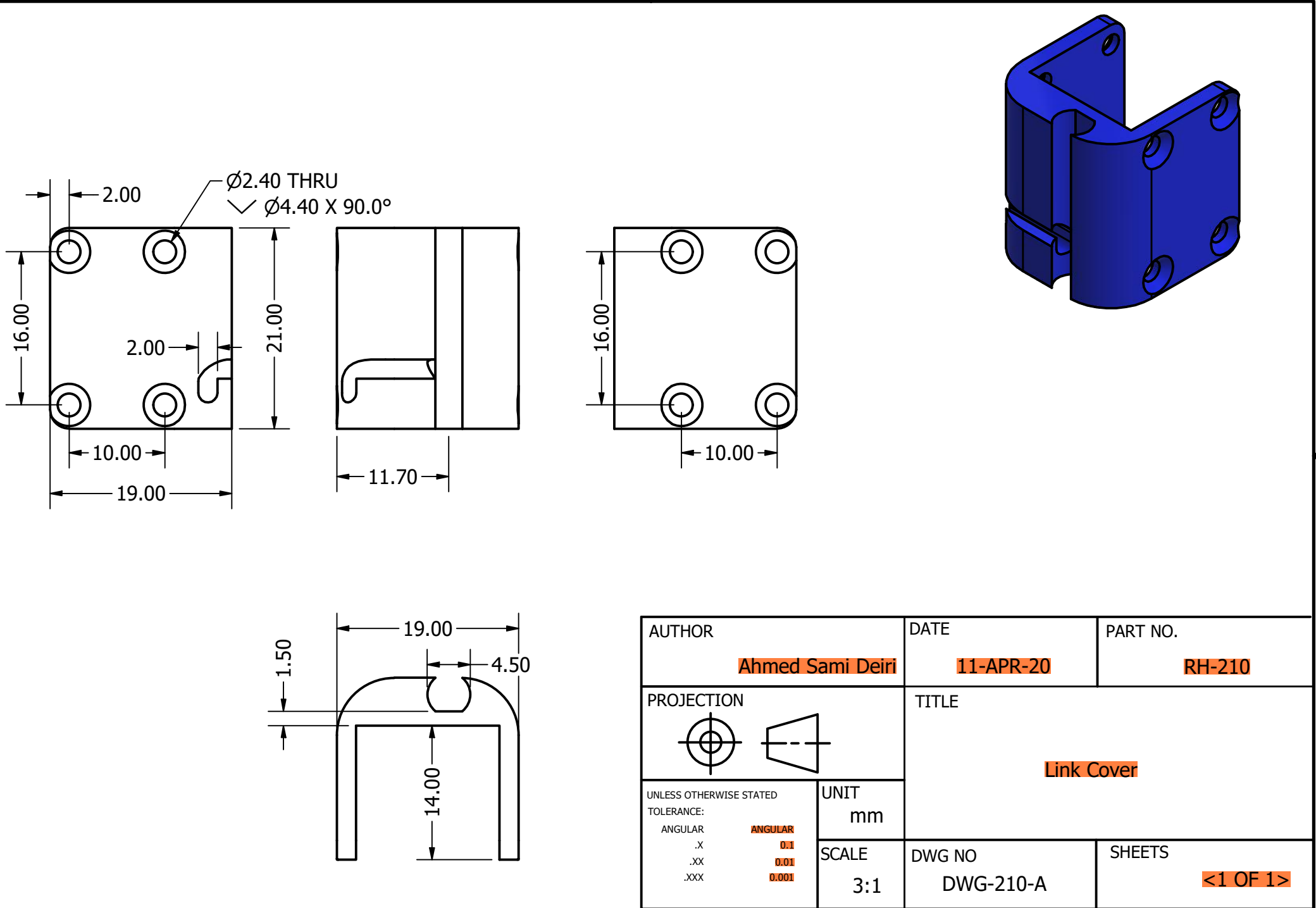


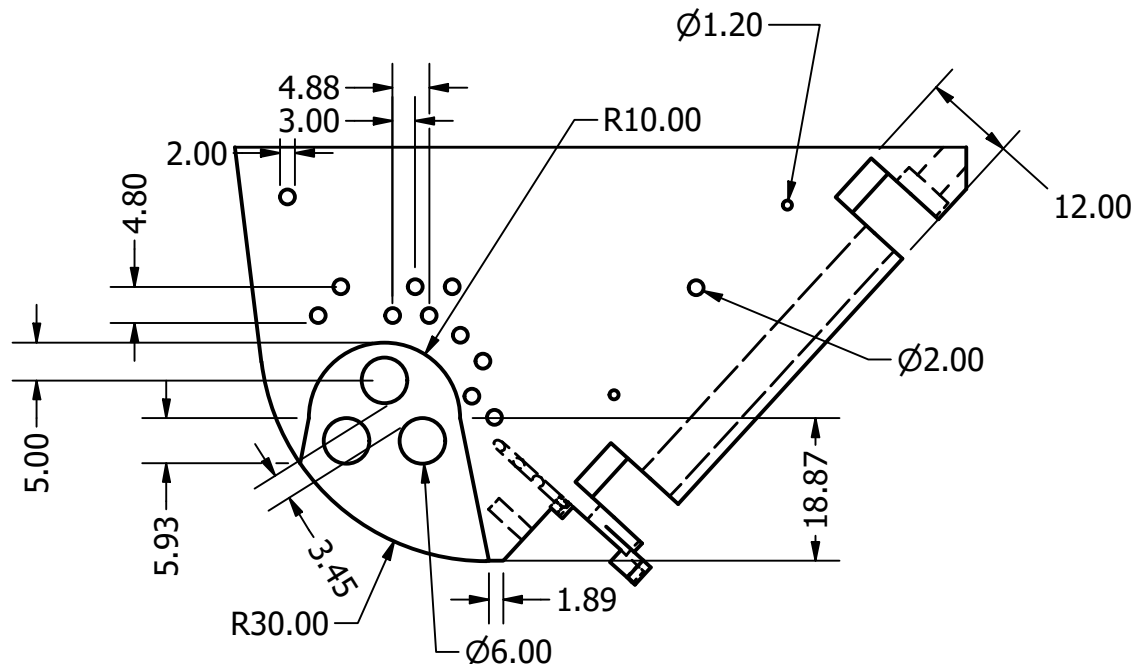
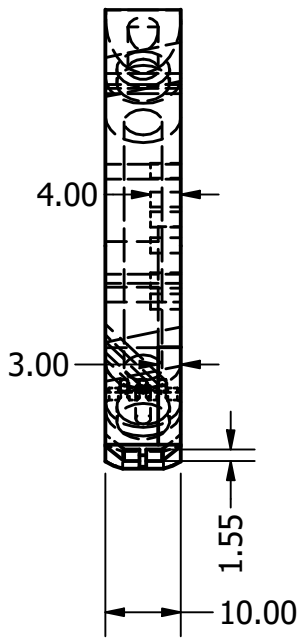
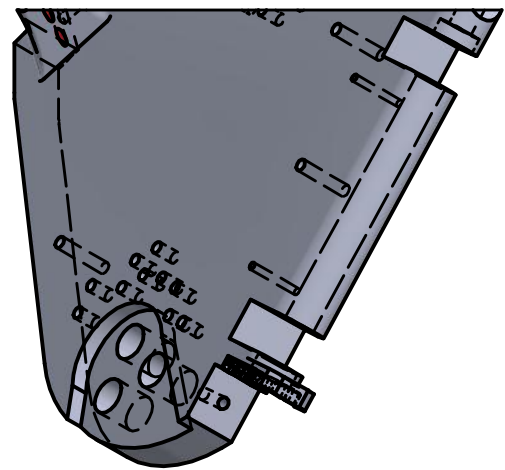
**SECTION B-B**  
**SCALE 1 : 1**

AUTHOR	DATE	PART NO.
Ahmed Sami Deiri	14-APR-20	RH-200 - 215
PROJECTION	TITLE	
	Link Body	
UNLESS OTHERWISE STATED TOLERANCE: ANGULAR .X ++ 0.15% ++ 0.15%	UNIT mm	SCALE 1:1
	DWG NO	SHEETS
	DWG-200-A	1 OF 2

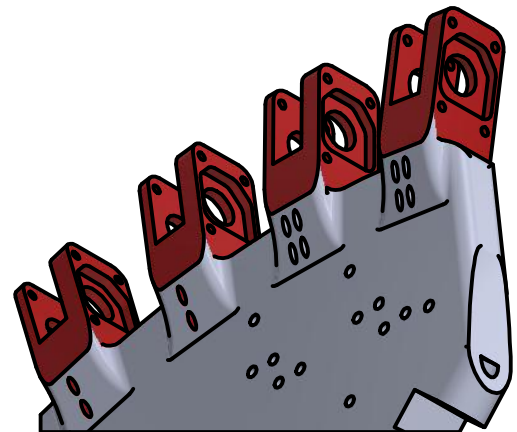
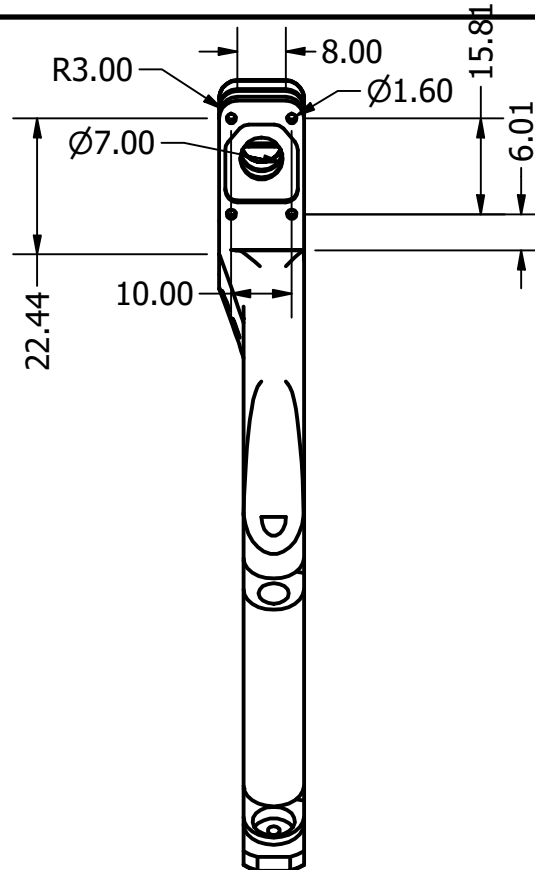
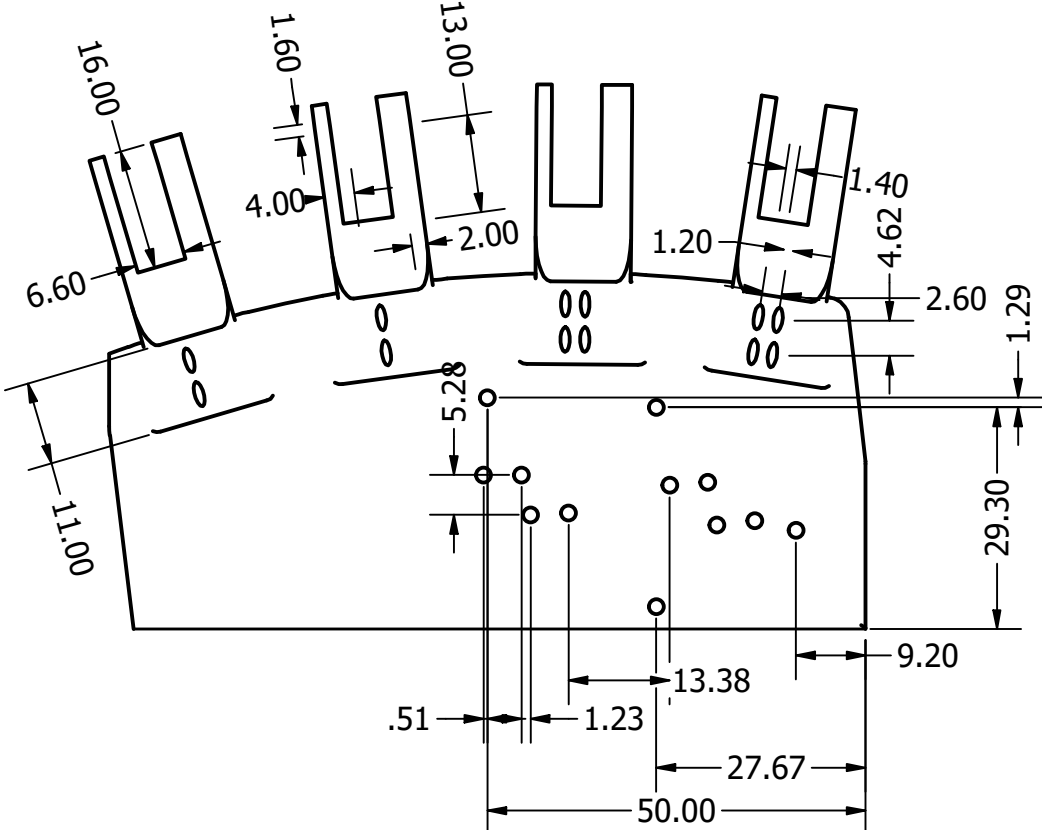


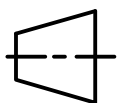
AUTHOR	Ahmed Sami Deiri	DATE	11-APR-20	PART NO.	RH-211 -> RH-215
PROJECTION		TITLE	Link Body 3		
UNLESS OTHERWISE STATED TOLERANCE: ANGULAR .X .XX .XXX	<b>ANGULAR</b> <b>0.1</b> <b>0.01</b> <b>0.001</b>	UNIT	mm	SCALE	DWG NO <DWG-211-A>
		3:1		SHEETS	<b>&lt;1 OF 1&gt;</b>

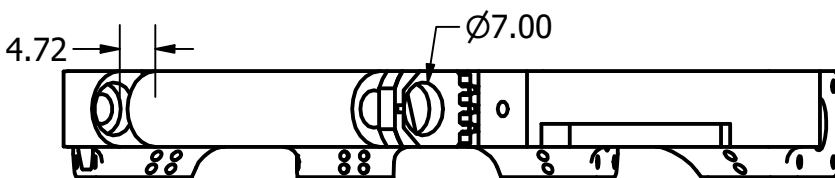
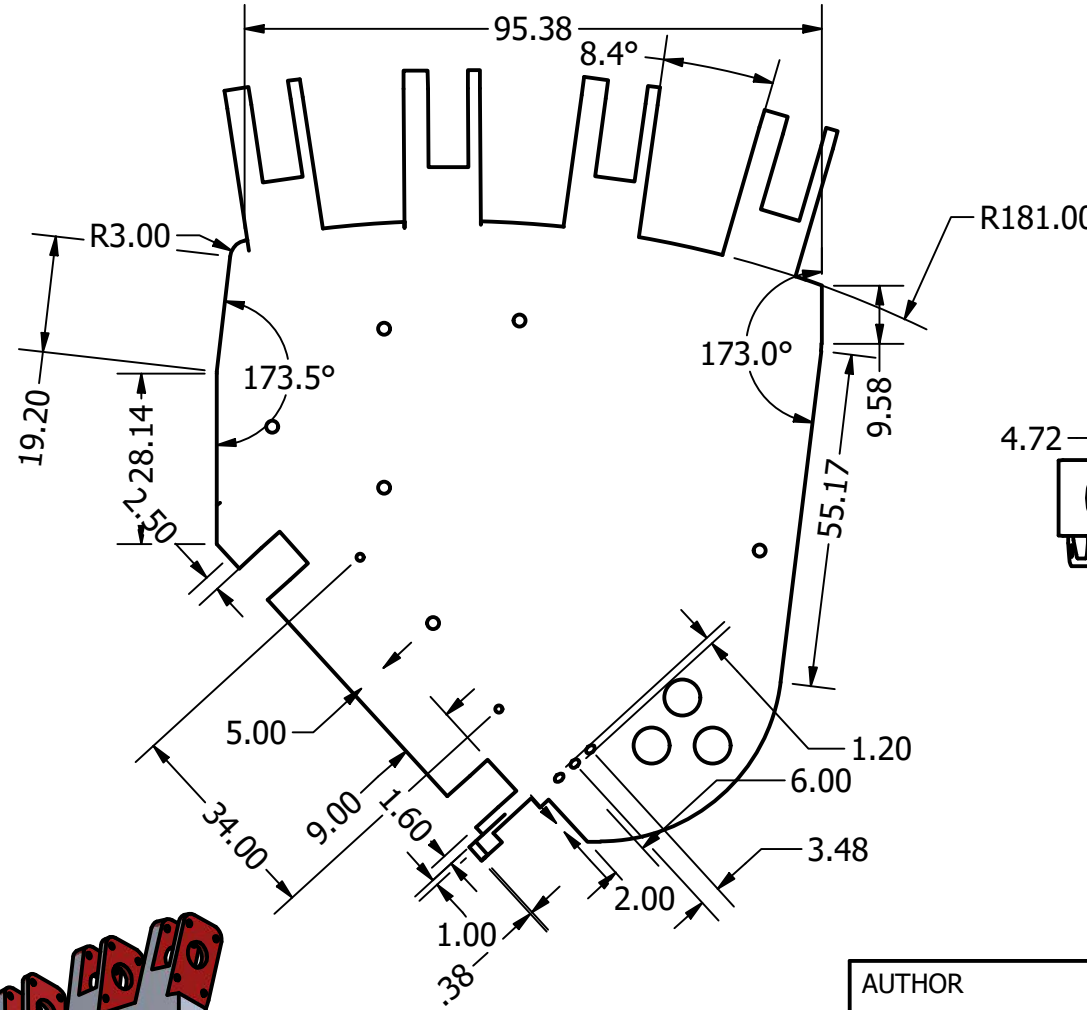
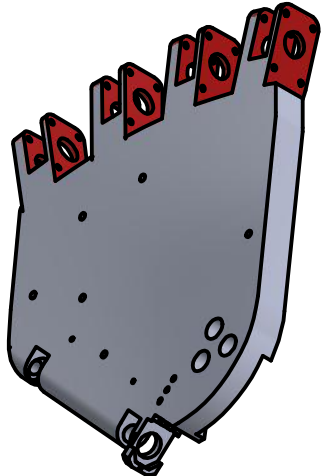




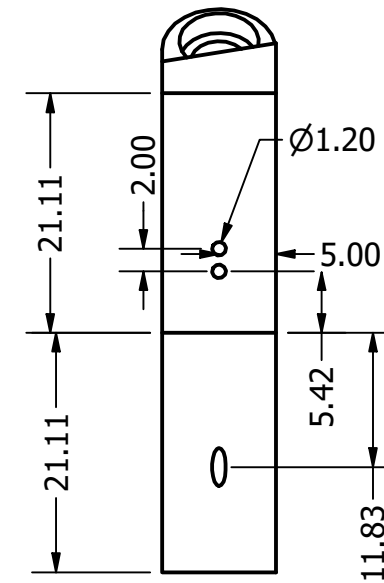
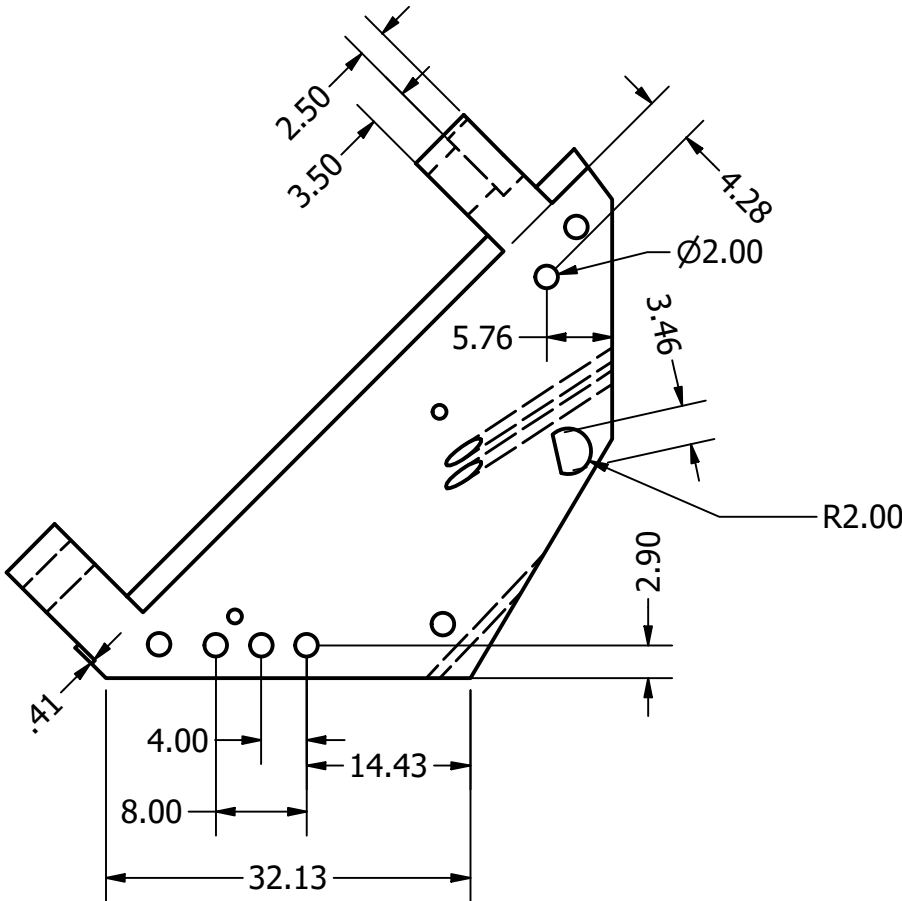
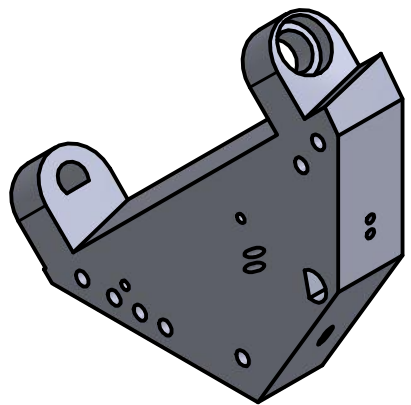
AUTHOR	T Tailor	DATE	04-May-20	PART NO.	<RH-300>
PROJECTION		TITLE		Palm Structure 1	
UNLESS OTHERWISE STATED TOLERANCE: ANGULAR .X	+0.15% +0.15%	UNIT	mm	SCALE	DWG NO <DWG-300-A>
		1:1		SHEETS	<1 OF 3>



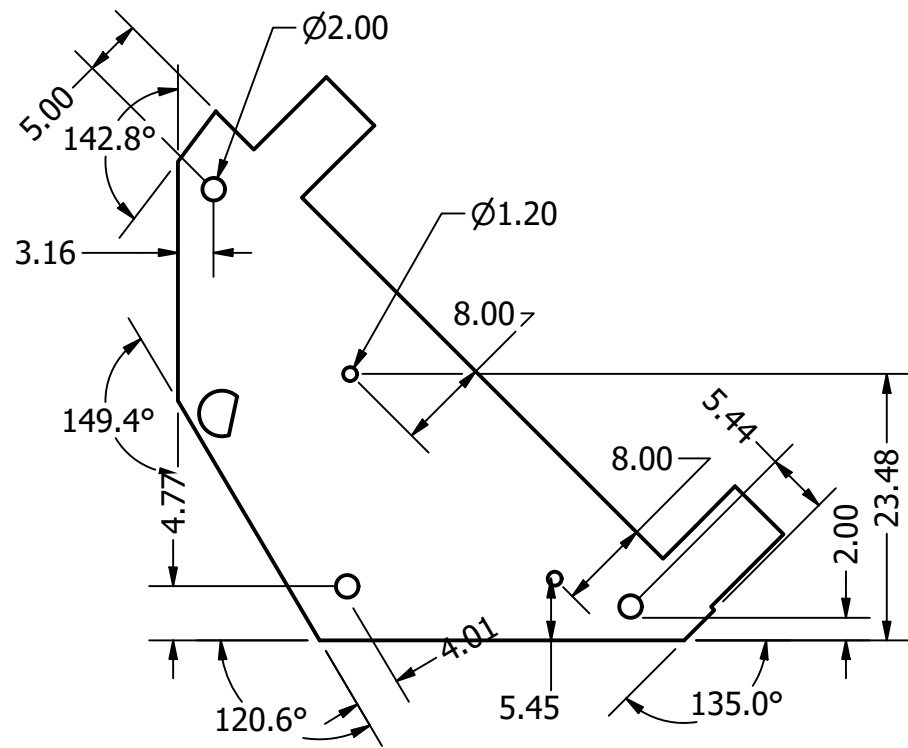
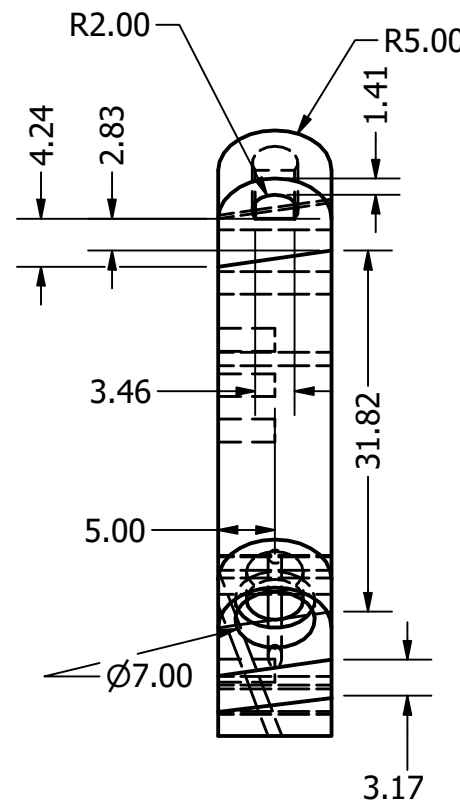
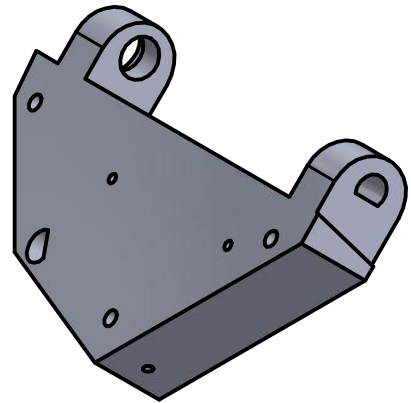
AUTHOR	T Tailor	DATE	04-May-20
PROJECTION	 	TITLE	Palm Structure 1
UNLESS OTHERWISE STATED TOLERANCE: ANGULAR .X	+0.15% +0.15%	UNIT	mm
		SCALE	DWG NO
		1:1	<DWG-300-B>
			SHEETS
			<2 OF 3>



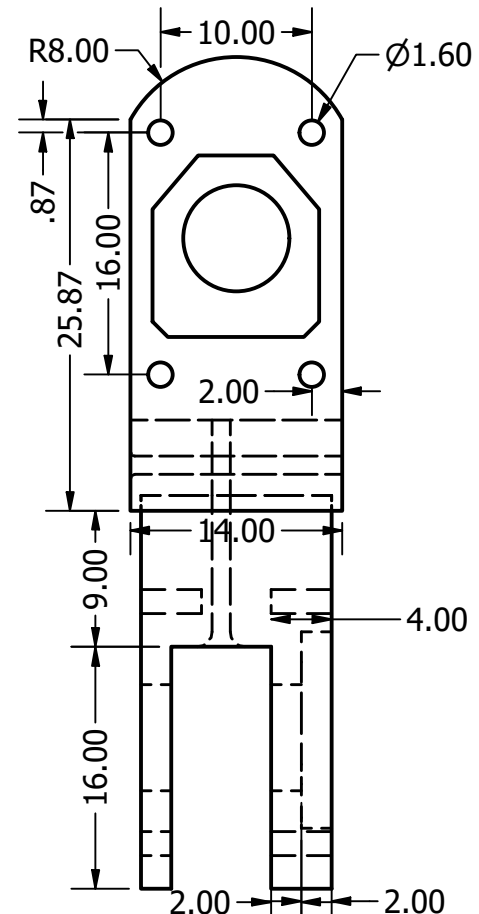
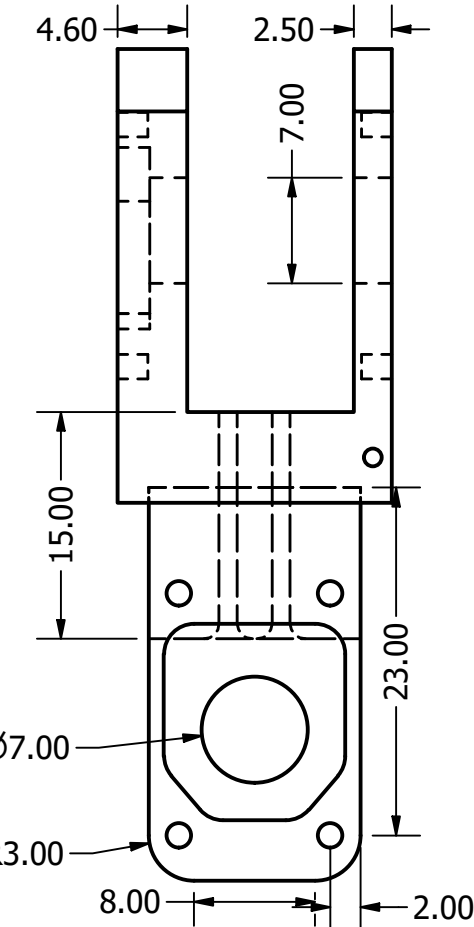
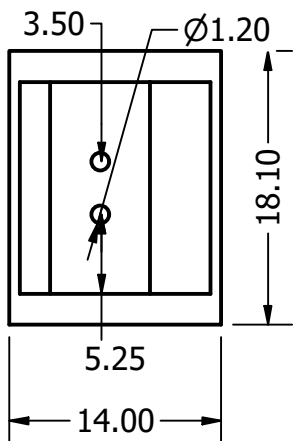
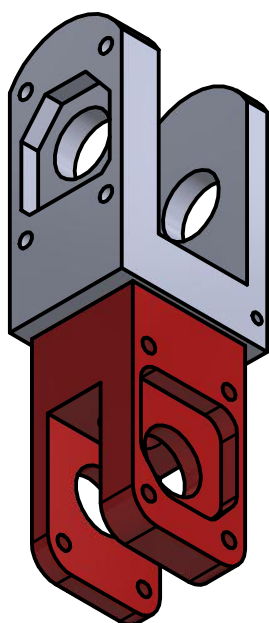
AUTHOR	T Tailor	DATE	04-May-20	PART NO.	<RH-300>
PROJECTION		TITLE		Palm Structure 1	
UNLESS OTHERWISE STATED TOLERANCE: ANGULAR .X	+0.15% +0.15%	UNIT	mm	SCALE	DWG NO <DWG-300-C>
		1:1		SHEETS	<3 OF 3>



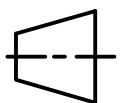
AUTHOR	T Tailor	DATE	04-MAY-20	PART NO.	RH-301
PROJECTION				TITLE	Palm Structure 2
UNLESS OTHERWISE STATED TOLERANCE: ANGULAR .X	$\pm 0.15\%$ $\pm 0.15\%$	UNIT mm		SCALE	DWG NO DWG-301-A
			3:1	SHEETS	1 OF 1

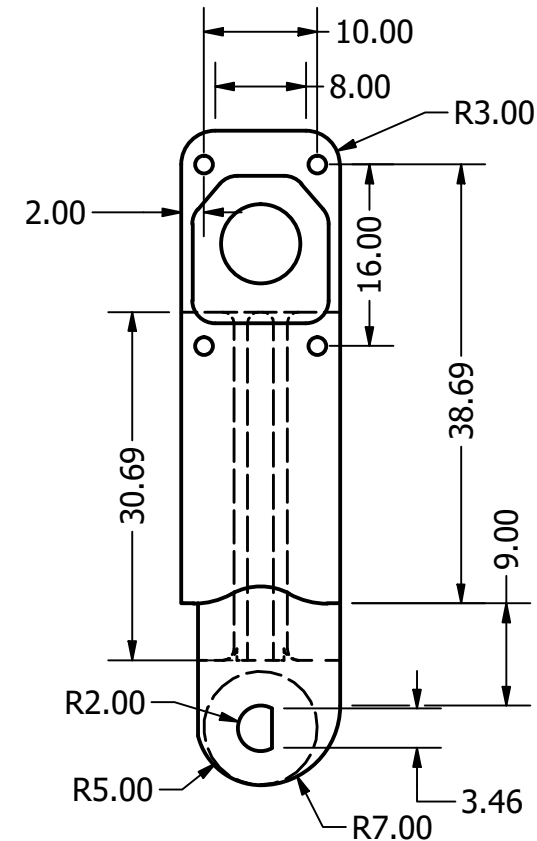
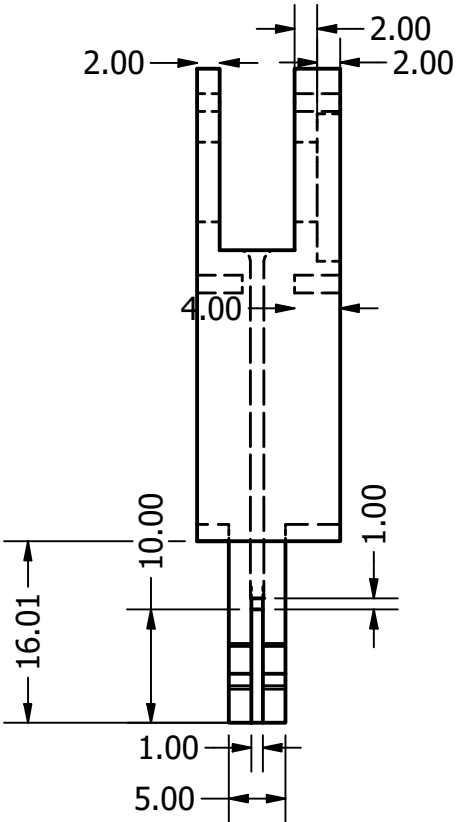
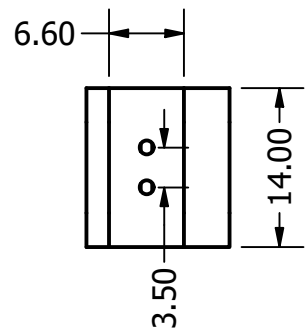
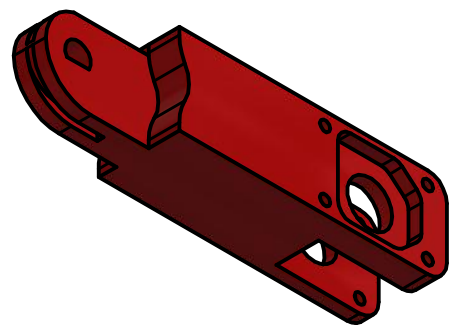


AUTHOR	T Tailor	DATE	04-MAY-20	PART NO.	RH-301
PROJECTION				TITLE	Palm Structure 2
UNLESS OTHERWISE STATED TOLERANCE: ANGULAR .X	$\pm 0.15\%$ $\pm 0.15\%$	UNIT mm		SCALE	DWG NO DWG-301-B
			3:1	SHEETS	1 OF 2



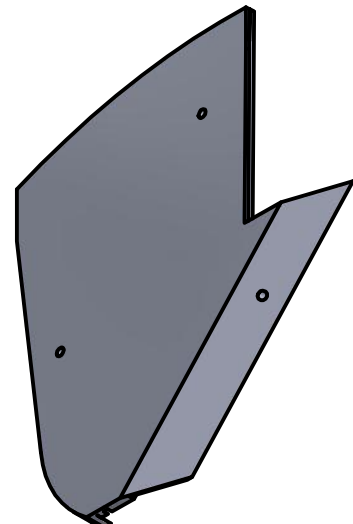
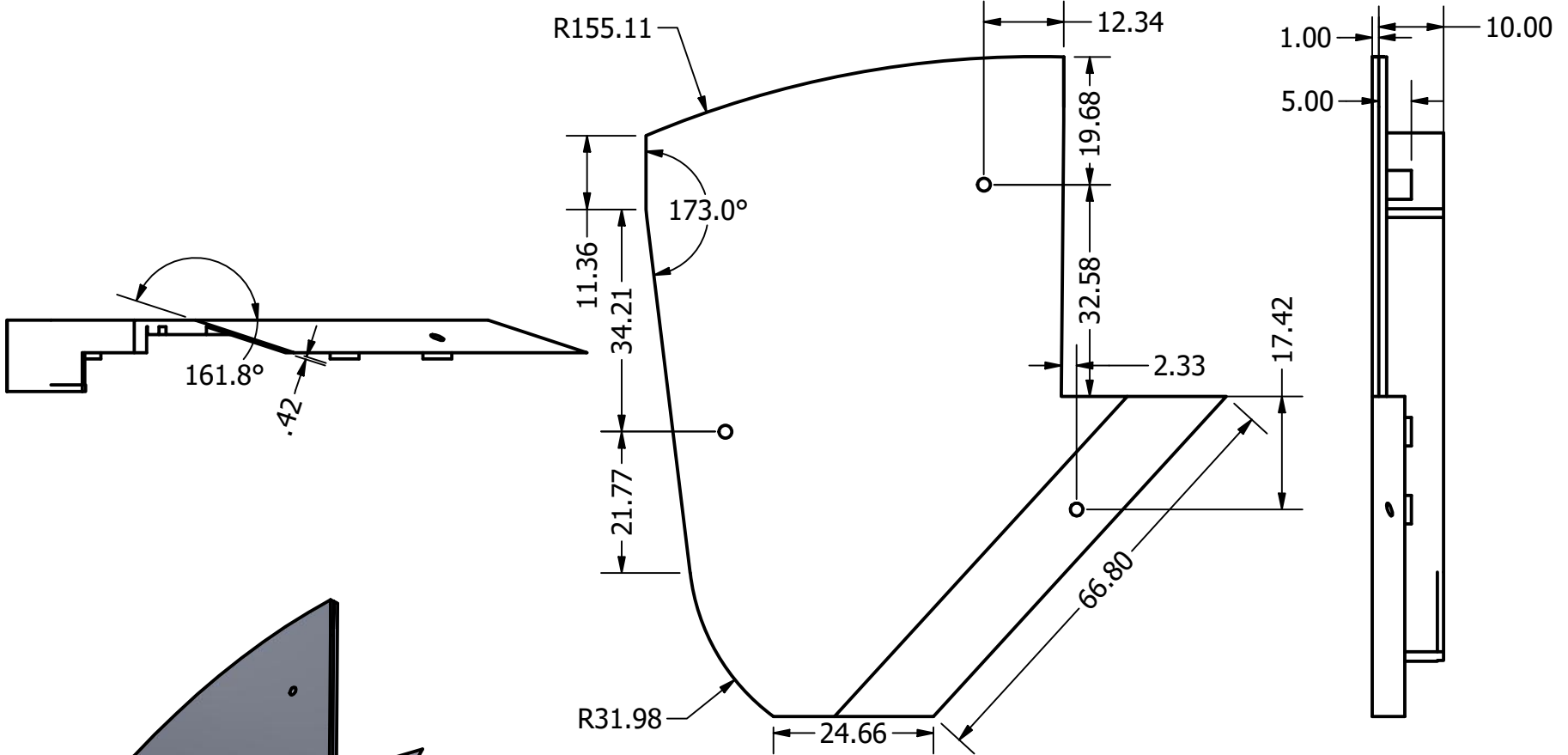
**Note:** Potenitometer dimension are identical to those of previous drawings, and thus are not explicitly stated in the following drawings.

AUTHOR	T Tailor	DATE	04-MAY-20	PART NO.	RH-302
PROJECTION	 	TITLE	Thumb Body 1		
UNLESS OTHERWISE STATED TOLERANCE: ANGULAR .X	+- 0.15% +- 0.15%	UNIT	mm	SCALE	DWG NO DWG-302-A
					SHEETS 1 OF 1



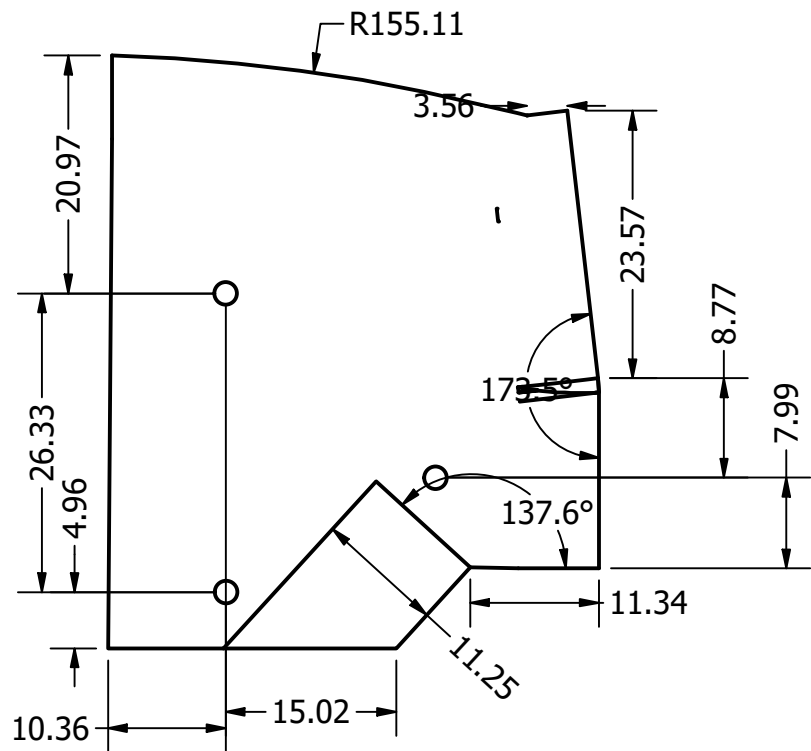
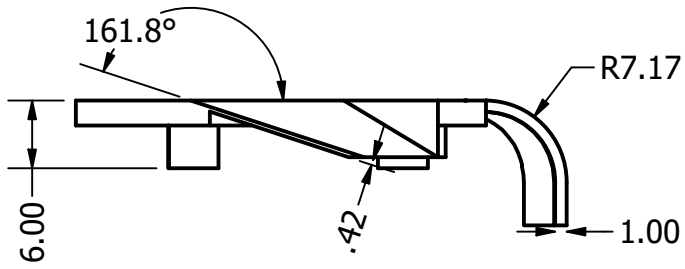
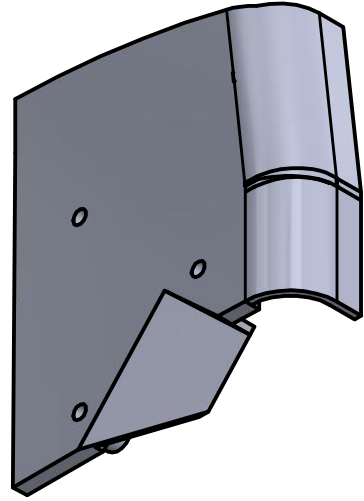
**Note:** Potentiometer dimension are identical to those of previous drawings, and thus are not explicitly stated in the following drawings.

AUTHOR	T Tailor	DATE	04-MAY-20	PART NO.	RH-303
PROJECTION		TITLE	Thumb Body 2		
UNLESS OTHERWISE STATED TOLERANCE: ANGULAR .X	$\pm 0.15\%$ $\pm 0.15\%$	UNIT	mm	SCALE	DWG NO DWG-303-A
					SHEETS 1 OF 1



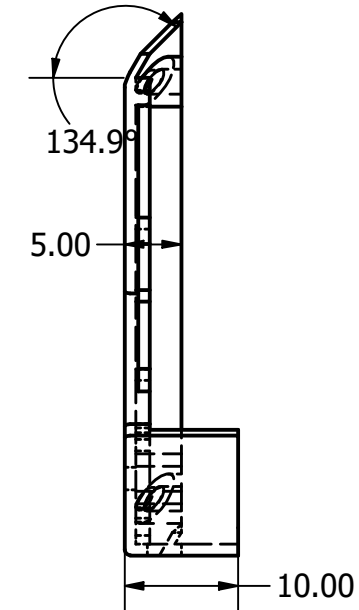
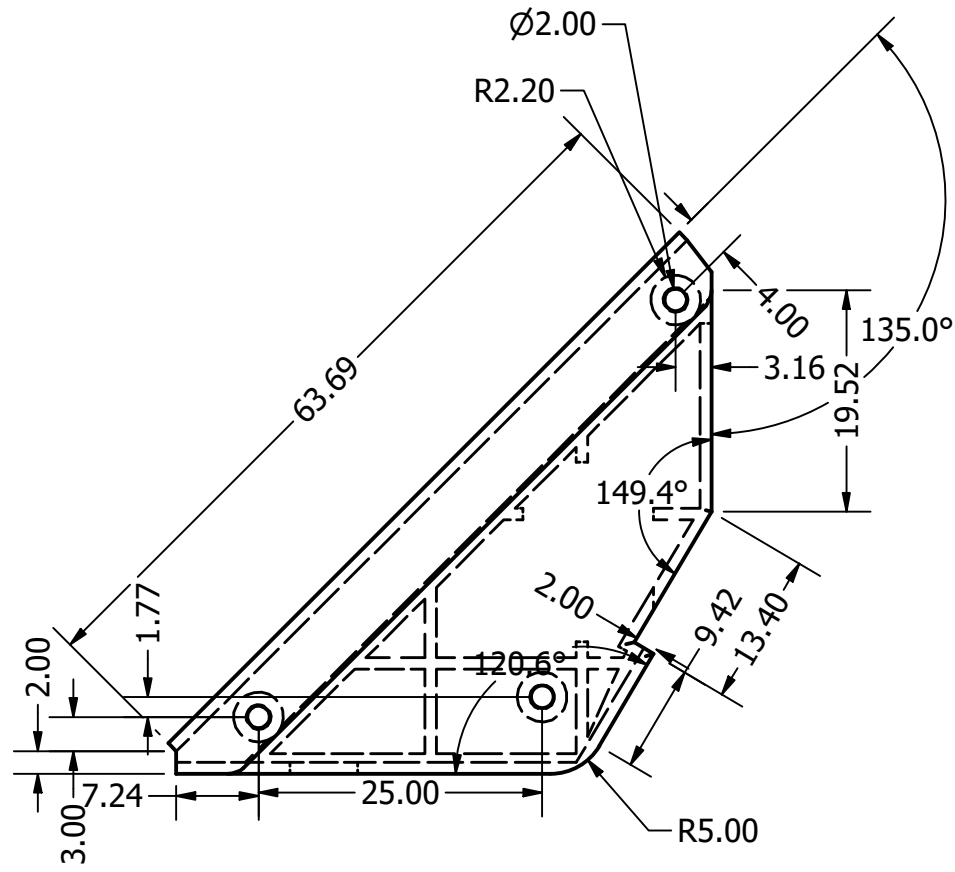
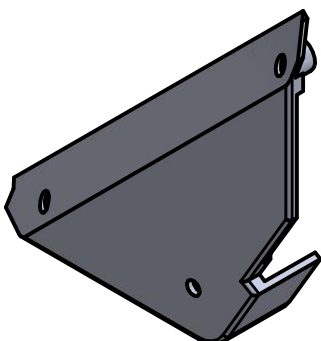
**Note-** Support rib measurements have been left undefined as they do not play a vital role to the concept design, and can thus be arbitrarily added if model is reproduced.

AUTHOR	T Tailor	DATE	04-MAY-20	PART NO.	RH-304
PROJECTION	 	TITLE	Palm Cover Front - C8		
UNLESS OTHERWISE STATED TOLERANCE: ANGULAR .X	$\pm 0.15\%$ $\pm 0.15\%$	UNIT	mm	SCALE	DWG NO DWG-304-A
					SHEETS 1 OF 1

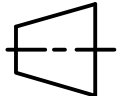


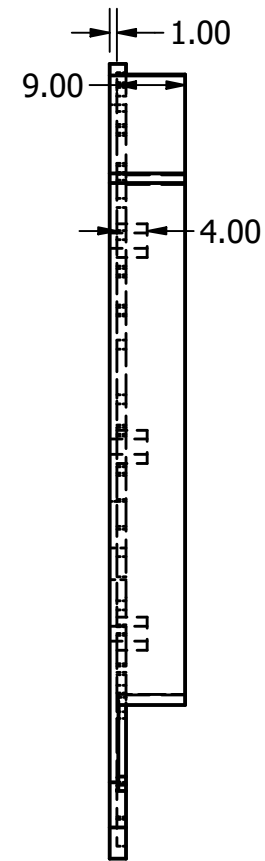
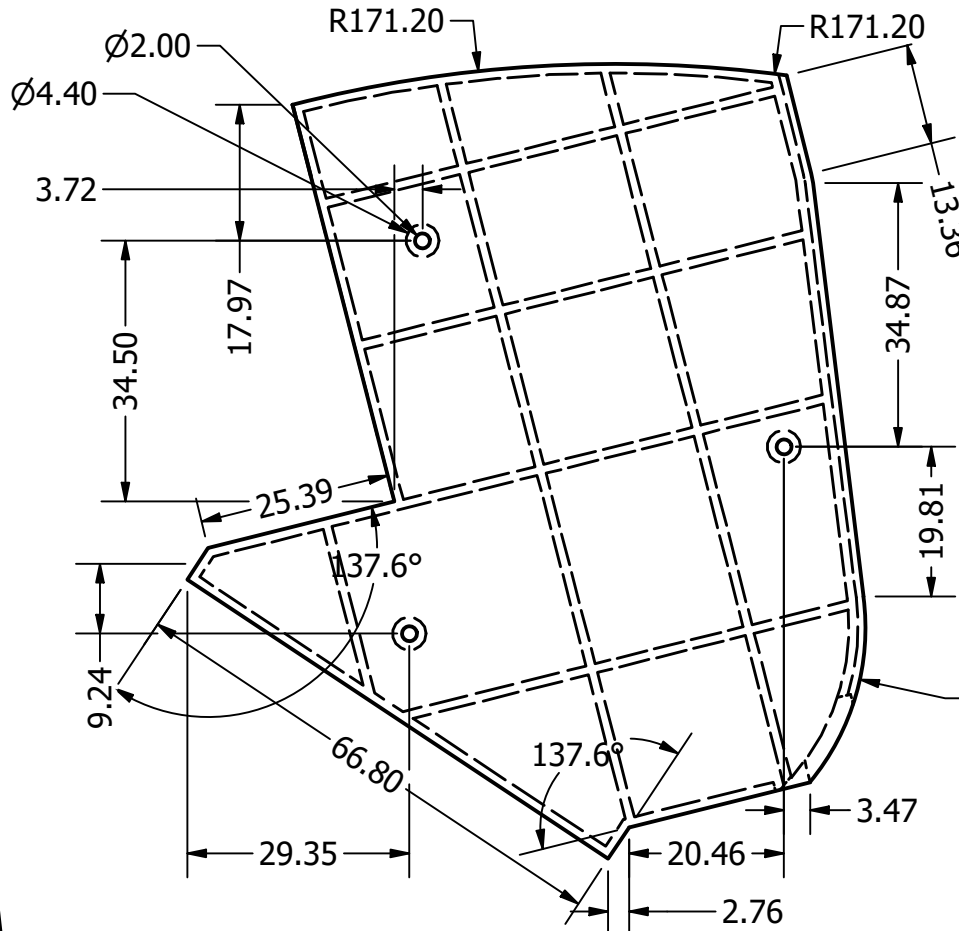
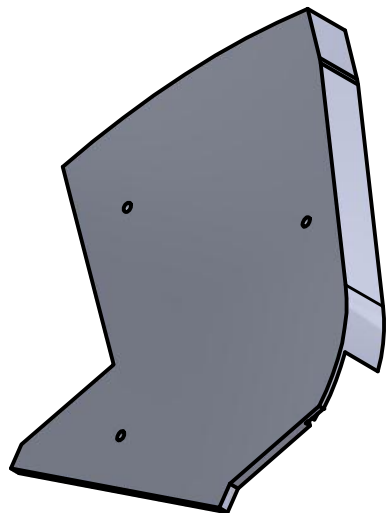
**Note-** Support rib measurements have been left undefined as they do not play a vital role to the concept design, and can thus be arbitrarily added if model is reproduced.

AUTHOR	T Tailor	DATE	04-MAY-20	PART NO.	RH-305
PROJECTION				TITLE	Palm Cover Front - C7
UNLESS OTHERWISE STATED TOLERANCE: ANGULAR .X	$\pm 0.15\%$ $\pm 0.15\%$	UNIT mm		SCALE	DWG NO DWG-305-A
			1.5:1	SHEETS	1 OF 1



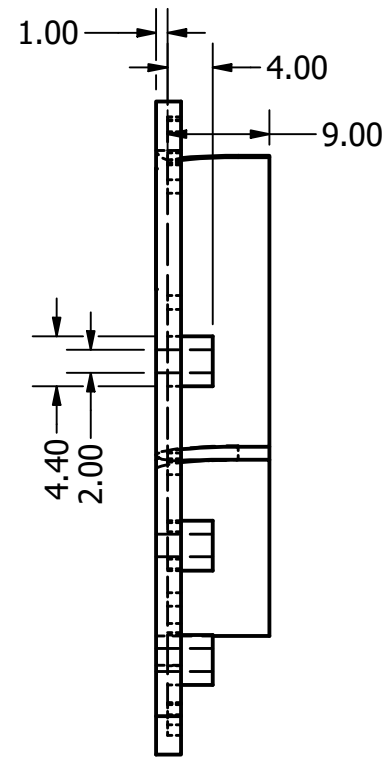
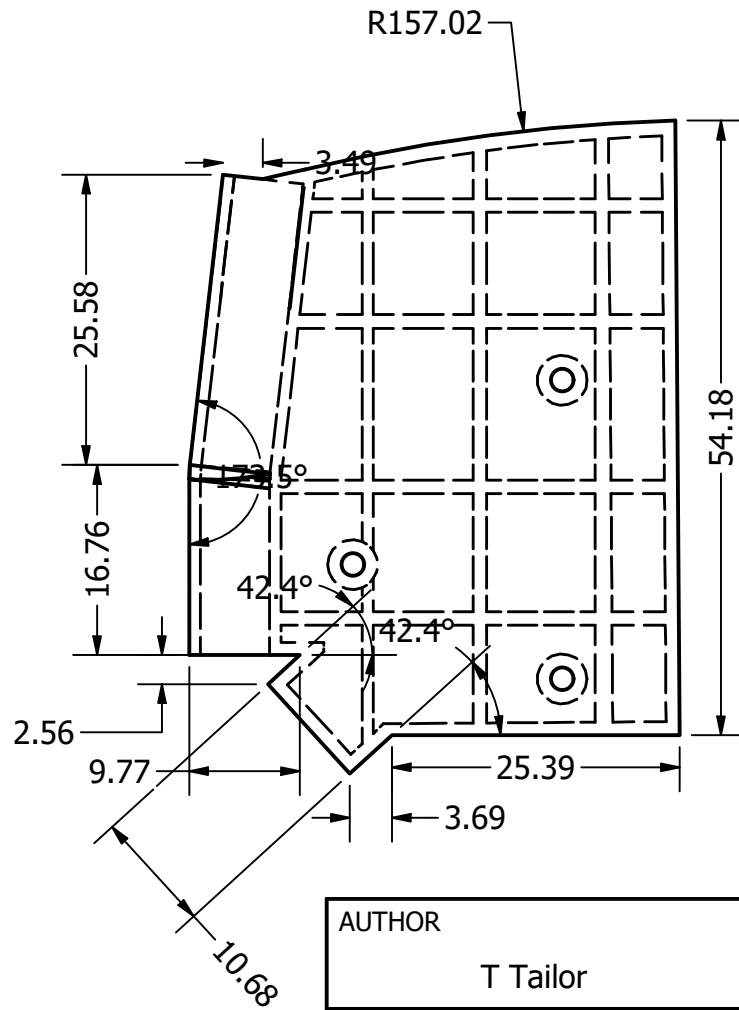
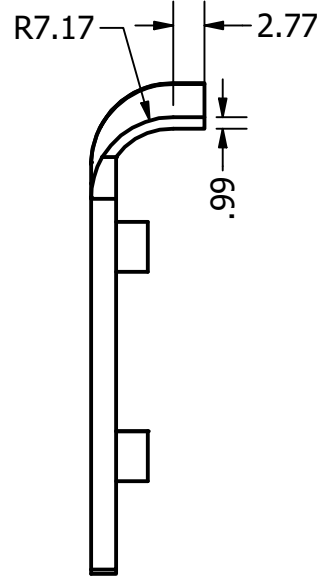
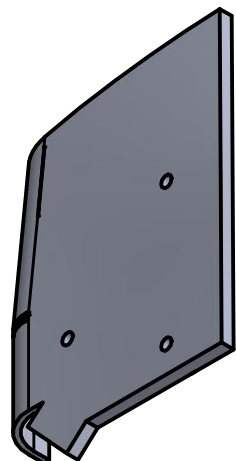
**Note-** Support rib measurements have been left undefined as they do not play a vital role to the concept design, and can thus be arbitrarily added if model is reproduced.

AUTHOR	T Tailor	DATE	04-MAY-20	PART NO.	RH-306
PROJECTION	 	TITLE	Palm Cover Front - C6		
UNLESS OTHERWISE STATED TOLERANCE: ANGULAR .X	+- 0.15% +- 0.15%	UNIT	mm	SCALE	DWG NO DWG-306-A
					SHEETS 1 OF 1

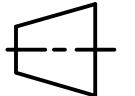


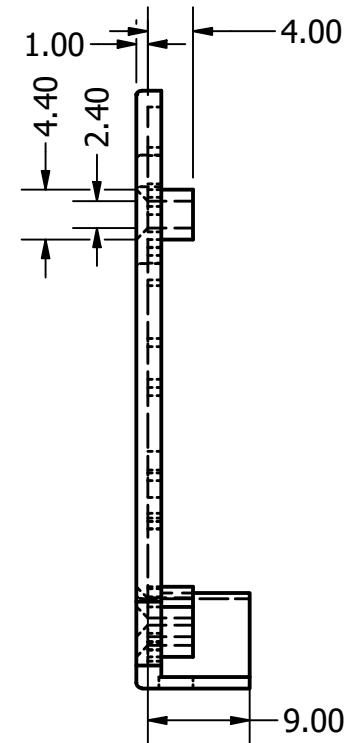
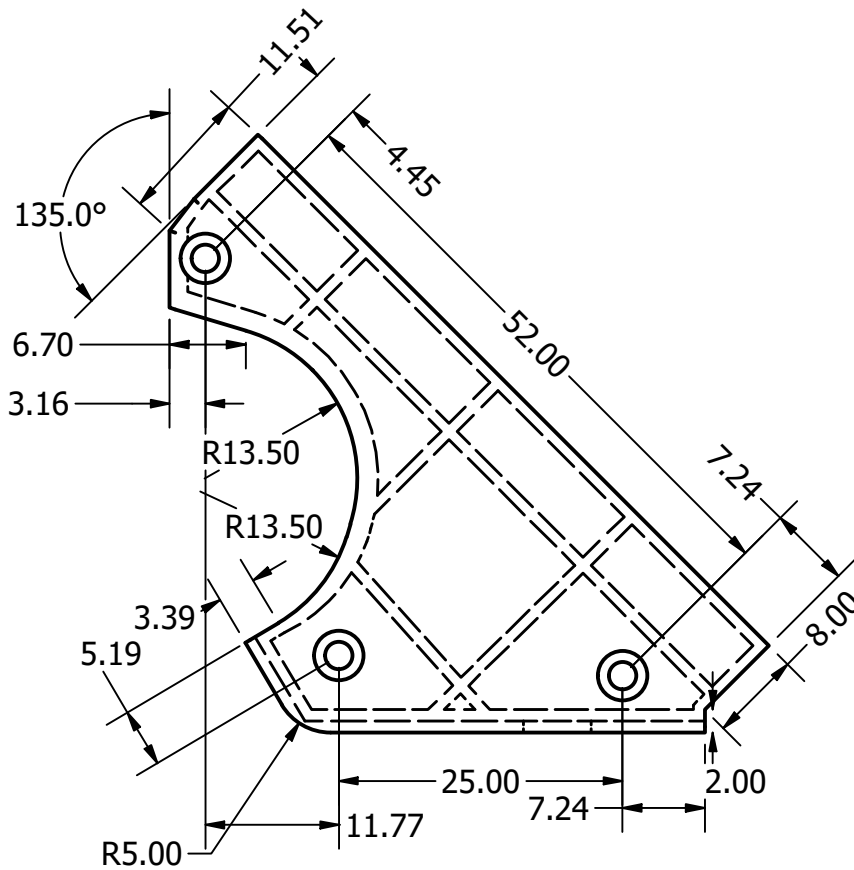
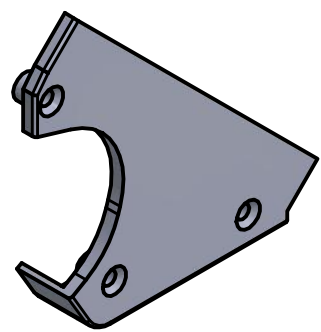
AUTHOR	T Tailor	DATE	04-MAY-20	PART NO.	RH-307
PROJECTION		TITLE	Palm Cover Back- C8		
UNLESS OTHERWISE STATED TOLERANCE: ANGULAR .X	$\pm 0.15\%$ $\pm 0.15\%$	UNIT	mm	SCALE	DWG NO DWG-307-A
					SHEETS 1 OF 1

Note- Support rib measurements have been left undefined as they do not play a vital role to the concept design, and can thus be arbitrarily added if model is reproduced.



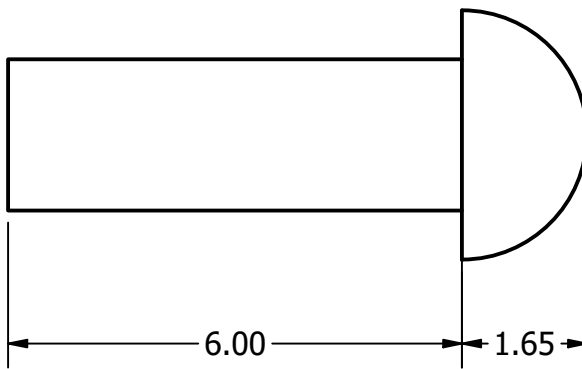
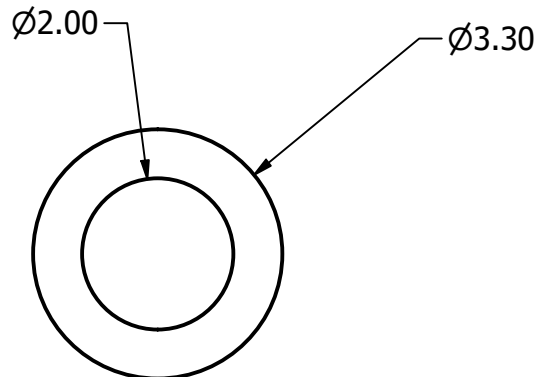
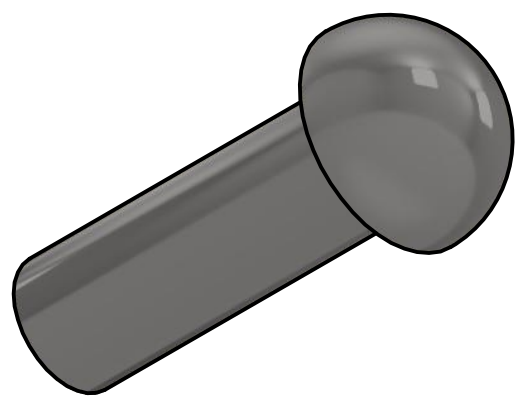
**Note-** Support rib measurements have been left undefined as they do not play a vital role to the concept design, and can thus be arbitrarily added if model is reproduced.

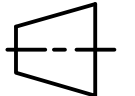
AUTHOR	T Tailor	DATE	04-MAY-20	PART NO.	RH-308
PROJECTION	 	TITLE	Palm Cover Back- C7		
UNLESS OTHERWISE STATED TOLERANCE: ANGULAR .X	+- 0.15% +- 0.15%	UNIT	mm	SCALE	DWG NO DWG-308-A
					SHEETS 1 OF 1

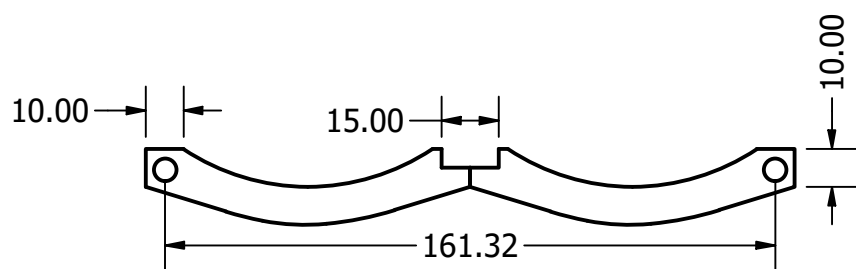
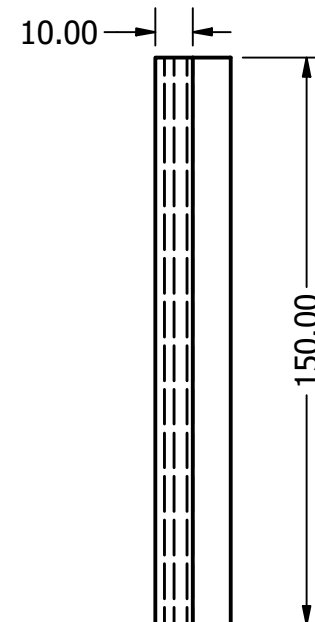
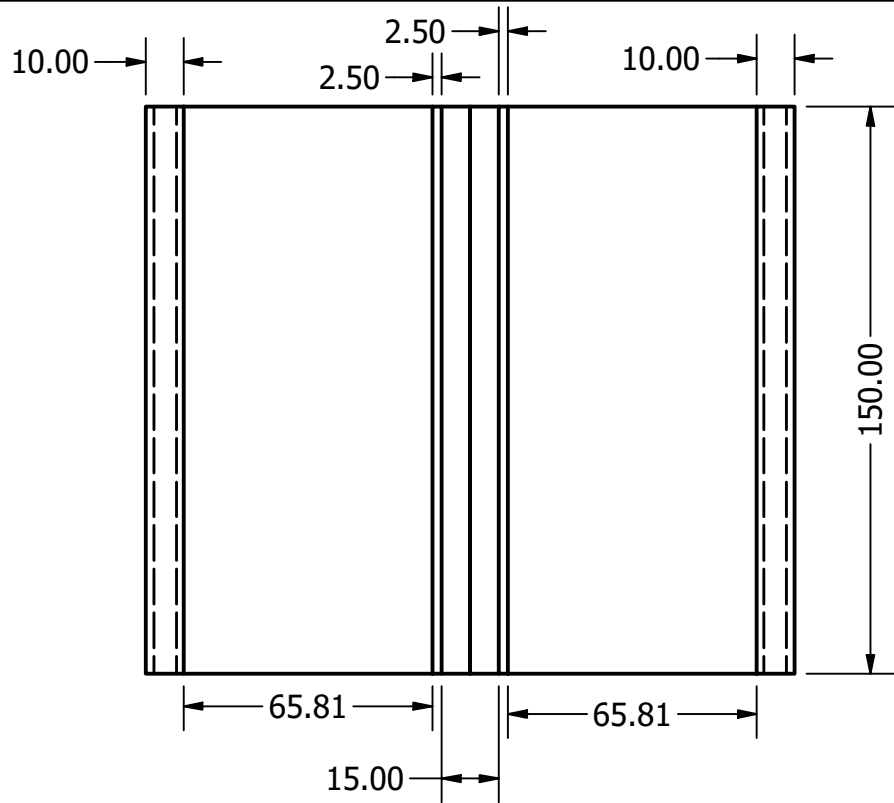


**Note-** Support rib measurements have been left undefined as they do not play a vital role to the concept design, and can thus be arbitrarily added if model is reproduced.

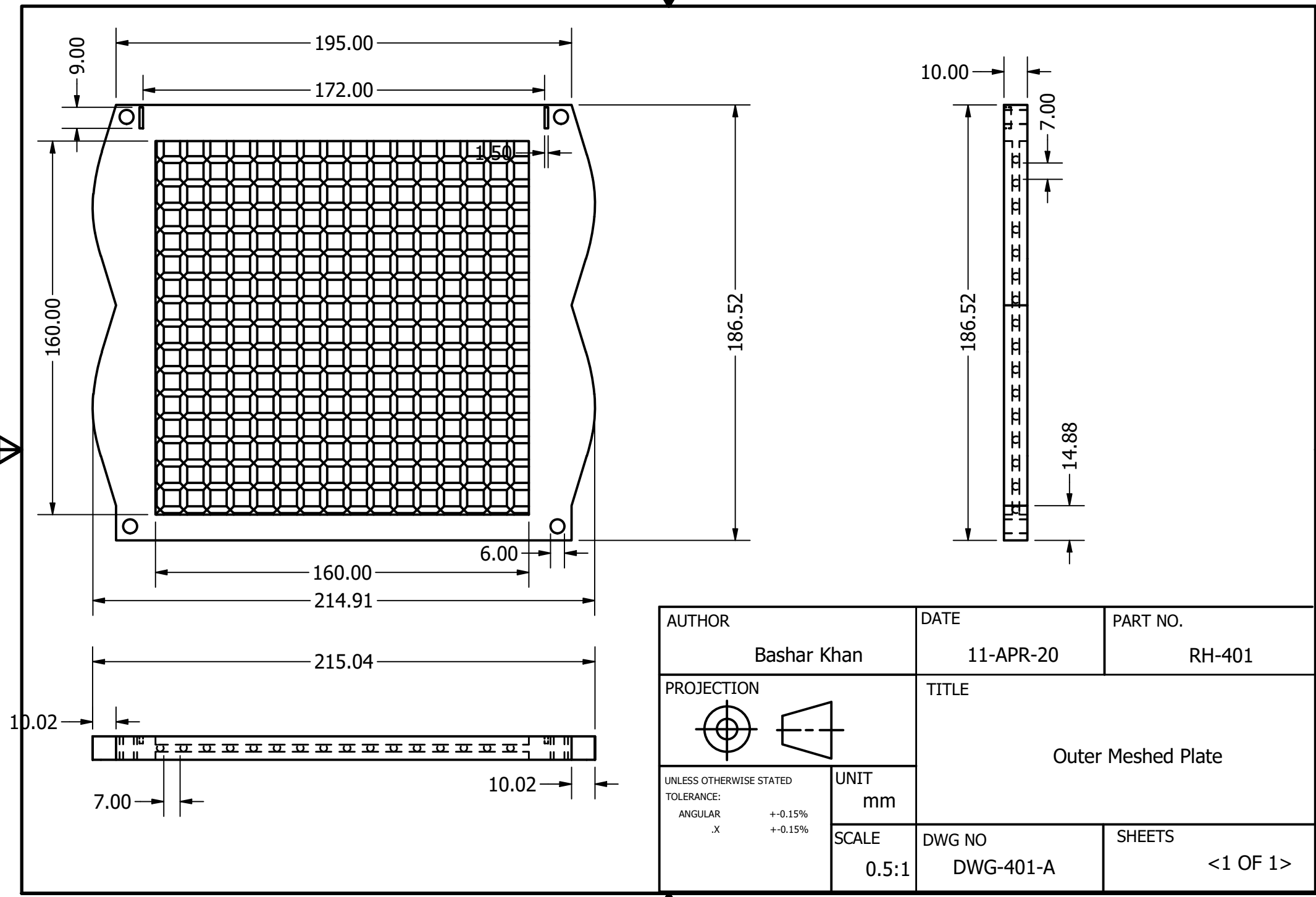
AUTHOR	T Tailor	DATE	04-MAY-20	PART NO.	RH-309
PROJECTION		TITLE	Palm Cover Back- C6		
UNLESS OTHERWISE STATED TOLERANCE: ANGULAR .X	$\pm 0.15\%$ $\pm 0.15\%$	UNIT	mm	SCALE	DWG NO DWG-309-A
					SHEETS 1 OF 1

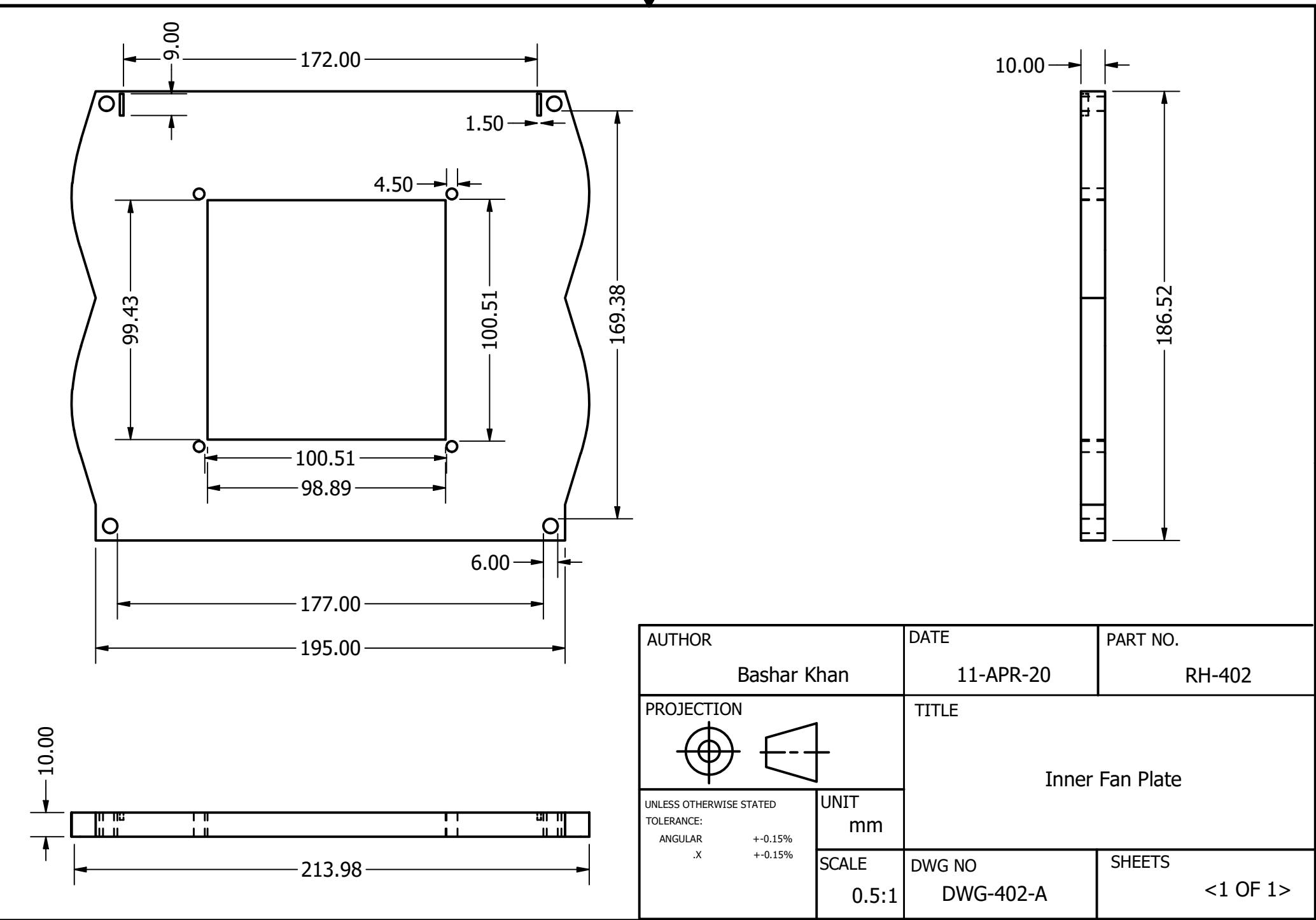


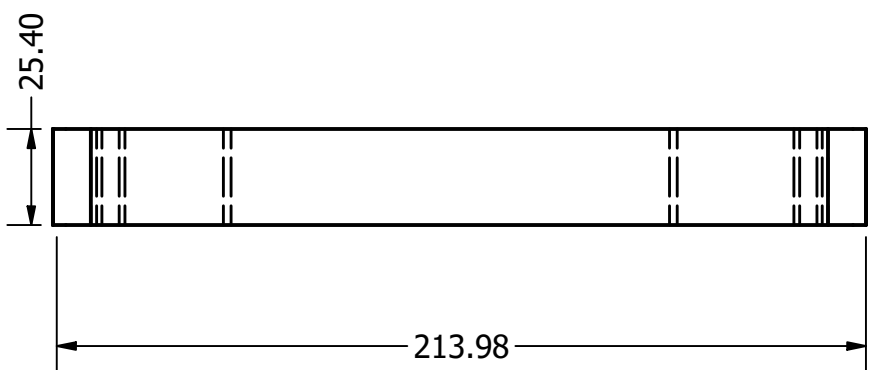
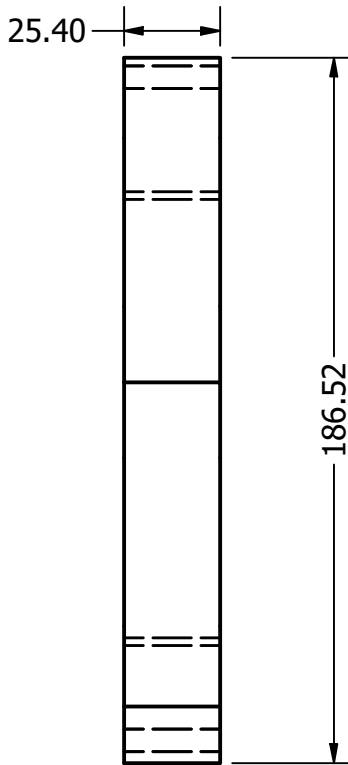
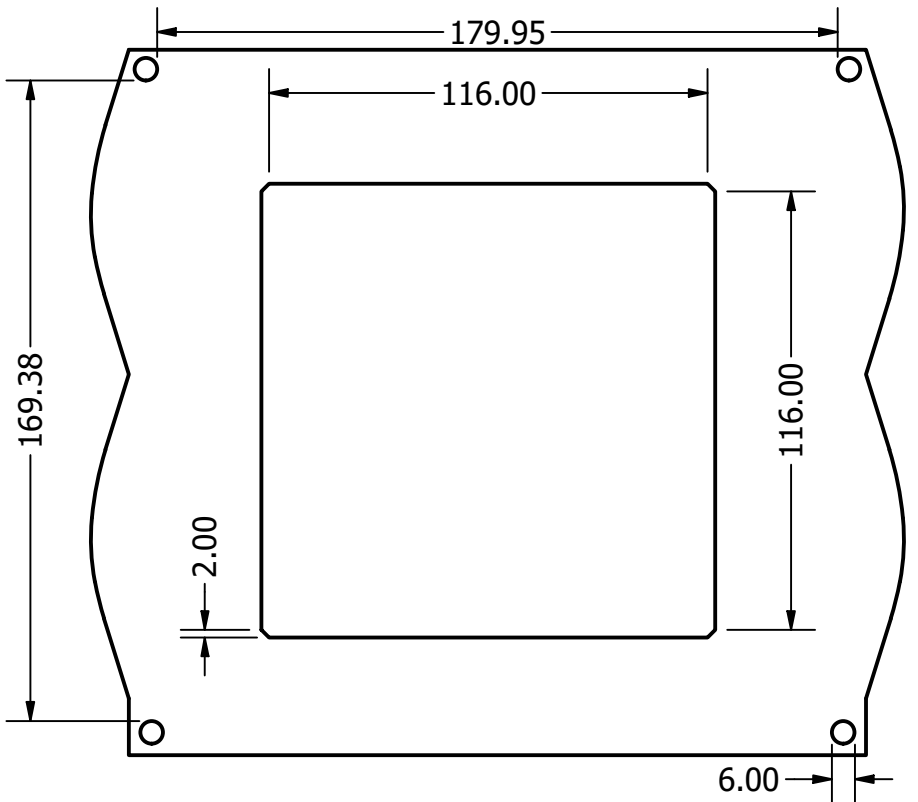
AUTHOR	T Tailor	DATE	04-MAY-20	PART NO.	RH-310
PROJECTION	 	TITLE	Routing Pin		
UNLESS OTHERWISE STATED TOLERANCE: ANGULAR .X	$\pm 0.15\%$ $\pm 0.15\%$	UNIT	mm	SCALE	DWG NO
		10:1	DWG-310-A	SHEETS	1 OF 1

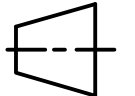


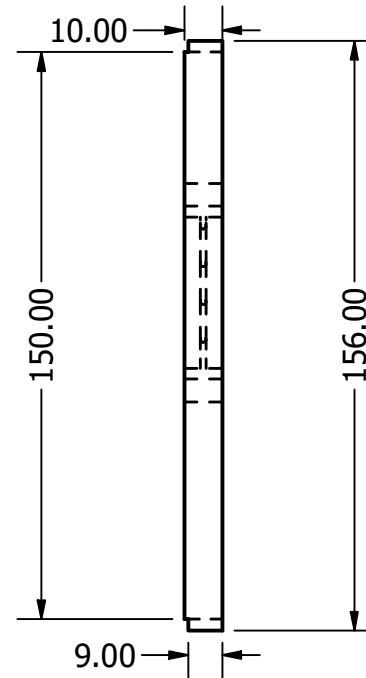
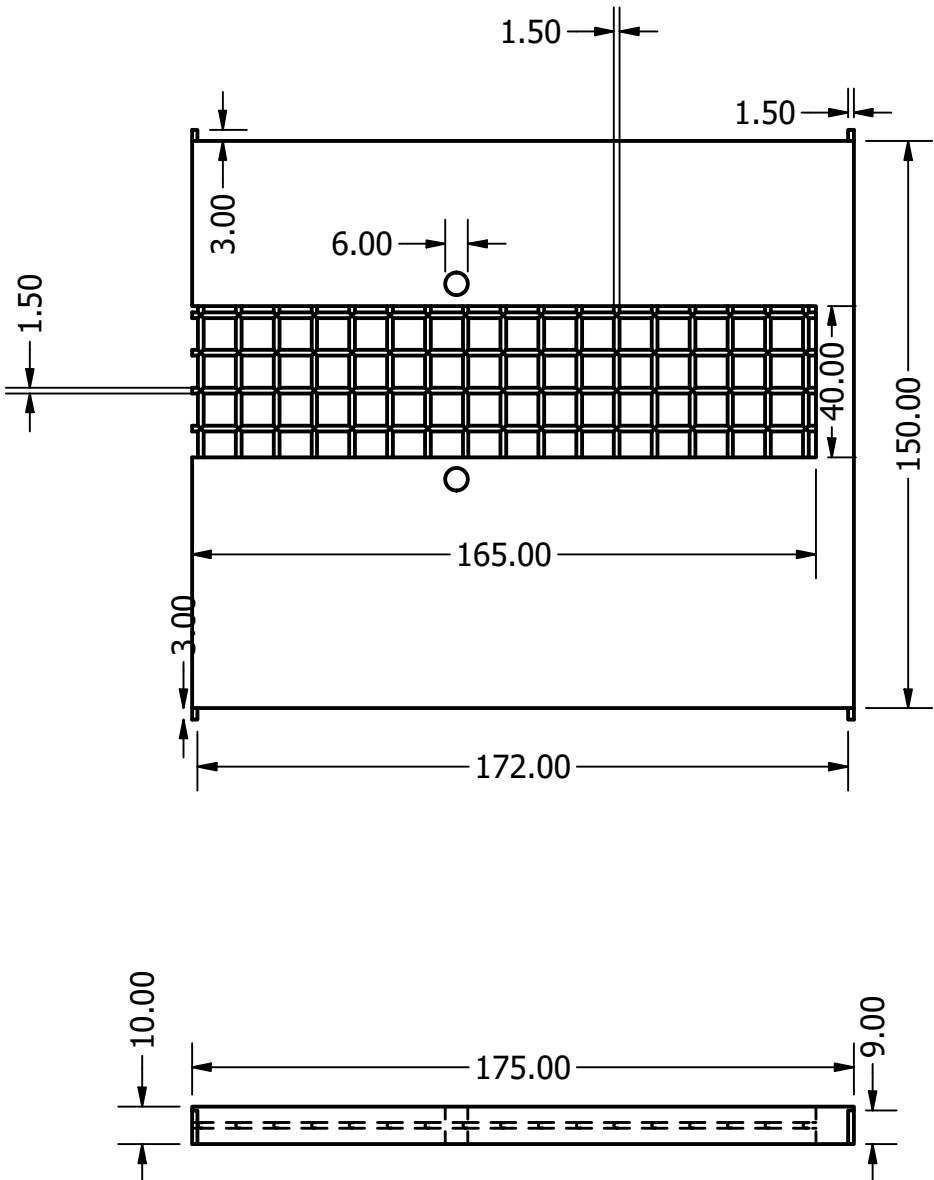
AUTHOR	Bashar Khan	DATE	11-APR-20	PART NO.	RH-400
PROJECTION	 	TITLE	Side Plate		
UNLESS OTHERWISE STATED TOLERANCE: ANGULAR .X	+0.15% +0.15%	UNIT	mm	SCALE	DWG NO DWG-400-A
					SHEETS <1 OF 1>



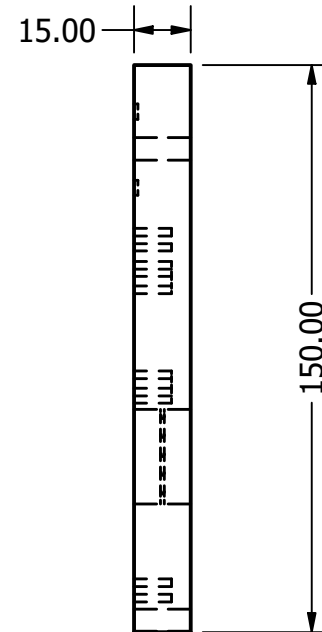
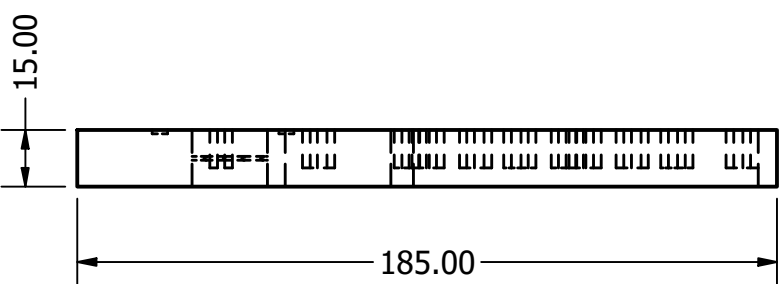
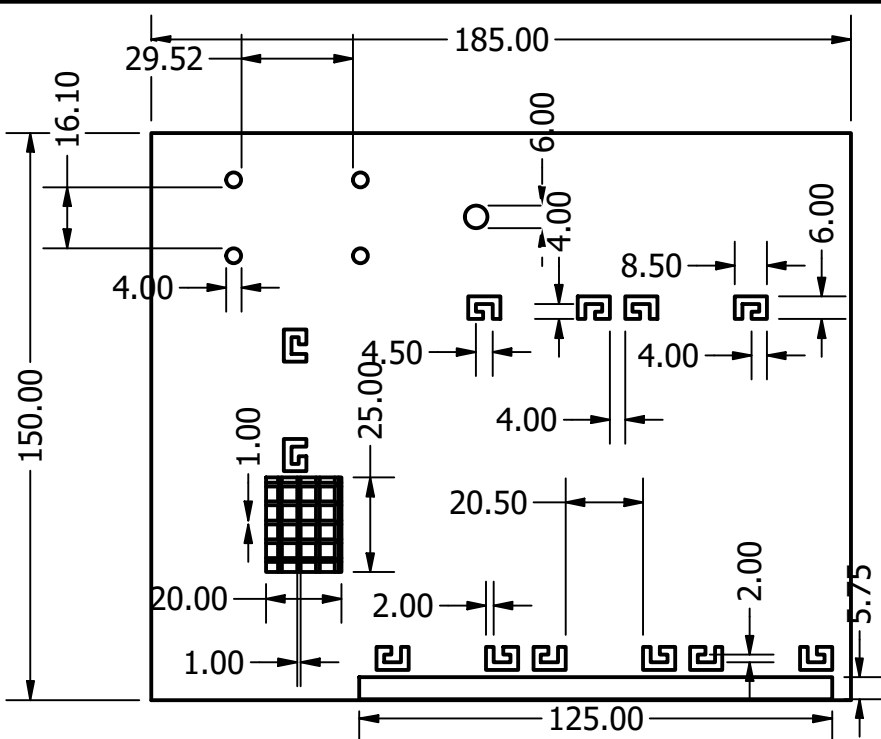


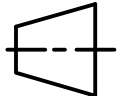


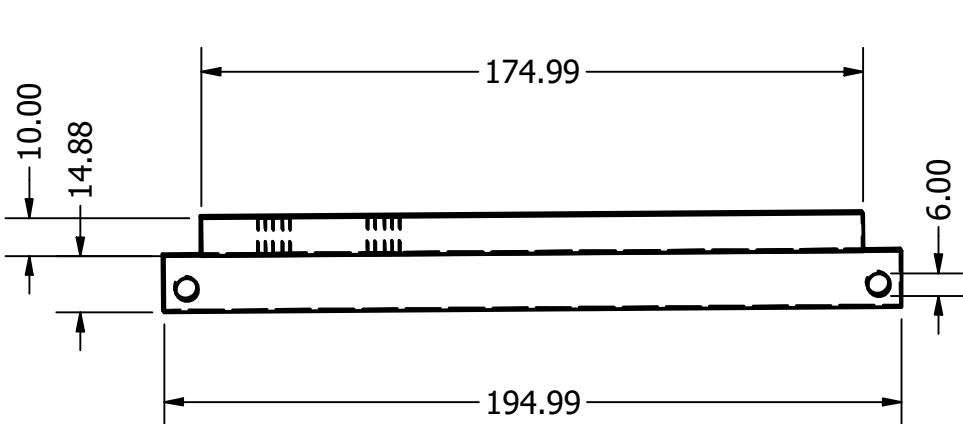
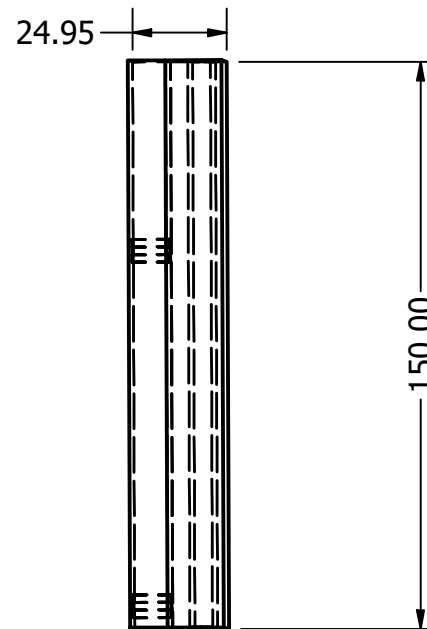
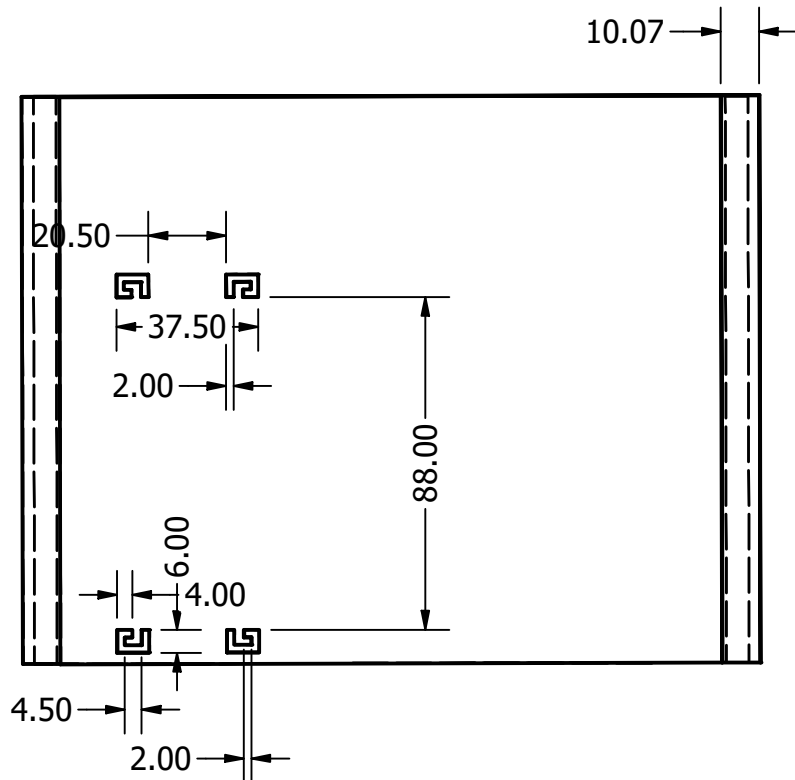
AUTHOR	Bashar Khan	DATE	11-APR-20	PART NO.	RH-403
PROJECTION	 	TITLE	Outer Fan Plate		
UNLESS OTHERWISE STATED TOLERANCE: ANGULAR .X	+0.15% +0.15%	UNIT	mm	SCALE	DWG NO DWG-403-A
					SHEETS <1 OF 1>



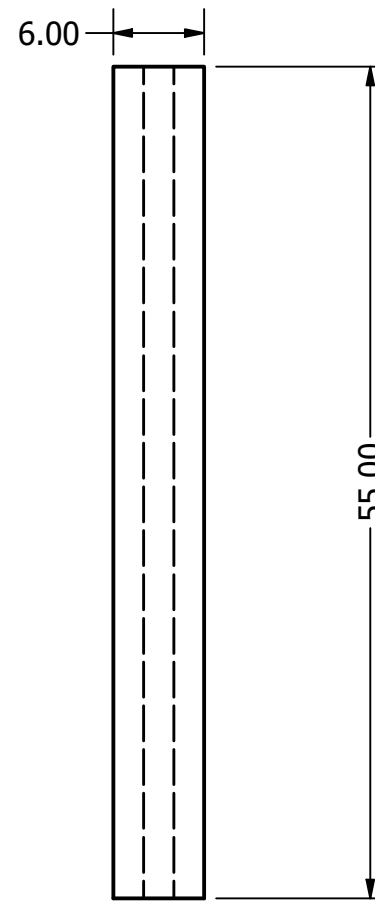
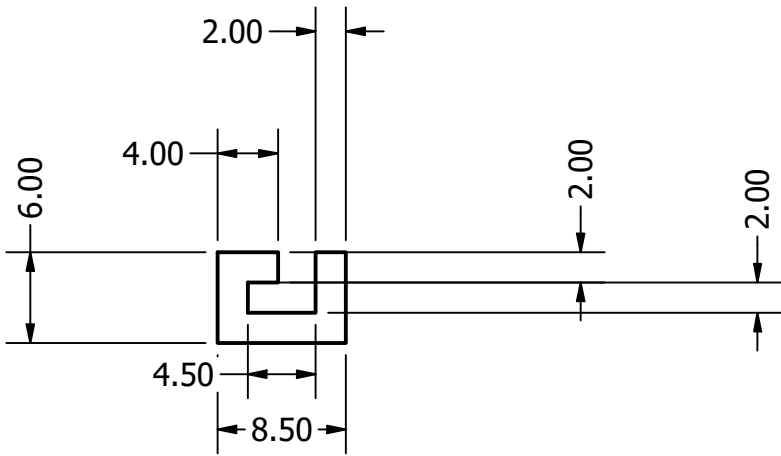
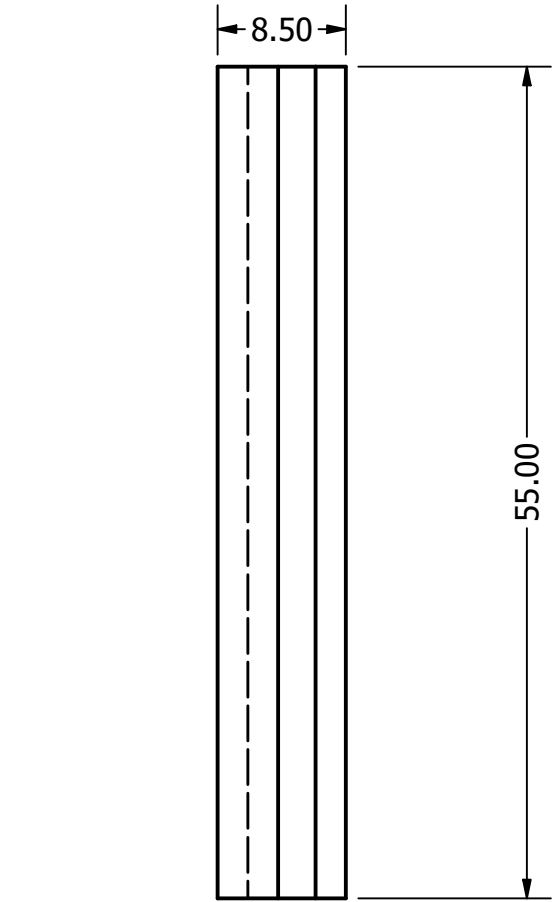
AUTHOR	Bashar Khan	DATE	11-APR-20	PART NO.
PROJECTION		TITLE	Top Plate	
UNLESS OTHERWISE STATED TOLERANCE: ANGULAR .X	$\pm 0.15\%$ $\pm 0.15\%$	UNIT	mm	
SCALE	0.5:1	DWG NO	DWG-404-A	SHEETS
				<1 OF 1>



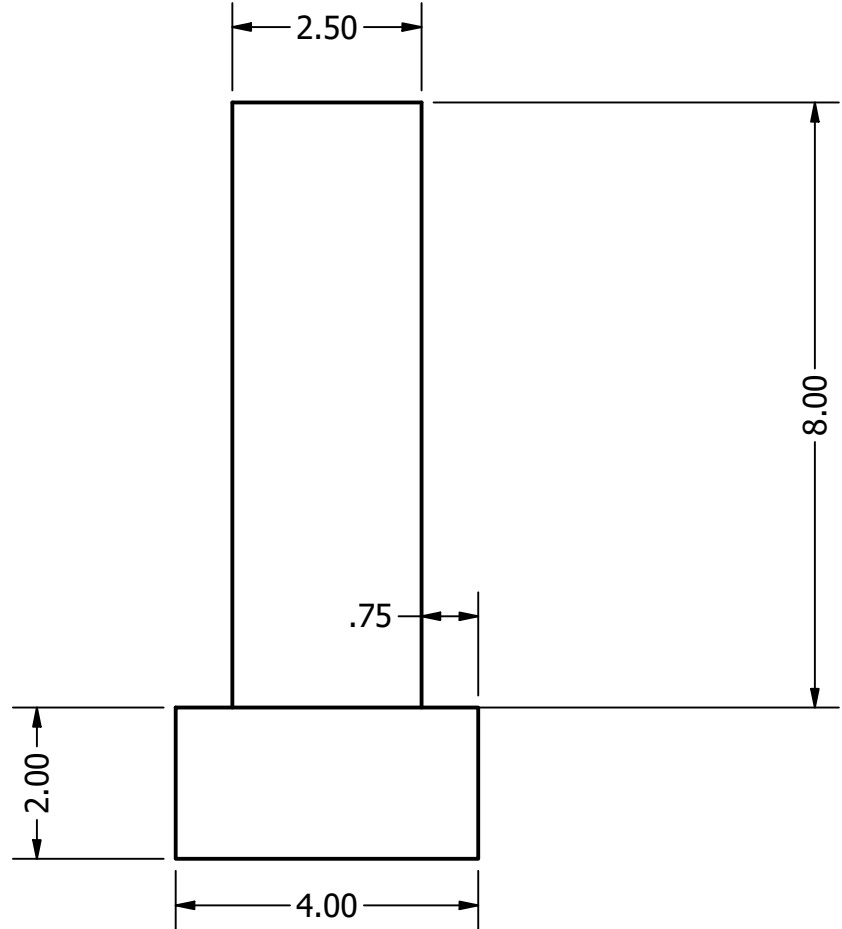
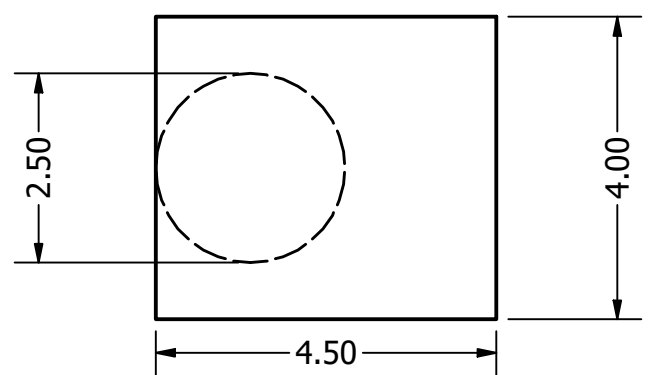
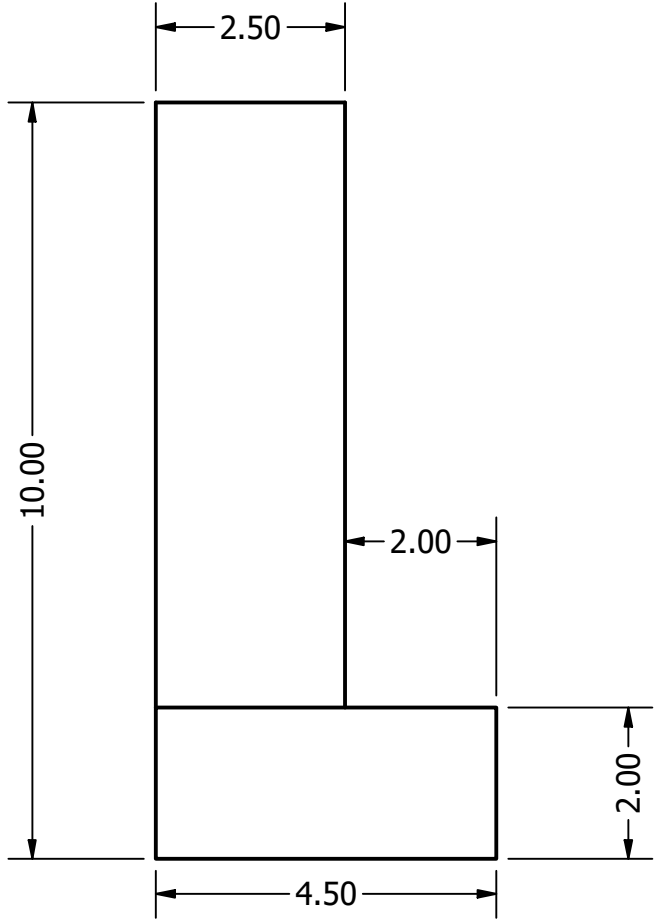
AUTHOR	Bashar Khan	DATE	11-APR-20	PART NO.
PROJECTION	 	TITLE	Middle Base Plate	
UNLESS OTHERWISE STATED TOLERANCE: ANGULAR .X	$\pm 0.15\%$ $\pm 0.15\%$	UNIT	mm	
SCALE	0.5:1	DWG NO	DWG-405-A	SHEETS
				<1 OF 1>

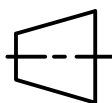


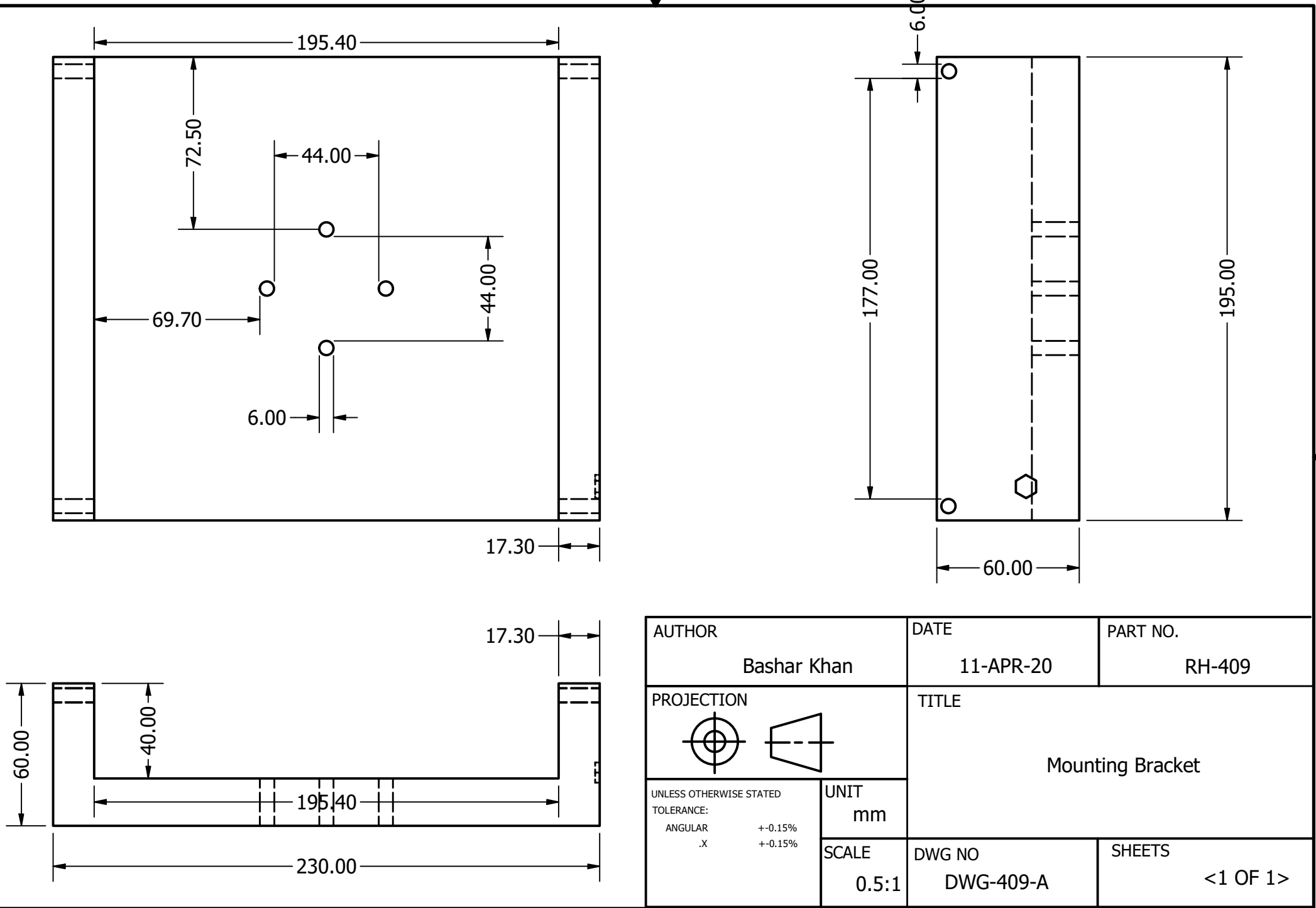
AUTHOR	Bashar Khan	DATE	11-APR-20	PART NO.	RH-406
PROJECTION			TITLE	Floor Plate	
UNLESS OTHERWISE STATED TOLERANCE: ANGULAR .X	+0.15% +0.15%	UNIT mm	SCALE 0.5:1	DWG NO DWG-406-A	SHEETS <1 OF 1>

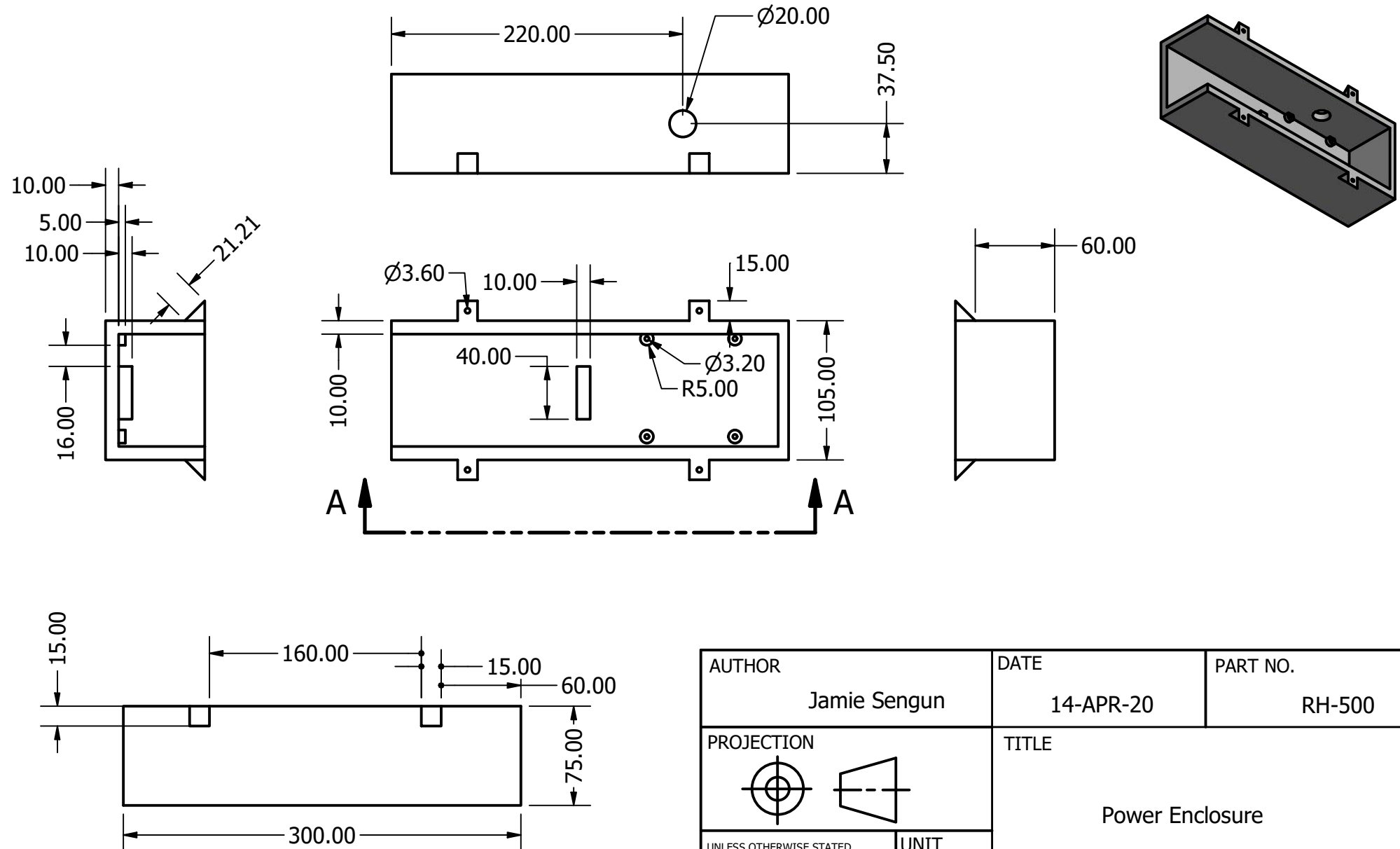


AUTHOR	Bashar Khan	DATE	11-APR-20	PART NO.	RH-407
PROJECTION	 	TITLE	Motor Rail		
UNLESS OTHERWISE STATED TOLERANCE: ANGULAR .X	+0.15% +0.15%	UNIT	mm	SCALE	DWG NO
		2:1	DWG-407-A	SHEETS	<1 OF 1>



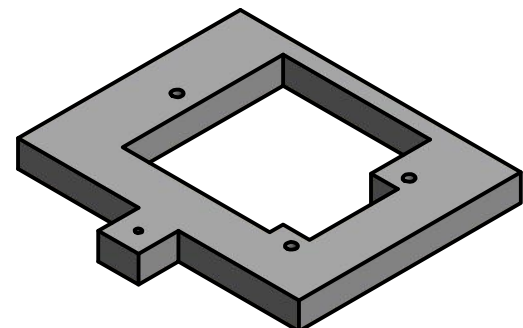
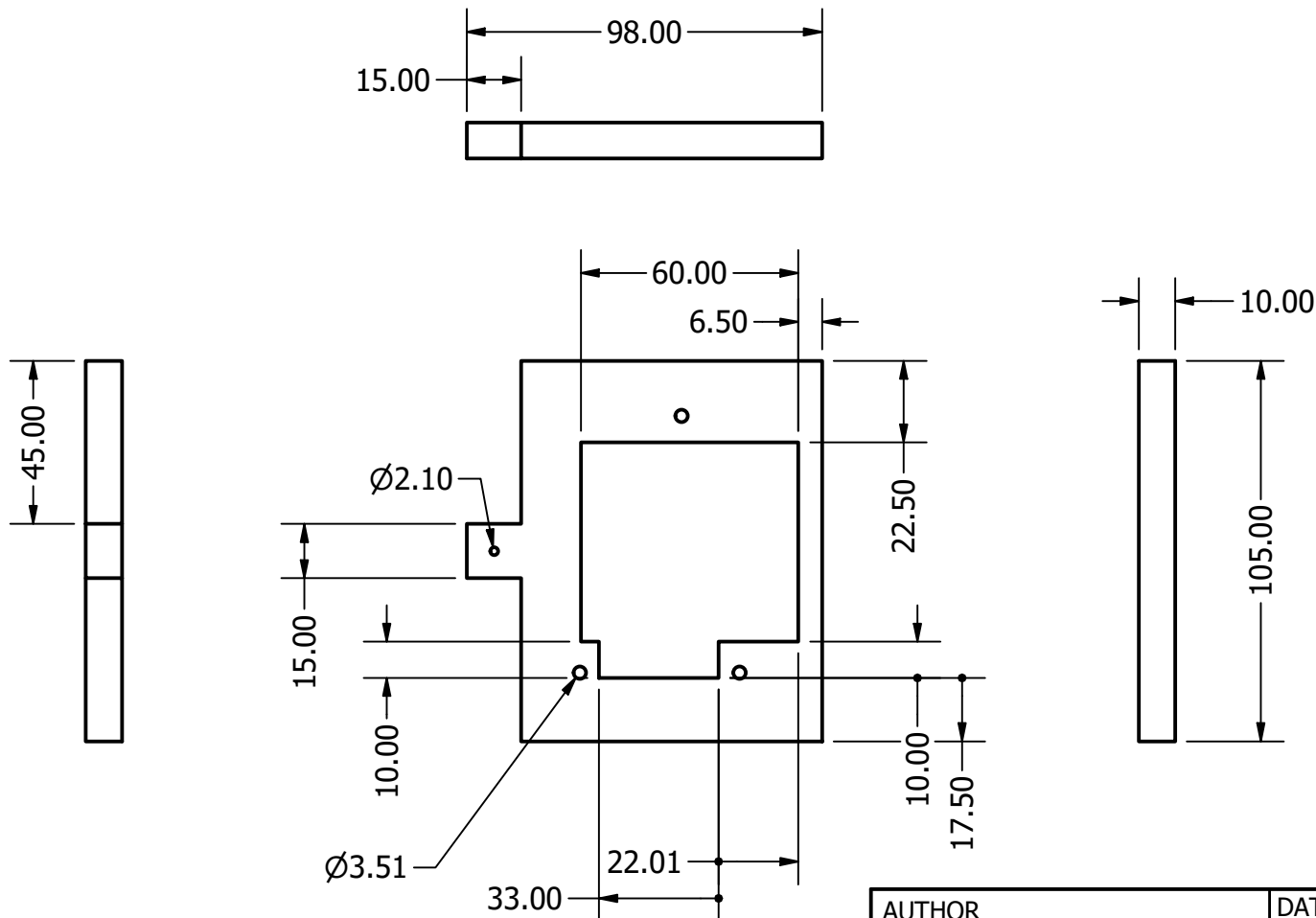
AUTHOR	Bashar Khan	DATE	11-APR-20	PART NO.	RH-408
PROJECTION	 	TITLE	Motor Rail Pin		
UNLESS OTHERWISE STATED TOLERANCE: ANGULAR .X	+0.15% +0.15%	UNIT	mm	SCALE	DWG NO
		5:1	DWG-408-A	SHEETS	<1 OF 1>

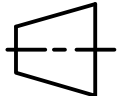


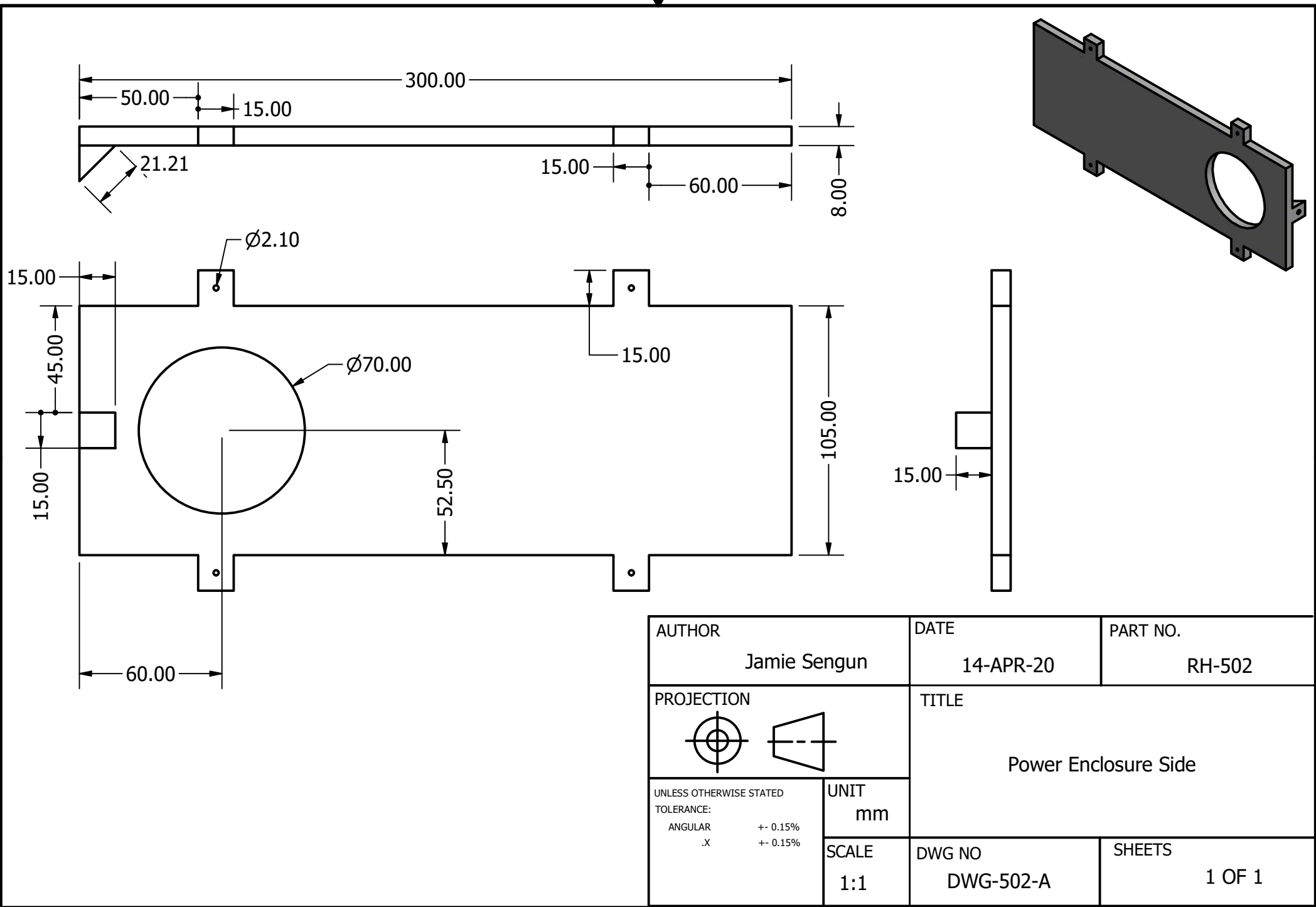


VIEW A-A  
SCALE 1 / 4

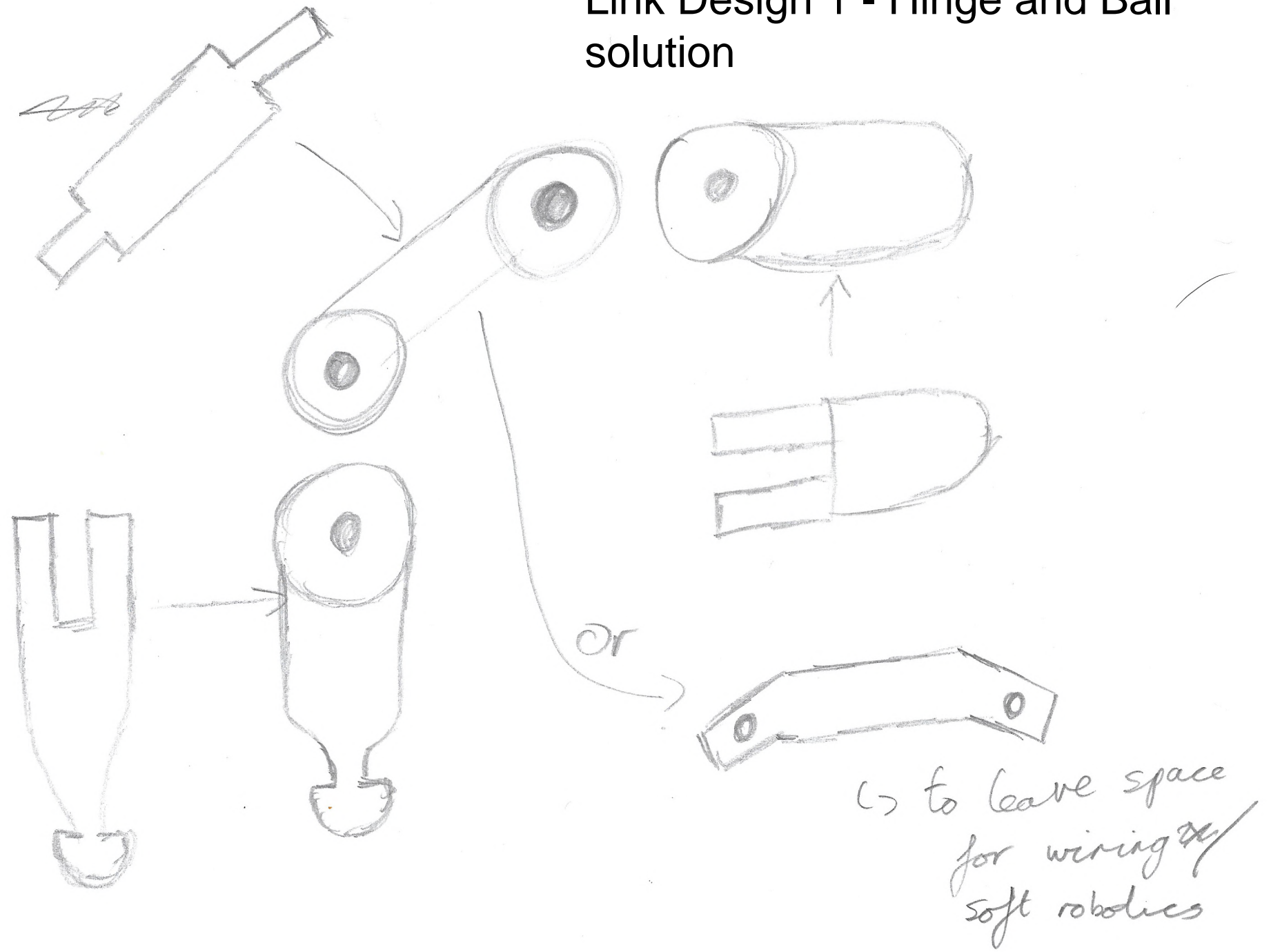
AUTHOR	Jamie Sengun	DATE	14-APR-20	PART NO.	RH-500
PROJECTION			TITLE	Power Enclosure	
UNLESS OTHERWISE STATED TOLERANCE: ANGULAR .X	++ 0.15% ++ 0.15%	UNIT mm			
SCALE 0.25:1	DWG NO DWG-500-A	SHEETS 1 OF 1			



AUTHOR	Jamie Sengun	DATE	14-APR-20	PART NO.	RH-501
PROJECTION	 		TITLE		
UNLESS OTHERWISE STATED TOLERANCE: ANGULAR .X	++ 0.15% ++ 0.15%	UNIT mm			Power Enclosure Cover
		SCALE 0.5:1	DWG NO DWG-501-A	SHEETS	1 OF 1

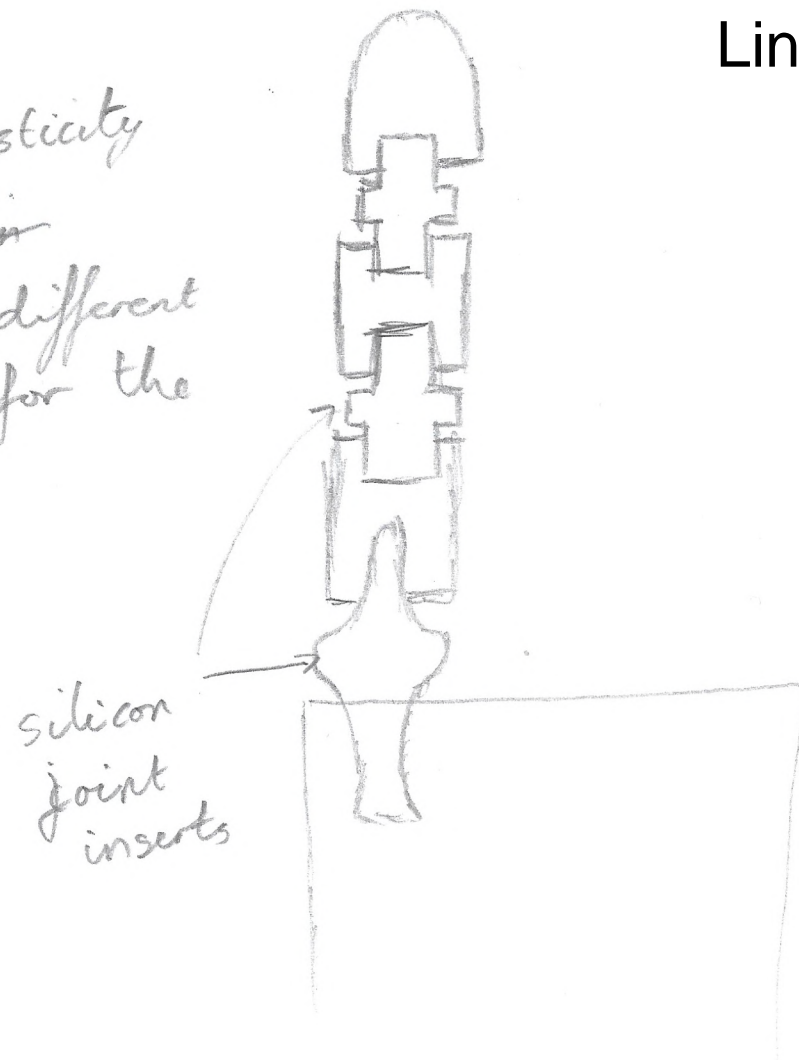


## Link Design 1 - Hinge and Ball solution

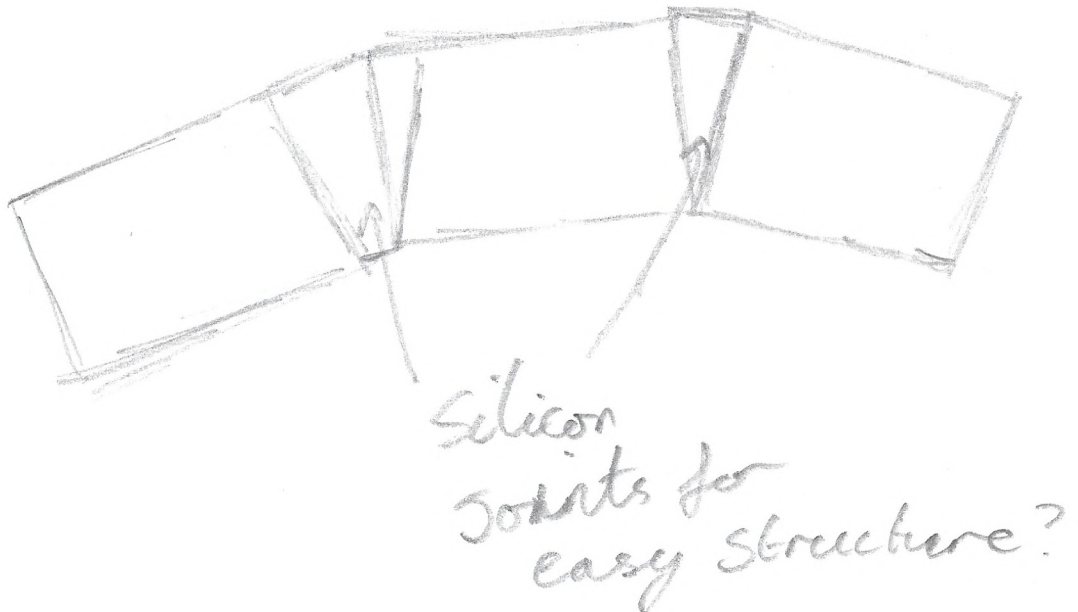


## Link Design 2 - Silicone Joints

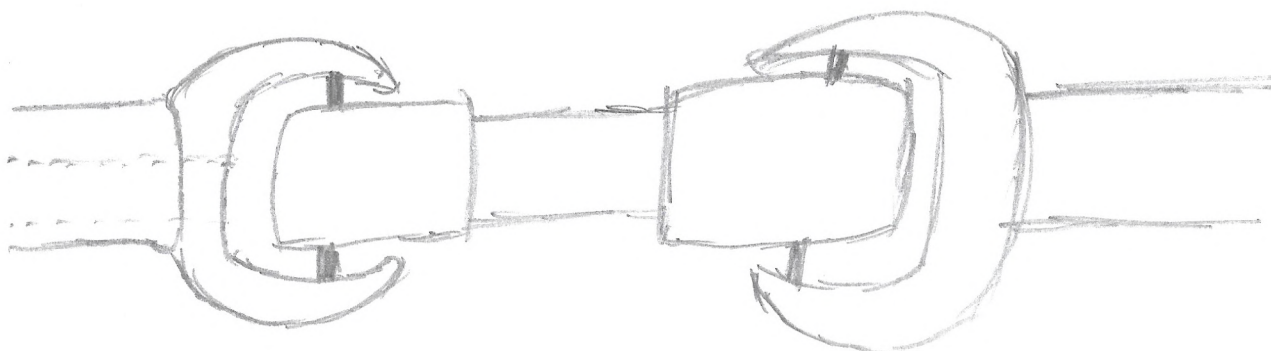
- natural elasticity
- can form air
- can use different geometry for the



## Link Design 3 - Simple Silicone Joint

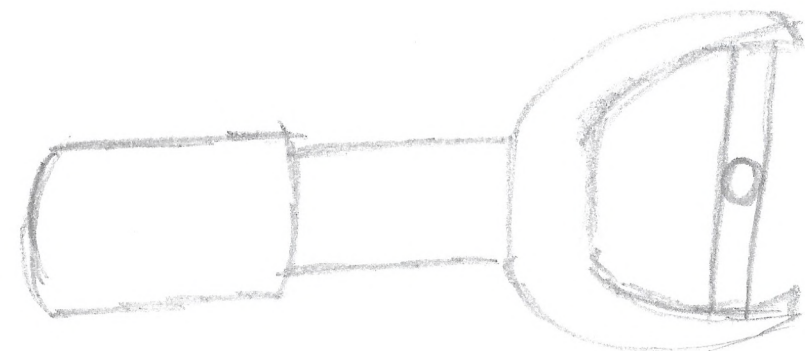


## Link Design 4 - Spanner Knuckle



Cup hinges

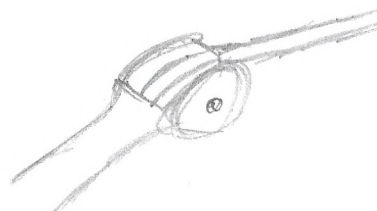
- lots of empty space
- 



## Link Design 5 - Basic Hinge

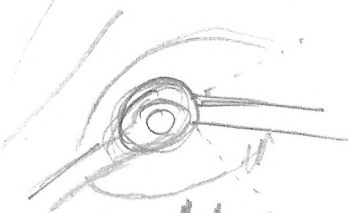
Basic hinge

- ↳ easy to make
- ↳ has internal bolt
- ↳ no ~~room~~ room to move



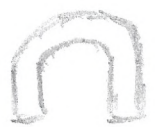
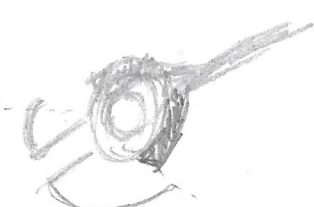
Ball and socket joint

- ↳ high range of motion
- ↳ hard to control



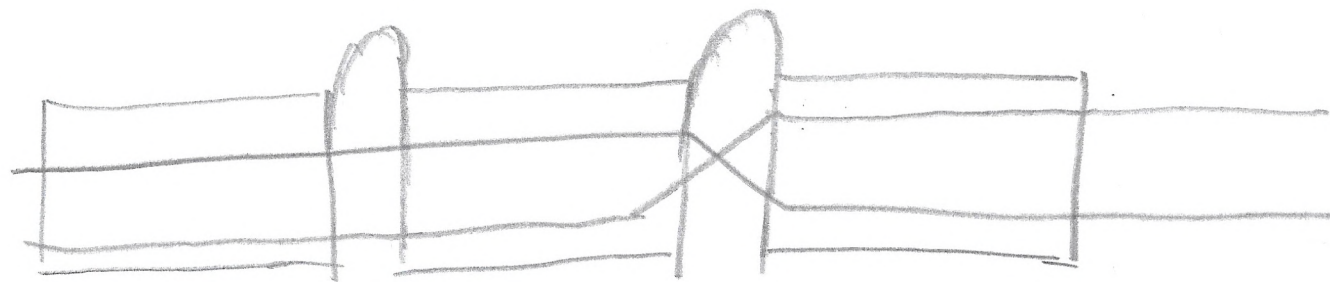
Restricted ball socket

- ↳ high range of motion
- ↳ can move side to side a bit

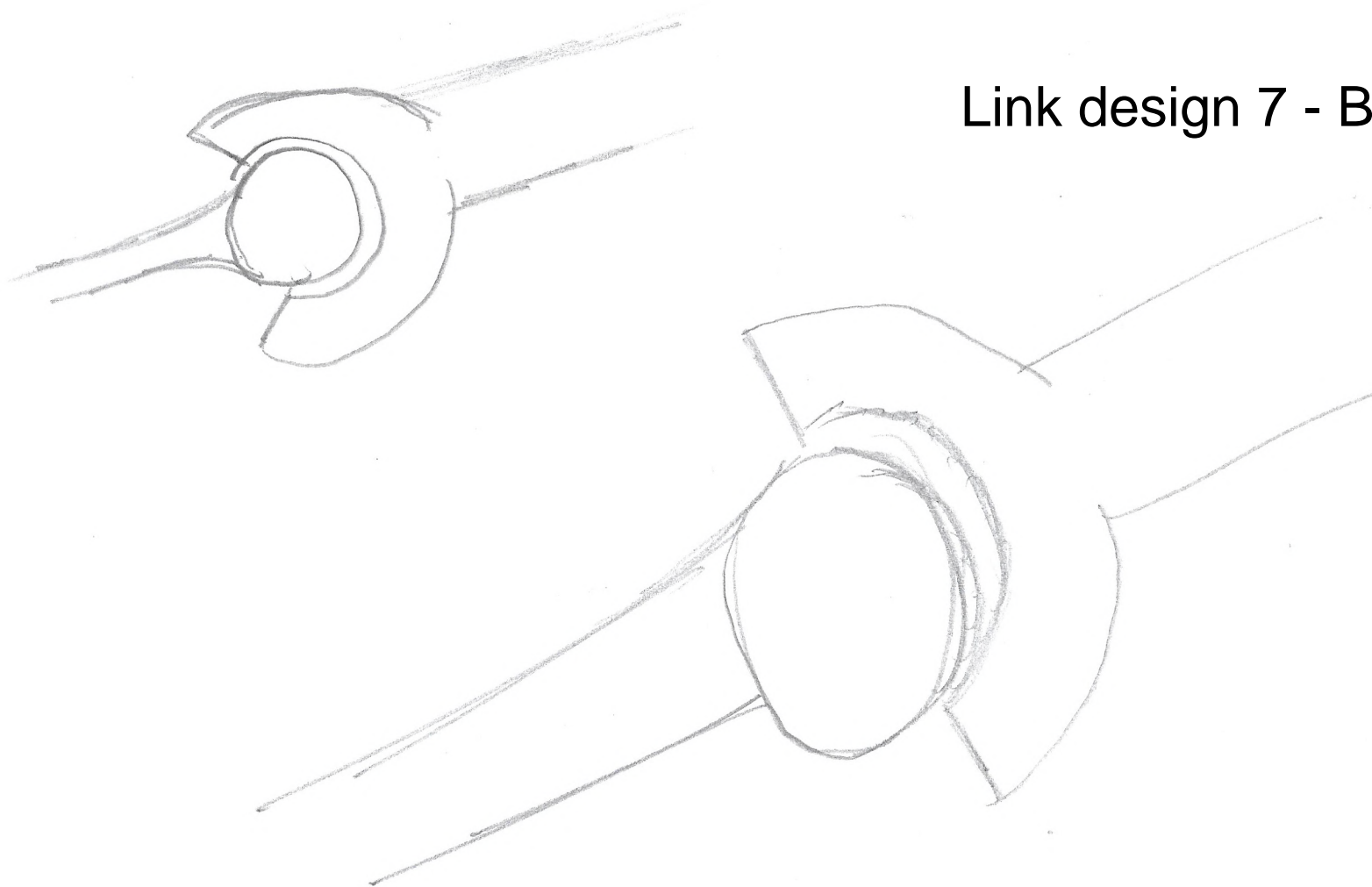


[01]

## Link Design 6 - Criss cross threaded joints



Link design 7 - Ball and socket



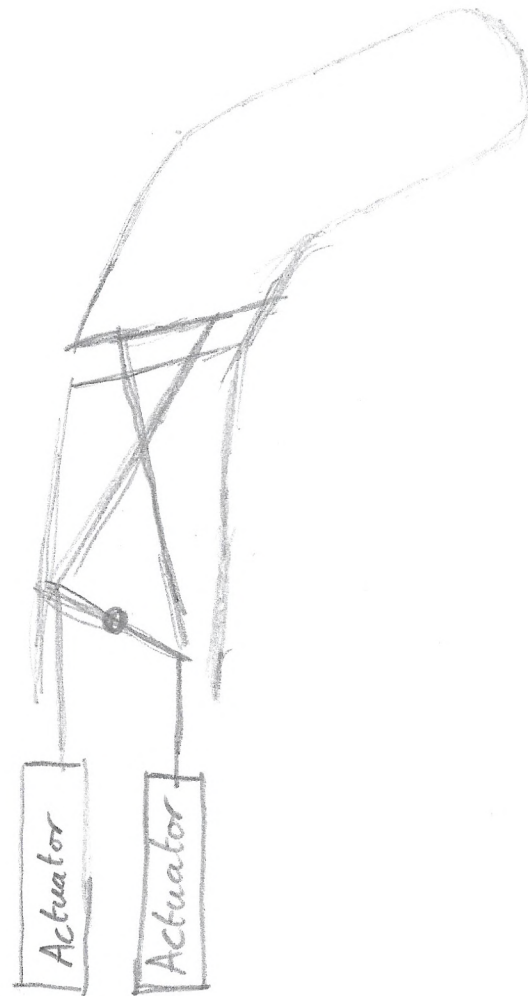
## Link Design 8 - Fully Silicone soft link

inrate spring?

So one material with high ~~elasticity~~<sup>stiffness</sup>  
but regions of lower stiffness



## Link Design 9 - Soft and rigid hybrid design



hard mechanism  
with soft actuators

- ↳ Plenty of space for wiring
- ↳ Simple mechanism
- ↳ not exactly the brief
- ↳ limited range of motion